

# Time Resolved 3D Momentum Imaging Spectroscopy with VUV-XUV Pulse Pairs

Dissertation  
zur Erlangung des Doktorgrades  
der Naturwissenschaften

vorgelegt beim Fachbereich Physik  
der Johann Wolfgang Goethe -Universität  
in Frankfurt am Main

von  
**Felix Paul Sturm**  
aus Frankfurt am Main

Frankfurt, 2015  
(D30)

vom Fachbereich Physik der  
Johann Wolfgang Goethe -Universität als Dissertation angenommen.

Dekan:	Prof. Dr. René Reifarth
1. Gutachter:	Prof. Dr. Reinhard Dörner
2. Gutachter:	Dr. Thorsten Weber
Datum der Disputation:	2016

*meinen Eltern*



# Contents

<b>1</b>	<b>Introduction</b>	<b>3</b>
<b>2</b>	<b>Physical Background</b>	<b>9</b>
2.1	Femtosecond Time Resolved Measurements . . . . .	9
2.1.1	Pump-Probe Spectroscopy . . . . .	10
2.2	Ultrafast XUV light sources . . . . .	10
2.2.1	Free-Electron Lasers . . . . .	12
2.2.2	High Harmonic Generation . . . . .	12
2.3	XUV Experiments in the Time Domain . . . . .	13
2.4	Dissociative Ionization of Hydrogen Molecules . . . . .	14
2.5	Dissociative Ionization of Oxygen Molecules . . . . .	16
<b>3</b>	<b>Ultrafast XUV Light Source</b>	<b>19</b>
3.1	Frequency Conversion in Optical Fields . . . . .	19
3.2	The Strong-Field Regime . . . . .	20
3.3	High Harmonic Generation . . . . .	21
3.3.1	The 3-Step Model of High Harmonic Generation . . . . .	21
3.3.2	Phase matching . . . . .	26
3.3.3	Reabsorption . . . . .	28
3.4	The High Flux HHG Source at LBNL . . . . .	29
3.4.1	Laser System . . . . .	31
3.4.2	High Flux Harmonic Generation . . . . .	31
3.4.3	Manipulation of Spectral Properties . . . . .	34
<b>4</b>	<b>XUV Beamline Components</b>	<b>39</b>
4.1	Energy Selection . . . . .	39
4.1.1	Fluoride Windows . . . . .	42
4.1.2	Metal Foils . . . . .	44
4.1.3	Gas Filter Cell . . . . .	44
4.1.4	Multilayer Coated Mirrors . . . . .	48
4.2	Pump - Probe Interferometer . . . . .	50
4.3	Energy Characterization . . . . .	56
4.3.1	XUV Spectrometer . . . . .	56
4.3.2	Spectral Analysis . . . . .	59
4.4	Vacuum Beamline Components . . . . .	63
4.4.1	Differential Pumping . . . . .	65
4.4.2	In-Vacuum Alignment Tools . . . . .	66
4.4.3	Beam surveillance . . . . .	67
<b>5</b>	<b>MISTERS Experimental End-Station</b>	<b>69</b>
5.1	Gas Target . . . . .	70
5.2	Focusing Optics . . . . .	75
5.3	3D Momentum Imaging Spectrometer and Detectors . . . . .	78
5.3.1	Geometry and Capabilities . . . . .	80

5.3.2	Signal Retrieval and Data Acquisition . . . . .	83
5.3.3	Spectrometer Resolution . . . . .	85
5.4	Beam Alignment and Control of the Infrared beam . . . . .	85
5.5	Vacuum System . . . . .	87
5.6	HHG Intensity Measurement . . . . .	88
5.7	Data Analysis . . . . .	89
5.7.1	Operation at High Count Rates . . . . .	90
<b>6</b>	<b>Experimental Results</b>	<b>95</b>
6.1	Data Analysis Information . . . . .	95
6.1.1	Reconstruction of the 3D Momenta . . . . .	95
6.1.2	Momentum Visualization . . . . .	96
6.1.3	VUV Pulse Sequences . . . . .	97
6.2	Argon Single Ionization . . . . .	98
6.3	Selection Rules for Optical Transitions . . . . .	100
6.4	Hydrogen Molecules . . . . .	102
6.4.1	Experimental Parameters . . . . .	102
6.4.2	Wave Packet Dynamics in Neutral H <sub>2</sub> . . . . .	104
6.4.3	XUV-IR Transitions . . . . .	104
6.4.4	XUV-VUV Transitions . . . . .	108
6.4.5	Predissociation . . . . .	110
6.4.6	3-Step Dissociative Ionization . . . . .	110
6.4.7	Ion Emission Along the Light Propagation Axis . . . . .	114
6.5	Oxygen Molecules . . . . .	114
6.5.1	Ultra High Resolution Spectroscopy . . . . .	116
6.5.2	IR Assisted Dissociation . . . . .	121
6.5.3	Coherent Attosecond Control . . . . .	126
<b>7</b>	<b>Conclusion and Outlook</b>	<b>135</b>
7.1	Summary . . . . .	135
7.2	Outlook . . . . .	137
7.3	Instrument Improvements and Development . . . . .	138
<b>8</b>	<b>Zusammenfassung</b>	<b>143</b>
8.1	Ausblick . . . . .	145
8.2	Verbesserung und Weiterentwicklung des Aufbaus . . . . .	146
<b>A</b>	<b>Appendix</b>	<b>151</b>
A.1	Pulse Propagation in a Dispersive Medium . . . . .	151
A.2	Beam Losses in the Mirror Gap . . . . .	152
A.3	Reflectivity Calculation . . . . .	153
A.4	Additional Filter Spectra . . . . .	154
A.5	Supersonic Jet Measurements . . . . .	155
A.6	Calculated transition energies for H <sub>2</sub> . . . . .	156
A.7	Additional MISTERS Spectra . . . . .	157
A.8	Measurement parameters . . . . .	163
	<b>Bibliography</b>	<b>167</b>
	<b>Acknowledgements</b>	<b>185</b>
	<b>Index</b>	<b>189</b>

# 1 Introduction

*“Das schönste Glück des denkenden Menschen ist, das Erforschliche erforscht zu haben und das Unerforschliche zu verehren.”*

— Johann Wolfgang von Goethe

Light and its interaction with the world around us is an integral part of our lives. In fact, the light emitted by the sun does not only allow us to see the world with our own eyes but it is the main source of energy for this planet. Due to its prominent role in life on earth, the interaction of light and other electromagnetic radiation with matter has been a major topic of research in the past century. In biology, photosynthesis, the conversion of light to other forms of energy, is the starting point for the development of organisms. This process was also responsible for the energy stored in fossil fuels which still drives the worlds economies. Much effort is invested into trying to understand the chemistry of photosynthesis in order to develop new bio-fuels imitating nature’s efficiency in light-to-energy conversion. In photo-voltaics, we try to convert electromagnetic radiation into electric energy as a way of directly transforming the energy of the sun into a universally usable form. The interaction of radiation outside the visible spectrum with our body is also extremely important for our survival on earth. Radiation in the ultraviolet spectrum can cause cancer in our body and nature has developed sophisticated mechanisms to protect our cells from damage. On earth, the atmosphere provides a barrier to most of the damaging radiation, but on other planets, humans would not survive long without new ways of photo-protection. These examples, emphasize the importance of studying light-matter interaction.

On a microscopic level, the absorption of light can be described by the absorption of portions of energy called photons. The electrons surrounding the nuclei can be described by specific *electronic states* and a transfer between different levels is called an electronic transition. The electrons are responsible for the structural arrangement of the nuclei in a molecule by forming bonds or repelling each other due to their charge. On the smallest scale of light matter interaction, photons are absorbed by the electrons causing electronic transitions or ionization, the removal of the electron from the molecule. Thus, the absorption of energy in the form of electromagnetic radiation changes the electronic structure of the molecule. This is the fundamental microscopic process of macroscopic photo-chemical reactions.

In atoms, the absorption of a photon causes an electronic transition that leaves the system in an excited state. This state is only transient, and the atom will eventually return to its electronic ground state by emitting a photon, known as *fluorescence*, or ejecting an electron. In molecules, the electronic structure is more complex as the electronic states depend on the nuclear degrees of freedom defined by the position of the nuclei with respect to each other. In linear molecules, such as hydrogen or oxygen molecules, the distance of the two nuclei is the only (internal) degree of freedom. The electronic structure can be described by potential energy curves (PEC) where the energy of each electronic state depends on the internuclear separation. This description is based on the assumption that the electrons move much faster than the nuclei and can therefore be treated separately from the nuclear motion, an approach called *Born-Oppenheimer approximation*. This picture becomes invalid when potential energy curves of different electronic states cross or come very close in energy. As a result, avoided crossings are formed where electronic and nuclear degrees of freedom are strongly coupled.

Molecules with three or more nuclei have additional vibrational modes such as bending and stretching. The electronic states are then described by surfaces in a multi-dimensional space spanned by all internal degrees of freedom. Points of avoided contact between potential energy surfaces (PES) form seams or conical intersections. Due to the strong non-Born-Oppenheimer coupling between electronic and nuclear motion at these nuclear configurations, so-called, non-adiabatic transitions between the neighboring states occur. These transitions can be extremely fast, on the order of just tens of femtoseconds ( $10^{-15}$  s), thus, they can be the dominant pathway of electronic relaxation outcompeting ionization or radiative decay. This form of energetic dissipation is extremely important, as the excitation energy is transferred into nuclear motions such as molecular vibration or bending, often preventing the molecule from ionization and subsequent fragmentation, the alternative fast relaxation process. Famous examples of macroscopic phenomena that include such ultra-fast relaxation processes include the energy transfer in photosynthesis [144], in vision [122], as well as photo-protection processes in our skin that prevent the development of cancer [139].

Evidently, the static picture of matter illuminated by electromagnetic radiation only provides a limited amount of information that is usually insufficient to understand the complete fundamental photo-chemical reaction, such as non-adiabatic transitions mentioned above. When energy is stored in a system, such as in any form of life, dynamical processes develop that are a key piece of the puzzle explaining nature. The ability to understand and the possibility to control these processes requires a thorough investigation of their dynamical real-time evolution at every step of the reaction on a fundamental molecular level.

In the macroscopic world, we capture motion by taking multiple images in a fast sequence. In order to capture the motion of an object without a blurring of the image, the illumination time of a single snap-shot needs to be faster than a significant change in the picture. In a film-camera, the object is continuously illuminated while the aperture speed defines the illumination time. If we want to look at processes much faster than the mechanical or electronic shutter speed, we can instead illuminate the object with ultra-short bursts of light, such as in a stroboscope.

A similar principle is used in modern day research for capturing the ultra-fast motion of atoms and molecules. In *pump-probe spectroscopy*, pairs of ultra-short light pulses are used to create a sequence of images of a reaction. The first pulse, called the pump pulse, is used to trigger a certain photo-chemical reaction. The second pulse, the probe, is delayed with respect to the pump pulse and creates a snap-shot of the current status of the system by ionization. In contrast to a movie camera, the images are not taken in a continuous sequence. Instead, one repeats the same reaction many times taking snap-shots at different well defined time delays between the start and stop signals of the pump and the probe pulses.

An ultra-short photon pulse has a broad energy spectrum that coherently excites multiple vibrational levels of an electronic state. This is equivalent to the creation of a nuclear wave-packet in the molecule that develops in time on the potential energy curves or surfaces. The ionization of the wave-packet by the absorption of the probe pulse and the measurement of the electronic fragments yields information about the electronic state at the time of ionization. By repeating this process many times at different pump-probe delays, a movie of the evolution of the wave-packet on the potential energy surfaces can be reconstructed.

In 1999, Achmed Zewail was awarded the Nobel Prize for his development of the field of *Femtochemistry*. In the years prior, lasers had been developed that deliver light pulses sufficiently short to illuminate molecular reactions without a blurring of the motion. Zewail had combined these light sources with various experimental techniques for studying photo-

chemical reactions, such as mass spectroscopy and electron diffraction, on a femtosecond time scale.

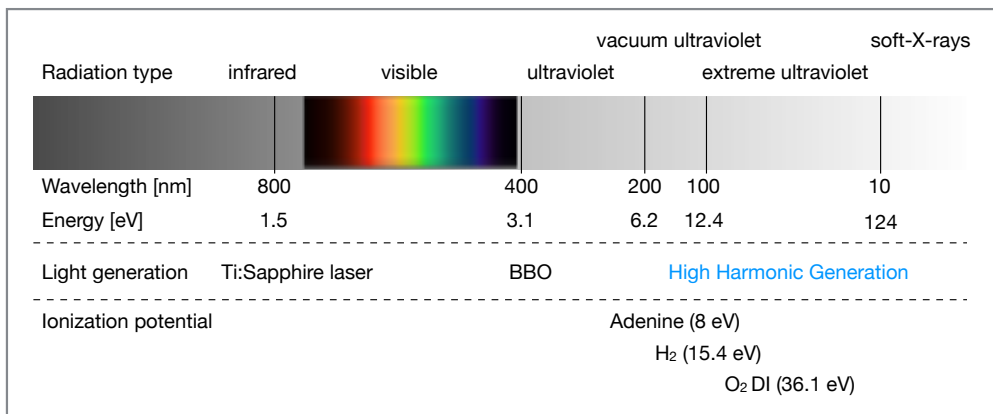
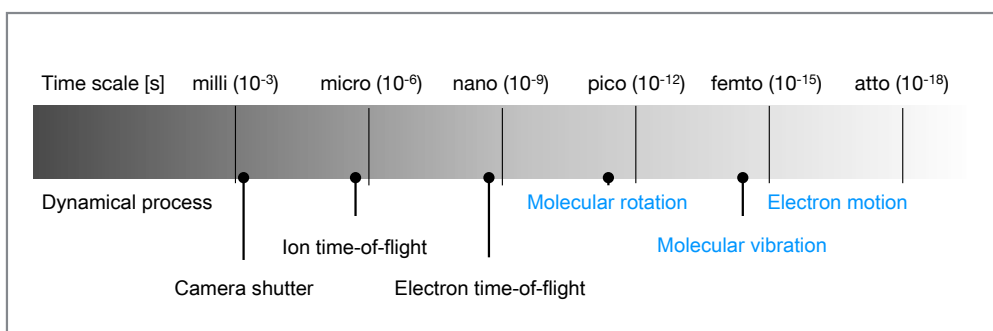
Since then, the time resolution of pulsed lasers has been improved successively and new techniques allow the generation of pulses as short as tens of attoseconds ( $10^{-18}$  s). However, a major challenge that limits the investigation of photo-chemical reactions has been the high excitation energy of many electronic transitions. The ionization energy as well as the majority of neutral electronic states of atoms and molecules is on the order of several eV energy, well above the energy of femtosecond lasers that operate at wavelengths in the infrared to the visible spectrum. Studying photo-chemical reactions or the electronic structure of those states requires an energy equivalent to the excitation in the vacuum ultraviolet (VUV) to the extreme ultraviolet (XUV) spectrum.

This problem has been circumvented by focusing high power laser beams onto the molecular target creating a strong electromagnetic field that leads to the absorption of a sufficient amount of energy to ionize the molecule. However, the ionization process is not selective but occurs successively starting from the most weakly bound electronic state. Additionally, the strong electromagnetic field modifies the electronic structure of the molecules, hence it does not allow to study the unperturbed state of the system. Using crystals such as *beta barium borate* (*BBO*), wavelengths in the ultraviolet (UV) spectrum can be generated by frequency doubling or tripling, but this is still insufficient to cover higher lying electronic states.

The development of High Harmonic Generation (HHG) has extended the energy range and shortened the pulse durations in pulsed laser sources significantly. By focusing a femtosecond laser into a medium, the fundamental (usually infrared) light can be converted into photons of higher energy, generating photon energies in the vacuum ultraviolet to the soft-Xray spectrum. These light pulses allow to selectively excite electronic states and trigger chemical reactions not accessible by strong laser fields. However, the conversion process of High Harmonic Generation is extremely inefficient, and obtaining a high amount of photon flux from HHG sources is very challenging. In Figure 1.1 (top), the spectrum of ultrafast light-sources is depicted together with some exemplary ionization potentials. The time scales of processes in molecular spectroscopy are shown below.

The availability of femtosecond pulses in the VUV and XUV spectrum opens the possibility to investigate nuclear and electronic dynamics in molecules using pump-probe spectroscopy. This raises many new and important questions: Which electronic states can be excited by a sequence of multi-color pulses? The nuclear dynamics induced by the pump pulse can enable new transitions that only occur at internuclear distances outside of the range of the molecular ground state (Franck-Condon region). With the absorption of multiple photons of different energy and polarization, new transitions could become optically allowed. This could lead to new dissociation pathways that involve different non-adiabatic transitions which are not accessible in single-photon absorption. In this work, I will try to find answers to at least some of these questions and investigate in which way we can use this knowledge to control the outcome of simple photo-chemical reactions.

Many different experimental techniques are employed to study photo-induced electronic transitions. The different approaches detect a certain characteristic of the fragments of the ionization reaction initiated by the probe pulse. In a majority of early time-resolved experiments, simple techniques such as ion mass-spectroscopy were used. Here, the total yield of a particular fragment, detected by selecting the corresponding ion time-of-flight in the spectrometer, is recorded with respect to the pump-probe delay. From this information, the time-scale and the efficiency of pathways leading to the selected fragment can be obtained. Nevertheless, multiple pathways that yield the same molecular fragment cannot be distinguished, and no information about the electronic state of the fragments can be

**Molecular Spectroscopy - energy scales****Time scales**

**Figure 1.1:** (Top) Energy range of HHG and laser sources with respect to typical single ionization potentials of Adenine and molecular oxygen, as well as the double ionization potential of oxygen molecules. (Bottom) Time scales of molecular and electronic motion, as well as typical particle flight times in a reaction microscope.

retrieved. Hence, more sophisticated experimental detection techniques or the combination of other methods restricting the accessible reaction pathways, such as molecular alignment, are required to distinguish complex molecular dynamics.

Arguably the most complete set of information from an ionization reaction can be obtained with a *reaction microscope*. In this technique, also known under the acronym *COLTRIMS* which stands for COLd Target Recoil Ion Momentum Spectroscopy, individual molecules are dissociatively ionized, and the velocity and impact positions of electrons and ions emerging from the reaction are collected with particle detectors in coincidence. Using algorithms, the measured data can be used to reconstruct the full 3D momenta of the particles at the instant of ionization. The coincidence measurement of the electrons and ion fragments allows to obtain the full set of information about the electronic states, including the energy and angular momenta corresponding to the fragments. A measurement of all fragments is possible, equivalent to a kinematically complete measurement of the fragmentation process (excluding the spin) [179]. Multi-differential conditions can be applied to the data to select particular processes and to investigate correlation in the molecular system not accessible with other methods.

Reaction microscopes have been developed and optimized over the past 20 years, but most studies have been limited to measurements at synchrotrons that have excellent energy resolution (1:5000 or better) but do not provide the time resolution for studying molecular

dynamics. Meanwhile, experiments with strong-field lasers cannot access specific electronic states requiring a high photon energy. A few time-resolved experiments with high photon flux in the XUV spectrum have been performed at Free-Electron lasers (see Section 2.3). Due to the complexity and novelty of both components, reaction microscopes have only been combined with High Harmonic Generation light sources at very few laboratories worldwide, and most sources produce a strongly limited output of photon flux.

In the years prior to this project, a group at Lawrence Berkeley National Laboratory (LBNL) had developed a HHG source, driven by a high power femtosecond laser system. The source produces an extremely high photon flux that opens the perspective for studying molecular photo-excitation and ionization in the time domain using VUV-XUV pulse pairs.

Under the direction of Dr. Thorsten Weber, I worked on the development and construction of a new experimental setup, called Momentum Imaging Spectroscopy for TimeE Resolved Studies (*MISTERS*), a reaction microscope for performing time-resolved 3D momentum imaging spectroscopy using the high-flux HHG light source that was being built in the laboratory. Due to the novel experimental approach of combining such a high-flux XUV source with a COLTRIMS type end-station, numerous technical challenges had to be resolved and new techniques developed in order to record nuclear motion with a reaction microscope in the time-domain.

The electronic transitions that are excited by a sequence of multi-color pulses with varying energy and polarization can be complex and may differ strongly from the strong-field or single photon experiments that have been performed extensively over the past years. However, even in simple molecules, such as molecular hydrogen, the multi-photon absorption of IR, VUV, and XUV pulses has only been studied sparsely, so far. Using 3D momentum imaging, information about the energy as well as the angular momentum of the states involved can be obtained. Specifically, the *MISTERS* setup allows for the investigation of the influence of the molecular orientation in multi-photon multi-color absorption and the role of dark states that cannot be reached by the absorption of a single photon.

Moreover, the inherent attosecond stability of the infrared driving field to the phase locked attosecond pulse train, generated in HHG, can be used to perform quantum control experiments on an attosecond time scale; by delaying the IR probe pulse with respect to the XUV/IR pump pulse, one can manipulate optical and quantum interference processes of electronic wave-packets. In such *coherent attosecond control* experiments, the optical transparency, ionization probability, or the branching ratio of dissociation channels can be modified. Meanwhile, the phase of such quantum beatings can reveal useful information about the electronic potential structure or the field induced states. Experiments have demonstrated these processes in the attosecond time domain mainly in atoms, but one objective consists in extending such techniques to molecular targets.

In the following chapters, I will first describe the various components of the experimental setup that had to be developed and constructed in order to perform 3D momentum imaging experiments with XUV/VUV/IR multi-color pulse pairs before presenting and discussing the observed molecular processes.

In Chapter 2, I will give a brief overview of the light sources available for studying femtosecond molecular dynamics in the extreme ultraviolet regime and present the standard technique. A summary of experiments with VUV-XUV pulse pairs as well as an overview of experimental efforts on the photoionization of hydrogen and oxygen molecules with a focus on molecular dynamics will be presented.

In Chapter 3, I will review the process of High Harmonic Generation and the challenges for building a high flux source, as well as the solutions in the laboratory at LBNL. The various tools developed for selecting specific photon energies and the characterization of the

XUV beam are described in Chapter 4. The design of the MISTERS reaction microscope and its specific technical features are shown in Chapter 5. In Chapter 6, the results of first experiments with argon atoms and small molecules will be presented. The experiments showcase not only the capabilities of such a novel experimental tool for studying molecular dynamics, but I will identify complex reaction pathways induced by multi-photon multi-color absorption and track and control molecular dynamics on femto and attosecond time scales. I will conclude with a summary of the achieved results and an outlook on future experiments and improvements to the setup specifically and the technique in general.

## 2 Physical Background

This chapter provides background information to put this dissertation into the context of current research. The advent of femtosecond lasers opened a new field of research where it became possible to observe the dynamics of atoms and molecules in real-time. Achmed Zewail founded the field of *Femtochemistry* by combining femtosecond lasers with ion spectroscopy and other techniques to achieve a time resolution that made the observation of molecular dynamics possible [188]. Since then, using different imaging techniques such as COLTRIMS and VMI (see Chapter 5), the tracking of molecular dynamics has been brought to a more fundamental level. It allowed a direct comparison of experiments with quantitative theoretical models for describing the interaction of individual particles that are not feasible with large scale systems (yet). Using High Harmonic Generation, the time-resolution of experimental methods has been pushed to the attosecond regime which has enabled the observation of electron dynamics.

Most small molecules have high photo-absorption probability, in the vacuum ultraviolet (VUV) and the extreme ultraviolet (XUV) spectrum, at wavelengths shorter than  $\sim 200$  nm [44, 16]. Femtosecond lasers that allow to observe the dynamics of those excited states have their spectrum in the visible or infrared. It is extremely difficult to obtain high gain at shorter wavelengths due to the scaling of  $1/\lambda^4$  of the power required to create the population inversion for lasing in a medium [153]. High energy conversion on the order of  $\sim 50$  % can be obtained from frequency doubling in crystals through second harmonic generation (see Section 3.1). However, this is still insufficient to reach most excitation energies. Therefore, most experiments require the non-sequential absorption of multiple photons. The strong laser field required for multi-photon absorption, however, can influence the electronic structure and the nuclear dynamics of a system. Furthermore, in a strong field, the ionization occurs successively starting from the weakest bound electron which is located in the *highest occupied molecular orbital (HOMO)*. In order to investigate specific neutral or ionic states, the excitation or ionization with a single photon is therefore preferred. XUV and VUV pulses can be used to probe the evolution of a nuclear-wave packet on the potential energy curves or surfaces at every point of the reaction, hereby tracking the nuclear dynamics without disturbing the system.

In section 2.2, the types of light sources available for experiments with ultrafast light pulses in the XUV spectrum will be presented. The main experiments using two-photon excitation and ionization in the XUV regime that have been published so far will be presented. An overview of the research on  $O_2$  and  $H_2$  molecules, focusing on the time domain, will be given in the last section.

### 2.1 Femtosecond Time Resolved Measurements

Information on the timing of an electronic process can sometimes be obtained from spectroscopic information such as the fragment energy or the momentum. In streaking measurements, the phase locked infrared field is delayed with respect to a single attosecond pulse. The momentum transferred from the electric field to the electrons depends on the direction and amplitude of the infrared field and allows to map the measured momenta to an attosecond time delay [37]. Similarly, the emission angle of electrons can be used

to measure the delay of a process using the well known rotation frequency of a circularly polarized IR pulse in a technique called attosecond angular streaking [38].

In double-photoionization, the energy of measured photoelectrons changes according to the emission time of a much faster second electron. This can be used to map the electron energy to emission times on a femtosecond level. Trinter *et al.* [171] demonstrated this technique in the ICD of helium dimers showing the Kinetic Energy Release (KER) for a varying decay time.

### 2.1.1 Pump-Probe Spectroscopy

A more direct approach to investigate molecular dynamics in the time domain is taken in *pump-probe spectroscopy*. Here, the timing information is obtained from actively initiating molecular dynamics with a pump pulse and then probing the process with a second pulse at various time delays. This can be realized by splitting a pulsed laser beam into two arms using a beam splitter or a split-mirror. In the interferometer, the pathway of the light in one arm is lengthened or shortened using a translation stage. The difference in propagation length creates a variable time-delay between the two pulses. The first pulse, called the pump pulse, promotes the molecular system to an electronic intermediate state, hereby starting a dynamical process. The second pulse, the probe, projects the intermediate configuration to a final state by ionization. If the probe characteristics are known, information about the process can be obtained from the measurement of the properties of the electron and ion fragments on the detectors of the experimental apparatus. A snapshot of the dynamics of the intermediate state can be recorded at many instants in time by repeated measurements of the pump-probe sequence while varying the delay between the two pulses. The pump-probe interferometer developed in this work is presented in Section 4.2.

## 2.2 Ultrafast XUV light sources

A light source that is suitable for studying molecular dynamics in the time domain without the influence of a strong field needs to provide both an adequate photon energy as well as sufficiently short pulses. The ionization limit of hydrogen, oxygen, and small hydrocarbon molecules are in the range of  $\sim 10 - 20$  eV. The binding energy of inner shell electrons usually requires several hundred eV. In order to cover the full range of neutral states, the photon energy produced by the light source should be on the order of the ionization potential, but an ideal light source provides a sufficient flux in the entire spectral range.

In order to resolve a dynamical process, the pulse duration of each pulse needs to be shorter than the dynamics to be observed. The timescale of geometry changes in small molecules is usually on the order of tens of femtoseconds for vibrations and up to hundreds of femtoseconds to picoseconds for more for complicated migration and rearrangement processes. Depending on the specific process, temporal and spatial coherence of the pulses can also be necessary to observe the process, as different phases could mix various signals such that no clear trace of the dynamics can be obtained.

Plasma sources and other discharge sources reach energies in the soft X-ray regime, but due the characteristics of the electron plasma, the short bursts are incoherent in space and time.

Synchrotron light sources have been a major source of photons in the soft X-ray regime, and they are accessible in various places around the world. Synchrotrons exhibit a high brilliance and reach energies from  $\sim 10$  eV - 10 keV with great spectral resolution (1:5000 or better). Modern, third generation synchrotron facilities use *undulators* for creating high

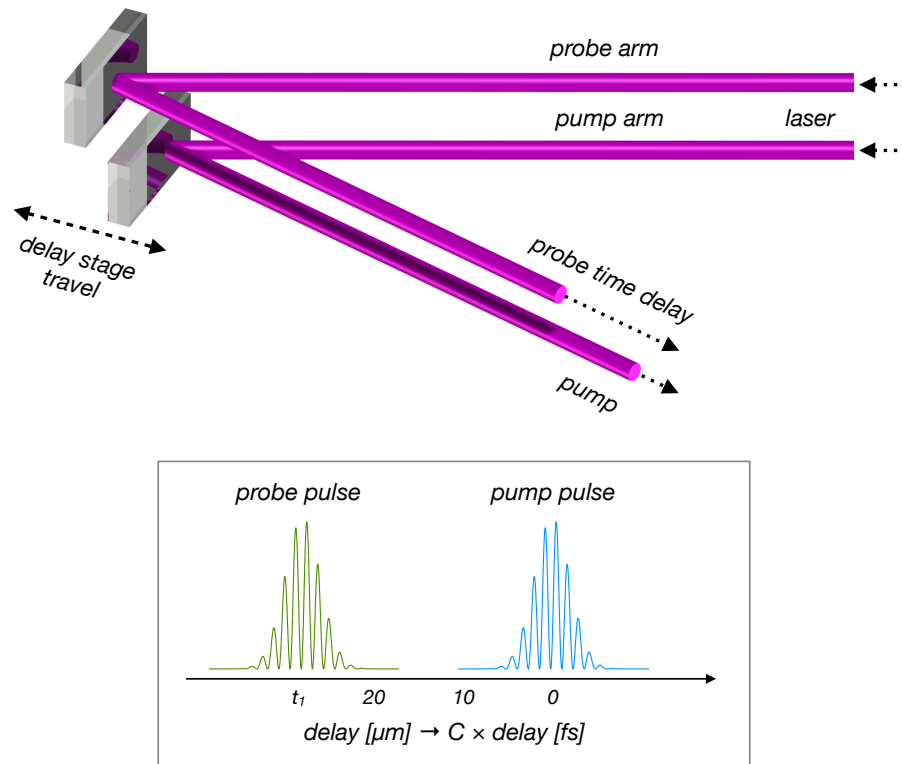


**Figure 2.1:** Schematic illustrating the pump-probe technique for time-resolved measurements. The laser beam is split into two arms that are reflected off mirrors in an interferometer. The path length of the laser beam in one arm is changed by means of a translation stage. The path difference between pump and probe arm results in a time delay between the pulses in each arm. The Split-Mirror Interferometer introducing the pump-probe delay in the current setup is shown in Figure 4.10.

brightness photon radiation from electron bunches. They consist of an array of dipole magnets arranged along the beam propagation direction. Electrons traveling through the device are forced onto oscillating trajectories by periodic dipole magnets hereby emitting Bremsstrahlung. In the undulator, the spacing of the magnetic dipoles is adjusted in a way such that the radiation of each oscillation adds constructively. In *variable gap undulators*, the energy of the emitted spectrum can be adjusted using a variable spacing between the dipoles. In the simplest case, the pulse duration of the photon bursts depends on the length of the electron bunches. Short electron bunches can be obtained using pulsed lasers to create the initial electron cloud from a cathode. They can be compressed further using bunch compression schemes. The pulse lengths of tens to hundreds of picoseconds, however, are much too long to observe dynamics of individual molecules.

### 2.2.1 Free-Electron Lasers

*Free-electron lasers (FELs)* create laser like radiation with high spatial and temporal coherence in the X-Ray regime at pulse lengths from hundreds to a few femtoseconds [40]. They use linear accelerators to feed electron bunches into arrays of undulators. The density of the electron bunches is increased prior to entering the undulators, such that the electromagnetic wave interacts with the relativistic electron cloud to form micro-bunches. In this process, the radiation adds coherently and the power increases exponentially along the undulator. The shot noise in the long undulator sections is sufficient to start the process of micro-bunching. This is called *self-amplified spontaneous emission (SASE)* [10]. It can also be initiated through *seeding* from an external laser source [187, 4]. Most current sources operate in SASE mode as it is technically less challenging.

Current FELs provide approximately  $10^{12}$  photons per shot at low repetition rates of tens of Hz [1, 40, 4]. While the pulse length can be as short as a few femtoseconds, shot stability and synchronization are very challenging and the final temporal stability is often on the order of hundreds of femtoseconds. Recently developed schemes might improve those difficulties [146], but the synchronization of an external laser to an FEL source, in order to provide a combination of UV and soft X-ray pulses, still remains challenging.

A practical challenge consists in the very short experimental as well as preparation time available for users at FEL sources. Usually, only a few days or shifts are allocated for any approved experiment. This renders complicated experimental efforts involving pump-probe setups extremely challenging. Any problems that delay the experiment, which regularly appear in complex experimental setups such as momentum imaging detectors and gas jet sources, can forge an experimental effort if the time required to fix the issue exceeds a few hours. Low repetition rates or unsuitable energy ranges for specific experiments will be addressed with future light sources. The short time window for experiments will likely not improve significantly because of the expensive generation process of FEL light involving linear electron accelerators. Therefore, the development of lab based approaches is indispensable to advance time-resolved measurements in the XUV to soft-Xray regime for a broad range of research.

### 2.2.2 High Harmonic Generation

*High Harmonic Generation (HHG)* is still the most promising laboratory based technique to obtain ultra-short pulses with photon energies in the XUV to the soft-Xray regime.

When a high power laser is focused into a medium, the strong optical field ionizes the medium and drives the free electrons. Electrons passing in the vicinity of the nuclei can recombine with the ions. The energy acquired in the optical field is coherently emitted as a

photon with an energy multiple times higher than the driving field. A detailed discussion of the process will be given in Chapter 3.

High Harmonic Generation has been realized in noble gases [48], molecules [92, 67, 150], clusters [36], liquids [35], and even solids [111, 53, 145]. Nevertheless, noble gases are still the most successful medium for High Harmonic Generation, and they are used in most studies.

Pulse durations of tens of femtoseconds are routinely obtained in HHG. The worlds shortest pulses of just tens of attoseconds have been created using HHG in combination with pulse shaping and gating techniques [189]. If challenges concerning the compression are overcome, pulse lengths of a few attoseconds or even zeptoseconds might be achievable in the future [124, 28]. Even with pulse envelope of tens of femtoseconds, the inherent synchronization of the driving field to the attosecond pulse train obtained in HHG can be used to perform time-resolved measurements on an attosecond time scale, as will be demonstrated in the experiments presented in Chapter 6.

Depending on the generation medium, the spectrum obtained in HHG spans from  $\sim 1 - 100$  eV but can be extended to energies in the keV regime using longer driving wavelengths and higher laser intensities [124]. There are ongoing efforts to extend both the energy range while maintaining a sufficiently high photon flux for performing experiments in low density targets such as gas sources. The latter is still the biggest challenge to the prospective of replacing other XUV sources with HHG in the laboratory. High harmonics pulses are coherent in space and time and are therefore an excellent source for molecular experiments.

The current setup uses a high power Ti:sapphire laser system to drive High Harmonic Generation in a gas cell. Photon energies of few to tens of eV at pulse lengths of tens of femtoseconds are obtained. A detailed discussion of the process of High Harmonic Generation, as well as the implementation in this setup are presented in Chapter 3.

## 2.3 XUV Experiments in the Time Domain

As mentioned above, the only sources that deliver photons in the VUV and XUV spectrum in combination with a femtosecond temporal resolution are free-electron lasers and High Harmonic Generation sources. In HHG, the low conversion efficiency makes it extremely difficult to produce a sufficient flux in the VUV and XUV spectrum that allows for a considerable two-photon absorption probability in the VUV/XUV. The low availability of FEL sources and the challenges connected to the synchronization and the temporal resolution have inhibited a large amount of pump-probe experiments at such facilities so far. For those reasons, only few pump-probe experiments on single molecules using VUV and XUV pulse pairs have been published so far.

### Experiments with High Harmonic Sources

The attosecond pulse train created in HHG is perfectly synchronized to the femtosecond driving laser. This enables a variety of techniques of combining the generated XUV light with the fundamental field with attosecond precision. A variety of such pump-probe experiments in hydrogen and oxygen molecules are cited in the Sections 2.4 and 2.5. The use of a strong infrared field, however, requires a rigorous consideration of its effects on the molecular system. A more selective approach consists in the direct excitation and probing of the molecular dynamics using VUV and XUV pulse pairs that only represent a small perturbation to the molecular system.

First experiments observing two-photon ionization in the XUV were reported in 1996 [186]. Two-color two-photon ionization in Helium was realized by Papadogiannis *et al.* [114]. Most pump-probe studies consisted of pulse metrology type studies such as the autocorrelation measurements using two-photon absorption of the 9<sup>th</sup> harmonic using split mirrors [79] or four-photon absorption of the 5<sup>th</sup> harmonic [148], as well as TPI FROG measurements [149]. The direct second-order autocorrelation of an attosecond pulse train was first measured by Tzallas *et al.* [172] and later extended by the measurement of the attosecond chirp [110]. Double ionization of helium and others gases through two-photon absorption of high order harmonics was reported by Nabekawa *et al.* [109] and Benis *et al.* [15].

Two-photon autocorrelation traces with VUV pulse pairs were recorded with a variety of atomic and molecular targets [118], representing a first step towards studying molecular dynamics in the VUV. Allison *et al.* [6, 7] demonstrated two-color time-resolved spectroscopy with VUV-pulse pairs in several measurements of gaseous water, oxygen, and ethylene. The measurements were limited to measuring the fragment yields by selecting individual ion species according to their time-of-flight.

In Xenon atoms, Tzallas *et al.* [173] traced electron dynamics on a one-femtosecond scale by direct and sequential two-photon ionization through overlapping a pair of single or double attosecond XUV pulses. Recently a new interferometer using comb-shape delay mirrors was reported that achieves a very high quality two-photon autocorrelation signal [51]. This setup, however, is unsuitable at this time for two-color measurements which are desired for studying molecules.

## Experiments with Free-Electron Lasers

Free-electron lasers deliver sufficient flux for multi-photon absorption in the XUV spectrum. Shot noise, temporal synchronization, and technical challenges at the facilities have limited the amount of successful pump-probe experiments thus far.

At the first free-electron laser, FLASH, the autocorrelation in N<sub>2</sub> molecules was measured by Jiang *et al.* [70] as well as nuclear wave packet dynamics in D<sub>2</sub> [71]. Further investigations included the ionization dynamics in clusters [83]. Using a momentum imaging spectrometer, Schnorr *et al.* reported the measurement of the decay time in Interatomic Coulombic Decay (ICD) in neon dimers using a pump-probe scheme [141] as well as a charge rearrangement in dissociating I<sub>2</sub><sup>n+</sup> molecules [142].

## 2.4 Dissociative Ionization of Hydrogen Molecules

Hydrogen atoms form the simplest neutral molecule consisting of just two protons and two electrons. It can be fully described theoretically and has therefore been one of the major subjects to test and benchmark theoretical modeling and calculations. Hydrogen molecules are also an ideal candidate to investigate fundamental processes such as interference and correlation.

In experiments, hydrogen molecules are often replaced by deuterium as the target. The additional mass of two neutrons in deuterium has no influence on the electronic states of the molecule, but it results in a slight shift of the vibrational levels. The findings in investigations of either molecule are therefore equivalent. For practical reasons measurements with deuterium are often preferred, because the different mass-to-charge ratio makes deuterium distinguishable from H<sup>+</sup> fragments stemming from reactions in the background gas.

The dissociative photoionization of hydrogen and deuterium molecules has been studied since the 1970s. This includes early experiments using single and multi-photon absorption (see [133] and references therein) and theoretical works [135, 73, 136]. Measurements in the molecular frame by Lafosse *et al.* [86] yielded rich information about the electronic states and pathways involved. Other spectroscopic studies were aimed at identifying the predissociation energies and pathways [94] as well as the role of super-excited states [55, 56].

The complete photo-fragmentation of the deuterium molecule with a coincident measurement of the 3D momenta of both ions and electrons was experimentally realized by Weber *et al.* [179]. The complex influence of the molecular geometry to the observed electron angular distributions was interpreted by a numerical solution of the Schrödinger equation by Vanroose and coworkers [175].

Photoionization of hydrogen as the simplest double slit experiment was used to investigate fundamental quantum-mechanical processes such as interference and entanglement [3, 23]. Interference between different dissociation pathways leads also to surprising effects such as the single-photon induced symmetry breaking observed in hydrogen [103].

Using focused laser beams, strong fields effects such as *bond-softening* in above-threshold ionization of  $\text{H}_2^+$  molecules were discovered in the 1990s [21, 54]. Here, the optical field modifies the electronic structure of the molecule enabling dissociation at lower energies than in the field free case.

The photo-fragmentation in strong fields was further studied in various experiments [125, 161, 162, 112] highlighting the complexity of the interaction of strong optical fields and the attosecond time dependence of the intensity of infrared lasers even in a simple molecule such as  $\text{H}_2^+$ . Strong-field effects in  $\text{H}_2$ , such as on the electron-nuclear energy sharing, remain an active topic of research [184, 155].

### Time resolved experiments

With the advent of femtosecond laser systems, it became possible to probe nuclear dynamics in the time-domain. Nuclear wave packets in neutral  $\text{H}_2$  and  $\text{D}_2$  and in their cations were mapped spatially and temporally on femtosecond time scales using strong infrared fields in combination with momentum imaging techniques [43, 42, 18]. The effects of the strong laser field on the nuclear dynamics were also investigated theoretically [99].

The direct observation of the nuclear wave packet in  $\text{D}_2^+$  in the time domain without the use of an infrared field was realized by Jiang *et al.* [71] in one of the first pump-probe experiments at the FLASH free-electron laser. Only recently, Cao *et al.* [25] investigated the photo-dissociation of  $\text{D}_2$  using long ( $\sim 100$ ) femtosecond pulses created by High Harmonic Generation in combination with the infrared field. Using a monochromator, they were able to select a specific harmonic order, identifying competing dissociation pathways that are very sensitive to the photon energy.

High harmonic spectra can also be used for probing nuclear dynamics. Baker *et al.* [12] demonstrated how the structural information of the molecule is encoded in the high harmonics spectrum due to the correspondence of electron trajectories and their emission time to the harmonic energy (for details see Section 3.3).

Kling *et al.* [78] demonstrated that the localization of electrons in  $\text{D}_2^+$  molecules can be controlled on a sub-cycle timescale. Using phase-stabilized few-cycle pulses, the localization causes a preferred dissociation pathway that is observed in a phase-dependent  $\text{D}^+$  energy using Velocity Map Imaging (VMI) (see Chapter 5 for details about VMI). Even when symmetrical femtosecond circular laser pulses are used, electron localization can lead to a phase dependent asymmetry of the photo-fragmentation of  $\text{H}_2$ , as observed by attosecond angular streaking measured in a COLTRIMS setup by Wu *et al.* [185].

In High Harmonic Generation, the attosecond bursts of XUV pulses that are inherently synchronized to the infrared driving field opened the way to investigate and control dynamics on an attosecond time scale. Kelkensberg *et al.* [75] used a two-color XUV-pump IR-probe scheme to follow the wave packet dynamics in  $\text{H}_2^+$  molecules. They highlight how the dynamics, even in a small molecule such as  $\text{H}_2$ , depend strongly on the characteristics of the infrared field. Using a similar XUV-IR pump-probe scheme, Singh *et al.* [156] observe localization in the dissociation of  $\text{D}_2^+$  ions on an attosecond time-scale using a COLTRIMS momentum imaging apparatus (see Chapter 5 for details about COLTRIMS). These measurements were further refined by using a single attosecond pulse in combination with a few-cycle infrared field to trace the electronic motion of photo-excited  $\text{D}_2^+$  [138]. Half-cycle yield oscillation of  $\text{D}^+$  from the dissociation of  $\text{D}_2^+$  were observed in another experiment [76]. Here, an attosecond pulse-train (APT) in the XUV spectrum was delayed with respect to an infrared field. The oscillation was attributed to the interference of different electronic pathways enabled by the coupling of the infrared field that varies with the intensity.

The attosecond experiments mentioned above were almost exclusively performed on the dynamics of cations, while the states of neutral molecules have only been investigated scarcely. Therefore, little is known about the evolution of neutral states which is equally important. This is because most excited neutral states are in the VUV spectrum, beyond the spectral range reached by frequency doubling with crystals, and below the energy of single attosecond pulses. Single attosecond pulses are not available in the VUV so far, as they can only be created above the ionization threshold near the peak of the laser intensity (see [28] for a recent review of techniques). Ranitovic *et al.* [129] presented first measurements of the neutral excited states of hydrogen using an attosecond pulse-train combined with an infrared field and used attosecond coherent control techniques to change the dissociation pathways.

While many experiments have been performed in the VUV and XUV regime, there are still many questions open. Different electronic transitions induced by multi-color pulses might induce new dissociation pathways of excited neutral hydrogen that are not accessible in single-photon ionization or the application of a strong field, and therefore, they have not been studied. In this context, the role of dark states in the electronic transitions and dynamics needs to be investigated. Additionally, combining photons with varying polarization axes could lead to a stronger restriction of the optically allowed transitions or instead, it could cause more complex electron angular distributions. Using 3D momentum imaging such questions, as well as the influence of the molecular orientation in the selection of specific dissociation pathways could be investigated.

## 2.5 Dissociative Ionization of Oxygen Molecules

In contrast to hydrogen molecules, the large amount of electrons (16) in oxygen molecules form a complex electronic structure. This renders the theoretical modeling of experimental observations very challenging. The orbital structure obtained from combining the electronic orbitals of atomic oxygen to molecular orbitals is shown in Figure 2.2.

The importance of this molecule in nature and as a fundamental system of strong electron correlation stimulated many spectroscopic studies. Already in the 1970s and 1980s, dissociative states of the  $\text{O}_2^+$  ion were discovered and studied in photoelectron-photoion coincidence experiments [59, 2, 131]. The production of auto-ionizing states by predissociation was the topic of a study by Wills *et al.* [182]. Baltzer *et al.* [14] performed high resolution photoelectron spectroscopy of inner-valence photoionization measuring the vibrational progression of the electronic states of the  $\text{O}_2^+$  ion. This work was further



internuclear separation. The competition of autoionization and predissociation of super-excited Rydberg states of the neutral  $O_2$  molecule was measured using XUV attosecond pulse trains and infrared pulses with varying delay in a study by Timmers *et al.* [168].

The nuclear wave-packet dynamics in the cations of  $O_2$ ,  $N_2$ , and  $CO$  initiated by strong few-cycle infrared pulses were investigated by De *et al.* [34] using a VMI spectrometer. Zohrabi *et al.* [192] employed momentum imaging with both VMI and COLTRIMS type spectrometers to further investigate the strong-field driven dissociation of  $O_2^+$  ions. They identify vibrational structures at low kinetic energies that correspond to the dissociation of metastable excited  $O_2^+$  ions through the bond-softening mechanism enabled by the infrared field. The relevant adiabatic curves in the dissociation dynamics were calculated in a theoretical work by Magrakvelidze *et al.* [100].

In a recent kinematically complete experiment, Cörlin *et al.* [30] were able to track the evolution of such a nuclear wave-packet in the  $a^4\Pi_u$  state of  $O_2^+$ . They prepared the nuclear wave-packet using an XUV attosecond pulse train and probed the nuclear dynamics with a time delayed infrared field. Additionally, the measurement allowed to benchmark theoretical calculations by comparing the measured results to calculations using different potential energy curves (PEC from [101] and [100]).

A first approach towards employing attosecond coherent control techniques, such as performed in the experiments with hydrogen molecules presented in the previous section, was taken in a work by Siu *et al.* [157]. In this experiment, an attosecond XUV pulse train was used to coherently excite several metastable states of the  $O_2^+$  cation. By varying the phase of an infrared probe pulse, they observe a modulation of the  $O^+$  yield at twice the frequency of the infrared field. This points towards the interference of coherently excited electronic wave-packets that are being coupled by the infrared field. While the experiments on attosecond control were mainly performed in atomic targets as well as hydrogen and deuterium, the latter measurement indicates the possibility of coherently controlling the dissociation pathways of larger molecules on an attosecond time scale. Further efforts applying attosecond coherent control in oxygen or other molecules are needed to advance in the understanding of these quantum processes. This is very important, as the technique promises to yield information about the dissociation dynamics in strongly-correlated systems and to advance efforts to manipulate photo-chemical reactions such as photo-dissociation of more complex molecules.

## 3 Ultrafast XUV Light Source

In this chapter, the ultrafast XUV light source used in this setup will be presented. A brief review as to how frequency conversion works at low to moderate intensities follows.

With rising intensity, the perturbative description breaks down and transitions to the *strong-field regime*. This gives rise to a new process of frequency conversion called *High Harmonic Generation (HHG)* that yields ultrashort pulses in the vacuum ultraviolet (VUV) to the soft X-ray spectrum. The *3-step model* represents an intuitive and successful description of this process. The temporal and spectral characteristics and their implications for the generation of high harmonics will be discussed in this chapter. Understanding the macroscopic effects of phase matching and reabsorption are key to the generation of a high flux source. The theoretical description of optical fields and the basics of strong fields and HHG can be found in a variety of review papers and textbooks. Unless otherwise noted, the formulae can be found in [153, 19, 119, 115, 8]. A large amount of literature has been published on the efficient harmonic generation, attosecond pulses, and the extension of the harmonics spectrum. References will be given throughout the text for further reading.

The propagation of an ultrashort pulse in a dispersive medium gives rise to a variety of effects that need to be considered in the design and operation of such a light source. Because of their relevance to the design of several components of the XUV source and the beamline, the important terms will be described. The experimental realization of a high flux HHG source in the laboratory at LBNL is presented in the second part of this chapter. Information on the spectral manipulation and characterization will be discussed in the Sections 4.1 and 4.3.

### 3.1 Frequency Conversion in Optical Fields

The presence of an optical field in a dielectric medium induces an electron density shift. The resulting electric dipole moments can be written as the *polarization density*

$$P = \epsilon_0 \chi E. \quad \text{Polarization in a medium} \quad (3.1)$$

Here  $\epsilon_0$  is the vacuum permeability,  $E$  the electric field, and  $\chi$  the *susceptibility* of the material. The latter describes the material's response to an electric field. At low intensities of light, the electric field strength is on the order of few V/cm, not strong enough to modify the optical properties of the medium. As a result, the total polarization of the medium is the sum of the polarizations by the different field contributions:

$$P(E_1 + E_2) = P(E_1) + P(E_2). \quad \text{Polarisation in linear optics} \quad (3.2)$$

The phenomena of linear optics include reflection and refraction.

At moderate to high intensities, the polarization behaves non-linearly and is treated as a perturbation. It can be expanded in a Taylor series:

$$P = \epsilon_0 \left( \chi^{(1)} E + \chi^{(2)} E^2 + \chi^{(3)} E^3 + \dots \right). \quad \text{Polarization in the perturbative regime} \quad (3.3)$$

Inserting the expression for an oscillating electric field of the form  $E = E_0 \cos(\omega t)$  in Equation 3.3, we obtain

$$P^{(2)} = \chi^{(2)} E_0^2 \left( \frac{1 + \cos(2\omega t)}{2} \right) \quad \text{Second order perturbation} \quad (3.4)$$

for the second order term. The polarization now contains oscillations at  $2\omega$ , twice the frequency of the driving field. Further terms introduce higher oscillations at multiples of the fundamental frequency called harmonics. Hence, a sufficiently strong optical field will create radiation oscillating at integer multiples of the frequency of the driving field. A variety of other phenomena emerge in non-linear fields including wave-mixing and self-phase modulation (see Section 3.4.3 and Appendix A.1).

The effects of frequency conversion was known before the invention of the laser and tested in the microwave regime. With the first implementation of the optical laser in 1960, it became suddenly possible to study the interaction of strong optical fields in dispersive media. Franken and coworkers observed the first *optical harmonics* in 1961 when they shined a ruby laser in a quartz crystal and generated the second harmonic at 347 nm [49, 11]. In the 1970s - 80s, multiple harmonics were created in noble gases but the intensity of harmonics generated in the perturbative regime drops fast with increasing harmonic order. Moderate yields could only be achieved by taking advantage of specific resonances in Xe, Li vapor or other gases [63]. Only low harmonic orders were observed and photons in the extreme ultraviolet were generated by up-conversion from UV driving lasers, such as 248 nm KrF excimer lasers.

## 3.2 The Strong-Field Regime

In the previous section, the perturbative expansion of the polarization was shown in Equation 3.3. This expansion is only valid if subsequent orders are much smaller than one. In order to estimate this limit, we consider an atomic system with resonance frequency  $\omega_{ik}$ , for a transition of state  $i$  to state  $k$ , that is driven by an electric field with amplitude  $E$  and frequency  $\omega$ . If ionization is ignored, quantum mechanical perturbation theory yields the following simple expression for the successive terms of the polarization:

$$\frac{\chi^{(k+1)} E^{k+1}}{\chi^{(k)} E^k} \approx \frac{\mu_{ik} E}{\hbar \Delta\omega} \approx \frac{e E a_B}{\hbar \Delta\omega}. \quad \text{Perturbative terms} \quad (3.5)$$

Here,  $\mu_{ik} = e a_B$  is the transition matrix element between the states  $i$  and  $k$ ,  $a_B$  is the Bohr radius, and  $\Delta\omega = |\omega_{ik} - \omega|$ . For optical lasers, the detuning is on the order of a few eV and the perturbative terms are  $\approx 1$  at fields of  $\text{V}/\text{\AA}$ , equivalent to intensities around  $10^{14} \text{W}/\text{cm}^2$ . In other words the electric field substantially changes the coulomb potential of the atoms. In reality, the strong-field regime is reached already at slightly lower intensities because of ionization, which was ignored in the expression above.

In the perturbative regime, ionization occurs through successive absorption of multiple photons (*multi-photon ionization*). In the strong-field regime, the atomic coulomb potential can be sufficiently suppressed by the laser field to allow the electron to tunnel into the continuum (*tunneling ionization*). At even stronger fields, the atomic potential is completely suppressed and the electrons escape directly without tunneling (*barrier suppression ionization*) [81, 147]. The ionization in a strong-field is well described in a general analytical theory by Ammosov, Delone, and Krainov (*ADK theory*) [9] and more recent generalizations [190].

Keldysh introduced a very useful parameter for distinguishing between the perturbative and the strong-field regime [74]. In the present form, it describes the ratio of multi-photon

to tunneling ionization in terms of the ionization potential of the atom,  $I_p$ , and the ponderomotive energy,  $U_p$ , of the laser field [119].

$$\boxed{\gamma = \sqrt{\frac{I_p}{2U_p}}} \quad \text{Keldysh Parameter} \quad (3.6)$$

The ponderomotive energy is given by

$$\boxed{U_p = \frac{e^2 E^2}{4m_e \omega^2}}, \quad \text{Ponderomotive Energy} \quad (3.7)$$

where  $e$  and  $m_e$  are charge and mass of the electron,  $E$  is the amplitude of the electric field, and  $\omega$  its frequency.

For  $\gamma \gg 1$ , ionization occurs mainly through multi-photon absorption. For values of  $\gamma \ll 1$ , tunneling ionization dominates and the strong-field regime is reached. It should be pointed out that the intensities required to reach the strong-field regime increase with the frequency. Optical lasers create sufficient intensity to reach the strong-field regime but the electric field of high harmonics can typically be treated perturbatively.

### 3.3 High Harmonic Generation

In 1987, McPherson and coworkers observed the generation of harmonics up to the 17<sup>th</sup> order of the fundamental radiation of a KrF laser (248 nm) [105]. Previously, only harmonics up to the 7<sup>th</sup> order had been created with this laser. The intensity of the observed harmonics only declined slowly with increasing order, in contrast to previous experiments. This is considered the first observation of *High Harmonic Generation (HHG)*, the process of frequency conversion in the strong-field regime.

#### 3.3.1 The 3-Step Model of High Harmonic Generation

In contrast to the frequency conversion in moderate fields where bound transitions dominate, ionization plays a key role in High Harmonic Generation. The *3-step model*, introduced by Corkum in 1993 [29, 82], provides an intuitive description of the process of frequency conversion in a strong-field. The model describes the conversion process for an individual atom and divides it into three independent steps (see also Figure 3.1).

1. The electric field of the laser distorts the coulomb potential binding the electrons of the atom. An electron is ionized by quantum mechanical tunneling through the suppressed potential barrier.
2. In the continuum, the coulombic potential is considered negligible and the electron motion is dictated by the electric field of the laser. Starting with zero kinetic energy, the electrons gain kinetic energy in the field and follow classical trajectories that vary depending on the release time.
3. Some trajectories lead back to the ion. With a small probability, the electron recombines to the ground state forming a neutral atom by emitting a photon.

In the 3-step model, recombination can only occur for a linearly polarized electric field because a rotating electric field would prevent the electron from returning near the ion.

Increasing the ellipticity of the driving laser field strongly suppresses the high harmonic emission. This has been confirmed in several experiments [22]. Under certain conditions, however, rescattering and harmonic emission in a circular polarized driving field has been observed [104, 191].

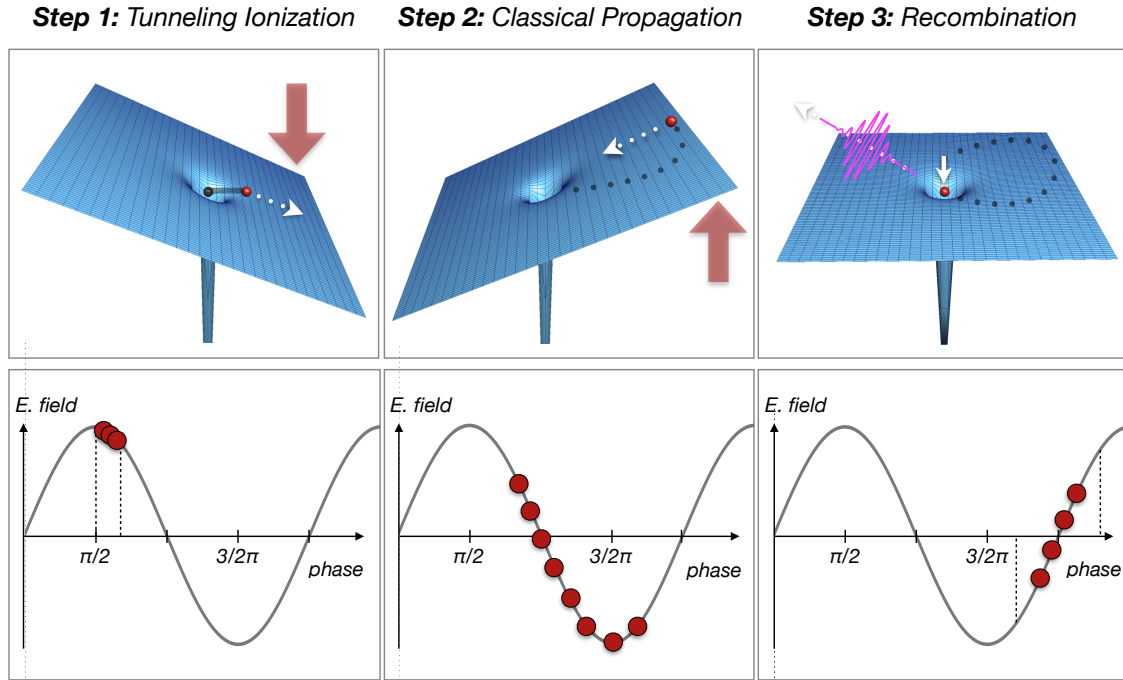


**Figure 3.1:** Schematic illustrating the concept of the 3-step model of High Harmonic Generation. **(Step 1)** The electric field of the laser suppresses the barrier of the atomic coulomb potential allowing the electron to escape by tunneling. The emission occurs in a time interval near the maximal intensity of the field. **(Step 2)** The free electron propagates in the laser driven electric field on classical trajectories depending on the time of emission. In a linearly polarized field, some electron trajectories lead back to the ion. **(Step 3)** The electron has a small probability of recombining with the ion emitting a photon equal to the sum of the ionization potential and the kinetic energy acquired during the propagation in the laser field. As this process repeats for every half-cycle of the laser field, a train of attosecond pulses is created. This corresponds to a discrete spectrum of frequencies at odd integers of the fundamental field.

### Photon Energy

The energy of the photon is dictated by the ionization potential of the medium  $I_p$  and the kinetic energy gained in the electric field of the laser.

$$\hbar\omega = I_p + E_{kin}. \quad \text{Photon energy} \quad (3.8)$$

Ionization occurs in a short interval around the maximal field strength. The electrons emitted at different phases of the field follow different trajectories and reach different velocities. Therefore, the photon energy depends on the phase of the field. Recombination and emission happen near zero field strength, and there are usually two trajectories leading to the same energy. Figure 3.2 illustrates the energy dependence of electrons emitted at different phases of the field and their recombination resulting in the emission of photons of

different energy. Electrons released at a phase of  $18^\circ$  acquire the highest kinetic energy equal to  $\sim 3.17 U_p$ . This can be expressed in terms of the ponderomotive energy,  $U_p$ , presented previously in Equation 3.7. This is called the *cutoff law* of High Harmonic Generation.

$$\boxed{E_{max} = I_p + 3.17 U_p.} \quad \textit{Maximal Harmonic Energy} \quad (3.9)$$

Higher photon energies can be obtained by increasing the laser intensity, because the ponderomotive energy depends linearly on the laser intensity. However, phase matching, described in the following Section (3.3.2), and ionization can adversely effect the harmonic yield. Alternatively, the  $1/\lambda^2$  dependence can extend the generated photon energies into the soft X-ray spectrum by choosing laser systems with longer wavelengths. From an intuitive perspective, the electron has more time to gain kinetic energy as the field is varying slowly. High energies into the *water window* have been obtained using short high intensity pulses from Ti:sapphire lasers [27, 158]. Using mid-infrared lasers, photon energies as high as 1.6 keV have been generated [124].

The cutoff law is well established and has been reproduced in many experiments [82, 176]. However, the maximal energy observed might be lower than predicted from the maximal intensity of the pulse. The highest photon energy requires tunnel ionization near the peak of the laser pulse. If the overall pulse length and intensity is such that ionization has saturated the medium before the maximal intensity of the pulse is reached, the harmonic cutoff will be lowered to a value corresponding to the intensity near saturation. An effective intensity can be defined for which the cut-off law provides the correct value for maximal intensity [108]. This indicates the importance of the pulse length for the creation of high harmonics. In a long pulse, multi-photon ionization can fully ionize the medium before the pulse intensity required for tunnel ionization is reached, completely frustrating HHG. This might have been the case for some experiments prior to McPhersons study that created sufficient intensities but with pulse lengths on the order of 10s of picoseconds.

### Coherence Properties

The 3-step process described above is repeated for every half-cycle,  $T/2$ , throughout the duration of the laser pulse. The result is a burst of pulses, each a few hundred attosecond long and spaced by  $T/2$ . As every emission is locked to the phase of the driving field, the emission of harmonics is coherent in time and space [96, 87]. A Fourier transformation of this *attosecond pulse train*, yields a frequency spectrum with discrete peaks spaced at odd integers of the frequency,  $\omega_0$ , of the fundamental laser field.

$$\omega_n = n \omega_0. \quad \textit{Frequency of the } n^{\text{th}} \textit{ harmonic} \quad (3.10)$$

Odd and even harmonics can be obtained when the inversion symmetry of the harmonic medium (gas) is broken and coherent emission only occurs once every cycle. This can be achieved by mixing of the fundamental and the second harmonic of the laser, which is usually generated by non-linear conversion in a crystal [87].

The effect of coherent superposition of single-pulses is illustrated in Figure 3.3. The measured harmonic spectra of pulses of two different lengths are shown in Figure 3.4. The short pulse produces a much less pronounced comb pattern than the longer pulse due to the coherent addition of fewer bursts. In the case of an ultrashort pulse of only few cycles, the highest photon energies can only be produced at one specific time because the required intensity is only reached once during the entire pulse. This manifests in a continuous spectrum near the high energy cutoff.

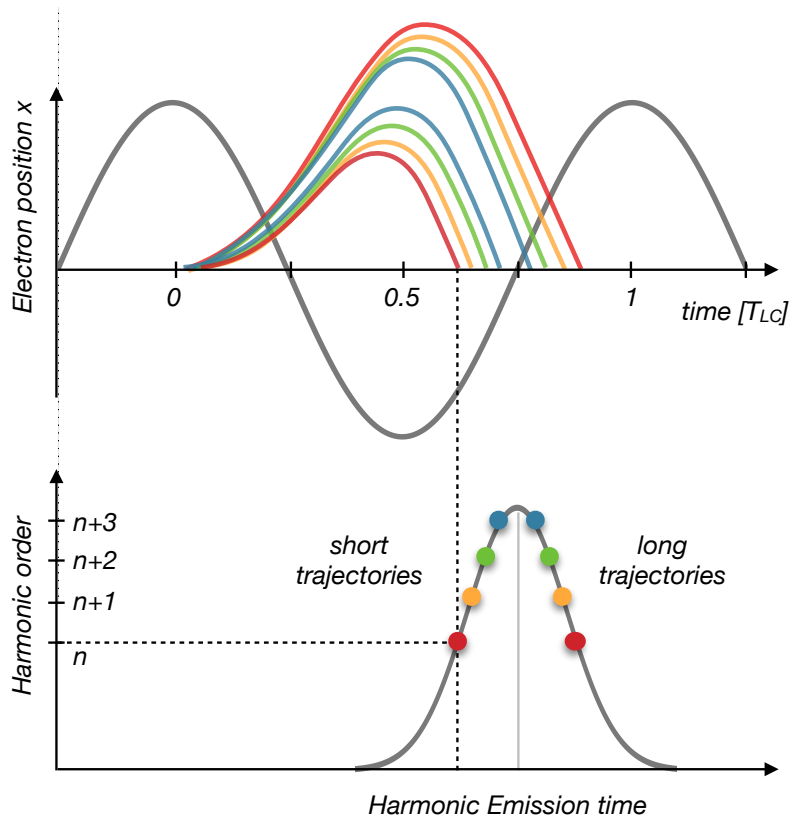


**Figure 3.2:** Schematic showing the different emission times and corresponding trajectories of High Harmonic emission. The electrons tunnel into the continuum near the peak of the electric field. Depending on the exact emission time, two sets of electron trajectories are formed where the electrons can recombine with the ion. For the short trajectories, electrons combining earlier have lower energy than electron arriving later in time. This energy dependence is reversed for the set of long trajectories (Figure inspired by Lou DiMauro).

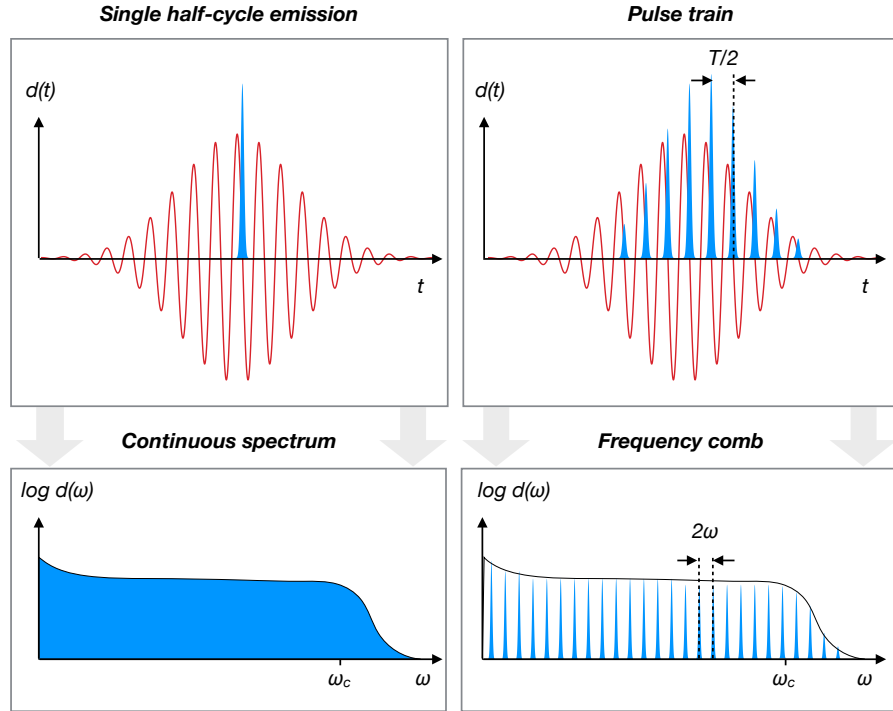


**Figure 3.3:** Sketch of the time-dependent dipole moment  $d(t)$  induced by an oscillating laser field with optical cycle  $T$  (top row) and the corresponding frequency spectrum of the emitted photons (bottom row). If we consider only the electron emission near the maximum of one half-cycle, we obtain a single attosecond pulse (left). The corresponding spectrum in the frequency domain is continuous. For emission at every half cycle  $T/2$ , the Fourier transform to  $d(\omega)$  yields a *frequency comb* with spacing  $2\omega$  (figure inspired by [8]).

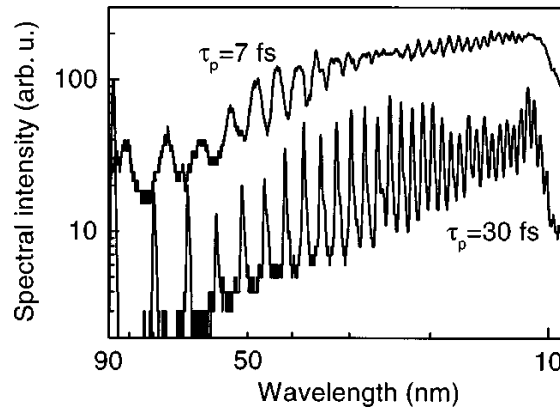


**Figure 3.4:** Harmonic spectra generated in neon with pulses of 7 and 30 fs duration. The 30 fs pulse produces a frequency spectrum of discrete peaks up to the cutoff. In the case of the short pulse the peaks become broader and completely disappear near the shortest wavelength. The highest photon energies are only created at maximal intensity which is only reached once during the short pulse leading to a continuous spectrum near the cutoff. Harmonics generated in neon (250 Torr) at a wavelength of  $\approx 0.8 \mu\text{m}$  and an intensity of  $\approx 3 \times 10^{14} \text{ W/cm}^2$  (data from M.Schnürer in [19]).

### Single Attosecond Pulses

It becomes clear that a single attosecond pulse can be generated if the electric field of the laser is either short enough or modified in a way that the harmonic emission occurs only in one half-cycle of the pulse. Single attosecond pulses shorter than 100 as have been generated with a variety of techniques that can be found in recent review articles [26, 28]. The spectrum of such a pulse is indeed continuous and its bandwidth is very large.

### Quantum Mechanical Model and Limitations

The simple classical description of High Harmonic Generation in the 3-step model was later recovered in a quantum mechanical treatment by Lewenstein *et al.* [89]. In this description, the time-dependent dipole moment of the medium can be written as the product of three terms: a) the ionization given by the transition probability to the continuum, b) the propagation of the electron in the field, and c) the recombination to the ground state, given by the complex conjugate of a).

Intrinsically, the 3-step model and the quantum mechanical description is only valid for energies above the ionization potential. For low orders, the electron trajectories remain near the ion and the coulomb potential, neglected in the model, influences the electron trajectories. The calculations become inaccurate for low energies as bound states play a significant role in this part of the spectrum [87].

For completeness it should be noted that HHG generation represents only one of the several processes of electrons in a strong-field. Only a small fraction of the electrons returning to the vicinity of the ion actually recombine emitting photons. Inelastic scattering of the electron leads to non-sequential double ionization and elastic scattering is responsible for *above-threshold ionization (ATI)* that produces a well investigated characteristic sequence of peaks in the electron spectrum.

### 3.3.2 Phase matching

In the previous section, High Harmonic Generation was explained in terms of the induced dipole moment of a single atom. In order to produce a measurable amount of harmonic photons, a coherent superposition of the emission from many atoms is required.

For constructive interference of the harmonic radiation in the generation volume, the oscillations of the respective fields with wavevector  $k(\omega)$  need to occur in phase.  $\Delta k$  represents the mismatch of the velocity of the phase of the fundamental to the harmonics. A mismatch results in destructive interference of the harmonic emission. In order to achieve a high flux of harmonic photons,  $\Delta k$  needs to be kept small. *Phase matching* is the process of adjusting the experimental parameters to minimize the phase shift. The mismatch of the phase velocities of the fundamental frequency,  $\omega_0$ , and the harmonics  $\omega_q = q\omega_0$  can be written as

$$\Delta k = qk(\omega_0) - k(\omega_q). \quad \text{Phase velocity shift} \quad (3.11)$$

In vacuum, this mismatch is zero as can be seen by inserting  $k_{vac} = 2\pi\omega/c$  into Equation 3.11. However, High Harmonic Generation occurs in a dispersive medium where the diffractive index  $n(\omega)$  changes with frequency (see also Appendix A.1). Aside from neutral dispersion, the free electrons created in the strong-field of the laser form a plasma that modifies the refractive index of the medium. Furthermore, the laser beam needs to be focused resulting in a position dependent phase. This adds a geometrical term to the

frequency dependence of the wavevector. Adding the different contributions, the total mismatch can be written as

$$\Delta k = \Delta k_{disp} + \Delta k_{plasma} + \Delta k_{foc}. \quad \text{Phase matching terms} \quad (3.12)$$

### Neutral Dispersion

The wavevector for a dispersive medium is given by

$$k_q = n(\omega_q) \frac{\omega_q}{c}. \quad \text{Wavevector in a dispersive medium} \quad (3.13)$$

The contribution of the neutral dispersion to the phase change is therefore

$$\Delta k_{disp} = q k_0 - k_q = q \frac{\omega_0}{c} (n(\omega_0) - n(\omega_q)). \quad \text{Dispersion mismatch} \quad (3.14)$$

Dispersion is caused by resonances in the medium. For photon energies below a few eV, the refractive index can be approximated with the *Sellmeier equation* using measured coefficients (see Appendix A.3). For higher energies, atomic scattering factors are available to obtain an estimate of the dispersive phase shift (see [8] for details).

We can see that the neutral dispersion rises linearly with the harmonic order. Therefore, phase matching becomes increasingly harder for higher harmonics.

### Plasma Dispersion

Only few electrons that are created by ionization in the strong laser field recombine with the ions. The large amount of free electrons in the medium creates a plasma with resonance frequency

$$\omega_p = \sqrt{\frac{e^2 N_e}{\epsilon_0 m_e}}, \quad \text{Plasma frequency} \quad (3.15)$$

where  $N_e$  is the free-electron density,  $\epsilon_0$  is the dielectric constant, and  $e$ ,  $m_e$  are the charge and mass of the electron. At usual gas pressures of 10s of Torr, this frequency is much lower than optical or harmonic frequencies,  $\omega$ . The refractive index induced by the plasma can then be approximated by

$$n_{plas}(\omega) \simeq 1 - \frac{1}{2} \left( \frac{\omega_p}{\omega} \right)^2. \quad (3.16)$$

The wavevector  $k_{plas}$  is obtained by inserting the refractive index of the plasma in Equation 3.13 giving

$$\Delta k_{plas} = q k_{plas}(\omega_0) - k_{plas}(\omega_q) = \frac{\omega_p^2 (1 - q^2)}{2q c \omega_0} \quad \text{Plasma phase shift} \quad (3.17)$$

for the phase velocity mismatch caused by the plasma.

### Geometric effects

Achieving a high electric field intensity requires focusing the laser beam. Using a lens or mirror of focal length  $f$ , a gaussian beam of radius  $w$  converges to a minimal size of

$$w_0 = \frac{f}{\pi w} \lambda. \quad \text{Gaussian beam waist at focus} \quad (3.18)$$

The waist of the beam remains constant for a length of

$$z_R = \frac{\pi w_0^2}{\lambda} \quad \text{Rayleigh length} \quad (3.19)$$

before and after the focus and increases approximately linearly outside. For simplicity, we consider the spatial phase dependence only for the propagation direction,  $z$ . Solving the wave equation in vacuum for an electric field with spatial phase  $\phi(\vec{r})$  (see [119]) leads to a phase change of

$$\phi_{Guy}(z) = \arctan\left(\frac{\lambda z}{\pi \omega_0^2}\right). \quad \text{Guy phase shift} \quad (3.20)$$

For ( $z \ll 2z_R$ ) this can be approximated by

$$k_{foc}(z) = \frac{d}{dz} \phi_{Guy}(z) \simeq \frac{1}{z_R}. \quad (3.21)$$

The mismatch of the phase velocity from focusing is then given by

$$\boxed{\Delta k_{foc} = q k_{foc}(\omega_0) - k_{foc}(\omega_q) = \frac{q-1}{z_R}} \quad \text{Geometrical phase shift} \quad (3.22)$$

This expression is only valid at the focus and in vacuum. A more rigorous treatment of the geometrical phase mismatch that includes the variation resulting from points away from the focus, as well as including the intensity dependent dipole moment, can be found in [8].

In summary, we obtain the following terms for the phase shift:

$$\Delta k = \Delta k_{disp} + \Delta k_{plas} + \Delta k_{foc} \quad (3.23)$$

$$= q \frac{\omega_0}{c} \left( n(\omega_0) - n(\omega_q) \right) + \frac{\omega_p^2 (1 - q^2)}{2q c \omega_0} + \frac{q-1}{z_R} \quad (3.24)$$

In practice, phase matching can be optimized by changing the pressure, which affects the plasma dispersion. The position as well as the intensity of the laser focus change the geometrical phase shift. Different focusing schemes such as the use of hollow waveguides can be used to keep a constant high intensity over a longer interaction length and usually improve geometrical phase mismatch. Multiple cells or jets have also been used to reduce the phase mismatch. For a more detailed review of phase matching in free focusing geometries and waveguides see [90, 13, 107, 97, 123] and references therein.

### 3.3.3 Reabsorption

Since the materials used for High Harmonic Generation have electronic states in the spectral range of the harmonics ( $\sim 10 - 100$  eV), the generated photons will be reabsorbed in the medium. The length after which the intensity has dropped to  $1/e$  is defined as the *absorption length*,  $L_a$ .

$$L_a = \rho \sigma \quad \text{Absorption length} \quad (3.25)$$

where  $\rho$  is the particles density and  $\sigma$  the photoionization cross-section. The intensity of the  $q^{\text{th}}$  harmonic can be written as the integral of the emission along the propagation direction,  $z$ , of the single particle amplitudes  $A_q(z)$  and the respective phases,  $\phi_q(z)$  [119]:

$$I_q \propto \left| \int_0^L \rho A_q(z) \exp\left(-\frac{L-z}{2L_a}\right) \exp(i\phi_q(z)) dz \right|^2 \quad (3.26)$$

Assuming the amplitude remains constant over the length  $L$  (which is a reasonable assumption for the loose focusing geometry used in this experimental setup, the integral yields the following expression:

$$I_q \propto \rho^2 A_m^2 \frac{4L_a^2}{1 + 4\pi^2 (L_a/L_c)^2} \left( 1 + \exp\left(-\frac{L}{L_a}\right) - 2 \cos\left(\frac{\pi L}{L_c}\right) \exp\left(-\frac{L}{2L_a}\right) \right) \quad (3.27)$$

Here, the *coherence length*,  $L_c$ , has been used, which is defined as the distance at which the phase shift is equal to  $\pi$

$$L_c = \frac{\pi}{\Delta k}. \quad \text{Coherence length} \quad (3.28)$$

When phase matching is optimized,  $L_c$  becomes large, and it represents a measure for the quality of phase matching.

Figure 3.5 shows the effects of absorption on the yield of high harmonic photons after going through the generation medium. The calculated harmonic photon yield from Equation 3.27 is plotted as a function of the propagation length,  $L$ , for different values of  $L_c$ . Even for perfect phase matching conditions,  $L_c \ll L_a$ , the emission of harmonics is still limited by reabsorption of the photon in the medium. The absorption rate increases with the number of photons in the field. When the harmonic absorption rate reaches the emission rate, no further gain can be achieved. This regime is called *absorption limited HHG*.

### 3.4 The High Flux HHG Source at LBNL

Despite efforts to use liquid [35] and solid targets [111, 53, 145] as the generation medium, noble gases such as argon, krypton, and neon are still the most widely used media for the conversion process. Despite the low conversion efficiency, the overall output flux generated is still significantly higher than with other media.

Titanium-Sapphire crystals are omnipresent as the lasing medium for ultrashort pulses. Ti:sapphire has a variety of states that allow them to be pumped efficiently using flash-lamp or diode based green (532 nm) lasers. The stimulated emission around 800 nm offers sufficient bandwidth to create pulses of tens of femtoseconds. Additionally, the widespread use of infrared lasers makes a variety of affordable optics available.

Several schemes have been implemented to generate high harmonics in a gas including tight focusing into a gas jet, loose focusing into half-open or closed gas cells, as well as focusing into a hollow, gas-filled waveguide. The latter has several advantages to the other techniques [167, 123] but is limited in the laser pulse energy to a few mJ in order to prevent damage to the waveguide.

In this setup, a loose focusing geometry combined with a gas cell was chosen in order to achieve a high photon flux. Even in well optimized setups, the conversion efficiency from the fundamental to the harmonic photons hardly passes  $10^{-5}$  to  $10^{-6}$ . Thus, obtaining a high flux of VUV and XUV photons requires initiation of the conversion process with a high amount of initial laser power. As discussed in Section 3.3.2, the intensity of the field cannot be arbitrarily increased due to phase mismatch of the emitted harmonics. Absorption sets a limit to a reasonable length of the interaction medium. In a loose focusing geometry, the

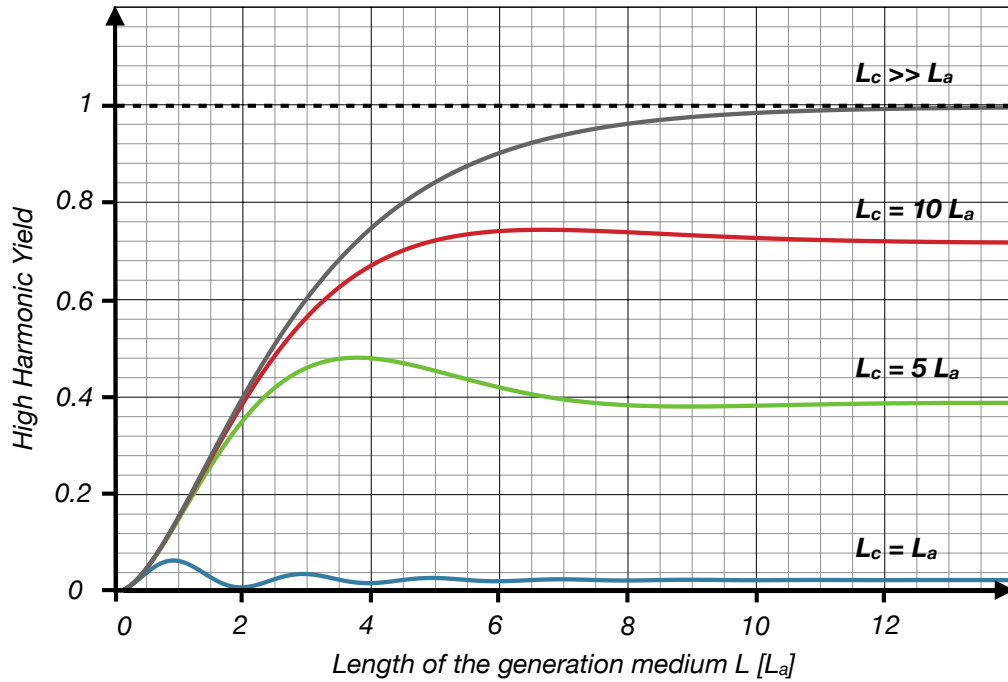


**Figure 3.5:** Plot of the high harmonic intensity versus the length of the generation medium in units of the absorption length,  $L_a$ . The curves for different coherence lengths  $L_c$  are shown in different colors. If the coherence length is on the order of the absorption length, only minimal yield can be achieved. Decoherence quickly suppresses the yield after propagation through the medium over several  $L_a$ . When the phase matching conditions are improved and the coherence length becomes significantly larger than the absorption length, the yield is ultimately limited by reabsorption in the medium.

focal size is increased. This distributes the available power to maintain an optimal laser intensity for High Harmonic Generation over a large area. As a result, more atoms become active and, at a similar conversion efficiency, a higher flux can be obtained. Of course, problems of phase matching persist but the highest total flux measurements of HHG have been achieved with this method [170, 107].

### 3.4.1 Laser System

The laser system at the Lawrence Berkeley National Laboratory is a high power, low repetition rate infrared laser. It combines a mode-locked Ti:sapphire oscillator with a two stage amplification scheme, based on the technique of chirped pulse amplification.

The 88 MHz oscillator cavity is built around a Ti:sapphire crystal (KM-Labs Dragon kit) pumped at 532 nm from a frequency doubled Nd:YVO<sub>4</sub> diode pumped laser (Coherent Verdi V6). The usual output power for mode locked pulses is about 0.5 W centered at 808 nm with a bandwidth of 40 nm. In order to avoid damage and allow high amplification, the pulses are first stretched in time and only recompressed after both amplification stages, a technique called *chirped pulse amplification (CPA)*. Gratings are used to spatially separate and subsequently temporally distribute the spectrum to create pulses longer than 200 ps width in a common stretcher setup [164].

The first amplification stage consists of a regenerative amplifier that traps the pulse in a cavity with entrance and exit controlled by pockel-cells. After about 30 passes through a Ti:sapphire crystal, which is pumped by a diode laser at 532 nm (Coherent EVO 15), the pulse energy reaches around 1.2 mJ. Pulses are released to the following stage at a rate of 50 Hz.

In the second amplification stage, the infrared pulses are amplified to about 60 mJ after six passes through a third Ti:sapphire crystal. This crystal is pumped by a high power flash lamp laser (Continuum Powerlite 9050, max 30 W, 50 Hz). The beam size is adjusted with a Galilean telescope and measures about 30 mm at the output of the multi-pass amplifier. At higher pulse energies or significantly smaller beam sizes, damage of the optics has been observed regularly.

Such high pulse energies can cause non-linear effects such as *self phase modulation* or *self focusing* even in air (see Appendix A.1). In vacuum, the high peak as well as the average power cause damage to the gratings and optics within days or weeks of operation. Therefore, the grating pair, as well as the focusing mirror and the folding optics, are kept in helium filled vacuum chambers at a pressure of 100 Torr. At this pressure, the heat transport in helium is comparable to air, and non-linear effects are negligible due to the very small dispersion coefficients of helium [130]. The uncompressed infrared beam enters the compressor chamber through a standard viewport and leaves the folding chamber through a window gate valve (UV fused silica, 0.25 mm thickness) that separates the helium environment from the vacuum beamline.

### 3.4.2 High Flux Harmonic Generation

High harmonics are generated by focusing the high power laser beam with a curved mirror  $f = 6$  m into a 10 cm long gas cell. The cell is placed inside a vacuum chamber and can be filled with various gases. A 1/4 in gas line connects it via a vacuum feedthrough to the gas delivery system. The cell is sealed off at both ends with thin (0.05 mm) stainless steel shims. After alignment of the cell to the laser beam path, the entrance and exit holes for the laser and the generated harmonics are drilled by the laser beam itself. The average laser power is sufficient to drill holes of approximately 1 mm diameter in the front and the back shim within seconds. As the beam pointing is not actively stabilized, the holes widen

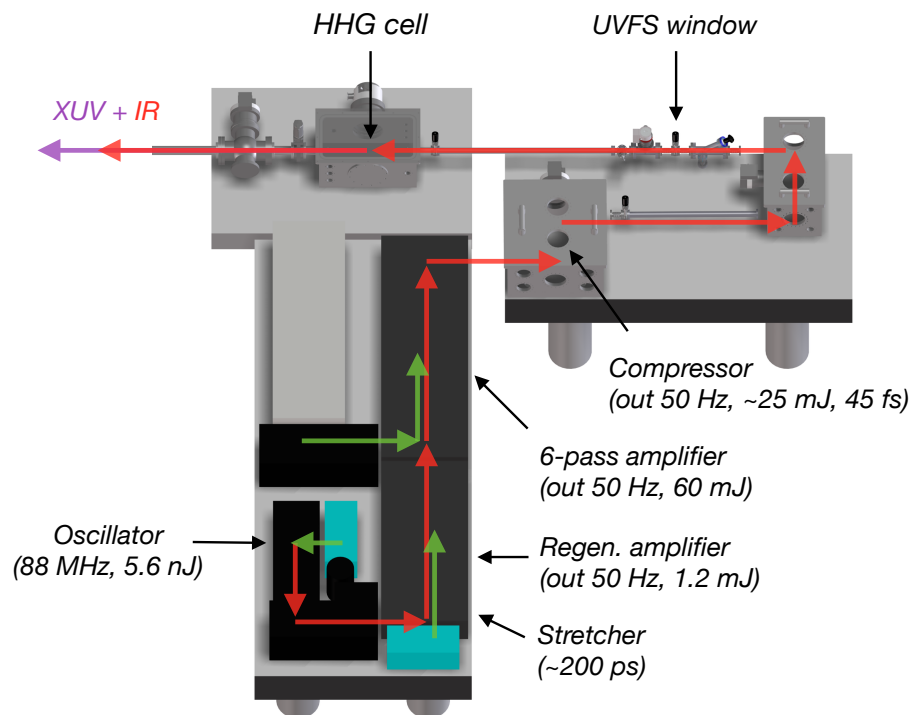


**Figure 3.6:** Overview of the laser system and its main components. The pulse amplification occurs with chirped pulses in air. Recompression and focusing is performed in a helium back-filled chamber. The compressed beam enters the vacuum beamline through a thin UVFS window. High Harmonic Generation occurs in a gas cell in differentially pumped chamber several meters downstream.

slightly after long operation. This requires readjustment of the backing pressure of the cell to obtain maximal harmonics yield in measurements lasting several days. The shims are usually changed before new runs.

Figure 3.7 shows a picture of the gas cell with drilled shims. The chamber containing the gas cell is pumped by a 1000 l/s turbo molecular pump. Continuous operation is possible at cell pressures up to 10 Torr. Higher pressures could be achieved by adding differentially pumped sections to the front and back of the cell.

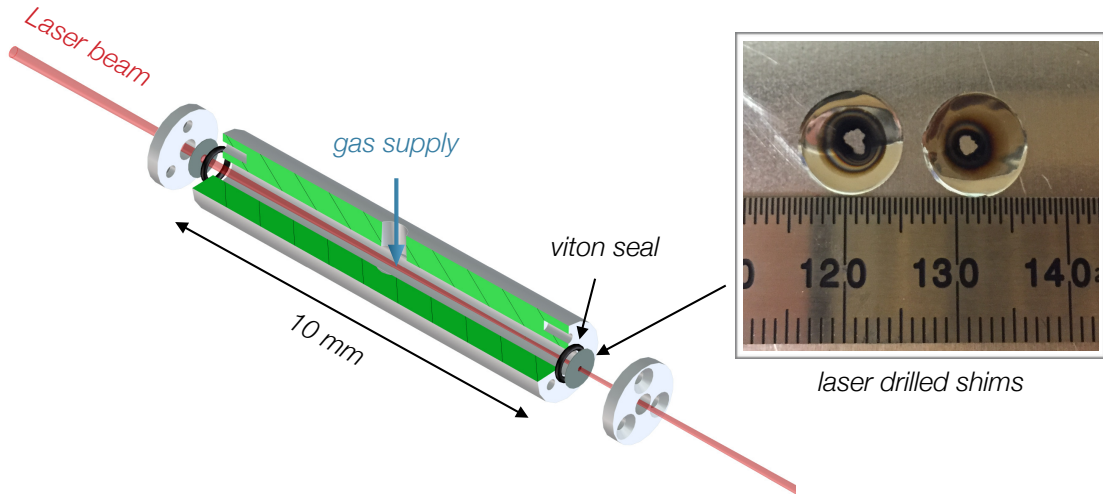


**Figure 3.7:** Drawing of the 10 cm gas cell used for High Harmonic Generation. The cell is sealed with stainless steel shims (0.05 mm thick) that are pressed onto viton o-rings. The inset shows a photography of shims drilled by the laser with a mm scale for reference

### Flux Optimization

Phase matching of the emission from atoms in the long interaction volume is critical to obtaining high flux (see Section 3.3.2). In practice, phase matching is optimized on a daily basis by adjusting the focal position, the pulse length, and the gas pressure. These parameters are tuned until the highest flux is measured on an aluminum coated photo diode (IRD UV). If maximal intensity for a particular harmonic is required, the XUV spectrometer (see Section 4.3.1) could be used for optimization.

For practical reasons, the focal position with respect to the gas cell is changed by moving the cell on a motorized stage ( $\sim 50$  cm travel). Optimal high harmonic flux is usually obtained for a focus centered about 50 cm downstream of the cell center.

The pulse duration can be adjusted by varying the grating position of the compressor using its motor controller. Shorter pulses usually create less plasma dispersion and produce a higher photon yield. Due to the faster increase in intensity, less free electrons are produced during a short pulse before the required intensity for tunneling is reached.

The gas pressure is controlled with a commercial precision pressure controller (MKS) that operates a valve in feedback with a capacitive pressure sensor. While the overall photon flux varies with pressure, optimal phase matching conditions are different for each harmonic. At high pressures, neutral dispersion causes the phase mismatch to increase with the harmonics order such that mostly low orders are obtained. This can be used to

modify the harmonic spectrum. Spectral manipulation is discussed further in the following section.

Figure 3.8 shows high harmonic spectra recorded with the home built XUV spectrometer for the conversion in krypton and argon gas in a 10 cm cell at various pressures. The intensity distribution of the harmonics varies due to the different ionization potentials ( $I_p(Kr) = 14.0$  and  $I_p(Ar) = 15.8$ ) and saturation intensities (for Argon  $\approx 2.5 \times 10^{14} \text{ W/cm}^2$ ) [176]. The maximal energy also differs, as can be calculated with Equation 3.9, although it is above the spectral range of the spectrometer. The highest flux of high orders is usually achieved at pressures between 4 and 6 Torr in a 10 cm long cell. For other gases a shorter cell can be beneficial [107]. The spectral shape obtained in the measurements using the XUV spectrometer will be discussed in more detail in Section 4.3.1.

The total high harmonics flux was measured in a very similar setup previously by T. Allison using a helium absorption cell and ion charge counting [8]. A value of  $10^9 - 10^{10}$  photons/harmonic/shot was obtained. The photon flux is measured daily using aluminum coated photo diodes (IRD UV) positioned downstream of the first silicon mirror and the Split-Mirror Interferometer (see Figure 4.2). The measured values of 300 nV/s after one silicon mirror reflection are consistent with the previous documented values. The 3<sup>rd</sup> and the 5<sup>th</sup> harmonic cannot be recorded with either the aluminum coated diode or the XUV spectrometer. Instead, an additional uncoated diode with a filter is used to measure the 5<sup>th</sup> harmonic after two mirror reflections with usual values of 50 - 100 nV/s.

Changes in beam mode and power can degrade the harmonics yield and daily monitoring and optimization are required. The main factor for the observation of significantly reduced flux was found to be non-permanent damage of the first silicon mirror resulting in a reduced reflectivity in the ultraviolet spectrum but increased reflectivity of the fundamental IR beam. The visible dull coating of the mirror can usually be removed by cleaning the substrate in a commercial ozone oven in a few hours. Similarly, the gratings as well as the optics closest to the laser focus (the last folding mirror and the UVFS window) show damage after long periods of use due to the small spot size ( $\sim 1$  in) and the resulting high intensity. Other groups have observed similar problems [5], and they seem to occur even at very low vacuum pressures  $< 10^8$  mbar. In-situ UV lamps or cleaning using RF-fields [117] are promising candidates to resolve such issues.

### 3.4.3 Manipulation of Spectral Properties

As mentioned earlier, phase matching and the dispersion depend on the gas pressure and the laser intensity. This can be used to intentionally modify the spectral shape and energy. This can be seen in the spectra in Figure 3.8, and it will be discussed further in the following.

#### High order suppression

As discussed in Section 3.3.2, the phase mismatch increases with the harmonic order (Equation 3.11). Increasing the gas pressure increases the mismatch beyond a certain pressure and suppresses the emission of high orders. This effect is demonstrated in argon in Figure 3.9. The top graph shows the yield of the harmonic orders 11 - 21 for different cell pressure between 4 and 12 Torr. While the overall yield decreases with pressure, the peak of the distributions shifts from the 15<sup>th</sup> to the 13<sup>th</sup> order. In the graph below, the normalized yield change of the different harmonics is plotted as a function of pressure (normalized to the yield at  $p = 4$  Torr). At pressures above 10 Torr, only harmonics below the 21<sup>st</sup> produce a measurable signal. In comparison, the yield of the 11<sup>th</sup> harmonic has only decreased by about 30%.

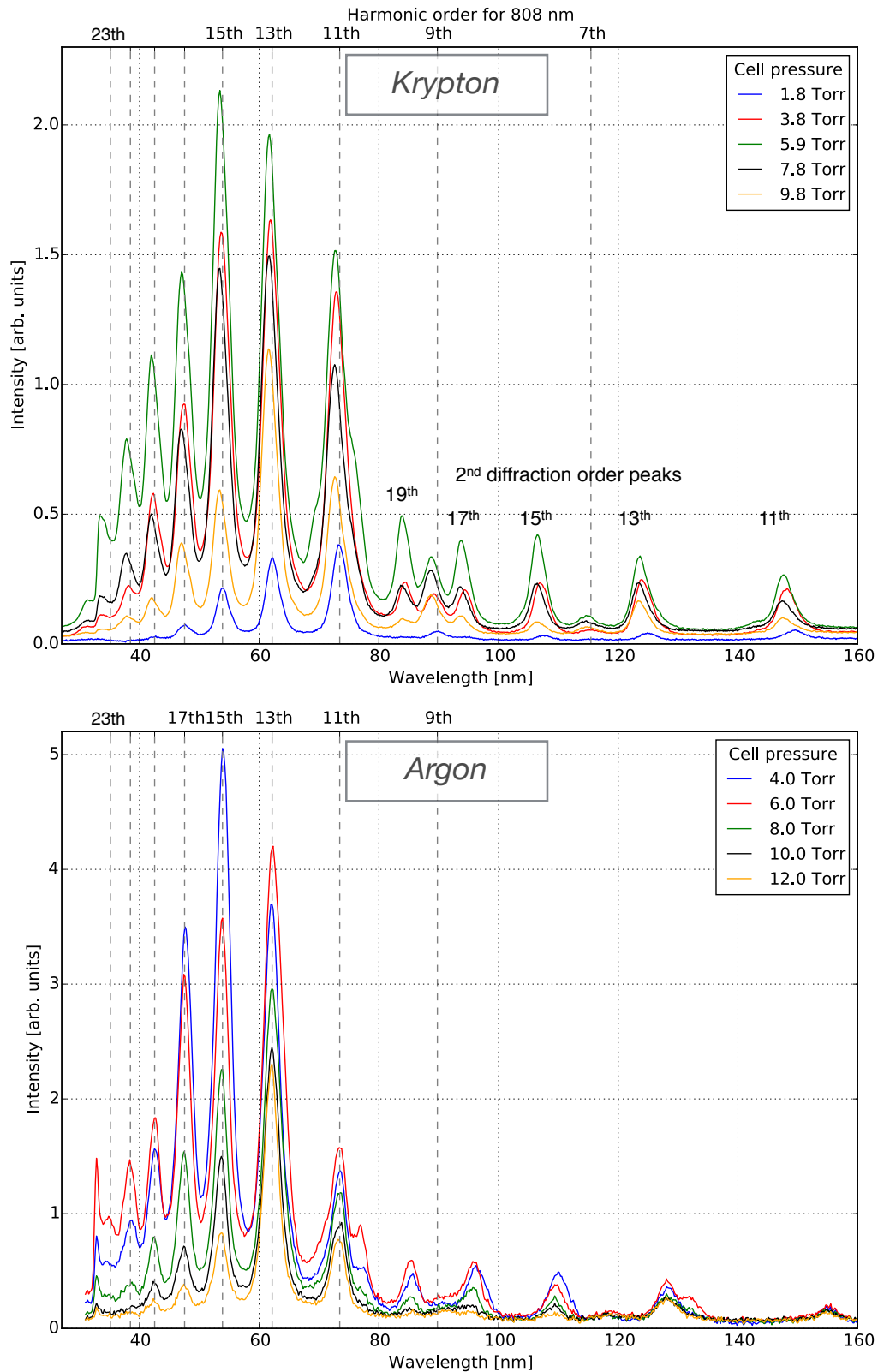


**Figure 3.8:** XUV spectra from High Harmonic Generation in a 10 cm cell. **(Top)** HHG in krypton gas at cell pressures of 1.8 to 9.8 Torr. While the harmonic yield varies with pressure, a shift of the harmonic wavelength to shorter wavelength is observed with increasing pressure. This blue shift is discussed in Section 3.4.3. The smaller peaks that become dominant at wavelength above 80 nm correspond to second order diffraction from the grating. **(Bottom)** HHG in argon at cell pressures of 4 to 12 Torr. See Section 4.3.2 for details on the spectral analysis.

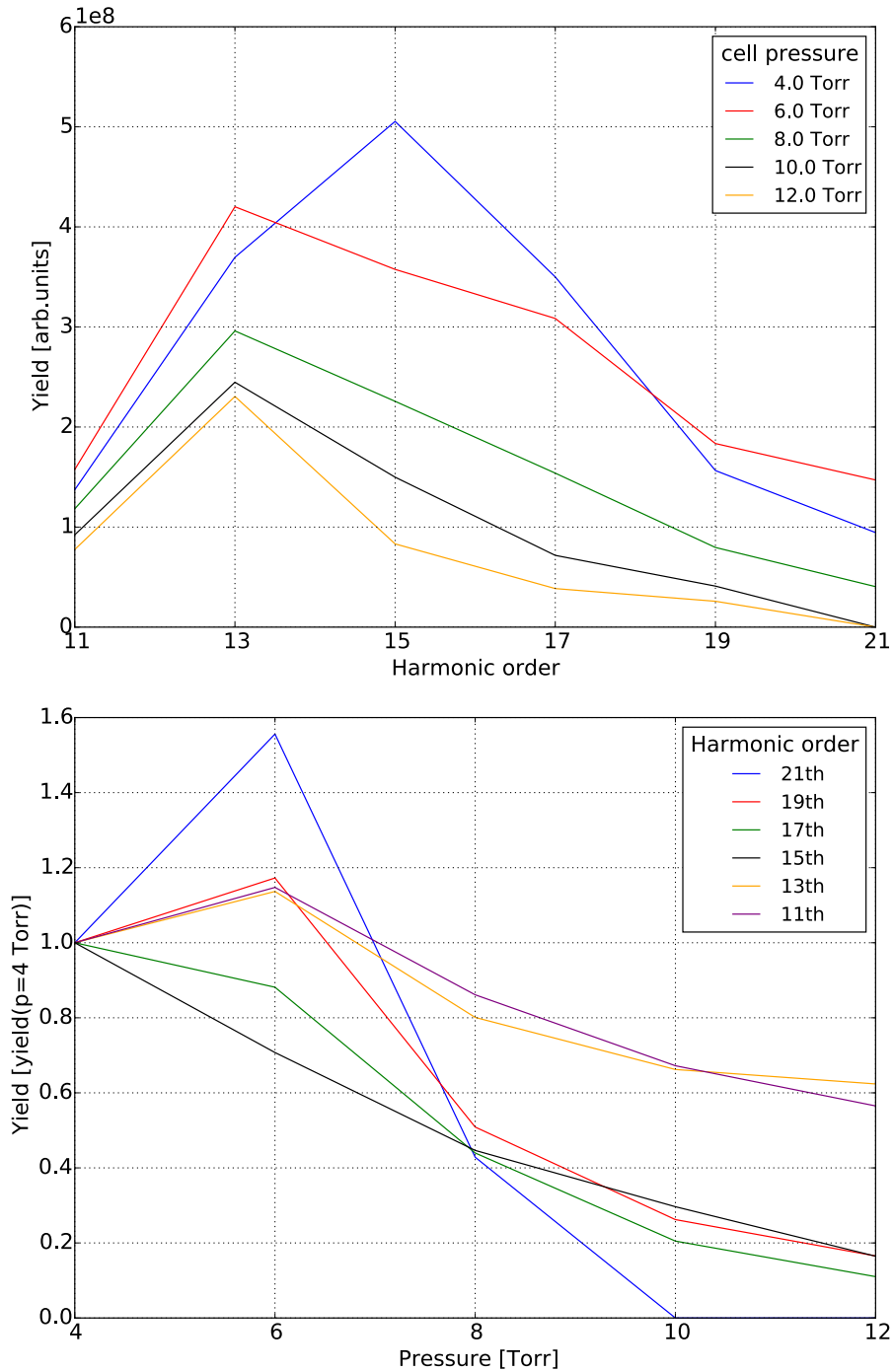


**Figure 3.9:** (Top) Yield of the harmonics produced in argon at different pressures as a function of the harmonic order. (Bottom) Normalized intensity as a function of pressure for different harmonic orders. The yield at  $p = 4$  Torr is normalized to one.

### Blueshifting

The wavelength of each harmonic can also be modified by changing the cell pressure or the laser intensity. The effect is known as *blue shifting* as the spectrum is shifted to shorter wavelengths. Two effects are known to play a role. At high laser intensities near the saturation limit of the gas, ionization produces a significant amount of free electrons which results in a change of the index of refraction. The change depends on the spatially and temporally changing electron density  $N_e(\mathbf{r}, z, t)$  and the frequency  $\omega$  of the radiation by the following equation [176, 90]:

$$\delta n_1(\mathbf{r}, z, t) = \frac{2\pi e^2}{m\omega^2} N_e(\mathbf{r}, z, t). \quad \text{Refractive index change} \quad (3.29)$$

The time-dependence of the refractive index results in a shifted spectrum of the fundamental beam towards shorter wavelengths. This is well known to occur in dispersive media known as *self-phase modulation (SPM)*. The harmonics created from the fundamental beam at wavelength  $\lambda_0$  inherit a wavelength shift  $\Delta\lambda_n$  according to

$$\Delta\lambda_n = \frac{\Delta\lambda_0}{n}. \quad \text{Blueshift of the } n^{\text{th}} \text{ harmonic} \quad (3.30)$$

For short wavelengths, i.e. high harmonic orders, the refractive index change is negligible as it scales with  $1/\omega^2$  (see Equation 3.29).

At intensities much larger than the saturation intensity, the non-adiabatic response of the atoms to a fast changing electric field can blueshift the harmonic radiation further. For very high orders, a shift on the order of the harmonics spacing ( $2\omega$ ) has been reported [151]. At such intensities, ionization can occur long before the peak intensity of the pulse is reached, such that the free electrons are subject to a much larger field change resulting in a blue shifted spectrum after recombination. Instead of decreasing with the harmonic order, as seen for the shifts caused by the dispersion of the fundamental beam, the non-adiabatic shift has been observed to rise linearly with respect to the order.

Blue shifting of the HHG spectrum was observed with the present setup in Krypton. While the strongest total harmonic yield with the most harmonics orders present is observed at 5.9 Torr, the spectrum in Figure 3.8 also clearly shows a shifting of the peak positions of the individual harmonics towards shorter wavelength with increasing pressure. This is quantified in Figure 3.10. The wavelength shifts are shown for every harmonic with respect to the calculated position based on the harmonics of a driving laser with a wavelength  $\lambda = 808$  nm. The corresponding energies are plotted below.

At orders above the 19<sup>th</sup> harmonic, the shift appears to be larger than expected from self-phase modulation of the fundamental beam only. This could be attributed to non-adiabatic blue-shifting or similar strong-field effects of ionization early in the pulse as observed in [108].

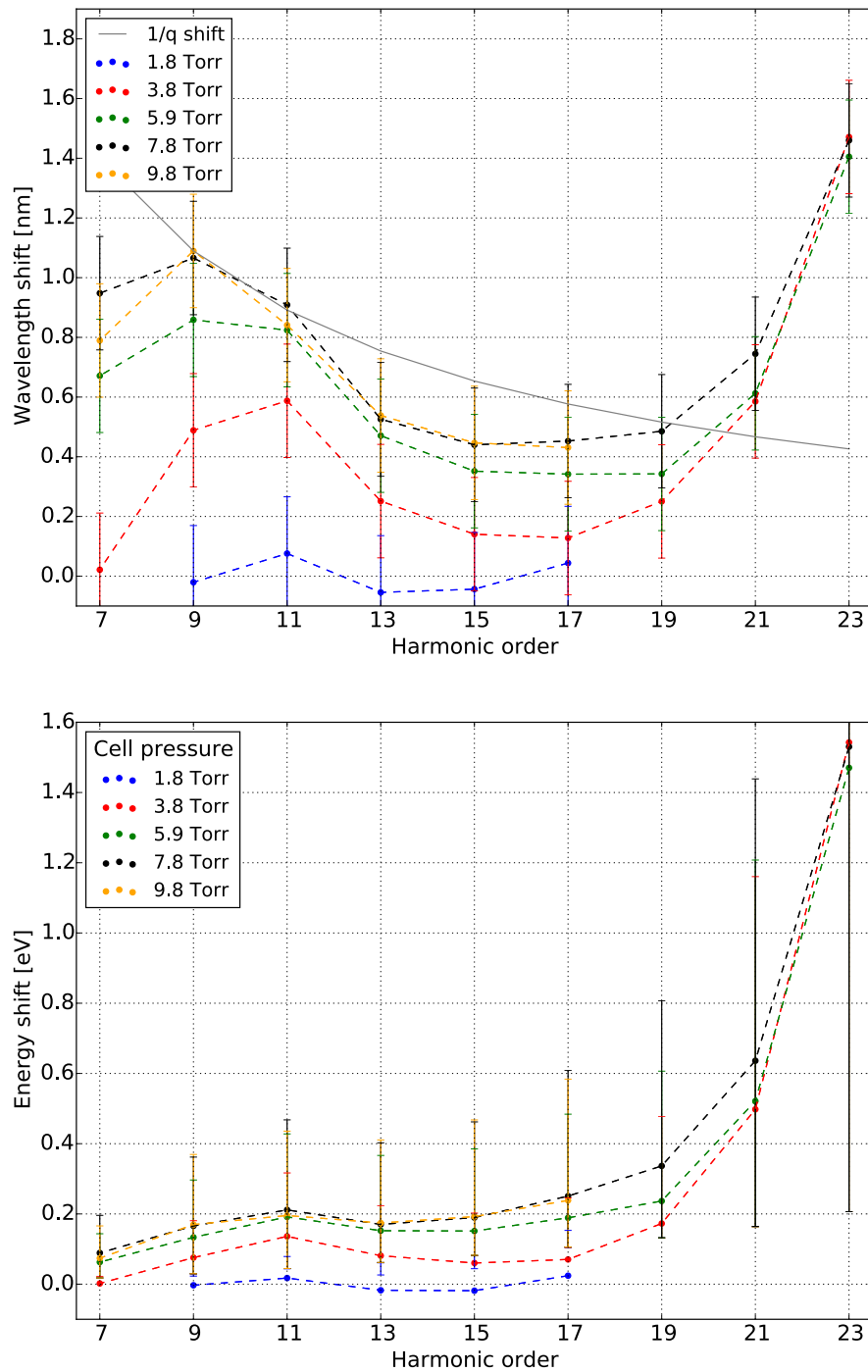


**Figure 3.10: (Top)** Blueshifting of the harmonic spectrum recorded in krypton at various pressures. The wavelength shift is shown with respect to the calculated values for harmonics from a fundamental wavelength  $\lambda = 808$  nm. The spectrum is calibrated from the peak positions at 1.8 Torr where no or only a small shift is expected. The gray line indicates the amount of shift expected from dispersion of the fundamental only. **(Bottom)** Corresponding energies for the shifts of each harmonic shown in the top graph. The estimated error is an upper limit from the peak position fit.

## 4 XUV Beamline Components

In this chapter, the various tools and components that are needed to deliver the photons produced in the high harmonics light source (see chapter 3.4) to the end-station for molecular experiments will be discussed.

Ideally, the experimenter selects specific photon energies at the molecular target initiating only the transitions and the processes which are the subject of study. Therefore, the ability to both select particular photon energies as well as to characterize the quality of the selection process are key capabilities of an experimental setup for molecular dynamics studies. Several techniques for selecting specific harmonics were employed in this setup and are presented in Section 4.1. In Section 4.3, the XUV light spectrometer which was developed to characterize the photon spectrum delivered to the gas target is described.

In order to create the temporal delay between pulses for pump-probe studies, a custom in-vacuum Split-Mirror Interferometer (SMI) was developed in collaboration with the Center for X-Ray Optics (CXRO) at Lawrence Berkeley National Laboratory. The interferometer is described in Section 4.2.

As light pulses at several eV energy are readily absorbed in air, the entire beamline has to be enclosed in vacuum chambers. This presents many technical challenges including heat transport, material choice, space constraints, and the control and manipulation of mechanical devices in vacuum. Section 4.4 provides some solutions for the engineering challenges that were encountered for a laboratory based vacuum beamline including in-vacuum alignment tools and differential pumping.

### 4.1 Energy Selection

The absorption of a single photon in the extreme ultraviolet can usually initiate a variety of different excitations or the ionization of the molecule. Adding an additional photon of a specific energy can furthermore initiate subsequent transitions and dissociation processes involving a range of electronic states. Hence, a measurement involving two photons of different color increases the complexity significantly. In many cases it is even impossible to unambiguously determine the pathway of the reaction without controlling the photon energy of both steps. Therefore, the ability to selectively initiate a particular process is of prime value in determining the electronic states involved in the processes.

Synchrotron radiation sources and Free Electron Lasers (FELs) achieve this goal by using monochromators. In the case of FELs, it is also possible to shape the electron bunch characteristics to produce the required photon energy. The latter method is excluded for High Harmonic Generation due to the different nature of the light generation process (see Section 3.3).

Monochromators usually use diffractive gratings or zone plates that disperse the spectrum spatially [121]. A particular photon energy can be selected by rotating the grating to a position where only the desired part of the spectrum passes through a slit opening. However, the optical path difference causes a temporal broadening of the pulse. This is not a concern for pulses of several hundred picoseconds but in the case of ultrashort pulses, this will cause stretching beyond the femtosecond regime. The effect can be compensated with the judicious choice of a matching second grating that recompresses the pulse in the

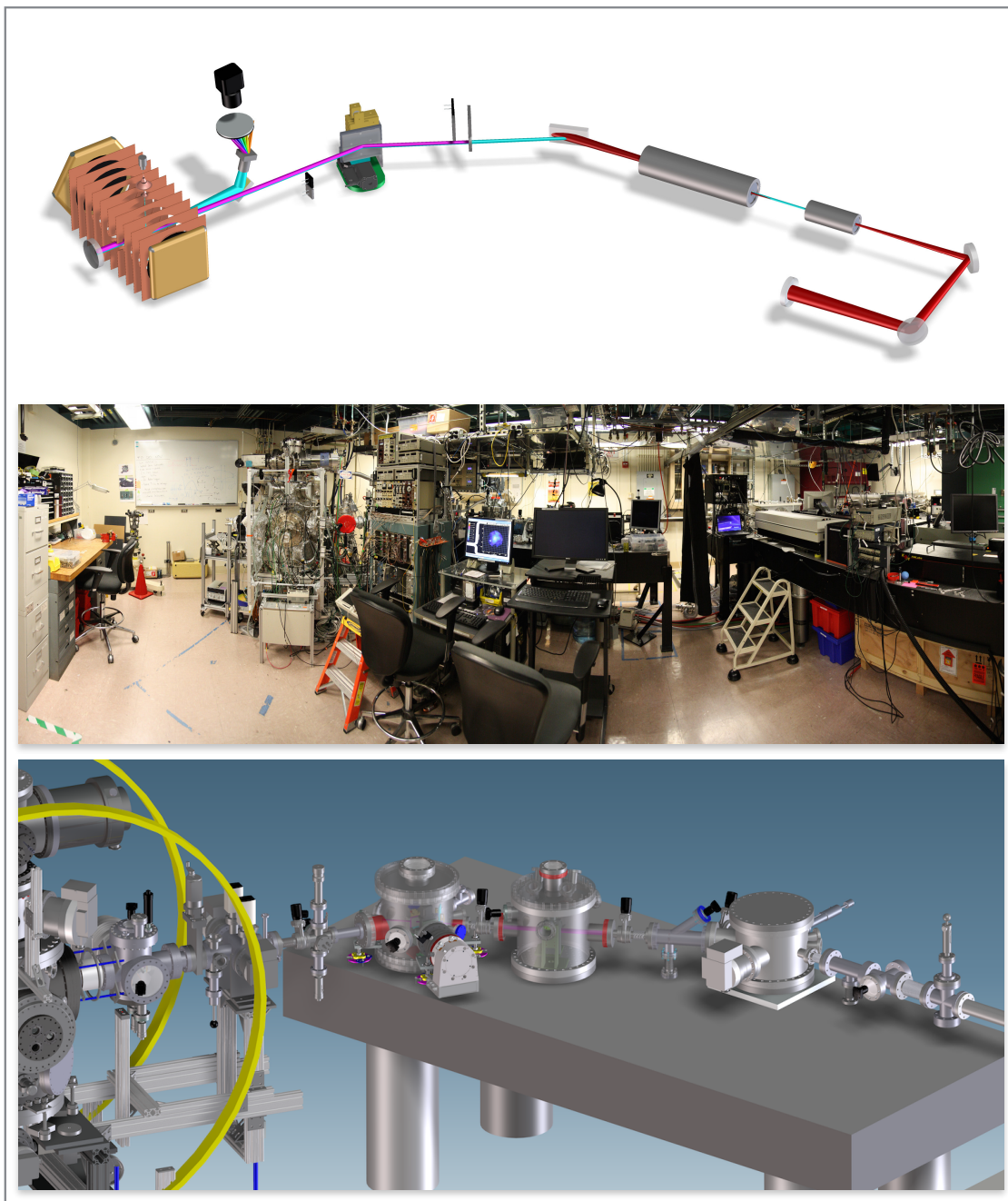


**Figure 4.1:** (Top) Schematic overview of the experimental setup. (Middle) The apparatus in the laboratory at LBNL. (Bottom) A 3D rendering of the technical drawings of the high harmonics beamline.

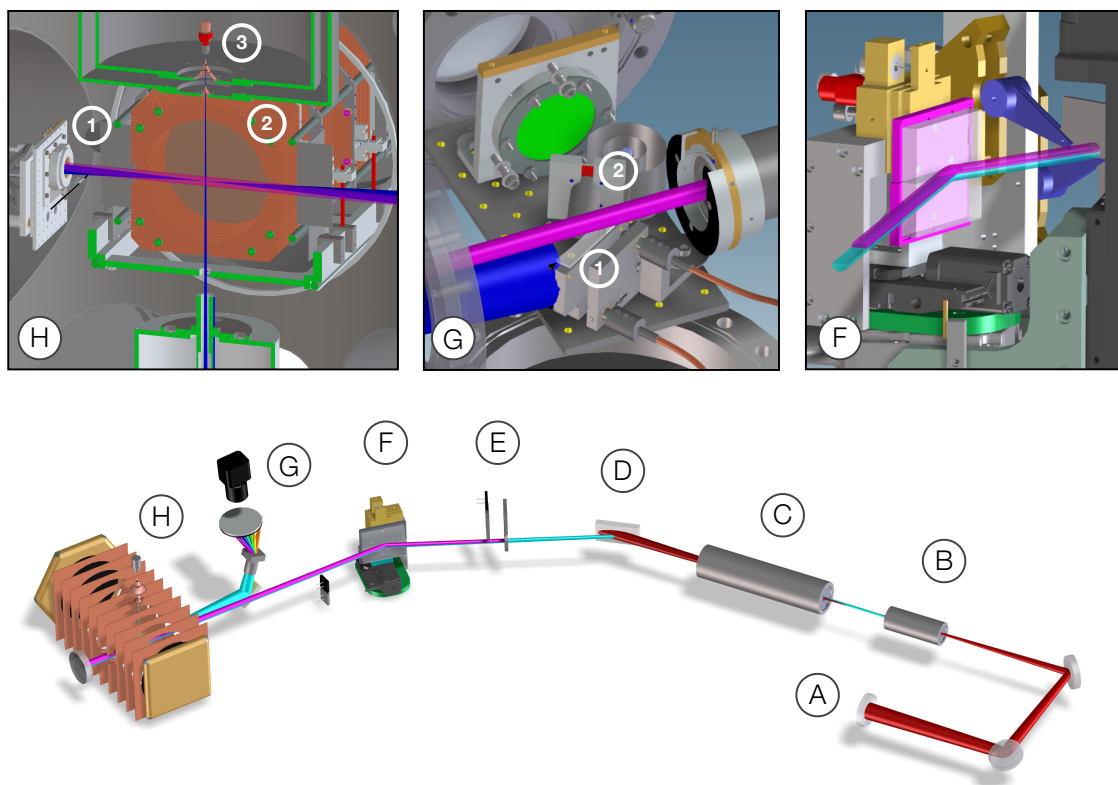


**Figure 4.2:** Schematic overview of the experimental setup and detail graphics of the key beamline components. After multi stage amplification in air, the infrared beam is compressed in a helium filled vacuum chamber (see Section 3.4.1). The beam is focused using mirror **(A)** ( $f = 6$  m) into a 10 cm long argon filled gas cell **(B)** for High Harmonic Generation (HHG). The broad spectrum of harmonics can be filtered using gas filter cell **(C)** or with a variety of solid filters and windows further downstream **(E)** (see Section 4.1). For separating the fundamental from the co-propagating harmonic radiation, the beam is reflected off a solid flat **(D)** and a split pair **(F)** of silicon mirrors at Brewster's angle for 800 nm ( $74.9^\circ$ ). This results in a total suppression of the fundamental by a factor of  $\sim 10^{-4}$  measured with a photo-diode. The vertically split pair of silicon mirrors is mounted on a precision motor control assembly that introduces the pump-probe delay (see detail **(F)** and Section 4.2). The harmonic beam then bypasses the XUV spectrometer unperturbed (see detail **(G)** and Section 4.3.1) and enters the reaction chamber. There, the beam is focused into a vertically downwards propagating gas jet inside the MISTERS spectrometer **(H.2)** using a back-focusing mirror ( $f = 15$  cm) at near normal incidence (see detail **(H)** and Section 5.3). The molecular jet is created in a supersonic expansion through a  $30\ \mu\text{m}$  nozzle **(H.3)** above the spectrometer. After passing through the reaction zone, the expanding light beam travels back upstream into the XUV spectrometer and where it is refocused **(G.1)** and dispersed using a transmission grating **(G.2)**. The spectral lines on the phosphor-MCP detector are recorded with a standard CCD camera through a viewport behind the detector.

time domain, allowing the retrieval of a pulse length close to the initial temporal width. Unfortunately, even with state-of-the-art optics, the use of two gratings and additional mirrors causes a reduction of photon flux on the order of 10 or more [121, 39]. At the photon flux rates currently obtained through High Harmonic Generation, such losses are prohibitive if the goal of the setup is to perform VUV pump - XUV probe experiments. In short, the low transmission of current monochromator technology does not permit its use in a High Harmonic setup for pump-probe studies.

In the present setup, three other methods are used to select a subset of the harmonic spectrum. Solid filters, gas filters, as well as special multilayer coated mirrors are described in the following sections. Solid and gas filters can be used to select a particular energy range as they have a material specific absorption spectrum. The energies obtained after transmission through the material correspond to the harmonics that did not match any electronic states or absorption bands in the gas or solid. There are only few materials that are useful for this purpose. Most materials either do not have sharp absorption features in the relevant energy range or they just cannot be obtained or produced in the form necessary for the use in a laboratory. Multilayer coated mirrors, on the other hand, can reflect photons at a particular wavelength. The details are discussed in the next sections.

#### 4.1.1 Fluoride Windows

Fluoride crystal windows made of  $\text{MgF}_2$ ,  $\text{CaF}_2$ , and  $\text{LiF}_2$  are commonly used as transmission optics in the ultraviolet spectrum.  $\text{MgF}_2$  and  $\text{LiF}_2$  transmit the fundamental and all low orders up to the 7<sup>th</sup> harmonic of 800 nm.  $\text{CaF}_2$  absorbs any order above the 5<sup>th</sup> harmonic. Furthermore, these windows can even be used to select an individual harmonic from the transmitted spectrum by taking advantage of the dispersion in the glass.

The delay introduced by dispersion in a medium is wavelength dependent. Thus, each harmonic acquires a different delay going through a given length of medium. The result is a train of pulses, each corresponding to one harmonic, separated by the difference in time delay introduced in the medium. If such a window is inserted into one arm (i.e. the pump arm) of an interferometer, the delay stage of the interferometer can be adjusted such that only one of the harmonic pulses overlaps in time with the other arm (the probe arm).

The delay between two co-propagating pulses, one going through vacuum, the other one going through a material of length  $L$  and group delay  $\frac{1}{v_g}$  is given by

$$\boxed{t_{\text{delay}} = \frac{L}{v_g} - \frac{L}{c}.} \quad \text{Pulse delay in a dispersive medium} \quad (4.1)$$

The group delay of a given material at a specific wavelength can be calculated using the refractive index  $n(\lambda)$  and the chromatic dispersion  $\frac{\delta n}{\delta \lambda}$ .

$$\boxed{\frac{1}{v_g} = \frac{1}{c} \left( n - \lambda \frac{\delta n}{\delta \lambda} \right).} \quad \text{Group delay} \quad (4.2)$$

Values for the refractive indices, the group delay, and the chromatic dispersion can be found in Table A.1 in the appendix.

Figure 4.3 shows the  $\text{C}_2\text{H}_4^+$  ion yield measured with respect to the delay stage position using the MISTERS spectrometer of the end-station. The ion yield was obtained by integrating the charge produced from ions impinging on the MCP using a boxcar integrator. In this measurement, a D-shaped  $\text{MgF}_2$  window of 155  $\mu\text{m}$  thickness was inserted into the

top arm of the beam, spreading the fundamental IR, the 3<sup>rd</sup>, and the 5<sup>th</sup> harmonic in time. The dashed lines indicate the calculated positions for the time overlap of harmonics that went through vacuum with the pulses that went through the window. Two peaks are visible corresponding to the overlap of the 5<sup>th</sup> harmonics from both arms, as well as to the overlap of the 5<sup>th</sup> and the 3<sup>rd</sup> harmonic. As the ionization threshold of C<sub>2</sub>H<sub>4</sub> lies at  $\sim 10.5$  eV, above the energy of the 5<sup>th</sup> harmonic (7.7 eV), the absorption of a second photon is required for ionization. Therefore, an enhancement of the yield appears when harmonics from different arms overlap in time, and two photon absorption becomes possible. No clear peak is visible at the overlap position of the infrared beam, indicating that the infrared beam was suppressed sufficiently in order to avoid the absorption of two or more IR photons.

The graph, however, also indicates a limitation of this technique. Despite the possibility of adjusting the time overlap to an individual harmonic, all harmonics transmitted will still reach the target gas, they just arrive at a different time. In the example above, the window thickness causes a delay of  $\sim 130$  fs. This leaves a time window of around 100 fs (taking into account the width of the pulses) where no other pump-probe effect occurs. One has to carefully assess whether harmonics arriving early or after the targeted pump-probe interaction influence the resulting dynamics of the molecule.

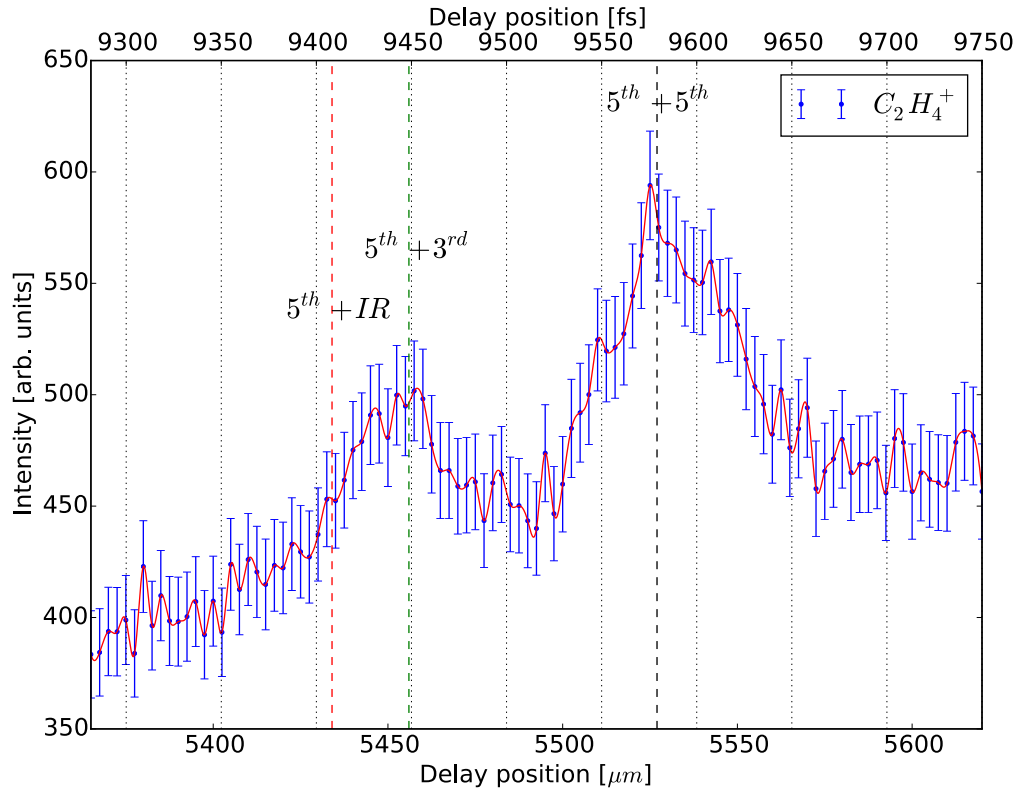


**Figure 4.3:** C<sub>2</sub>H<sub>4</sub><sup>+</sup> ion yield versus delay stage position with a MgF<sub>2</sub> window inserted in one half of the beam. Dashed lines indicate the calculated positions for temporal overlap of the 5<sup>th</sup> harmonic of the pump arm with the IR, the 3<sup>rd</sup> and the 5<sup>th</sup> harmonic of the probe arm.

Aside from the fluoride windows presented above, additional window materials exist that could be used to select the 3<sup>rd</sup> harmonic. These include NaCl or UV fused silica. Depending on the exact fundamental frequency, a fraction of the 5<sup>th</sup> harmonic might be

additionally transmitted, as observed at 780 nm. These materials have not been tested in this setup to date. A wider range of materials is available that transmit the infrared beam, such as borosilicate (BK7) and many other glasses. Attention needs to be paid to birefringence and stability which might render some materials unsuitable for use with high power lasers.

### 4.1.2 Metal Foils

Metal filters offer a simple way to select certain harmonics in the XUV regime. Figure 4.4 shows the calculated transmission curves for the most common metal foil materials aluminum, indium, and tin at a thickness of 150 nm. The low orders that are transmitted by fluoride windows are absorbed in these filters.

Indium almost exclusively transmits the 9<sup>th</sup> harmonic while tin mainly transmits the 13<sup>th</sup> and the 15<sup>th</sup> harmonic with a small contribution from the 11<sup>th</sup> harmonic. Aluminum, the most commonly used metal filter material has particularly high calculated transmission above the 11<sup>th</sup> harmonic. However, a comparison to the harmonics spectra measured in the XUV spectrometer in this setup (see Figure 4.5) shows a strongly reduced transmission. Aluminum and indium are very susceptible to oxidization, while the foil measured here seems to have been particularly highly absorbing. Transmission values of  $\sim 50\%$  have been reported for aluminum foils. Indium oxidizes instantaneously and the transmission is reduced to only a few percent. Other groups have reported moderate transmission ( $\sim 10\%$ ) by keeping the foils in an argon gas environment during transport and installation, hereby avoiding any contact with air that would initiate oxidation. This is not an easy task as metal foils of 100 to 200 nm thickness are extremely delicate. These materials break or rip easily and any air current by sudden movements or strain from mounting has to be avoided.

In the XUV beamline at LBNL, a separate chamber is dedicated for solid filters. Gate valves at the entrance and exit flanges allow the isolation of the delicate foils from the rest of the beamline. Figure 4.6 shows an overview of the setup used to insert the filters into the beam path. Two motorized stages hold a variety of metal filter frames, fluoride windows as well as a photodiode for photon flux measurement. The foils and windows used are D-shaped, which can be selectively used to cover only one half of the harmonics beam, equivalent to the pump or the probe arm. In this configuration, two windows and three foils enable the energy selection from a choice of six filter combinations.

### 4.1.3 Gas Filter Cell

Gases also exhibit an absorption spectrum that can be used to filter specific energies out of the photon beam. Gas cells are routinely used at synchrotrons and free electron lasers but are not very common in high harmonics laboratories. The advantage of a gas cell is the possibility to choose the filter material simply by connecting a different gas bottle to the inlet. The transmission can be regulated by adjusting the cell pressure. Figure 4.5 shows the transmission curves measured for several gases. The transmission of energies that have no matching absorption in the filter gas is extremely high as can be seen in the example of helium.

In the present setup, the gas absorption cell is a part of the vacuum beam tube itself and can be turned on and off by changing the vacuum pump configuration and the gas pressure. It is placed in the beamline between the HHG cell and the first silicon mirror (see beamline overview in Figure 4.1). Figure 4.7 shows a cross section of the gas filter cell. It consists of three DN38 CF Tees connected with a long tube. Both Tees serve as differential pumping stages to separate the gas filled center tube from the high vacuum

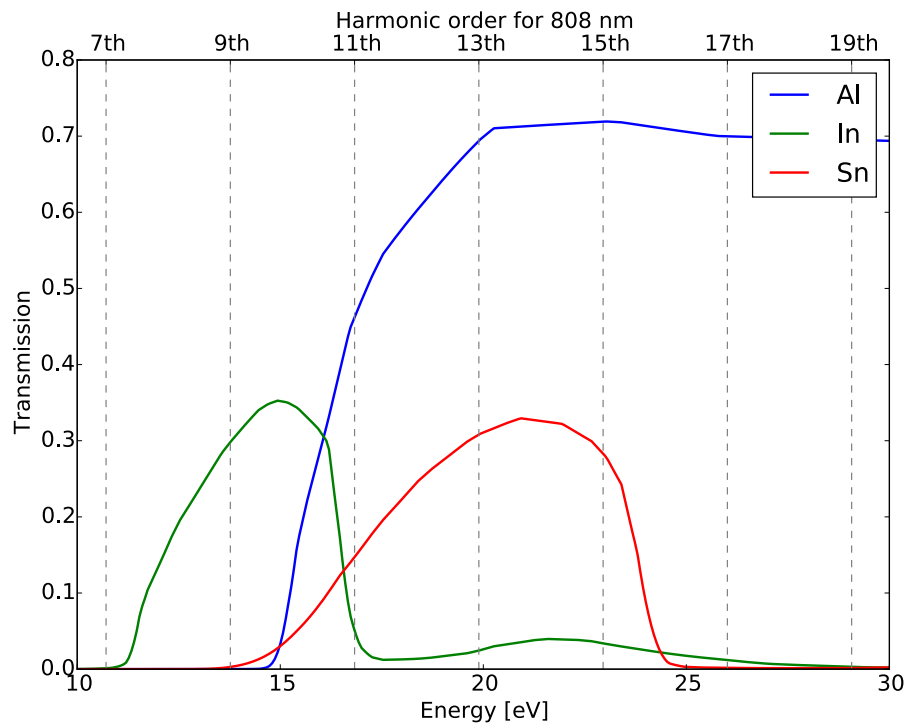


**Figure 4.4:** Calculated transmission of solid aluminum (blue), indium (green), and tin (red) filters at 150 nm thickness in the HHG energy range. The dotted lines correspond to the spectral position of the harmonic orders. The transmission can be increased by reducing the foil's thickness. However, foils thinner than 100 nm are not robust enough for handling. The actual transmission observed is significantly reduced due to oxidization. A logarithmic plot of the transmission of tin at energies  $> 25$  eV is shown in Figure A.1 in the appendix (Data taken from the CXRO database [32]).

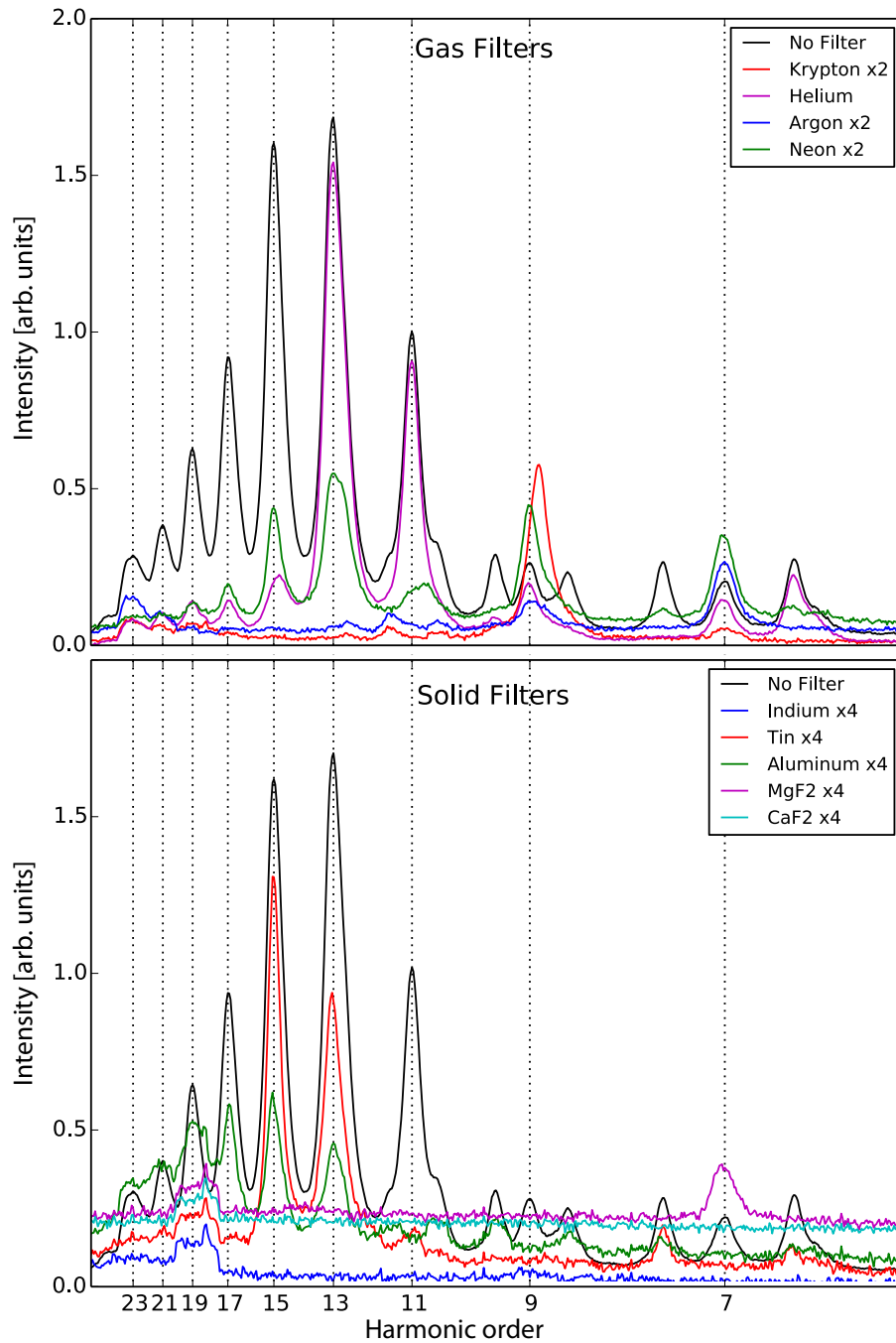


**Figure 4.5:** XUV spectra from Krypton harmonics after transmission through a variety of gas filter materials (top) and solid filters (bottom). For better visibility, the spectra with low intensity have been scaled using a factor indicated in the legend. See Section 4.3.1 for additional explanation.

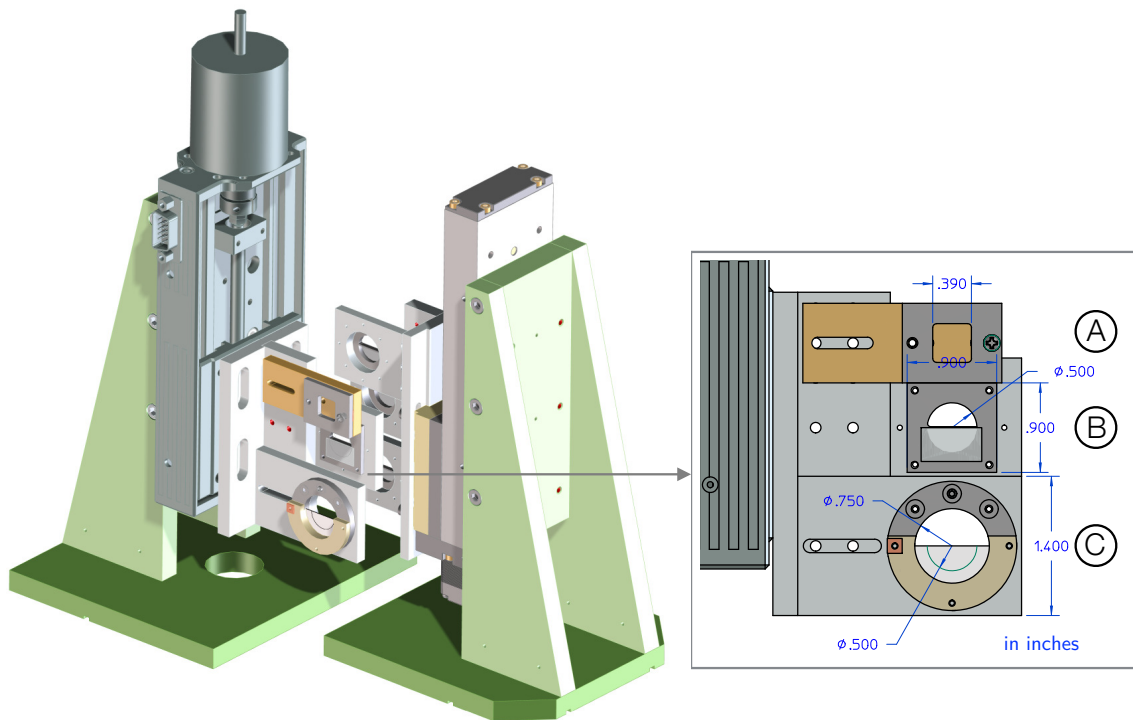


**Figure 4.6:** Rendering of the filter holder setup. Two motorized linear stages, placed perpendicularly to the laser beam, are equipped with a variety of filters that can be moved in and out of the beam path with micrometer precision. This allows a quick change to one of the 6 possible filter combinations. On the right side, the different mounts for the diode (A), metal filters (B), and D-shaped fluoride windows (C) are shown.

beamline. In order to achieve low gas conductivity between the high and the low pressure side, each section is separated using solid copper plates with  $\sim 1$  in diameter holes that are covered with  $\sim 0.1$  mm thin stainless steel foil. The pre-aligned laser itself is used to drill holes into the foils (few mm diameter), similar to the procedure of the High Harmonic gas cell. A pressure controller (MKS) is used to dial the desired backing pressure ( $\sim 1 - 5$  Torr) of the attenuation cell. The differential pumping sections before and after the cell are pumped using a scroll pump (Varian TriScroll 600). At 3 Torr cell pressure, the vacuum measured in the silicon mirror chamber directly downstream of the cell is  $\sim 7 \times 10^{-4}$  mbar but less than  $10^{-6}$  mbar in the SMI chamber.

The gas attenuation with respect to the pressure as measured with the XUV spectrometer is shown in Figure 4.8. With increasing pressure a strong suppression of the harmonic orders above the 9<sup>th</sup> harmonic is observed. At 3 Torr cell pressure, the spectrum does not show a measurable flux of the orders 11 - 17. The detailed view of low intensity of the spectrum shown on the bottom reveals, however, the presence of higher orders in the range of 19 - 25.

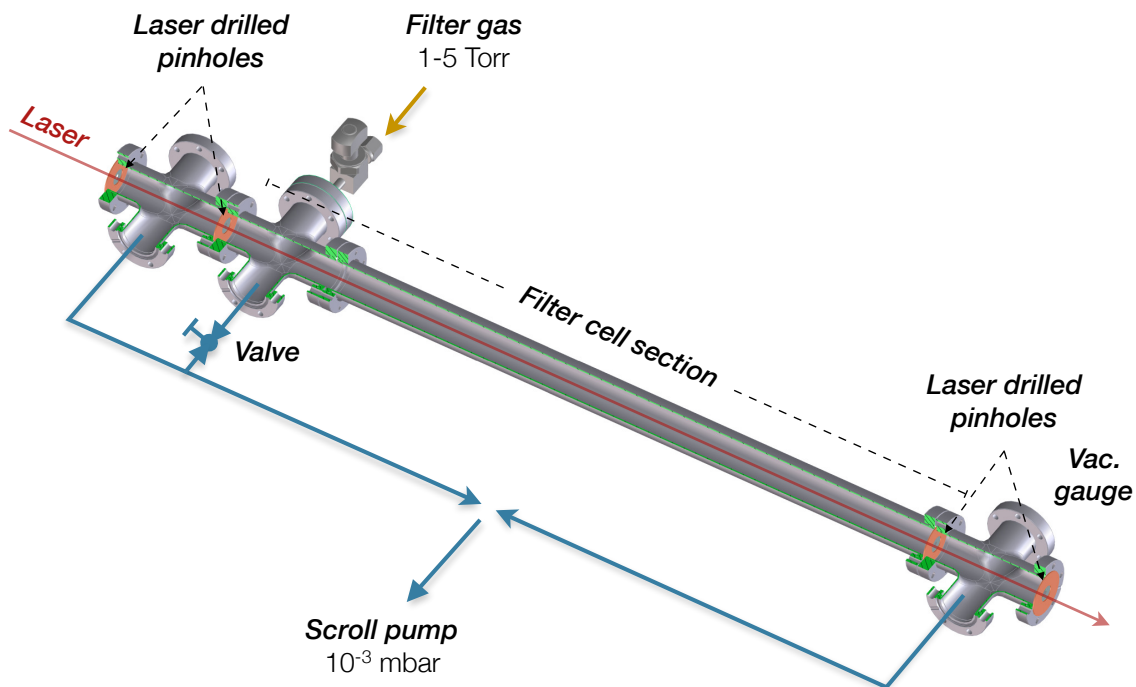


**Figure 4.7:** Schematic of the gas cell used for attenuation. The setup is built directly into the High Harmonics beam line. A section, 32 in long and separated by laser drilled pinholes, can be filled with various gases at several Torr pressure. In order to preserve high vacuum in the beamline, differentially pumped sections are added up- and downstream of the filter cell.

#### 4.1.4 Multilayer Coated Mirrors

A specific photon energy can also be obtained from the reflection of a multilayer mirror. Such mirrors are coated with multiple thin films of materials such as SiC, Al, MgF<sub>2</sub> or B<sub>4</sub>C. They are deposited using ion beam sputtering or chemical vapor techniques at thicknesses of just a few to tens of nanometers. The different layers can be chosen in such a way that constructive and destructive interference results in a relatively high reflectivity (typically

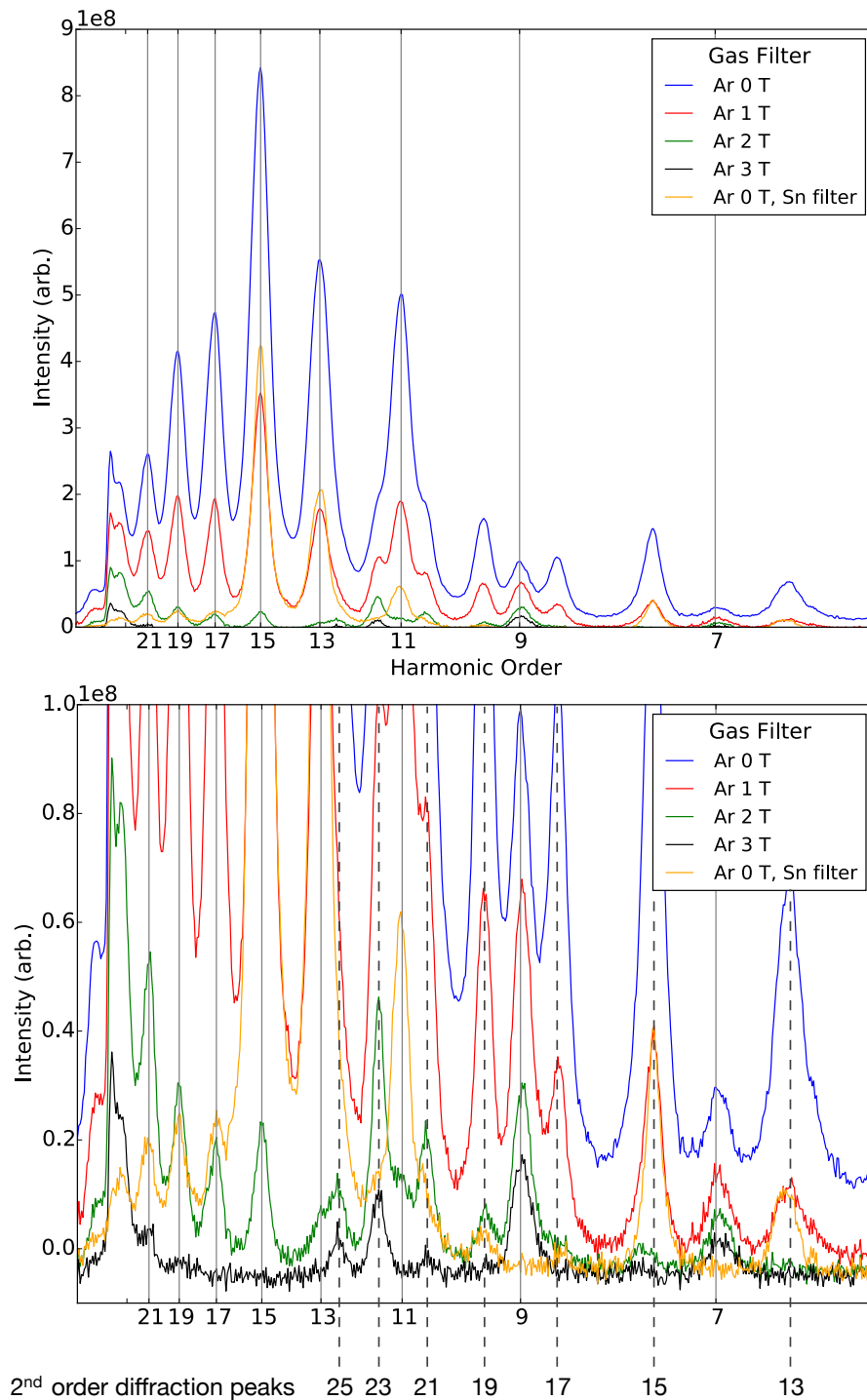


**Figure 4.8:** HHG spectra generated in krypton (10 cm cell) after passing through the separate argon filled gas attenuation cell. The different spectra correspond to varying backing pressure of the attenuation cell. **(Top)** Full spectrum, **(Bottom)** low intensity detailed view. At 3 Torr, the orders 11 - 17 are almost completely suppressed while the transmission of the lower orders are not affected significantly. The spectrum was recorded with the XUV spectrometer reflected off a B4C back-focusing mirror (see Section 4.3.1 for details).

$\sim 30 - 50\%$ ) at only a specific photon energy, usually more than two orders above the rest of the spectrum. However, it is extremely difficult to obtain multilayer mirrors in the spectral range between  $\sim 10$  to  $20$  eV. This is likely due to intermediate penetration depth in this spectral range between surface reflection and the atomic-response at high energies.

To date, only few companies or institutions in the world can produce such custom mirrors in the XUV spectrum including the Center For X-ray Optics (CXRO) based at LBNL. Figure 4.9 shows the calculated reflectivity for a mirror substrate with two coatings prepared by CXRO. Each coating was applied to only one half of the mirror creating two D-shaped surfaces. Steering two spatially separated beams onto the different surfaces allows for the selection of a different energy in the pump and the probe arm.

Measured reflectivity curves for energies below  $30$  eV are not readily available due to the difficulty in creating such specific radiation wavelengths. Most synchrotron beam lines do not cover this spectral range, and usually table top sources are rare or are not used to perform reflectivity or transmission experiments in the XUV.

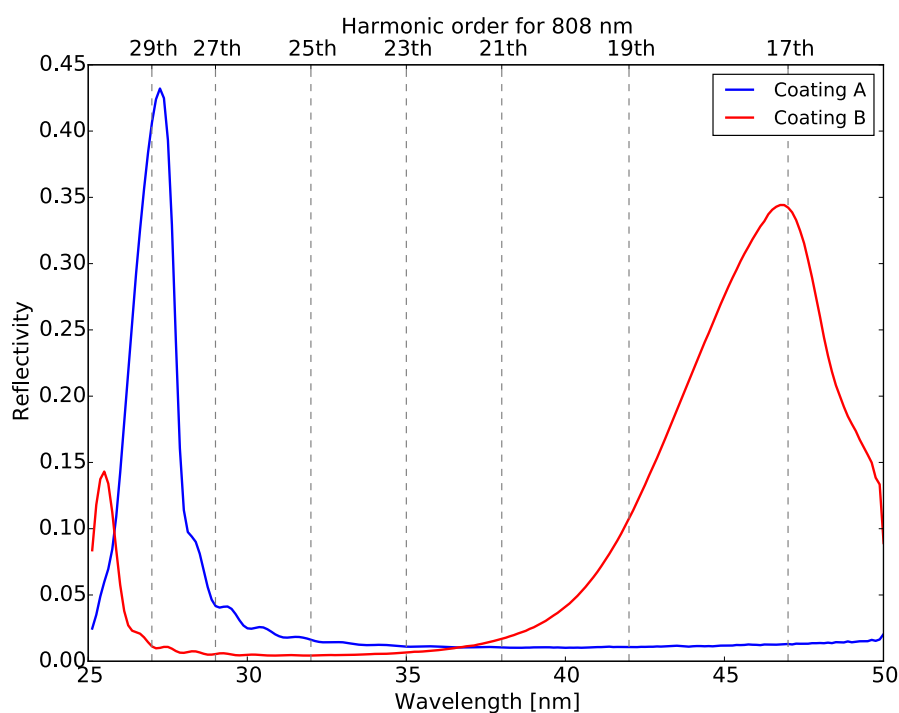


**Figure 4.9:** Calculated reflectivity for a focusing mirror with two different multilayer coatings. Coating A (blue) was optimized for selecting the 29<sup>th</sup> harmonic, while coating B (red) reflects mostly the 17<sup>th</sup> harmonic of 800 nm (data provided by CXRO [134]).

## 4.2 Pump - Probe Interferometer

Dynamics studies in the time domain can be performed by splitting the laser beam into two beam paths, called the pump and the probe arm. By changing the path length of one arm, a fixed time delay between pump and probe arm can be created. A series of measurements at different delay positions can then be used to investigate the temporal dynamics of a reaction.

In XUV - IR experiments the interferometer is usually placed in air before the generation of higher harmonics. A Michelson-type interferometer with an optical beam splitter

separates the infrared beam in the desired ratio and introduces a delay to one pulse. The beam then propagates in two separate beamlines to the experiment where it is recombined. At low power, the infrared beam is not significantly affected by non-linear effects and can be propagated in air.

If both pump and probe pulses are in the VUV or XUV spectrum, the interferometer needs to be placed in vacuum. The requirement for in-vacuum motor control not only increases the price of the setup significantly but also limits the attainable vacuum. Stages that operate below  $10^{-10}$  mbar are commercially available but achieving these pressures in a complete setup is very challenging.

Only a few split-mirror interferometers operating in vacuum exist around the world, as only few sources produce a sufficient amount of flux for performing VUV-XUV pump-probe studies [70, 6, 172, 166].

While semitransparent optics can be used to split the beam in the optical spectrum, such optics do not exist in the XUV without affecting the temporal profile. The spatial separation of the two arms is usually created by directing the beam onto two closely positioned mirror surfaces that can be controlled individually.

Two geometries that differ in the position of the split-mirror interferometer in the beamline are commonly used. The advantages and disadvantages are discussed in the following.

In the first design, the interferometer is positioned directly downstream of the interaction region holding a split back-focusing optic. As the focusing optic consists of two separate mirrors, the overlap of the pump and the probe arm are very sensitive to alignment and stability. Fluctuations and instabilities are a common problem at very high power because of the non-linear nature of the process of high harmonic generation. In some experiments, the low repetition rate of the laser requires measurements for several days. Therefore, stability and ease of alignment are important factors for the interferometer design in this setup.

Furthermore, in this design, the interferometer would have to be placed in a differentially pumped section, in order to achieve very low background pressures ( $< 10^{-10}$  mbar). This limits the focal length that could be used. A short focal length is required to reach the high intensity necessary for a strong pump-probe signal.

### The Split-mirror interferometer design at LBNL

For this beamline, an alternative geometry was chosen where the Split-Mirror Interferometer (SMI) is placed upstream of the experimental end-station (see **(F)** in Figure 4.2), independent from the focusing optic. The interferometer holds two super polished flat silicon substrates (Gooch and Housego, wavefront error =  $\lambda/20$  at 630 nm, roughness  $< 1$ ) that split and transport the beam. The focusing is performed by a solid back-focusing mirror close to the interaction region in the MISTERS endstation.

Figure 4.10 shows a rendering of the setup and its placement in the beam path. The two mirror substrates **(D)** are vertically separated by a small gap of less than one millimeter, required to allow free movement of the individual surfaces. The top mirror is equipped with two pico-motors actuating tip and tilt for adjusting the overlap of both arms. The bottom mirror is mounted on a precision encoded stepper motor stage **(C)** with closed-loop position readout (Micos VT-21 with Corvus Eco encoder). The stage has a travel of 10 mm (17.3 ps delay) and a minimal step size of 100 nm (170 as). Both mirrors can be rotated and translated together using a rotational stage **(B)** and a vertical stage **(A)**. The stage can be moved out of the beam path, allowing the beam to exit through a window for diagnostics or alignment. Two aluminum plates serve as beam stops for the top and the bottom arm. They can be moved quickly in and out of the beam with electrically

actuated rotating flappers (**E**) and can be positioned to precisely cover each mirror using a pico-motor. The ratio of pump and probe arm can be adjusted by changing the illumination of top and bottom mirror using the vertical stage. This geometry improves and eliminates some problems inherent to the first design mentioned above.

### Design advantages

The photon beams of the top and the bottom arm are reflected off a solid curved focusing optic near normal incidence. The foci of the pump and the probe arm are therefore inherently overlapped. This largely eliminates the need to find spatial pump-probe overlap. The tip and tilt of the top arm of the interferometer can be adjusted visually to form a full beam. Slight angle changes have not been observed to affect the overlap. This becomes more important when a back-focusing mirror with different coatings on the top and the bottom half are used (see Section 5.2).

The temporal overlap of the pump and the probe pulses is adjusted by translating the delay stage. In the case of a split focusing optic, the focal position in the beam propagation direction is coupled to the delay stage position. Hence, the overlap in the propagation direction is lost when the delay is equal to the Rayleigh range. In the case of high harmonics at focal distances of a tens of centimeters, the Rayleigh range is on the order of a few hundred microns. This limits the time range available for the dynamics study (to  $\sim 1$  ps).

In the present setup, the time delay introduced in the bottom arm of the harmonics beam has virtually no impact on the focal position. This is not entirely true, because the translation of the delay stage moves the beam perpendicular to the propagation direction (see Drawing 4.12). Nevertheless, this should only become problematic near the maximal travel of 5 mm from the overlap position where a deterioration of beam intensity might be observable due to astigmatism of the focusing optics.

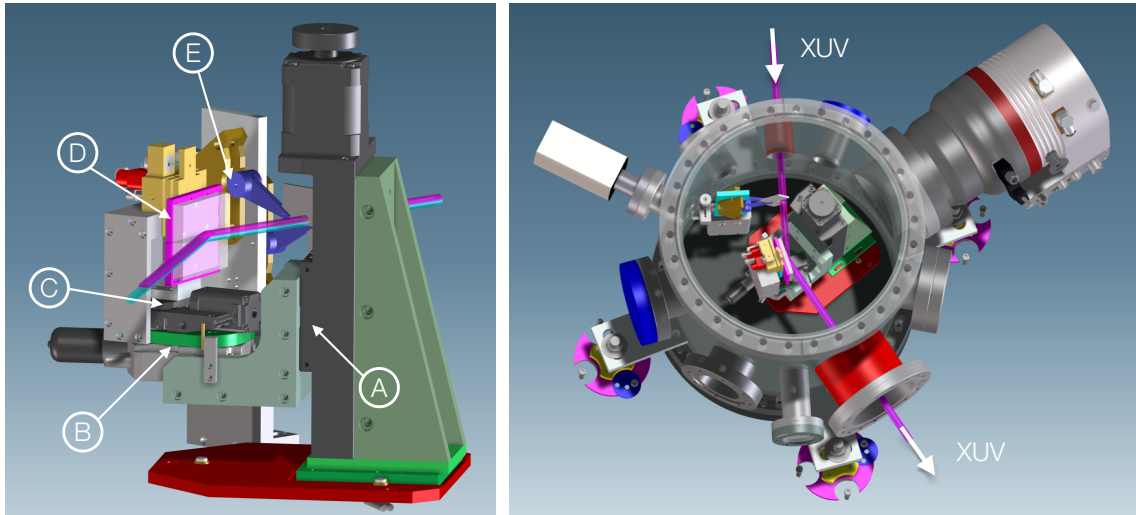
### Suppression of the fundamental beam

Due to the low conversion efficiency of HHG ( $\sim 10^{-6}$ ), most photons of the fundamental beam are still co-propagating with the harmonics. The infrared intensity needs to be significantly reduced in order to avoid its influence on the molecular target. Aluminum filters can be used for this purpose but the high intensity of the pulse used in this setup would damage the foil without prior attenuation of the power in the beam.

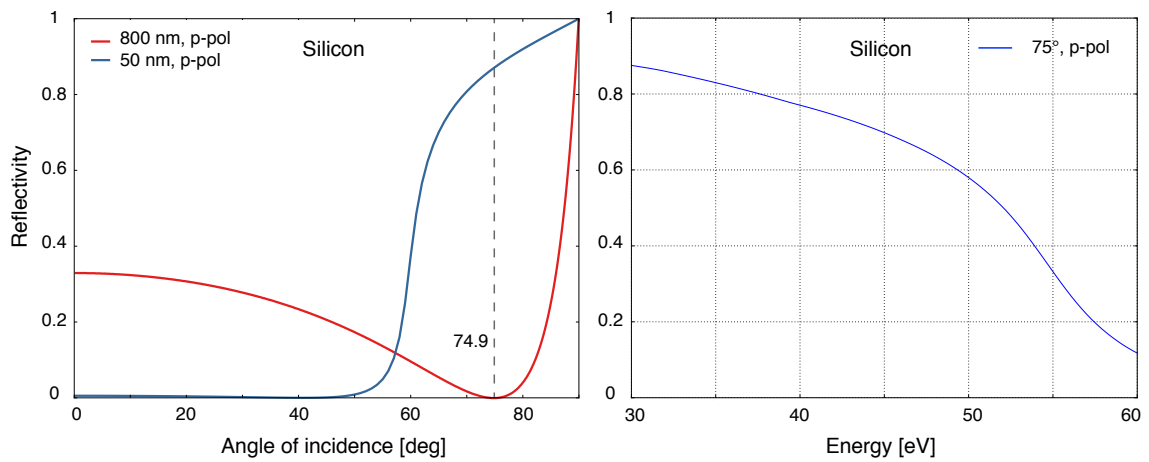
Instead, silicon mirrors were chosen for separating the harmonics from the fundamental beam. At the Brewster's angle,  $74.9^\circ$  incidence angle for 800 nm, the theoretical reflectivity of a purely p-polarized beam is zero. Any deviation from this angle causes a measurable reflectivity ( $\sim 10^{-3}$  at  $76^\circ$ ).

Figure 4.11 shows calculated reflectivity curves for the XUV as well as the fundamental radiation. At shallow grazing angles (large incidence angles), the reflectivity for energies in the XUV is high. The infrared beam is reduced by two reflections of the silicon mirror surfaces at the Brewster angle (see Figure 4.1 (D) and (F)). The substrates have a length that accommodates for the elongated beam profile footprint at shallow angles.

In practice, the total attenuation was  $\sim 10^4 - 10^5$ . This was likely the result of the ellipticity of the beam which produces s-polarized light that is well reflected ( $R = 0.74$ ). Misalignment of the silicon surfaces with respect to the Brewster angle might also have contributed to the reflectivity. In order to obtain a precise value for the reflected infrared beam, a specifically designed IR detector consisting of a photodiode and a calibrated filter could be used. Such a measurement using a bandpass filter for 157 nm did not produce reliable numbers as the attenuation factor of the filter was insufficiently characterized at 800 nm.



**Figure 4.10:** Rendering of the Split-Mirror Interferometer (SMI) chamber (**right**) and a detail view (**left**) that separates the XUV beam into pump and probe pulses. The incoming beam is reflected off a pair of vertically separated silicon mirrors (**D**) at  $15^\circ$  incidence angle (Brewster's angle for 800 nm). The top mirror is equipped with a Picomotor driven tip and tilt mechanism. The bottom mirror is mounted on a precision translation stage (**C**) that introduces the time delay between pump and probe arm. A vertical translation stage (**A**) is used for adjusting the ratio of pump and probe by moving the entire mirror setup vertically. The beam alignment downstream can be controlled additionally with a rotational stage (**B**). Each mirror half can be shadowed by two motor actuated aluminum plates (**E**) that serve as beam stops for top and bottom arm respectively.



**Figure 4.11:** (**Left**) Theoretical reflectivity for a silicon mirror versus angle of incidence at 800 nm (1.55 eV, red line) and at 50 nm (30 eV, blue line) for p-polarized light (axis out of mirror plane). (**Right**) Energy dependence of the reflectivity for silicon at  $75^\circ$  incidence. The actual reflectivity for high harmonics observed in the laboratory is usually on the order of 0.5 - 0.7. This is due to the formation of oxide layers and hydrocarbon contamination on the mirror surface. For measured reflectivity curves see [8]. Data compiled from [32] and [130].

### Delay stage characteristics and stability

In setups where the back-focusing mirror is mounted on the delay stage, one micron travel of the delay-stage corresponds to a delay of  $2 \times 3.34 = 6.68$  fs because the beam travels to the stage and back. At the grazing angle of  $15^\circ$  in this setup, the delay,  $\Delta L$ , introduced by the translation of the stage,  $D$ , is

$$\Delta L = D \frac{1 - \cos(30^\circ)}{\sin(15^\circ)}. \quad \text{SMI delay calculation} \quad (4.3)$$

This results in a delay of 1.73 fs per  $\mu\text{m}$  stage travel. This is almost a fourfold increase in precision in comparison to a translated back-focusing mirror.

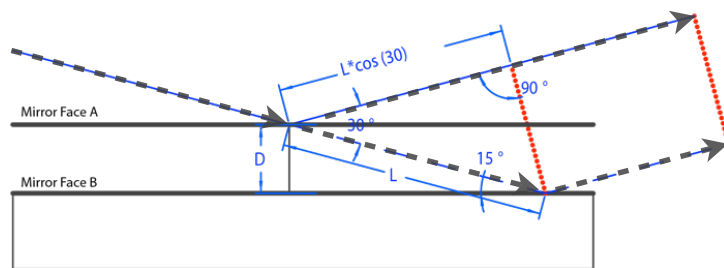


**Figure 4.12:** Schematic of the delay introduced by the two split mirrors at grazing angle of  $15^\circ$ . The shallow angle increases the delay precision. This also results in a small translation of the beam orthogonal to the propagation direction.

Figures 4.13 and 4.14 show autocorrelation measurements that demonstrate the attosecond resolution and the stability of the Split-Mirror Interferometer. A stability better than 200 as is observed, possibly limited by the stage resolution of  $\sim 170$  as. In order to avoid the coupling of vibrations from the vacuum pumps to the beamline, the fore pumps are decoupled from the turbomolecular pumps (TMPs) using weights and sand buckets, dampening the vibrations on the interconnecting vacuum hoses. The chamber housing the Split-Mirror Interferometer (SMI) is pumped using a TMP with magnetic bearings. The other sections of the beamline are decoupled using very soft, edge welded bellows. The reduced sensitivity of the pointing instability to the focal overlap mentioned earlier limits the impact of vibrations or thermal instabilities introduced in the system.

The decoupling of interferometer and focusing optic also allows for a simple adjustment of the pump-probe ratio. The amount of beam that is reflected off the top and the bottom mirrors can be adjusted precisely by moving the vertical stage (see (A) in Figure 4.10). Contrary to a setup with a split back-focusing mirror arrangement, this does not move the focal position at the target.

One disadvantage that is inherent to split mirrors should be mentioned at this point. There is a loss of photon flux due to the small gap between the two silicon mirror halves. The mirrors were polished to the edges but the quality of the mirror surface up to the sharp edge is very important. As the beam is diverging constantly starting from the generation cell, the loss of flux increases the further upstream the mirror setup is placed, favoring a placement of the split-mirror as far downstream as possible. Assuming a symmetrical gaussian beam profile, the amount of photon flux lost in the gap of width  $d$ , can be estimated with the error function

$$L_{(d,w)} = \text{erf} \left( \frac{d\sqrt{\ln 2}}{w} \right) \quad \text{Beam lost in mirror gap} \quad (4.4)$$

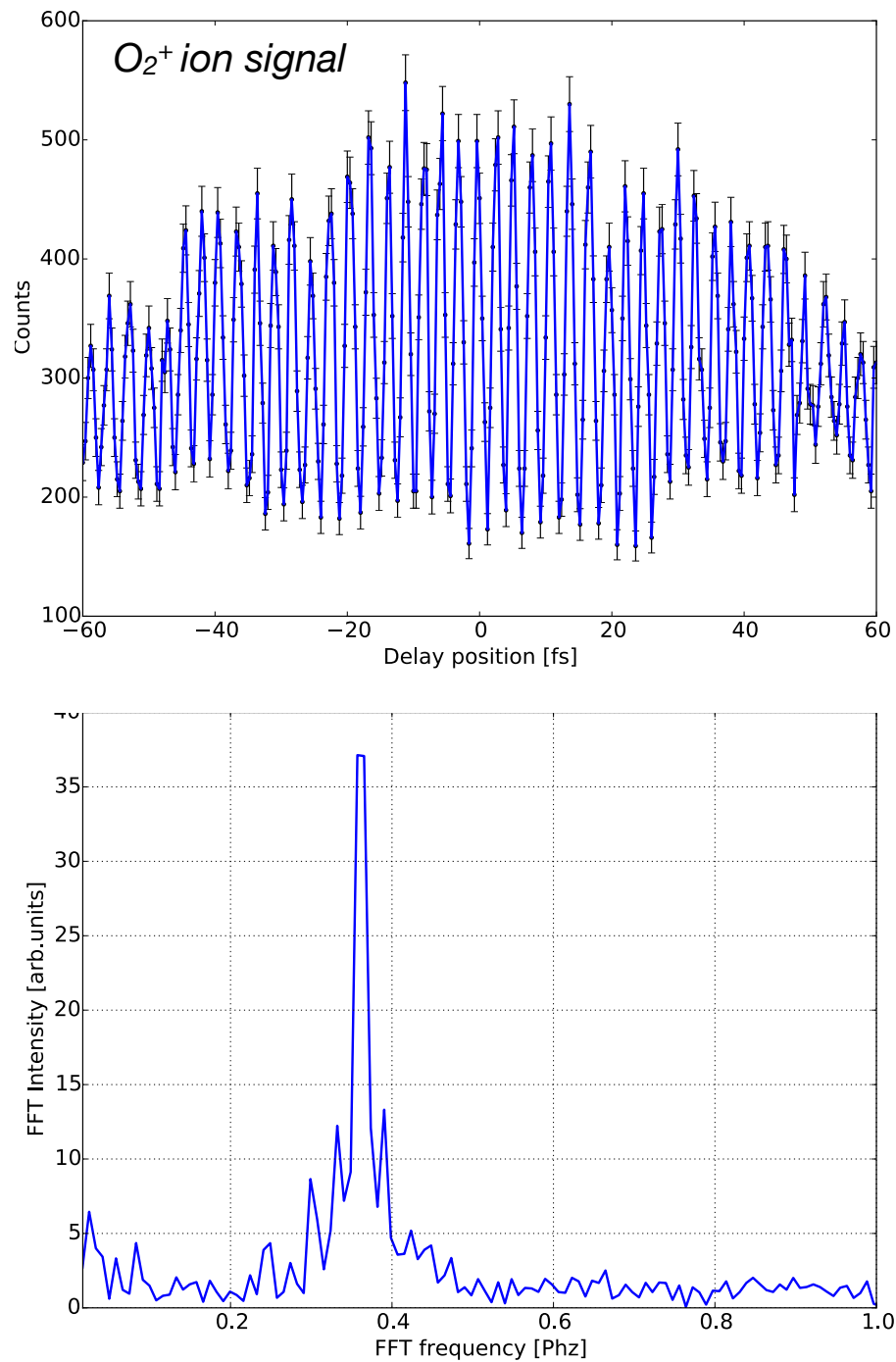


**Figure 4.13:** O<sub>2</sub><sup>+</sup> ion yield measurement with respect to pump-probe delay using two infrared pulses. The data shows a yield oscillation with a frequency of one optical cycle (2.7 fs at 808 nm). This autocorrelation signal is a result of the electrical field intensity modulation from constructive and destructive interference of the pump and probe arms. The trace demonstrates the sub-cycle stability even over long time delays larger than 100 fs.

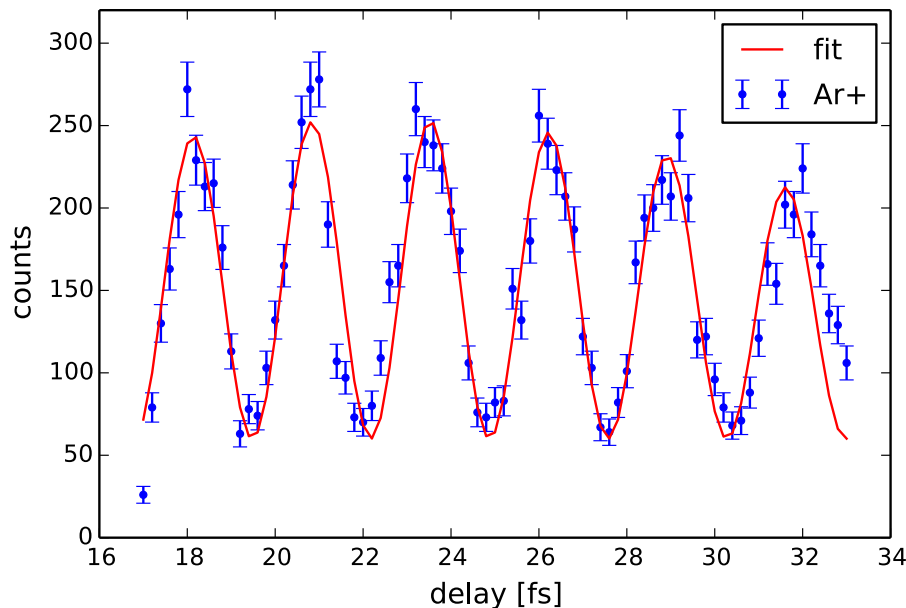


**Figure 4.14:** Ar ionization using infrared pulses at small delays. At a step size of 200 as, the ion yield clearly retraces the intensity oscillation of the infrared field with a cycle time of 2.7 fs.

where  $w$  is the full width at half maximum (FWHM) of the gaussian profile (see Appendix A.2). At a beam size of 6 mm and a gap width of 0.9 mm, about 14 % of the beam is lost.

### 4.3 Energy Characterization

In sec 4.1, the various methods for selecting particular energies have been presented. Calculations for the transmission or the reflectivity of most materials are readily available (see i.e. [32, 130]). The spectra created from High Harmonic Generation with noble gases have also been published extensively ([176, 98, 108]). However, with complex experiments triggering rich dynamics that can strongly depend on the photon energies involved, it is important to characterize the photon beam delivered to the target. In some cases, a mirror or a foil might be lacking the required markings, it might have been placed in the wrong container, or has heavily degraded over time resulting in an unexpected photon spectrum. Hence, control of the photon beam is very important for successful experiments.

Furthermore, the use of solid focusing mirrors with different D-shaped coatings requires ensuring that the reflected spectrum of the pump and the probe arm produce the expected outcome, i.e, that the top and the bottom beam arm each illuminate only the intended surface. Therefore, a spectrometer was needed that covers the relevant spectral range of the high harmonic source after reflection and transmission through all energy modifying optics, particularly designed to mitigate the mixing of pump and probe energies.

#### 4.3.1 XUV Spectrometer

The spectrometer developed for this beamline is based on a design developed at LBNL from Kornilov *et al.* [80]. They reported a transmission grating based spectrometer and beam profiler mounted on a CF 200 flange that can be inserted into the beam path using an in-vacuum translation stage.

A photon beam that illuminates a transmission grating with a spacing on the order of the wavelength spatially separates the spectrum. The interference of the diffracted waves from different points of the grating structure with spacing  $d$  creates intensity maxima at angles  $\alpha$  for every wavelength  $\lambda$  according to the formula:

$$\boxed{n \cdot \lambda = d \sin(\alpha)} \quad \text{Diffraction on a grating} \quad (4.5)$$

Recording the diffraction pattern on a position sensitive detector allows for the reconstruction of the wavelength spectrum from a measured and calibrated configuration using a precisely known geometry.

For the current configuration, it was necessary to characterize the spectrum after reflection off the last focusing optic in order to record the actual photon energies delivered to the target. The use of a refocusing geometry at normal incidence required the XUV spectrometer to be mounted upstream of the experimental end-station. This made several modifications to the reported design necessary:

- An extremely compact design was needed to fit into the beamline between the interferometer and the end-station.
- The beam had to pass unperturbed through the spectrometer, reflected by the back-focusing mirror before being diffracted.
- Refocusing of the strongly diverging harmonic beam in order to capture a sufficient harmonic flux to create a spectrum.

The XUV spectrometer is depicted in Figure 4.15. All components are mounted on a 7.0 x 3.6 inch aluminum breadboard that is attached to a custom DN160 CF cluster flange. The incoming harmonics beam exits a differential pumping section through an alignment iris (F) and passes through the spectrometer unperturbed. After back-reflection off the focusing mirror in the end-station, the strongly diverging beam is refocused by a broadband mirror at a shallow angle (UV fused silica with broadband gold coating,  $f = 10$  cm). The mirror is mounted on a custom tip-tilt mount with minimal height in order to avoid interference with the incoming beam path. Tip and tilt of the mirror can be controlled manually using rotational feedthroughs that connect to the mirror mount with flexible coupling wires. The focusing mirror is necessary to capture a sufficient amount of flux for a high quality spectrum. No slit was used in this geometry.

A transmission nano grating consisting of a Ta structure on a SiC membrane (200 nm pitch, 1.2 x 1.2 mm area, NTT AT) diffracts the harmonics onto a commercial multi-channel plate (MCP) photon detector mounted on a custom holder. A one inch diameter tube prevents stray light from illuminating the grating.

The detector ( $\varnothing = 40$  mm, Beam Imaging Solutions) consists of two resistance matched MCP plates in a chevron configuration with an aluminum coated back stacked with a phosphor coated glass plate. The XUV photons generate an electron cloud in the channels of the MCP that causes fluorescence of the phosphor screen. The diffraction pattern of the harmonics visible on the back side of the phosphor screen is imaged through a DN63 viewport behind the detector using a standard c-mount usb camera with a zoom lens. The strong zero-order beam transmitted through the grating is captured by a metal spiral that traps the photons. In order to reduce the amount of stray light on the imaging detector further, the breadboard is enclosed inside a metal housing (not shown in the figure). Typical operation voltages for the detector are noted in Table 4.1.

When the spectrometer is not in use, a copper plate blocks the back-reflected beam from entering the XUV spectrometer. This prevents damage to the transmission grating which

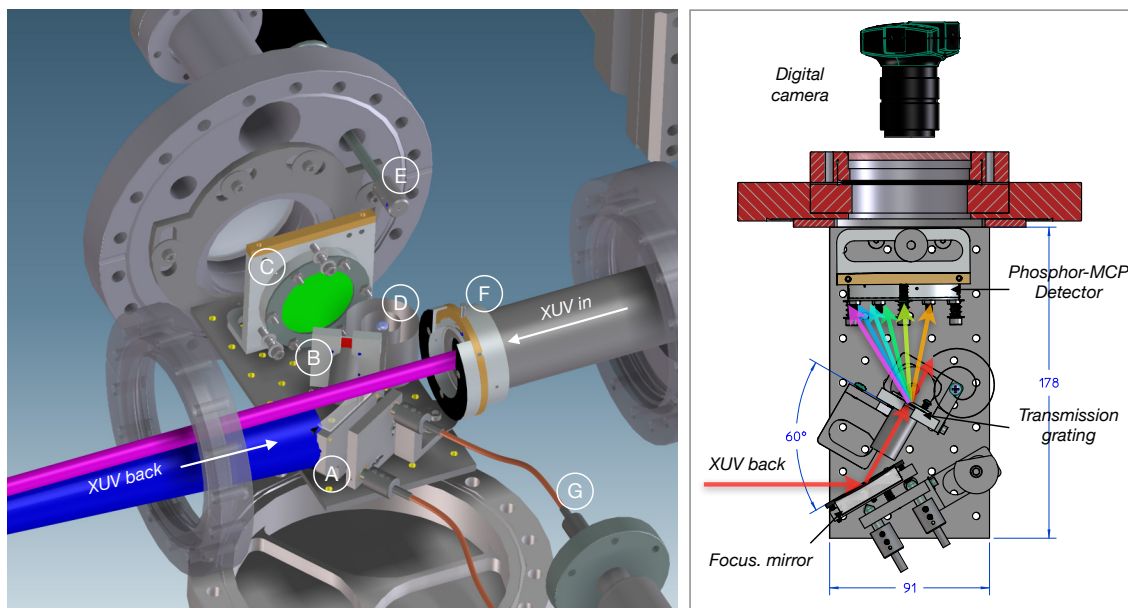


**Figure 4.15:** (Left) Rendering of the XUV spectrometer setup. (Right) Drawing of the ultra-compact breadboard supporting the spectrometer parts. The incoming XUV beam first passes the spectrometer and continues into the MISTERS end-station where it is back-focused into the gas jet. The diverging beam travels back upstream and is re-focused by a mirror (A). The nano transmission grating (B) diffracts the spectrum onto a phosphor-MCP detector. The fluorescence image is recorded with a digital camera through a viewport behind the detector. Mirror (A) can be adjusted using rotational vacuum feedthrough (G). The opening of the alignment iris (F) is controlled with a linear feedthrough (E) (see Section 4.4.2).

is especially important when a high infrared flux is used. There is a sufficient amount of energy in the refocused infrared beam to destroy the grating. The plate is rotated into the beam path using a feedthrough on the bottom of the chamber. It can also be used for a relative measurement of the harmonics intensity (see Section 5.6).

The entire assembly is inserted vertically into a DN160 CF cross that is attached to the upstream entrance of the experimental end-station. The bottom flange holds the rotational feedthroughs for the mirror control and the beam block. Facing the spectrometer board, a large DN160 viewport allows observation of all components including the alignment iris (see Section 4.4.2).

Potential [V]	Voltage
MCP front	-1400 -1500 V
MCP back	0 V
Phosphor	+2400 - 2500 V

**Table 4.1:** Typical operation voltages for the MCP-phosphor detector of the XUV-Spectrometer

### 4.3.2 Spectral Analysis

Figure 4.16 (A) shows a raw image of the XUV spectrum recorded with the camera. A sequence of vertical, slightly curved, lines with bright spots is visible on the left side of the image corresponding to diffraction maxima of the harmonics beam. The lines have an additional interference structure with periodic maxima in the vertical direction. These features are caused by diffraction from the support structure of the grating. A detailed description and explanation can be found in [181] and [80]. Diffusely scattered photons cause some residual illumination of the MCP mount. This is eliminated by subtraction of a background image recorded without XUV beam. The raw image is rotated by  $\sim 1.5^\circ$  to account for camera misalignment. The resulting cropped image is shown in (B). A projection of this slice reveals the harmonic spectrum as a function of pixel position. The various peaks can be identified by comparing spectra using different filters. Several additional peaks are prominent on the right part of the spectrum corresponding to second order diffraction of higher harmonics. In the current configuration, a spectral range of about 35 - 180 nm can be recorded covering the harmonic orders from the 7<sup>th</sup> to the 23<sup>rd</sup>.

The wavelength for the recorded pixel positions on the detector can be retrieved from the geometry parameters. Figure 4.17 shows a sketch of the diffraction geometry. The photon detector is tilted at a small angle,  $\theta_0$ , with respect to the grating normal. The position in the dispersive direction (orthogonal to the grating lines),  $x$ , for a diffraction at a parallel detector-grating geometry can be expressed in terms of the position  $u$  with arbitrary offset  $u_0$  on the detector.

$$x = (u - u_0) \cos(\theta_0) + L \sin(\theta_0). \quad (4.6)$$

Using the diffraction Equation 4.5, the formula for the wavelength with respect to the recorded position,  $u$ , reads

$$\lambda = d \sin \left( a \tan \left( \frac{u - u_0}{A} \right) + \theta_0 \right). \quad \text{Wavelength-position conversion} \quad (4.7)$$

The scaling factors,  $a$  and  $A$ , depend on the distance of the detector and the grating.

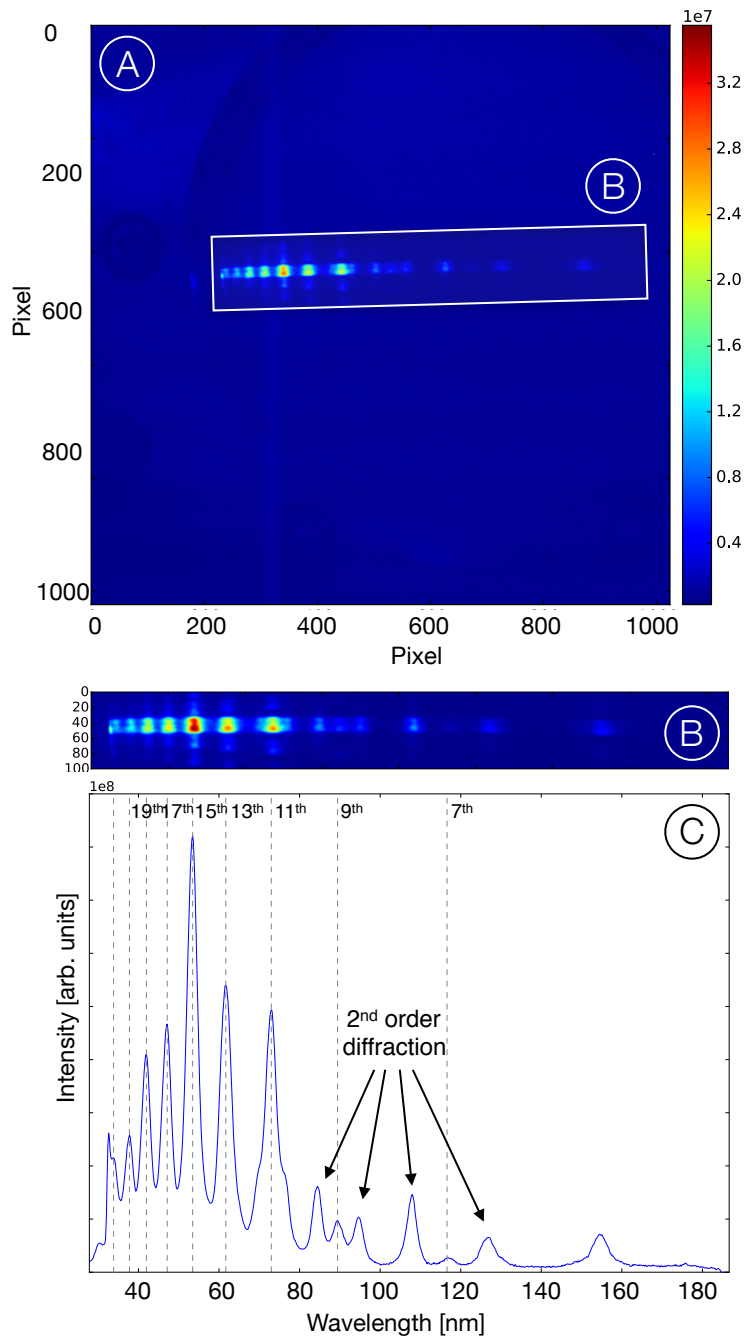


**Figure 4.16:** Retrieval process of the XUV spectral data from the digital camera image to the final spectrum. (A) Raw image of the diffracted photon beam on the phosphor screen. The mounting ring of the detector is faintly visible on the left. (B) After background subtraction, a subsection of the image is selected and rotated. (C) A projection of the image shows the spectrum of the harmonics created in Krypton at 5 Torr pressure. Additional to the 1<sup>st</sup> order diffraction peaks of the harmonics of 808 nm, several 2<sup>nd</sup> order peaks are visible. The low intensity of the lower harmonic orders is due to the loss of detection efficiency (see Section 4.3.2). The gradual decline of intensity visible for harmonics above the 15<sup>th</sup> matches the reflectivity curve for a B<sub>4</sub>C coated back-focusing mirror (see Figure 4.20) that was used in all measured XUV spectra.

As the geometric factors are difficult to measure, it is practical to calibrate the spectrometer using a known harmonics spectrum. After identifying the maxima and their corresponding harmonic number from known filter transmission curves ( $S_n$ ,  $I_n$ ), the wavelength for the peaks can be labeled based on the measured spectral center wavelength of the harmonics,

$$\lambda_q = \frac{808 \text{ nm}}{q}.$$

The parameters for function 4.7 can then be obtained using a standard minimization algorithm of an error function using the known peak position/ wavelength pairs. This calibration is limited to the uncertainty caused by *blueshifting* of the harmonic wavelength as described in Section 3.4.3. Therefore, low pressure spectra were used to minimize such effects.

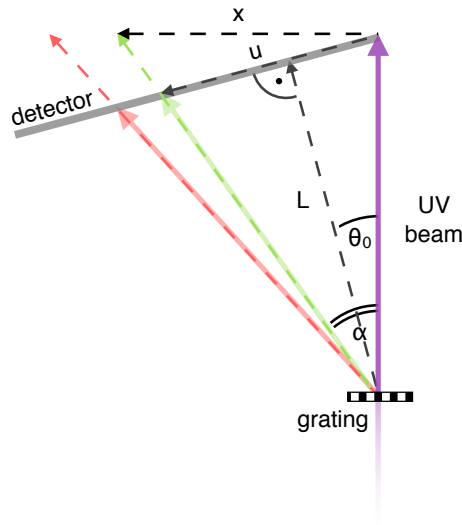


**Figure 4.17:** Sketch of the geometry of the diffraction setup. The detector is tilted with respect to normal incidence at an angle  $\theta_0$  and positioned at a distance  $L$ . Diffraction at angle  $\alpha$  creates a maximum at position  $x$  parallel to the grating and position  $u$  on the detector.

### Resolution

The resolution of the spectrometer is influenced by a variety of factors which include the pixel size, the electron bunch size generated by the MCP, as well as the illumination area of the grating. The latter is believed to contribute the largest uncertainty as no slit was used to limit the illumination area. We can estimate the resolution by looking at the width of the harmonics observed. Measurements from T. Allison using a Rowland monochromator with high resolution [8] yield typical harmonics widths of  $\sim 0.4$  eV for the 11<sup>th</sup> harmonic and  $\sim 0.5$  eV for the 19<sup>th</sup> harmonic. The extracted full-width at half maximum (FWHM) for each harmonic are plotted in Figure 4.18. The measured FWHM increases linearly with the energy. Due to the geometry and energy conversion, the lowest energies yield the highest resolution. The width of the second order peaks that fall in positions of low energies reveal a much smaller spread FWHM/E than the measured spread of the corresponding first order peak. This is a clear indication that the width caused by the spectrometer

resolution is larger than the natural harmonic width. The estimated resolution is on the order of  $\sim 250$  meV at 10 eV photon energy up to  $\sim 1.7$  eV at 33 eV.

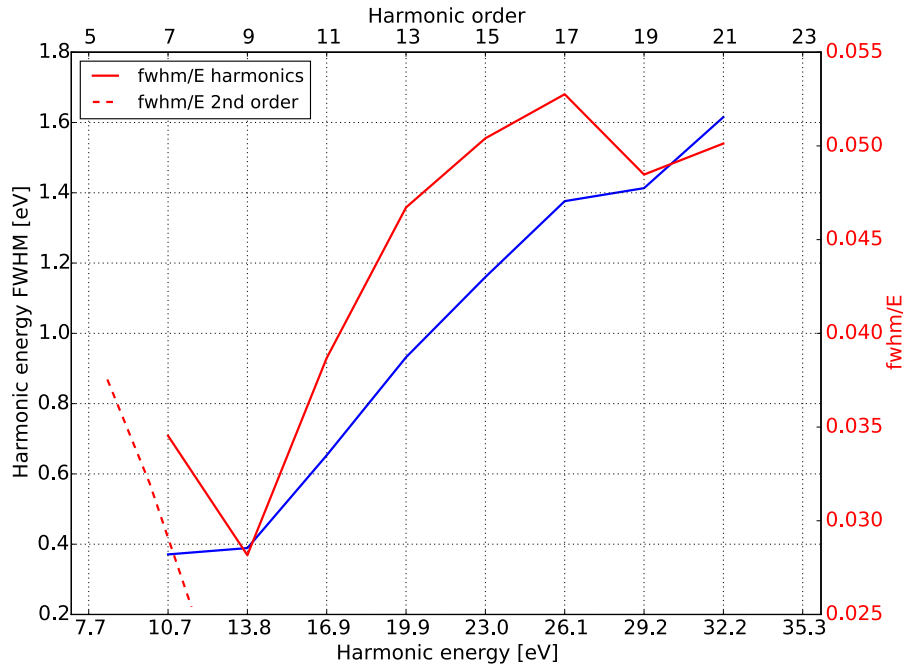


**Figure 4.18:** (blue, left scale) Measured harmonic width (FWHM) across the spectral range in HHG generated in Krypton at 5 Torr. (Red, right scale) Corresponding energy resolution FWHM/E for the harmonics as well as for second order peaks in the low energy range.

### Spectral Sensitivity

The interpretation of the intensity profile of the harmonic spectrum measured is very complex due to the multiple components that modify the spectrum. The intensities of the diffraction maxima of the harmonics observed vary strongly. This is in contrast to the mostly flat intensity profile of the so called plateau region of harmonics, that is expected in the range of the present harmonic orders.

Firstly, the photon flux of a given harmonic imaged in the spectrometer does not always correspond to the actual flux delivered to the experiment. The stronger divergence of low orders results in a larger spot size on the back-focusing mirror. The diverging beam of those orders expands to a size larger than the re-focusing mirror in the XUV spectrometer. As a result, only a fraction of the low harmonic orders is captured and refocused in the spectrometer, and a significantly reduced intensity is expected ( $\sim 50\%$  for the 7<sup>th</sup> harmonic).

Secondly, the spectrum observed is directly influenced by the reflectivity curve of the back-focusing mirror used in the end-station. This is a desired effect as it corresponds to the harmonics delivered to the target. However, the actual spectrum also contains the convolution of the gold-coated uv-fused silica mirror of the XUV spectrometer used for refocusing. The calculated reflectivity for gold, at a grazing angle of  $30^\circ$ , is plotted as a function of wavelength in Figure 4.19. The reflectivity slowly decreases with shorter wavelength but the overall change is only on the order of 20%. Figure 4.20 shows measured reflectivity curves for a 30 nm  $B_4C$  coating, equivalent to the back-focusing mirror coating

used in all data presented here. At normal incidence, the reflectivity remains nearly constant from 130 nm to about 90 nm when it drops with increasing rate towards shorter wavelengths [80]. These spectra reproduce the sharp intensity decrease of about a factor of three observed from the 15<sup>th</sup> to the 23<sup>rd</sup> harmonic order.

Furthermore, the grating transmission as well as the angle and energy dependence of the quantum efficiency of the MCP modify the intensity profile. The grating transmission is constant to a few percent over the range from 35 to 100 nm [80]. The MCP efficiency decreases by a few percent with increasing wavelength. The efficiency also varies from normal incidence to 13° by almost 50 % [62]. In combination with the loss of flux collected by the mirror, this might be responsible for the low intensity of the orders below the 11<sup>th</sup> harmonic.

In practice, the intensities were considered only in relative measurements to compare filter versus open configurations. For absolute flux measurements, photodiodes were used (see Section 3.4.2). In experiments involving the excitation or ionization of atoms or molecules, the difference in cross-section near threshold between adjacent harmonics is likely to dominate over a small variation in harmonic intensity. Therefore, a more quantitative analysis including estimated harmonics beam sizes, energy and angle dependent efficiencies of the components would include considerable error bars and was not considered necessary.

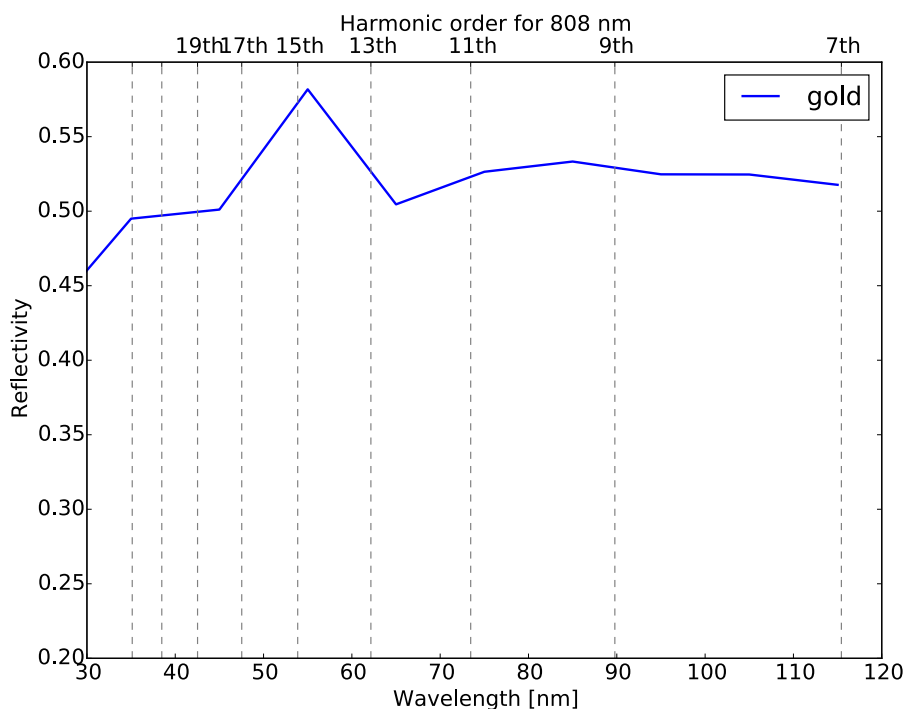


**Figure 4.19:** Calculated reflectivity dependence of a gold surface in the UV to XUV spectral range at 30° grazing incidence angle. The curve is generated using measured data for the refractive index ( see Appendix A.3 for details.).

## 4.4 Vacuum Beamline Components

The strong absorption of XUV radiation in air requires the propagation of high harmonic radiation entirely in vacuum. In comparison to the experimental end-station, where the mean free path of the molecules is of concern, the vacuum level necessary to limit the

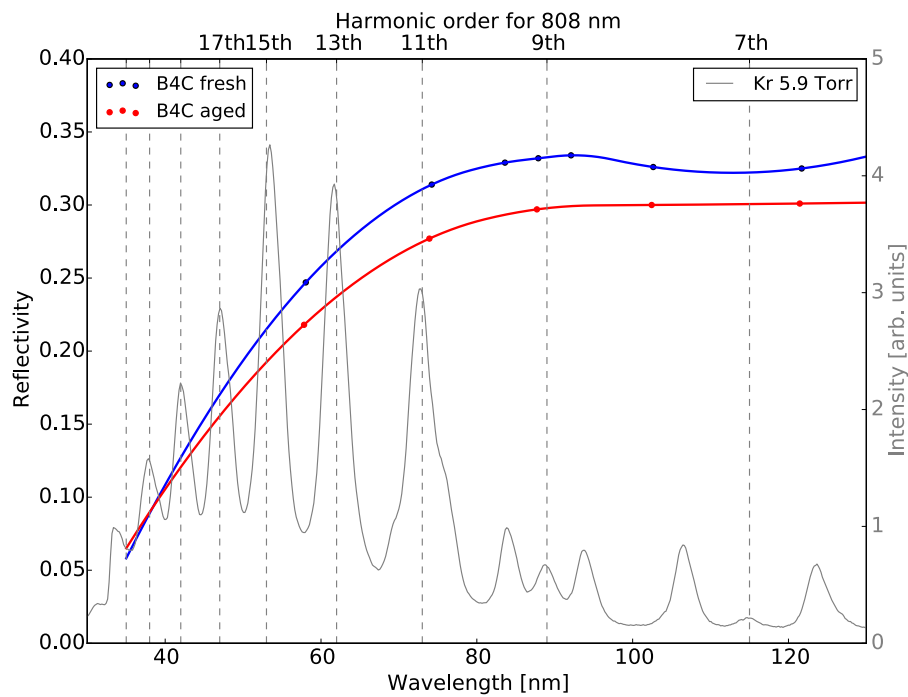


**Figure 4.20:** Reflectivity measurement of a substrate with 30 nm B<sub>4</sub>C coating at normal incidence from Larruquert *et al.* [88]. The blue points are data from a freshly prepared coating, whereas the red points are measured after about 3 months. Oxidation of the surface results in a slightly reduced reflectivity. The data points are connected with spline-fits to guide the eye. The actual reflectivity is likely decreasing even more rapidly for higher energy.

absorption losses of the XUV beam is significantly lower. Already at a pressure of  $10^{-3}$  mbar, the absorption in nitrogen is less than 0.1%.

Great care should be taken with the choice of materials used in vacuum and with their handling. This is not primarily because of their outgassing rates, as the vapor pressure of most materials only becomes important at pressures below  $10^{-5}$ , but rather due to the hydrocarbon residues which coat the optics in the vacuum beamline. Such coatings increase the absorption of the infrared beam which can result in damage due to the high beam intensity. In this context, not the absolute vacuum achieved is important but rather the composition of gases causing the pressure. Even at vacua on the order of  $10^{-7}$ , damage has been observed as a result of hydrocarbon deposition on the optics in combination with the strong infrared beam.

In this setup, standard optical mounts and parts have been used where available, but often it was necessary to disassemble mounts, strip parts of their anodization coating, and to replace them with vacuum compatible parts.

#### 4.4.1 Differential Pumping

In order to bridge the gap of a vacuum beamline, operated at a pressure around  $10^{-6}$  mbar, to the experimental end-station that should be kept around  $10^{-10}$  mbar, a differential pumping section was required. The pressure of a system can be lowered by increasing the pumping speed of the volume. This is achieved by attaching more turbomolecular pumps to the system.

Alternatively, one can restrict the flow of molecules into the system. At pressures below  $10^{-3}$  mbar, the mean free path of particles is longer than the dimension of the reservoir. In this regime called *molecular flow*, particles move straight from wall to wall in a random walk manner. In this probabilistic system, the flow into the system can be restricted by reducing the open area between reservoirs.

The resistance to flow is quantified by a parameter called *conductivity*. In the molecular flow regime, the gas flow between two reservoirs at a pressure difference  $\Delta p$  with conductivity  $C$  per unit time is given by

$$Q = C \Delta p. \quad (4.8)$$

The conductivity for a orifice or area  $A$  can be calculated by

$$C_{or} = A \frac{\bar{c}}{4}. \quad \text{Conductivity of an orifice} \quad (4.9)$$

The mean thermal velocity,  $\bar{c}$ , is a function of temperature and mass. It is on the order of 500 m/s at room temperature. For a long round tube of diameter  $d$  and length  $l$ , the conductivity is a product of the orifice and a passage probability proportional to  $d/l$ .

$$C_{tube} = \frac{\bar{c} \pi d^3}{12l}. \quad \text{Conductivity of a long tube} \quad (4.10)$$

Hence, low conductivity can be achieved by using orifices with small cross sections or long tubes.

When placing multiple conductance limiting elements in series, the conductivities add as

$$\frac{1}{C_{tot}} = \frac{1}{C_1} + \frac{1}{C_2} + \dots \quad (4.11)$$

More information on conductivity and the design of vacuum systems can be found in [120].

Figure 4.21 shows a rendering of the differential pumping stage designed for this setup. The assembly consists of a pinhole and two conductivity limiting tubes with 0.5 in diameter

that separate two individual sections. Both sections are pumped by a turbomolecular pump on a DN100 CF flange. In order to reduce the length of the setup in the beam line, the pumps are mounted orthogonal to the beam direction on opposite ends of a DN100 CF cross. A custom viton rubber sealed inset separates the tube into two sections. Each one is pumped by one TMP through a D-shaped opening on opposite sides of the inset. A long tube along the beam axis is the only connection between the sections limiting the conductance significantly. Each pumped section adds a pressure differential of  $\sim 1.5$  orders of magnitude. In combination with a pinhole at the entrance and a second long tube at the downstream end, a total differential of  $\sim 10^4$  is obtained over a length of 58 cm. It should be noted that the reduced open area in front of the pumps also reduces their actual pumping speed. Given the space limitations, the conductance limitation achieved by the tube outweighed the losses in pumping speed.

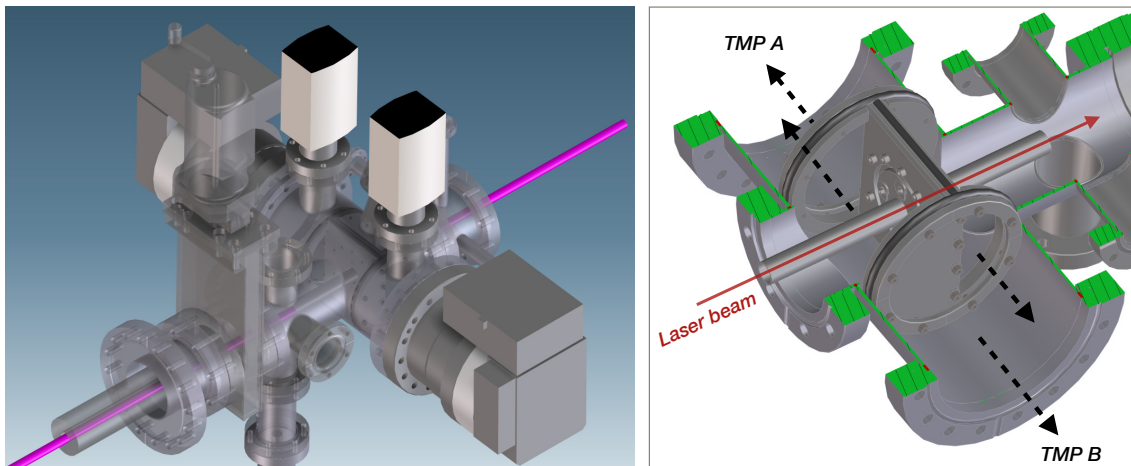


**Figure 4.21:** Rendering of the ultra compact differential pumping setup. A pinhole as well as two long tubes ( $\varnothing = 0.5$  in) limit the conductivity. A custom inset with D-shaped openings on opposite sides allowed for the mounting of two turbo molecular pumps opposite to each other with each pumping one section. This reduces the footprint of the setup significantly. The custom Tee also hosts a variety of ports that are used to connect vacuum gauges, collimators, as well as a phosphor screen.

#### 4.4.2 In-Vacuum Alignment Tools

With the transition to an in-vacuum photon beam line, another simple task suddenly becomes non trivial. Irises used for alignment of the laser beam are omnipresent in laser setups, and they are usually actuated manually. While motorizing an iris in vacuum is not an unsolvable technical challenge, such devices are not widely available and are very costly.

For the current setup, a compact, manually actuated iris, as well as a spring loaded non-magnetic iris were designed. Figure 4.22 shows a technical drawing of the custom DN63 CF Tee housing an iris with 12 mm clear aperture (up to 1 in possible). The iris sits on a standard optical post that is screwed onto a base plate, which is clamped onto the laser table. In order to prevent misalignment after pump-down of the beam line, the iris mounting is decoupled from the vacuum tube using a DN38 CF bellow. This method is used on all pre-aligned in-vacuum optics including the compressor and folding chambers. An angled viewport on the top allows a camera with zoom lens to be focused on the iris in the center of the tube. A strong rare earth magnet is glued to the head of the iris actuator.

The iris opening can be controlled by sliding an additional magnet around the tube surface above the iris.

The use of magnetic materials was strictly avoided for any components near the experimental end-station, as the magnetic field guiding the electron motion would be unpredictably compromised. Therefore, a second iris design without magnetic components was necessary for the last alignment iris close to the entrance of the MISTERS end-station.

Figure 4.23 shows a rendering of the non-magnetic iris. The iris leaves are closed by moving a linear feedthrough that pulls a metal wire, which is connected to the iris pin. A spring that is wrapped around the iris holder closes the iris leaves when the wire tension is released. While the linear motion does not allow the control of the iris opening over the full range, sufficient travel was obtained in order to cover the positions from closed to 0.5 in opening, equivalent to the inner diameter of the tube the iris was attached to.

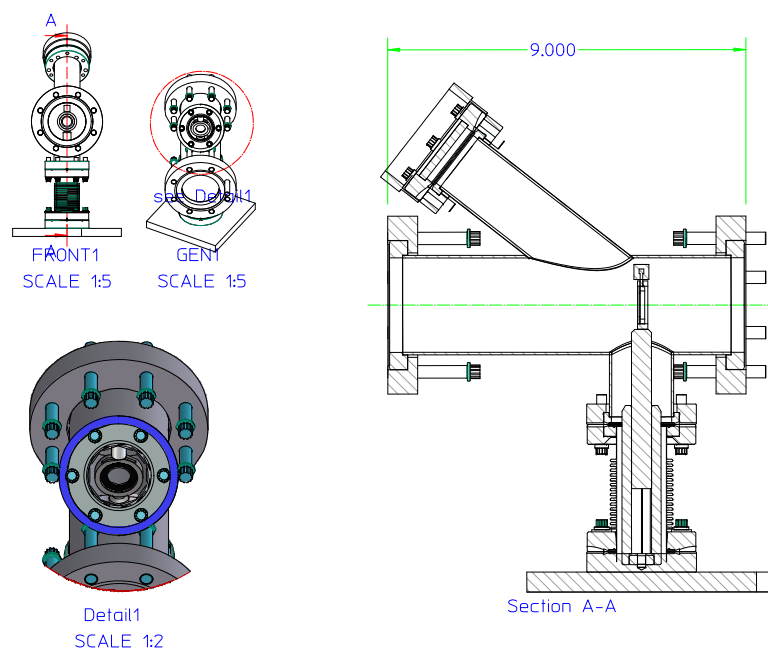


**Figure 4.22:** Drawing of the magnetical iris setup. The iris opening in the center of a DN63 CF tube is actuated by sliding a magnet on the tube surface. The iris mount is fixed on the laser table and decoupled from the vacuum beam line using a DN38 CF bellow.

#### 4.4.3 Beam surveillance

The intensity of the photon beam is sufficient to cause eye damage at virtually any stage of the beamline if the direct beam or a significant portion is reflected into an eye. In order to visually control all alignment tools, beam positions, and the correct movement of motorized stages and mechanical feedthroughs, a number of cameras with the appropriate lenses were used along the beam line. This allows to safely observe the function and position of all beam line components. An easy, reliable, and cost effective solution was found by using standard c-mount analogue cameras that are designed for surveillance systems. Analogue to digital converters are readily available to connect the camera directly to a VGA computer display, without the use of a computer. More than 10 cameras were used in this setup, facilitating the alignment and operation of the beamline and the end-station.

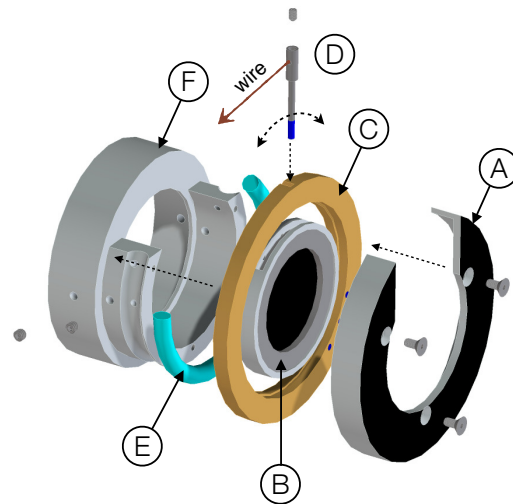


**Figure 4.23:** Rendering of the non-magnetic mechanic iris. The iris (**B**) is opened by means of a linear motion vacuum feedthrough (not shown) that pulls on a wire which is fixed with a set screw on the actuating lever (**D**). A long spring (**E**) is attached at one end to the holder (**F**) and on the other end to a PEEK ring (**C**) that grabs the iris lever. When the wire tension is released the spring closes the iris leaves. A carbon coated front shield (**A**) holds the assembly together and limits direct reflections from the surface.

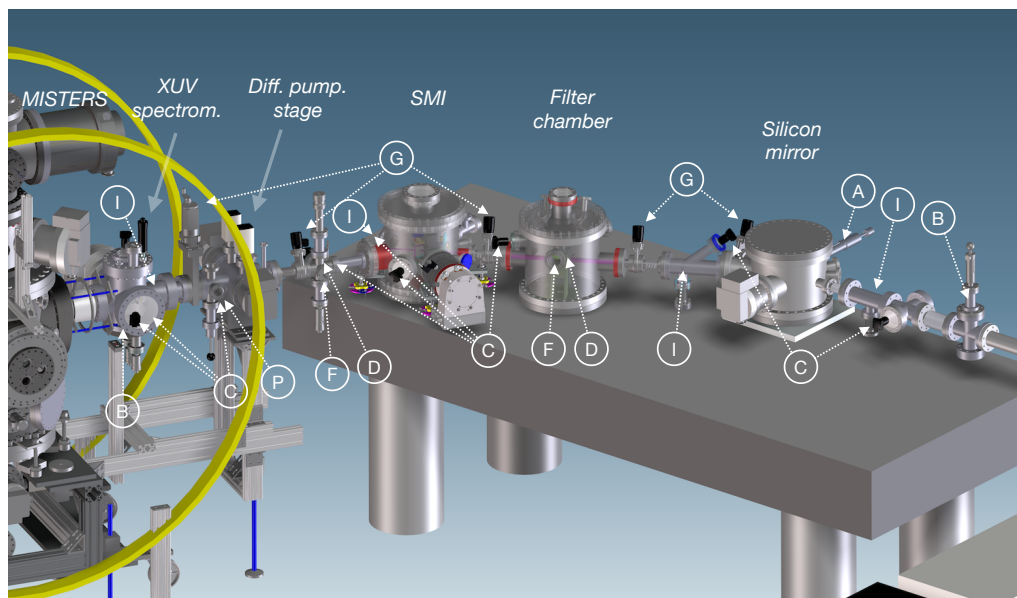


**Figure 4.24:** Drawing indicating the components used for alignment and control in the XUV beamline. (**A**) Actuator for moving silicon mirror 1 in and out of the beamline. (**B**) Beam blocks, (**C**) cameras, (**D**) photo diodes, (**F**) solid filters, (**G**) gate valves, (**I**) alignment irises, (**P**) phosphor screen.

## 5 MISTERS Experimental End-Station

Multiple techniques are available for measuring the energy, emission angles, or momenta of ions and electrons emitted in a photoionization reaction. Each method has its strengths at answering a particular question given the experimental parameters. Arguably the most versatile method is three dimensional momentum imaging, where the momentum vectors of the charged particles produced in the ionization are reconstructed. This yields the energy and the angle of emission of the particle which are both important characteristics to identify the electronic states and the geometry of the molecular system. Two techniques for momentum imaging have been established over the past years.

*Velocity Map Imaging (VMI)* is a technique that allows measuring the two dimensional momentum of electrons or ions in the detector plane [41, 52]. A gas source consisting of a molecular jet, a pulsed nozzle, or a capillary injects the target into the spectrometer where it is crossed with the laser beam. High electric fields ( $\sim 1000$  V/cm) are used to extract charged fragments created in the laser focus. The velocities of photo-fragments are imaged using one or multiple electrostatic lenses onto a MCP-phosphor detector, and the 2D pictures are recorded using commercial cameras.

In the imaging mode, pulsed ion extraction (or pulsed detector operation) enables the collection of the 2D distribution of a particular molecular fragment by gating of a specific time-of-flight (TOF). Assuming cylindrical symmetry around the polarization axis of the photon beam, algorithms enable the reconstruction of the momentum vector in three dimensions if sufficiently high statistics have been collected for the molecular system. Switching to a static electric extraction field, a VMI can also collect the TOF spectrum of all fragments.

Electron angular distributions in the molecular frame are obtained if dissociation happens preferentially at a fixed angle with respect to the polarization axis of the photons. An alternative method consists in the pre-alignment of the target molecules with a strong static or pulsed electric field produced by an additional laser beam (see review article [159] for details). However, both methods have a fairly large angular uncertainty due to the  $\cos^2$ -type distribution of angles. Both, the strength and the weakness of VMI consist in the ability of recording multiple events at the same time. The fluorescence detector allows simultaneous detection of the position of a large amount of particles. Using a pair of detectors for ion and electron imaging, the position of individual hits can be recorded in coincidence if the hit rate is kept strictly below one per shot. However, the assignment of multiple hits on one detector is not possible, limiting the ability to record ion-ion coincidences currently. Therefore, ion-electron correlation studies are the preferred method with VMI detectors.

The end-station developed in this work is based on a technique known as *Cold Target Recoil Ion Momentum Spectroscopy (COLTRIMS)* or *Reaction Microscope*. It combines a cold molecular gas jet with a spectrometer for coincident electron-ion 3D-momentum imaging. The combination of position sensitive detectors with a time-of-flight measurement at a low extraction field retrieves the full 3D-momentum without symmetry considerations. Several ions and electrons can be recorded on an event basis in coincidence, but the delay-line detector used in this technique has strict multi-hit limitations. Operation near this limit will be discussed in Section 5.7.1. The set of kinematically complete data allows to study multi-differential reactions in the molecular

frame and with respect to the polarization axis, without the need for prior alignment, in cases where the *Axial Recoil Approximation* is valid. The ion momentum only corresponds to the molecular axis if the molecule did not undergo a significant rotation between the moment of ionization and dissociation. The approximation breaks down in the case of some small molecules that can undergo fast rotations, as well as in cases of ultrafast conformational changes around conical intersections.

In this setup, a COLTRIMS type experimental end-station was constructed named the *Momentum Imaging Spectroscopy for Time Resolved Studies (MISTERS)*. The experimental setup consists of a molecular beam source, a multi-purpose momentum imaging spectrometer, as well as a focusing mirror setup. All components are placed inside a specifically designed large ultra-high vacuum chamber.

The design, characteristics and operation of cold jets and COLTRIMS style spectrometers have been described in numerous publications. Therefore, the description of common components are kept short in this work. References for further reading can be found in each section.

Figure 5.1 shows a cross section of the MISTERS end-station. The height from top to bottom is  $\sim 2$  m and the footprint not including the Helmholtz coils is  $\sim 1 \times 1.2$  m. The main components inside the chamber are identified in a detailed view in Figure 5.2.

The harmonics beam enters the chamber after passing the XUV-Spectrometer. It has an offset of  $\sim 2 - 4$  mm to the gas jet in the direction of the DLD detector, in order to reduce single ionization of the unfocused beam. The central plates of the spectrometer are cut on all four sides, providing a clear path for the laser beam as well as the gas jet for entering and exiting the spectrometer. Metal plates in the front and the back of the spectrometer, extending the cut out region along the photon beam axis, help to reduce electric field distortion caused from the entrance and exit openings. Additionally, shields block stray photons around the beam axis from hitting the spectrometer plates.

The photon beam is focused with a curved and usually coated mirror ( $f = 15$  cm) back into the gas jet. The specially designed holder and manipulator is described in further detail in Section 5.2. The gas jet is created in a supersonic expansion above the spectrometer and travels on an unobstructed path vertically through the spectrometer and the target chamber. It is collected in a jet dump on the bottom of the chamber. The generation and the properties of the supersonic jet are discussed in Section 5.1. The COLTRIMS type spectrometer consists of an array of metal plates that are stacked in the direction perpendicular to the jet and the laser beam. Position and time sensitive Multi Channel Plate (MCP) detectors with delay-line readout on both sides collect ions and electrons. The design of the spectrometer, the detectors, and the key components for the operation and data acquisition are discussed in Section 5.3. The specifications of the ultra-high vacuum (UHV) chamber can be found in Section 5.5. In the last section, 6.1, the elaborate post-processing of recorded data is outlined.

## 5.1 Gas Target

At room temperature, molecules have a considerable momentum spread according to their thermal energy. For an ideal gas, the energy stored per degree of freedom is equal to  $0.5 k_B T$ . Taking the example of a simple diatomic such as nitrogen ( $m = 28$  amu., 5 active degrees of freedom), we obtain a thermal momentum of  $\sim 0.36$  a.u. This limits the resolution of any momentum measurement at room temperature.

Molecular beams can reduce the momentum uncertainty by converting the thermal energy into a directed motion. When expanding a gas adiabatically at high pressure into a vacuum reservoir, the atoms or molecules of the gas convert the energy stored

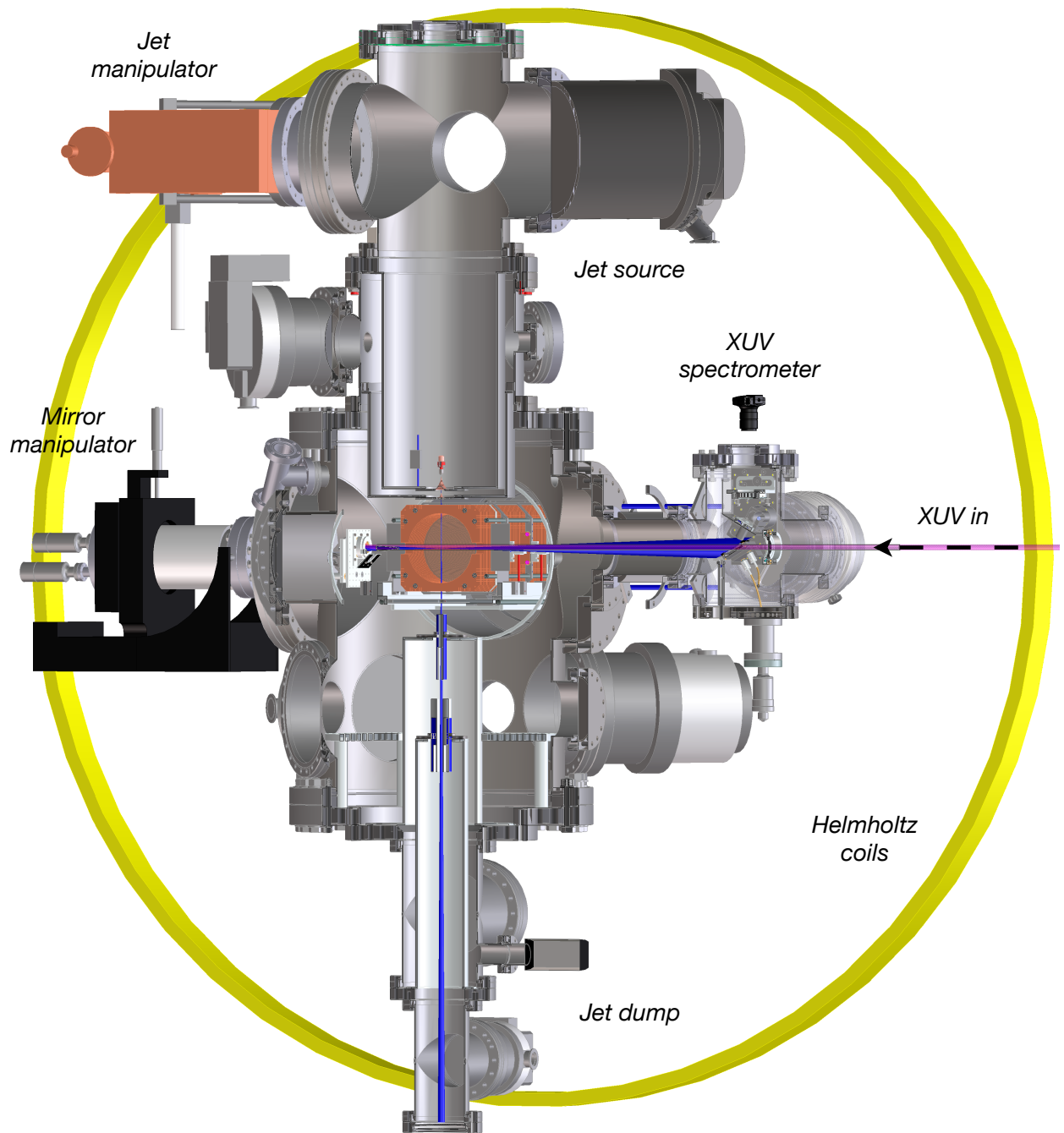


**Figure 5.1:** Cross section of the MISTERS experimental end-station. An expanded view of the interaction zone in the center of the chamber is shown in Figure 5.2. The long arm holding the jet nozzle, as well as the gas and cooling connections in the jet source chamber are not shown in this picture.

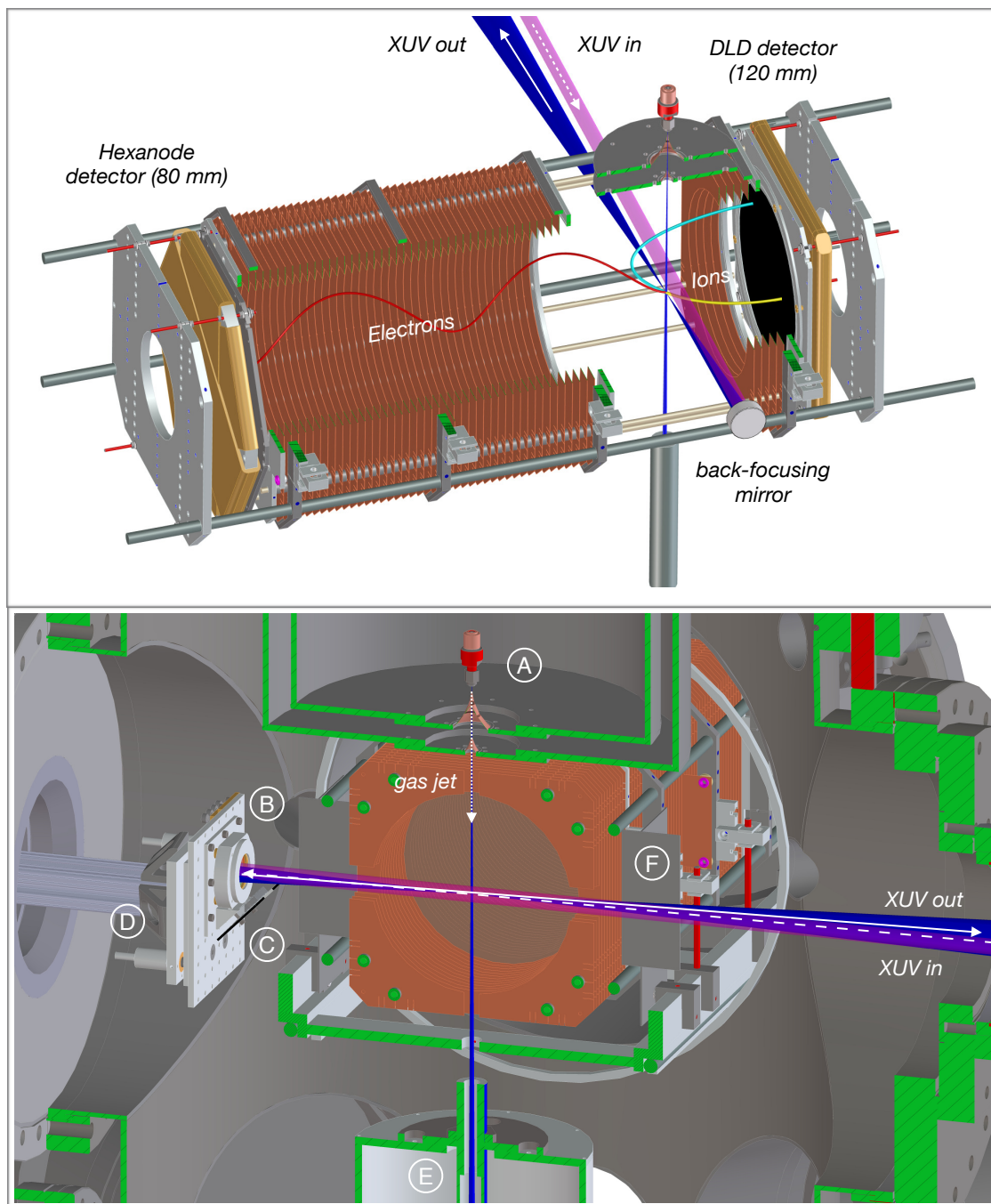


**Figure 5.2:** (Top) Rendering of the MISTERS spectrometer and the beam path. (Bottom) The reaction zone inside the MISTERS end-station. The central plates are not shown to improve visibility. The incoming XUV laser beam passes the gas jet in the center of the spectrometer at a small offset (2-4 mm). The back-focusing mirror then back-reflects the beam into the gas jet at a small angle ( $\sim 1^\circ$ ). The supersonic molecular beam is produced from a 30  $\mu\text{m}$  nozzle above the spectrometer (A) and travels downstream through the chamber before being captured in a two stage jet dump configuration (E). The back-focusing mirror (B) is mounted together with a 45° mirror (C) (see Section 5.4) on an XYZ-manipulator by means of a long aluminum arm (D). Tip and tilt of the mount can be controlled using rotational feedthroughs that are coupled with flexible wires (not shown).

in the various degrees of freedom into kinetic energy in the propagation direction. The momentum transfer happens through collisions between the particles. Around the nozzle, a *zone-of-silence* forms in which no more internal collisions of gas molecules occur.

A directed supersonic jet can be obtained by placing a conically shaped opening, also called a skimmer, into the zone-of-silence. The extent of this zone is defined by an equilibrium between the gas expansion and the background pressure that establishes depending on the geometry, the nozzle pressure, and the vacuum conditions in the expansion chamber. Over the past decades, supersonic gas jets have been tested and developed extensively.

Figure 5.3 shows the common two stage expansion scheme that was chosen in this setup. The gas jet is injected into the source chamber using a 30  $\mu\text{m}$  microscope aperture (Ted Pella Inc.) as the nozzle. The shape of this aperture enables an effective expansion. The nozzle is sealed on the gas line by pressing it onto a copper stamp using a solid gold gasket. A standard filter (Swagelok Inc.) prevents particles from clogging the small nozzle orifice. Copper is used for the stamp material, as it offers excellent thermal conductivity.

The supersonic beam is skimmed from the zone-of-silence using a 19 mm long conical skimmer ( $\varnothing = 0.3$  mm, Beam Dynamics Inc.). The source chamber is pumped by a large turbo molecular pump (TMP) with magnetic bearings (Shimadzu). It has a nominal pumping speed of 2000 l/s for  $\text{N}_2$ , which allows for high jet driving pressures of up to several bars in most gases.

The position and the distance of the nozzle can be adjusted with a three-axis manipulator that holds the nozzle assembly on a  $\sim 40$  cm long arm. The closest distance of the nozzle to the skimmer yields the highest jet density. However, if the distance becomes too small, reflected molecules from the surfaces around the skimmer compress the zone-of-silence. At large distances, the skimmer does not penetrate the zone of silence and the jet is not supersonic. The typical nozzle skimmer distance is on the order of 5 - 15 mm. Curves for various jet parameters are shown in Appendix A.5. Heating elements as well as a cryogenic-cooler can heat or cool the nozzle in order to obtain a minimal target temperature or to prevent or enhance the generation of clusters (see [68] for details).

Adding a second skimmer ( $\varnothing = 0.5$  mm) with an independently pumped vacuum reservoir after the jet source limits the divergence of the jet and reduces the flow of warm background gas to the target zone. The small orifice of the skimmer has low conductance for randomly flowing gas (see Section 4.4.1). As a consequence, the second jet stage acts effectively as a differential pumping stage allowing for low background pressures in the target chamber.

The target extension can be approximated from a geometry calculation using the skimmer diameter,  $d_{sk2}$ , and the distances of the skimmer and the target to the nozzle,  $l_{sk2}$  and  $l_{tar}$ .

$$\boxed{d_{tar} = \frac{d_{sk2} l_{tar}}{l_{sk2}}.} \quad \text{Target diameter} \quad (5.1)$$

A rough estimate for the area density in the target  $\rho_{tar}$  can be obtained by measuring the pressure rise  $p_d$  in the jet dump, assuming the entire beam is deposited in this volume [68].

$$\boxed{\rho_{tar} = \frac{N_A}{22.4} \frac{p_d L_d}{v \frac{\pi}{4} d_{tar}^2},} \quad \text{Target density} \quad (5.2)$$

where  $N_A$  is Avogadro's number, and  $L_d$  is the pumping speed of the TMP pumping the jet dump reservoir.

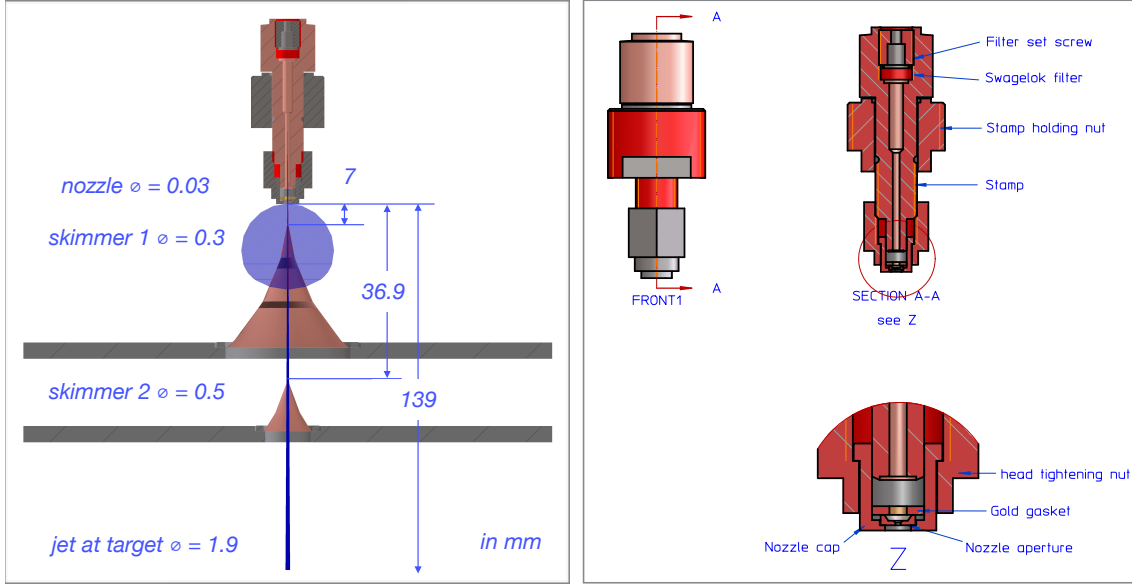


**Figure 5.3:** Technical drawing of the jet expansion parts used to produce the supersonic beam. In the cross section on the right side, the various parts of the nozzle assembly are labelled. Copper is used for the holder material as it offers good thermal conductivity. Therefore, the gaskets used to seal the nozzle to the stamp are made of gold.

One can obtain an estimate for the temperature and the resulting momentum spread of the gas target by treating the target as an ideal gas with a Boltzmann energy distribution. The energy per degree of freedom at temperature  $T$  is given by

$$E_f = \frac{1}{2} k_B T. \quad \text{Energy per degree of freedom} \quad (5.3)$$

If we take the work of the expansion,  $pV = kT$ , into account, we obtain for the total internal energy

$$E_{tot} = \frac{f}{2} k_B T + k_B T = \left( \frac{f+2}{2} \right) k_B T. \quad (5.4)$$

The expansion converts most of the internal energy into translation resulting in a thermal temperature  $T_{exp}$  after the expansion.

$$\left( \frac{f+2}{2} \right) k_B (T_0 - T_{exp}) = \frac{1}{2} m v_{jet}^2 \quad (5.5)$$

The velocity expressed by this temperature reads

$$v_{jet} = \sqrt{(f+2) \frac{k_B (T_0 - T_{exp})}{m}}. \quad (5.6)$$

It is common to quantify a supersonic expansion by defining a *speed ratio* as the ratio of the jet velocity to the width of the velocity distribution.

$$S = \frac{v_{jet}}{\sqrt{2k_B T_{exp}/m}}. \quad \text{Speed ratio} \quad (5.7)$$

The temperature can then be expressed in terms of the speed ratio using equation 5.5. For  $T_0/T_{exp} \gg 1$  this yields

$$T_{exp} \simeq \left( \frac{f+2}{2} \right) \frac{T_0}{S^2}. \quad \text{Temperature of the expanded jet} \quad (5.8)$$

Measurements and more accurate calculations for the speed ratio using different expansion models are available in the literature (see e.g. [116]). Empirical and theoretical values for the speed ratio can be found in the literature. A practical equation that was found empirically allows the calculation of the speed ratio for small molecules to about 10% accuracy [116]. Note, that the value for the nozzle pressure,  $P_0$ , and the nozzle diameter,  $d$ , have to be inserted in Torr and in cm respectively.

$$S_{\parallel} = 5.4(P_0 d)^{0.32}. \quad \text{Empirical speed ratio for molecules} \quad (5.9)$$

The thermal momentum half-width of the jet after the expansion is given by

$$\Delta p_{\parallel} = m \cdot v_{jet} \left( \frac{2\sqrt{\ln 2}}{S} \right). \quad \text{Parallel momentum half-width} \quad (5.10)$$

In the directions perpendicular to the propagation direction, the beam is cut geometrically by the skimmer. The uncertainty in these directions can be quantified as

$$\Delta p_{\perp} = m \cdot v_{jet} \left( \frac{d_{sk2} + d_{noz}}{l_{sk2}} \right). \quad \text{Transverse momentum uncertainty} \quad (5.11)$$

A detailed discussion of the thermodynamics of a supersonic expansion and other parameters for characterization can be found in [47, 116] and references therein. Typical values for experimental conditions in this setup are noted in Table 5.1,

Parameter	O <sub>2</sub>	H <sub>2</sub>	Ar	Unit
Mass	32	2	40	amu
Backing pressure	6.9	6.2	6.2	bar
Temperature	296	296	269	K
Jet speed	734	2935	555	m/s
Speed ratio	13*	13*	10*	
Parallel momentum	2.51	0.65	3.08	a.u.
Transverse momentum	0.17	0.04	0.16	a.u.
Pressure rise (corrected)	$2 \times 10^{-8}$	$7.2 \times 10^{-8}$	$3.4 \times 10^{-8}$	mbar
Target density	$5.6 \times 10^{10}$	$4.3 \times 10^{10}$	$1.3 \times 10^{11}$	1/cm <sup>2</sup>

**Table 5.1:** Calculated jet characteristics for oxygen, hydrogen, and argon. The speed ratio for oxygen and hydrogen were calculated using Equation 5.9. For argon it was estimated according to the literature. For H<sub>2</sub>, the readout pressure and the pumping speed were adjusted according to the manufacturer specifications.

## 5.2 Focusing Optics

In a pump-probe type experiment, the molecular dynamics are started by the absorption of a photon from the pump pulse that promotes the molecule from its ground state to an intermediate state. The molecular configuration is left to propagate freely in time until a second

pulse, called the probe pulse, ionizes the molecule, projecting it to the final state that is ultimately measured. This process is called *resonant- or sequential two-photon absorption*.

In the spectral range  $\sim 0 - 100$  eV, equivalent to the photon energy range produced by high harmonic sources, the wavelength of the radiation is much larger than the length scale of atoms and molecules. The multipole expansion of the electric field can therefore be truncated to the first order, the so-called *electric dipole approximation*. This means that only transitions caused by the electric dipole moment will contribute to the photon absorption. The probability for a dipole transition from state  $\mathbf{a}$  to state  $\mathbf{b}$  is

$$P_{a \rightarrow b} = \frac{2\pi}{\hbar^2} |E_0|^2 |\langle b | \boldsymbol{\mu} | a \rangle|^2, \quad \text{Electric dipole transition} \quad (5.12)$$

where  $\hbar$  is Planck's constant,  $E_0$  the electric field Amplitude, and  $\boldsymbol{\mu} = e \mathbf{r}$  the *electric dipole operator*.

As this process happens twice in a pump-probe experiment, we can write the probability for the pump-probe process by the product of the probabilities of the individual one-photon absorptions with transition specific cross-sections  $\sigma_i$ . At the low absorption rate in a gas, the intensity of the electric field,  $I$ , is not affected by the absorption of a single photon. The probability for two-photon absorption is then

$$P_{2\gamma} \propto \sigma_1 \sigma_2 I^2. \quad \text{Resonant two-photon absorption probability} \quad (5.13)$$

Hence, if the absorption occurs in the same laser field, the probability for the pump-probe process scales as  $I^2$ . For a fixed amount of photons available from the light source, the intensity increases quadratically with the inverse of the beam diameter. For this reason, minimizing the focal size is extremely important for multi-photon absorption.

Two different focusing geometries are usually employed in laboratory based harmonics sources. In the first, the high harmonics beam is reflected and focused with a *toroidal mirror* at a shallow angle into the target volume. The advantages of this geometry are the high reflectivity of the mirror at a shallow angle, as well as the possibility of performing further beam characterization downstream of the target or efficient dumping of the photon flux to avoid stray reflections. An XUV-Spectrometer or a spatial mode analyzer can be used to obtain spectral, spatial, or even temporal information of the pulse after passing through the target. The disadvantages of a toroidal mirror are in the focusing and the challenging alignment. The characteristics of the focus of a toroidal mirror are extremely sensitive to the beam pointing or the polarization axis [177]. Small changes of the beam upstream can result in large changes of the focal intensity or the position. This means that the alignment is more elaborate, and the stability of the source parameters has to be controlled carefully. More importantly, the focal size that can be achieved using a toroidal mirror is on the order of 1:1 of focus to source size. In the case of High Harmonic Generation, the source size is equivalent to the region where the harmonics are generated. For high harmonic sources using a gas jet or a capillary, the infrared beam is focused tightly to a small spot. The source diameter is on the order of tens of microns, and a comparable focal size in the target of the experimental end-station might be acceptable. In the case of the loose focusing geometry employed in this setup, the harmonics are generated from a focus on the order of 200  $\mu\text{m}$ . This would be equivalent to a loss of more than two orders of magnitude in beam intensity compared to the tight focus given by a back-focusing mirror. Consequently, the use of a spherical back-focusing mirror was necessary because it can yield smaller focal sizes. A solid one inch back-focusing mirror was placed at 150 mm distance to the spectrometer in order to achieve the smallest focal size (see Equation 3.18).

In Table 5.2, some calculated focal parameters of the harmonics beam, assuming a Gaussian beam shape, are listed. The beam quality is strongly affected by the propagation

optics and apertures. For the 5<sup>th</sup> harmonic, T. Allison measured a beam size corresponding to a beam quality parameter of  $M^2 \simeq 2$  [8]. This factor was added in the tabulated values. In the y-direction, the spatial profile of the beam is strongly modified from being reflected off the two, vertically split, mirror surfaces in the Split-Mirror Interferometer. The central gap cuts the beam intensity and changes the mode which results in strongly deteriorated focusing. Therefore, the calculated focal sizes were multiplied by a factor of 2.5 in the y-direction. As the generation of high harmonics requires a different intensity for each order, the divergence and consequently the beam size varies. The actual divergence for each order might be different to the calculation due to geometric effects in the generation medium [8]. More information on beam quality can be found in [154].

In the current setup, the spatial mode was not routinely measured. Daily adjustment of the multi-pass amplifier was performed while observing the beam mode on an optical card. This optimization was cross-checked by comparing the harmonics flux measured on a photo diode to the optimal yield.

Parameter	IR	3 <sup>rd</sup>	(5 <sup>th</sup> )	13 <sup>th</sup>	21 <sup>th</sup>	unit
Focal length			150			mm
Wavelength	808	269.3	161.6	62.2	38.5	nm
Beam diameter	12*	11.9	9.2	5.7	4.5	mm
Focal diameter x	25.7	8.7	6.7	4.2	3.3	$\mu\text{m}$
Focal diameter y	64.3	21.6	16.8	10.4	8.2	$\mu\text{m}$
Raleigh length	643	218.5	218.5	218.5	218.5	$\mu\text{m}$

**Table 5.2:** Calculated focal parameters of the fundamental and the XUV beam assuming a gaussian beam shape. The divergence of the infrared beam,  $\theta_0$ , is estimated from an initial beam size of  $\varnothing = 19$  mm focused with  $f = 6$  m. The divergence is expected to depend on the harmonic order by  $\theta_q = \theta_0/\sqrt{q}$ . A factor of 2 is applied to the focal diameter for taking into account the beam quality. The focal size in the y direction was multiplied by a factor of 2.5 to account for the modified beam shape due to the beam splitting on the Split-Mirror Interferometer. (\*) The beam diameter of the fundamental is limited by the opening size of the conductance tubes.

In order to reduce single ionization created from the incoming beam, the harmonics pass the jet at a slight offset of 2 - 4 mm. This results in a tilt of the mirror axis of  $\sim 0.8^\circ - 1.5^\circ$  with respect to normal incidence.

It is a well-known problem that XUV and X-ray beams cause ionization on the mirror surface as typically less than 50 % of the beam is reflected. The electrons created on the surface can travel into the spectrometer and create a background of low energy electrons. In order to avoid this problem, the mirror mount, shown in Figure 5.4 has two electrically insulated shields positioned around the mirror. Applying a positive voltage to the inner shield will attract emerging electrons to the side. The outer cover can be set to a potential similar to the spectrometer. This will minimize field distortion caused by the mirror being close to the open spectrometer. Additionally, electrons are prevented from entering the spectrometer by a negative bias of the spectrometer, as well as from the magnetic field created from the Helmholtz coils.

### Photon and Electron Background

A severe problem that is much harder to control is the diffuse reflection of photons. Diffuse reflection occurs from particles and imperfections on the front surface of the mirror. If

the mirror material is transparent to the 3<sup>rd</sup> or the 5<sup>th</sup> harmonic, photons penetrating the substrate material have a small probability of being back-reflected from the rear surface of the mirror or the holder. At an initial photon flux of  $1 \times 10^{10}$  photons, even a suppression of several orders of magnitude, caused by low transmission and diffuse reflection in the mirror material, still yields thousands of photons that are emitted into the spectrometer. Virtually every XUV photon impinging on the surface of a spectrometer plate will cause the ejection of an electron. If this occurs inside the spectrometer, the electron will be guided by the electric field onto the respective detector creating a background of random electrons.

This problem persists to date and several approaches are being taken to minimize this effect. A substrate material can be chosen that absorbs all harmonics unless they are reflected from the multilayer coating. One can aim at reducing the solid angle for photons penetrating the spectrometer. This can be achieved by increasing the distance of the mirror to the spectrometer. However, this will cause the above mentioned loss in intensity in the target and is therefore not favorable. An alternative way is the use of a baffle extension around the mirror surface. Such an approach was tried in this setup with limited success.

### Mirror Control

The adjustment of the mirror position and the tip-tilt angles is performed without the use of any in-vacuum motors that would limit the attainable vacuum level. The position of the back-focusing mirror is controlled with a three-axis manipulator that is mounted to the rear flange facing the beamline. The mirror mount is attached to the manipulator base by means of a long aluminum rod that allows close positioning to the spectrometer. Tip and tilt of the mirror surface are adjusted using two micrometer screws that are connected to rotational vacuum feedthroughs on the rear flange of the manipulator using flexible couplings, similar to the mirror control of the XUV-Spectrometer (see Figure 4.15). While the backlash of the rotational control using flexible couplings is considerable, the absolute tip and tilt position is encoded in a high precision distance measurement close to each micrometer screw.

The capacitive distance sensor is a special development from Paul Denham from CXRO. It represents a variation of the LVDT type distance measurement used for the readout of the tip and tilt position in the Split-Mirror Interferometer (see Section 4.2). In a *Linear Variable Differential Transformer (LVDT)* the displacement can be determined by a differential measurement of the induced current between three linearly arranged magnetic coils (see [102] for more details). As magnetic fields this close to the spectrometer would interfere with the electron trajectories, a non-magnetic device was needed. In the sensor used here, the position is encoded in a change of capacity. Three small aligned cylinders are attached to one side of the mirror mount. The outer cylinders are charged using an AC power supply, and the inner cylinder serves as a pickup. An insulated metal cylinder that slides freely inside the outer cylinder array is attached to the opposing side of the mount. It couples the charge from the outer capacitors to the central pickup. When the distance of the mirror mount changes, a wire enclosed in an insulating peek cylinder moves inside the tube. This induces a small charge that is amplified and measured with a standard ampere meter.

## 5.3 3D Momentum Imaging Spectrometer and Detectors

In this setup a COLTRIMS type spectrometer is used to retrieve the full three dimensional momentum vectors of ions and electrons. The imaging of the momenta of charged particles

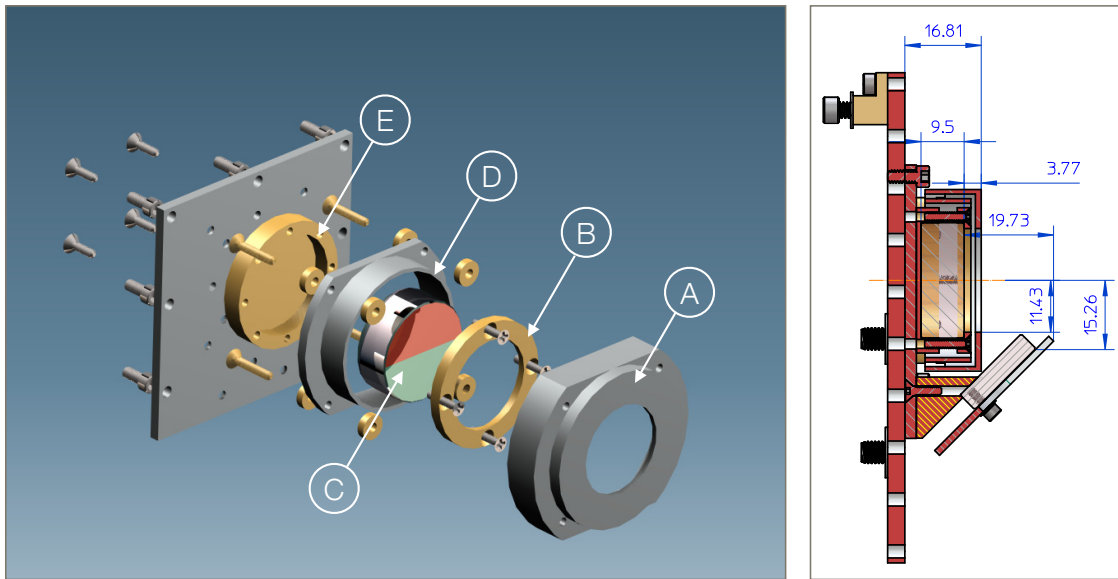


**Figure 5.4:** Rendering of the back-focusing mirror mount assembly. The mount was designed to prevent issues stemming from electrons created at the surface of the mirror substrate (C) which had been observed in previous experiments with similar setups. The ring (D) can be biased positively to trap electrons while the outer shield (A) is set to a specific potential in order to minimize the electric field distortion in the spectrometer. The mirror is clamped onto a base plate (E) using an electrically isolated PEEK ring (B).

is based on the direct measurement of the time-of-flight (TOF) and the position of impact of each individual particle on time and position-sensitive detectors. Guided by a low electric field, ions and electrons fly according to their charge to detectors on the opposite sides of the spectrometer.

A well-defined homogeneous electric field is generated by applying a voltage to the evenly spaced and insulated stack of copper plates with large round central cutouts. The plates are connected using large resistors ( $\sim 300 \text{ k}\Omega$ ) creating an even potential gradient. Large Helmholtz type coils ( $\varnothing = 2 \text{ m}$ ) are placed around the spectrometer axis to create a homogeneous magnetic field that forces the electrons on spiral trajectories inside the spectrometer. Depending on the particular ionization reaction, electric fields on the order of 5 - 50 V/cm and magnetic fields of a few Gauss (4 to 14 G) are typically required to collect ions and electrons with full solid angle.

As the detectors are sensitive to the impact of individual particles, coincidence measurements of multiple ions and electrons are possible in a single ionization event. The limitations of such multi-hit detection are discussed in Section 5.7.1.

### Multi Channel Plates

The detectors consist of a pair of microchannel plates (MCPs) combined with a two layer (DLD) or a three layer (Hexanode) delay-line anode mounted on the back. MCPs serve as an amplifier converting a single photon or charged particle into a cloud of electrons that provide sufficient charge to be detected as an electronic pulse signal. The plates are made of a highly resistive material with an array of microchannels of about  $25 \mu\text{m}$  diameter. The plates have a diameter of 80 and 120 mm at a thickness of  $\sim 1.5 \text{ mm}$ . When the particle

hits one of the microchannels, the strong potential (800 to 1200 V) applied across each plate accelerates the electrons. Multiple recollisions with the channel walls that are slightly tilted to the surface normal ( $\sim 8^\circ$ ) cause a cascade of about 1000 electrons. The plates are usually rotated by  $180^\circ$  around the normal axis to improve the amplification and to reduce ion feedback (Chevron configuration). This results in a total charge amplification of  $\sim 10^6$  for a Chevron stack. The time-of-flight signal of a particle is obtained by the time difference between the MCP signal and a reference signal triggered by the laser.

### Delay-line anode

Each delay-line anode layer consists of a pair of long wires which are densely wound in parallel,  $\sim 0.5$  mm spaced lines, around a rectangular insulated frame. The electron cloud creates a signal pair traveling to each end on the wire. The parallel wires form a, so-called, *Lecher line* that is favorable for the transport of high frequency signals and allows a reduction of noise. One wire is biased  $\sim 40$  V more positive such that the electronic charge is collected in this wire. If external noise is equally recorded in both wires, subtracting the second reference wire from the signal wire will eliminate the noise. The position of impact perpendicular to the winding direction of the wires is proportional to the signal runtime given by the difference of the time signals at both ends. The conversion factor between runtime and spatial distance is defined by the ratio of detector size to maximal runtime on the layer. The full position information in the detector plane can be obtained by using two delay-line layers rotated by  $90^\circ$  with respect to each other.

In the *Hexanode* configuration, three delay-line layers are rotated by  $60^\circ$  to each other, which results in an over determined position measurement. This redundancy increases the ability to correctly assign multiple signals and to reconstruct missing signals. Therefore, it improves the capability to record multiple fragments arriving in a smaller time interval (multi-hit capability). Additionally, the average position resolution over the detector is significantly improved by a post-processing algorithm based on the redundancy in deriving the detector image.

The time and the position resolution of the detector depend not only on the detectors, but also on the electronics for signal retrieval and timing, as well as on the setup and the adjustment of the hardware for signal retrieval (see Section 5.3.2). More information on delay-line detectors and typical values for the resolution and the dead-time can be found in [68, 178] and on the RoentDek website [132].

### 5.3.1 Geometry and Capabilities

The design of the spectrometer for the MISTERS end-station is similar to existing COLTRIMS spectrometers, but it required some additional considerations. While the geometry of a spectrometer is usually adapted to a single experiment, the design for the current setup was required to be more universal and adjustable. The photon beam conditions under which the MISTERS spectrometer need to operate differ from other end-stations built so far. The amount of photon flux per shot exceeds the rates at synchrotrons and all other harmonics sources using COLTRIMS spectrometers by orders of magnitude. Free Electron Lasers deliver an even higher flux per shot but the spectrum is usually mono-energetic, and it does not contain the low photon energies that a high harmonics source produces in high quantity. Furthermore, an ultra-high vacuum environment which requires baking of the chamber makes changes to the spectrometer time intensive, as every venting process would require several days of bake out to recover the desired vacuum level.

After some simulations, an asymmetric design was chosen which provides an acceptable resolution for a wide range of atomic and molecular experiments. Figure 5.5 shows a drawing

of the MISTERS spectrometer. Measuring from the interaction zone, the spectrometer consists of one short side, 6.3 cm long, and one longer side which is separated by a metal mesh into two sections, 6.8 and 23.6 cm long. A mesh on each end allows for a short high field region between the spectrometer and the detector, necessary to post-accelerate the particles for efficient detection on the MCPs. A 120 mm dual layer delay-line anode detector is mounted on the short side, while the long side is equipped with a 75 mm Hexanode (both detectors from RoentDek GmbH [132]).

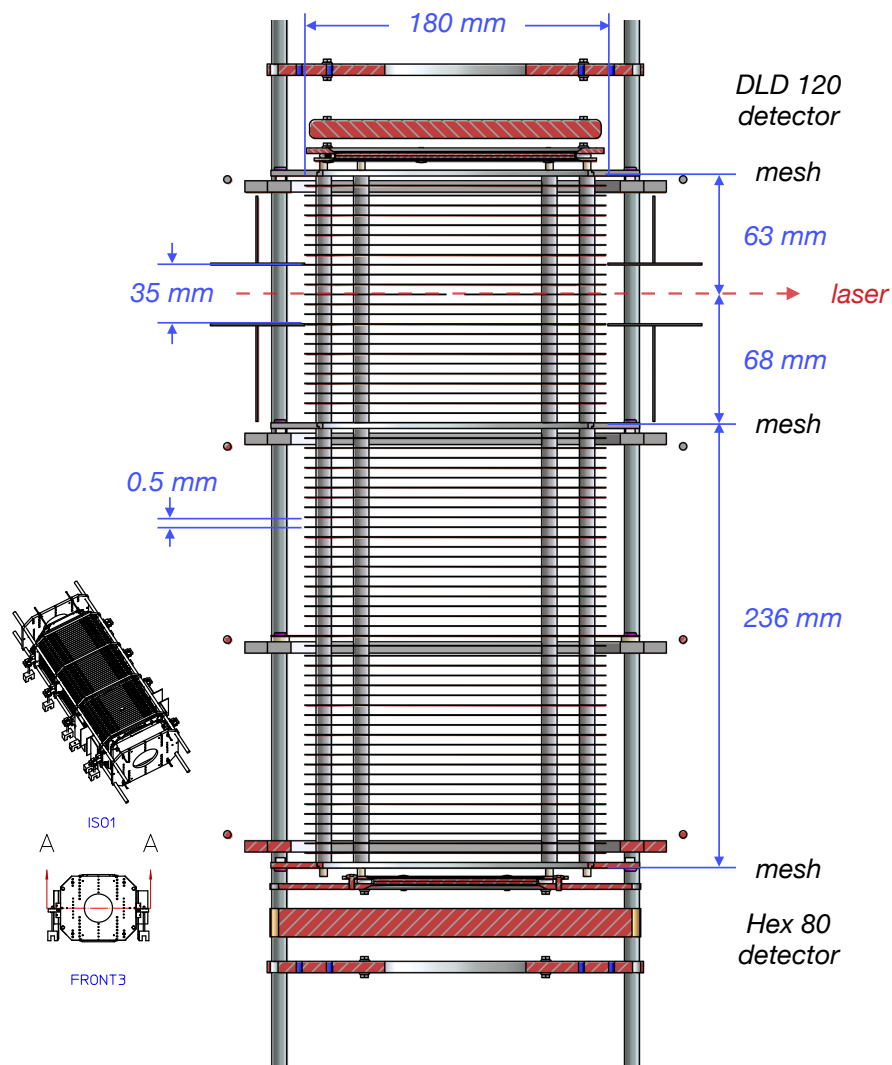


**Figure 5.5:** Drawing of the MISTERS momentum Spectrometer. The plates around the target area have cutouts for the gas jet as well as the laser beam. Extension plates along the beam direction limit the field distortion that occurs due to the cutouts. Additional stainless steel plates around the target area prevent scattered light from entering the spectrometer.

In most molecular experiments, the short side is used for collecting molecular fragments with high kinetic energy. The corresponding electrons are imaged using an acceleration region and a longer drift region such that particles starting from different positions along the TOF-axis reach the detector simultaneously. This, so called, Wiley-McLaren geometry [180] reduces the momentum uncertainty introduced by a spatially extended target in

the TOF direction. In this spectrometer, the length of the drift region was increased in comparison to the standard 2:1 ration of acceleration to drift region in order to match cases where an electrostatic lens is used (see below).

The Hexanode detector is usually chosen for the detection of electrons due to its better multi-hit capability, required from the small time spread of the electrons. Nevertheless, the long spectrometer side is also suitable for detecting atomic ions that do not acquire a high kinetic energy due to the lack of coulomb repulsion of a partner ion or neutral atom. The long flight tube gives ions more flight time to spread over the detector increasing the momentum resolution in the spatial direction. Spatial focusing using the electrostatic lens mode can be used additionally, while the resolution is only improved in the photon propagation direction (see 5.3.3).

Several plates in the spectrometer stack are connected to vacuum feedthroughs (see Figure 5.6). By adjusting their potential individually, a variety of additional electric field geometries can be implemented.

1. The long spectrometer side can be switched from a combination of short acceleration and drift region to one homogeneous acceleration region. This provides an improved resolution in the TOF direction (see Section 5.3.3).
2. An *Electrostatic focusing lens* can be implemented that focuses ions from different starting positions in the target region onto the same position on the detector. This reduces the uncertainty caused by the spatial target extension in the detector plane. Such a focusing lens has been successfully implemented in several previous measurements (see [143, 165] for more information).
3. The potential can be adjusted to form an *electrostatic defocusing lens* that magnifies small changes in the starting position of ions. This field configuration was designed to facilitate the overlap of the pump and the probe pulses by magnifying the expected focal spot of a few microns (in the jet direction) by a factor of up to 100 on the detector. Figure 5.7 shows a simulation of singly charged ions starting from an extended target in the center of the spectrometer. The ion trajectories spread the target image over a wide area on the detector. In this configuration, a strong potential step ( $\sim 2500$  V) is applied to the ion mesh as well as to the last plate before the drift region (Def. lens back). The field around the target region is kept around 1 – 2 V/cm. This results in a field shape acting as a concave electrostatic lens around the reaction zone. In practice, this mode was not used regularly due to the inherent overlap of the different beam arms (see Section 4.2). It should be noted though, that the magnification and the position of the image on the detector are very sensitive to the target position and the fields involved, such that a careful adjustment of the fields is necessary in order to obtain good results.
4. Due to the expected high flux of ions and electrons per shot, the application of a pulsed voltage to the last plate in front of each detector was considered. This was expected to deviate the trajectories of unwanted particles sufficiently, preventing them from hitting the detector. In order to limit the induction of pulses to the nearby detector, these plates were connected using a coaxial in-vacuum cable with a grounded shield on both ends. Some tests were performed using a commercial pulser, but the induced voltage spikes on the detector were too large. Further development is required to ensure a very low rise time and the effective dumping of induced fast pulses during the operation in a pulsed mode.

The entire spectrometer including the detectors sits on a sled that can be pushed horizontally in and out of the target chamber. The detectors and the spectrometer are

connected using several save high voltage (SHV) vacuum feedthroughs on the large CF 300 flanges behind each spectrometer side, as well as on the chamber walls.

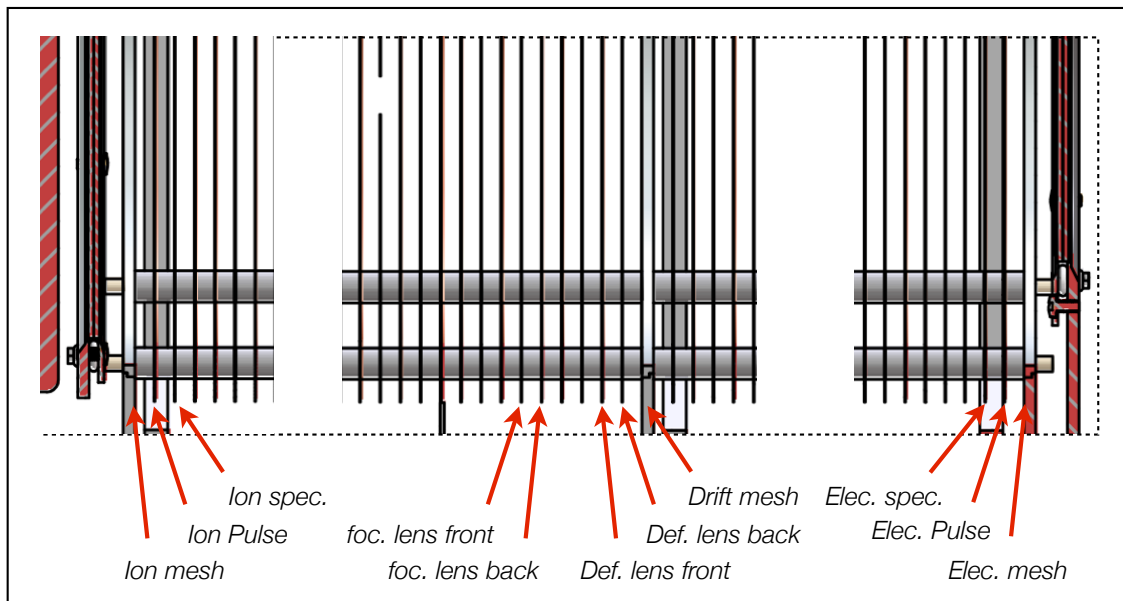


**Figure 5.6:** Schematic of the spectrometer plates that are connected individually to the SHV vacuum feedthroughs. External resistor chains allow switching between the different spectrometer modes described in Section 5.3. All other plates are connected in a sequence with high  $k\Omega$  resistors.

### 5.3.2 Signal Retrieval and Data Acquisition

The MCP delay-line detectors require high voltages in order to achieve the necessary gain for single particle detection. The signals created on the MCP and on each delay-line have a height of tens of meV. These signals need to be decoupled from the high voltage of the signal wires. Decoupling is performed by a home built high-pass filter consisting of a capacitor (5 nF) in combination with resistors to adjust for an impedance mismatch between connections. The isolated signal is amplified by a fast amplifier (RoentDek FAMP) to signal heights around 0.6 – 1.2 V. A *constant fraction discriminator (CFD)* is used to limit the dependence of signal timing to the pulse height and converts the analogue signal into a NIM standard signal.

The timing signals are recorded in a data acquisition computer using *time-to-digital converters (TDCs)* (Cronologic GmbH [31]). The TDC has a shift register that constantly records signals and discards the oldest entries when the buffer is full. The buffer is read out in a specified time window with respect to a user defined trigger channel. The data are stored for every read-out, called event, in *list-mode files (lmf)*. A commercial acquisition software, *COBOLD PC* [132], processes the raw time information from all anode layers and the MCP signals and converts them into time-of-flights and detector positions. This includes a sophisticated resorting algorithm that can reconstruct the position and the MCP signals for events with incomplete data using consistency considerations. The large amount of recorded hits provides rich possibilities for post-processing of the recorded data. If the amount of data in the maximal time window becomes too large, further logic modules can be used to restrict the signal processing of the constant fraction

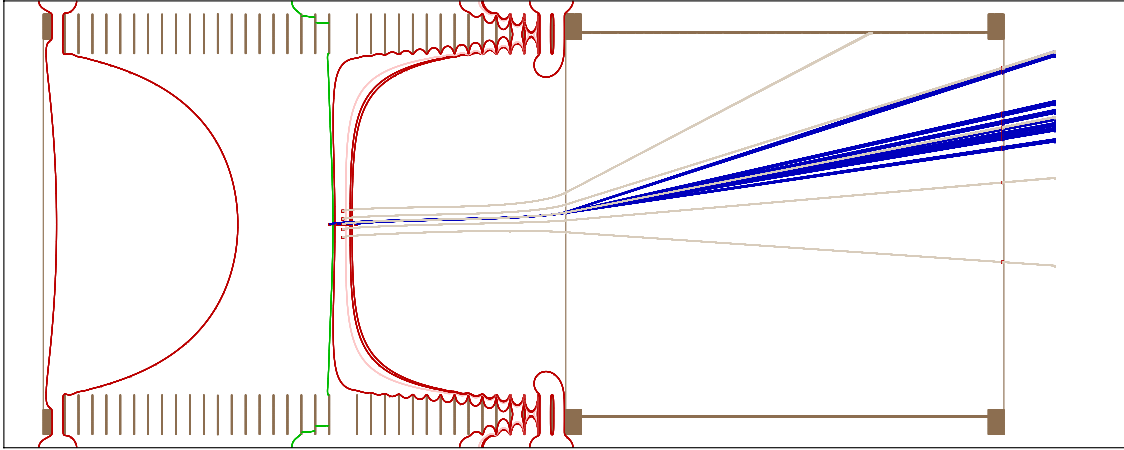


**Figure 5.7:** Simulation of ion trajectories in the MISTERS spectrometer in defocusing mode for magnified imaging the target position on the Hex detector. A low electric field around the target region combined with a high voltage on the DLD mesh and the last plate in front of the Drift mesh form an electric field shape similar to a concave lens. Ions with different starting points fly on positions far apart on the Hexanode detector.

discriminator to only consider signals in a particular TOF range (gating). A photo-diode in the laser system serves as the time reference signal and is usually used to trigger the recording. The exact starting point of the ionization is found from the TOF peak of scattered and fluorescence photons that hit the detector.

Typical operation voltages are shown in Table 5.3. In the current setup, adjustable resistor chains, called *voltage dividers*, were used to limit the amount of stabilized power supplies required for the operation of the spectrometer. When two power supplies are connected to the ends of a resistor chain with potentials of the same polarity, it is necessary to add a high Ohm resistor in parallel to the ground (*load resistor*), in order to avoid charge buildup.

Potential	Hex (electrons) [V]	DLD (ions) [V]
Detector mesh	-300	-450
MCP front	-100	-2350
MCP back	+1800*	-450*
MCP holder	+2000*	-250*
Anode Signal/ (Ref.)	+2100 (+50)*	-150 (+50)*
Anode holder	+2250	0 (ground)

**Table 5.3:** Typical operation voltages for both delay-line detectors recording electrons and ions with a homogeneous electric field of  $\sim 4$  V/cm across the spectrometer. The voltage of the spectrometer is kept at a negative potential in order to repel stray electrons outside of the spectrometer. (\*) Values are only estimated due to the use of a voltage divider.

### 5.3.3 Spectrometer Resolution

The resolution of the measured momenta is a result of the convolution of the measurement uncertainty of the detectors, the electric field of the spectrometer, the uncertainty of the target position, as well as the momentum uncertainty introduced by the finite temperature of the gas target. Depending on the transition, the energy uncertainty of the photons given by the natural width of the harmonics can also be imprinted on the observed momenta. The resolution of a specific experiment will therefore depend on the target and the spectrometer field chosen for a particular experiment. Typical values for the detector resolution can be found at [132].

Figure 5.8 shows the momenta and the ion energy recorded from single ionization of oxygen molecules with multiple harmonics. In the top panel, the momentum in the  $z$ -direction is plotted versus the transverse momentum,  $p_{xy} = \sqrt{p_x^2 + p_y^2}$ . The  $z$ -direction is equivalent to the TOF-axis,  $y$  is the direction of the gas jet, and  $x$  is the propagation direction of the photon beam.

Very sharp features are visible for momenta along the  $z$ -direction that correspond to the dissociation of metastable vibrational states in the excited  $O_2^+$  molecule. The sharp structure washes out perpendicular to the  $z$ -axis. The bottom panel shows the corresponding energy of the  $O_2^+$  ions in a cone around the  $z$ -axis. A multi-gauss fit of the vibrational progression yields a full width at half maximum (FWHM) of 45 meV at an ion energy of 779 meV. A comparison with the natural bandwidth obtained from high-resolution electron spectroscopy [14] yields an energy resolution of 43 meV along the  $z$ -direction.

The measurement indicates that the highest overall resolution is achieved along the TOF-axis. This can be explained from the individual contributions of target uncertainty and temperature that vary in every directions. The target uncertainty is defined by the focal size which is shown in Table 5.2. The smallest focus is obtained in the  $z$ -direction while the target extension in the  $x$ -direction is about 100 times larger due to the Rayleigh range. As discussed in Section 5.1, the target temperature is much lower in the  $x$  and  $z$  directions, where the jet is skimmed, than in the jet propagation direction,  $y$ . Thus, only the  $z$ -direction features a combination of low target uncertainty and low temperature that results in the ultra high resolution observed in this measurement.

## 5.4 Beam Alignment and Control of the Infrared beam

One disadvantage of the geometry used in this setup consists in the obstruction of the direct beam path out of the chamber by the back-focusing mirror. Therefore, two mirrors were installed for guiding the beam through a viewport below the focusing mirror. Figure 5.9 shows a side view of the beam path. One mirror is attached directly below the back-focusing mirror at a  $45^\circ$  angle. It is screwed to the same breadboard base, hence it shares the full adjustability of the back-focusing mirror. A large silicon wafer serves as the second mirror to direct the laser beam through a DN CF100 viewport. The UV grade sapphire window transmits the fundamental as well as the 3<sup>rd</sup> harmonic. A standard commercial digital camera in combination with a tele-zoom lens is used to image the infrared beam.

The alignment of the beam is performed using a cross that is scratched into the surface of the  $45^\circ$  mirror as a reference point. During the alignment, a quarter-wave plate in the compressor chamber is used to slightly rotate the laser polarization axis. The two silicon mirrors used for suppression of the infrared beam have a low reflectivity for s-polarization only. Any added polarization perpendicular to the rotation axis of the mirror is strongly reflected. The amount of infrared beam delivered to the end-station can

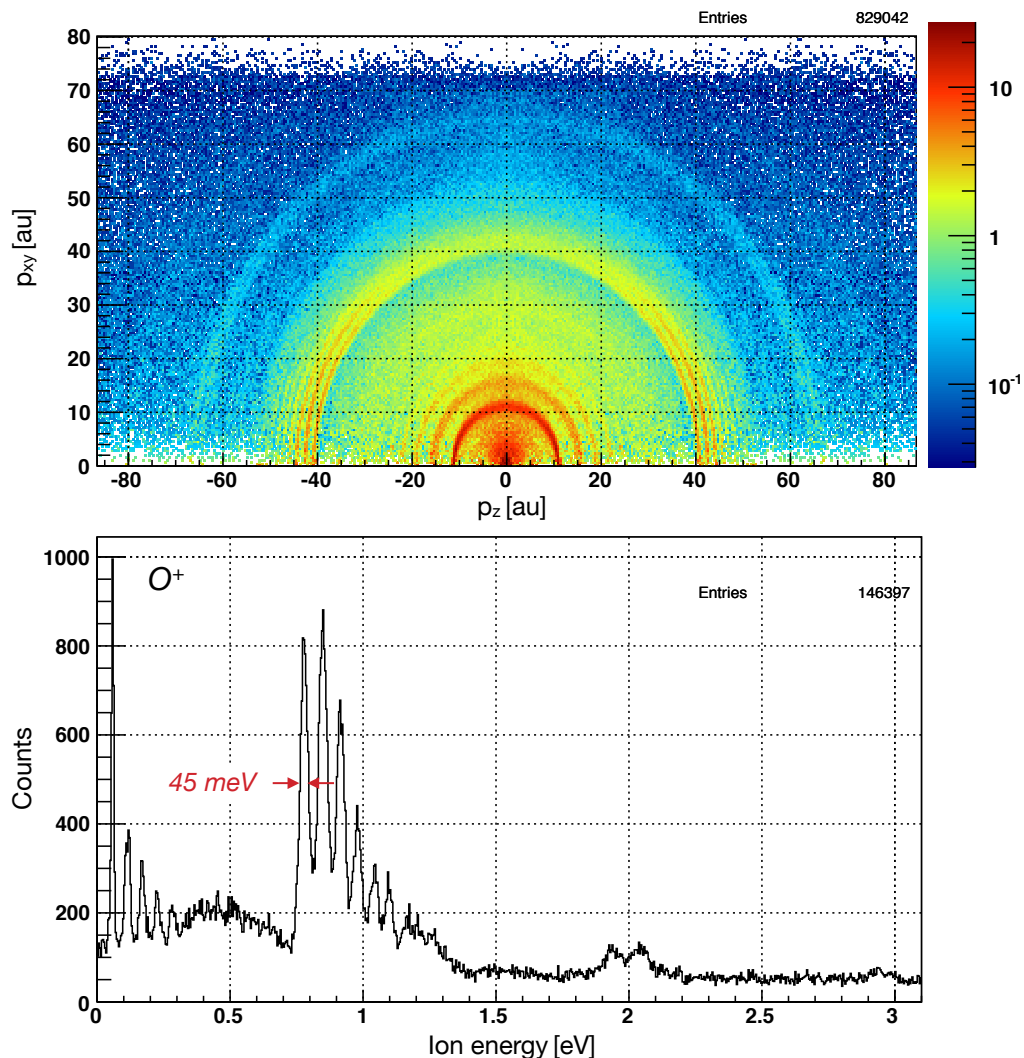


**Figure 5.8:**  $O^+$  ion momenta and corresponding energies from the single ionization of oxygen molecules using a range of high harmonics. **(Top)** Momentum in the z-direction (TOF direction),  $p_z$ , versus perpendicular momentum,  $p_{xy} = \sqrt{p_x^2 + p_y^2}$ . **(Bottom)** Corresponding ion energy spectrum. At 0.779 eV, a width of 45 meV is measured corresponding to a width of 43 meV caused by the instrument (20.3 V/cm extraction field).

therefore be controlled nearly continuously by rotating the motor controlled wave plate, and is quantified using the photo-diodes in the beam line.

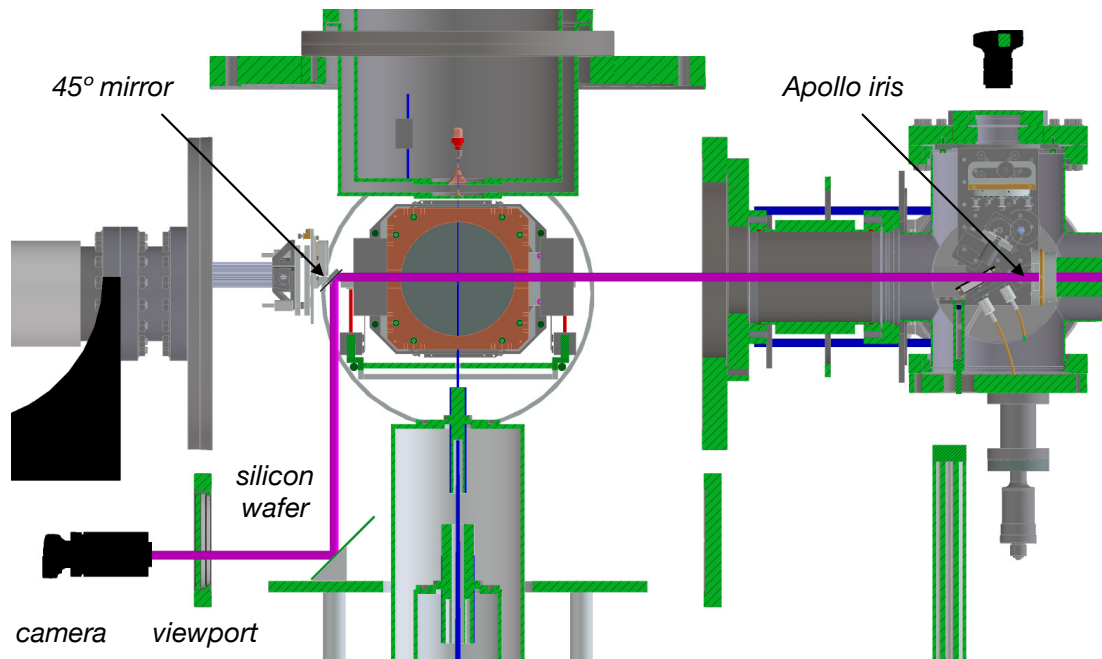


**Figure 5.9:** Side view of the beam path in the MISTERS end-station showing the mirror system used to image the direct beam.

## 5.5 Vacuum System

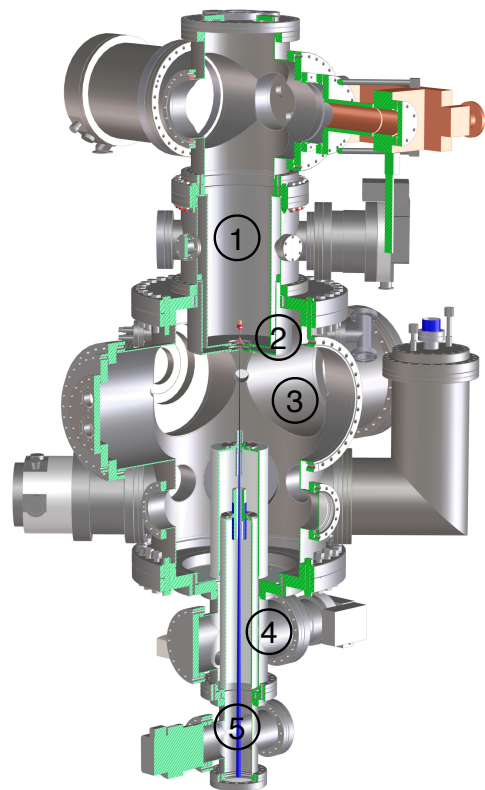
The MISTERS vacuum chamber is designed for operation at ultra-high vacuum levels. The vacuum vessel is made of a special steel with low magnetic activation (316-LN ESR) that is heated to high temperature to reduce the amount of trapped hydrogen. Great care was taken during cleaning and handling of all parts in order to avoid any hydrocarbon contamination of the in-vacuum surfaces. Only materials with low outgassing rates were used inside the chamber including aluminum, stainless steel, copper, PEEK, Kapton and low quantities of other metals. All flanges use Con-Flat type knife edges sealed with copper gaskets or wire seals. For testing, viton o-rings were used that allow to reach a pressure of  $8 \times 10^{-9}$  mbar. After bake-out at a temperature of  $\sim 150^\circ$  celsius, an ultimate pressure of  $5 \times 10^{-11}$  mbar was measured using a hot filament ionization gauge (Leybold extractor gauge).

The different reservoirs of the MISTERS chamber are pumped using a variety of turbomolecular pumps (TMPs) as well as one titanium sublimation cryo-panel in the target chamber. Figure 5.10 shows a cross section of the different sections of the vacuum chamber. The backing pressure for the gas jet is provided by a large scroll pump (Varian TriScroll 600), and the second stage by a smaller scroll pump. In order to achieve the compression ratio required for maintaining a vacuum level below  $10^{-9}$  mbar, the forelines of the TMPs in the target chamber as well as in the beam dump sections are connected to the inlet of a 80 l/s TMP. The backing pressure for this pump is provided by a two-stage piston pump (Pfeiffer Xtra-dry) that can be operated in interval mode to extend the maintenance

intervals and to reduce vibrations. Bypass lines allow to connect the different vacuum sections in order to prevent damage to the skimmers during pump-down and venting.

*N<sub>2</sub> jet at 50 psi (3.4 bar)*

- |   |  |
|---|--|
| ① | <b>Jet source</b><br>$7 \times 10^{-4}$ mbar               |
| ② | <b>Jet 2<sup>nd</sup> stage</b><br>$3 \times 10^{-6}$ mbar |
| ③ | <b>Target chamber</b><br>$8 \times 10^{-9}$ mbar           |
| ④ | <b>Jet dump 1</b><br>$5 \times 10^{-9}$ mbar               |
| ⑤ | <b>Jet dump 2</b><br>$4 \times 10^{-8}$ mbar               |



TMP 2000 l/s

2x TMP 420 l/s

2x TMP 1000 l/s  
TSP (2000 l/s)\*

210 l/s TMP

210 l/s TMP

**Figure 5.10:** Schematic of the vacuum system. Typical system pressures are shown for the different sections at a driving pressure of 50 psi for an unbaked system. When the water background is removed by baking of the chamber, the pressure in the target chamber is limited by the flow of residual jet gas to  $2 \times 10^{-10}$  mbar for a skimmer size of  $\varnothing = 0.5$  mm.

## 5.6 HHG Intensity Measurement

As described in Section 3.3, High Harmonic Generation is a non-linear conversion process that depends strongly on the laser intensity. Small changes in the beam mode induced by pointing instability or fluctuations in the amplification process in the multi-pass amplifier can cause strong intensity fluctuations between laser shots. In measurements where only a small amount of laser shots is recorded for each delay-stage position, those random intensity fluctuations can cause a change in event rate observed in the measurement that is not a result of the process to be studied. Therefore, an additional tool was designed that allowed for measurements of the relative intensity of the harmonics beam simultaneously with the spectrometer data on a per shot basis.

The device consists of a copper plate ( $\sim 5$  by 10 cm) which is connected via an electrical feedthrough to several electronics modules. The plate is mounted to a rotational feedthrough in the XUV-Spectrometer chamber upstream of the spectrometer and is illuminated by the diverging beam reflected off the back-focusing mirror. Photons with an energy larger than the work function of copper (4.7 eV), i.e. above the 5<sup>th</sup> harmonic, will photoionize the

material. As a result, the harmonics beam creates a small current between the plate and a power supply connected to it. The charge is amplified and converted into a DC voltage between 0 - 10 V. Due to the low repetition rate (pulse separation time of 20 ms), the current can be read out for every shot individually.

A custom analog pulse height to time converter, built by Lothar Schmidt, IKF Frankfurt, is used to record the flux for every event stored in the TDC (see Section 5.3.2). The device is based on the comparison of the input pulse with a pulse generated by a ramp generator. At the beginning of the pulse it delivers a standard NIM pulse as the start signal and sends a stop pulse when the pulse height of the generated pulse reaches the pulse height of the input pulse. The difference of start and stop is a linear function of the pulse height. Figure 5.11 shows the intensity distribution recorded with the TDC for all shots of an experiment.

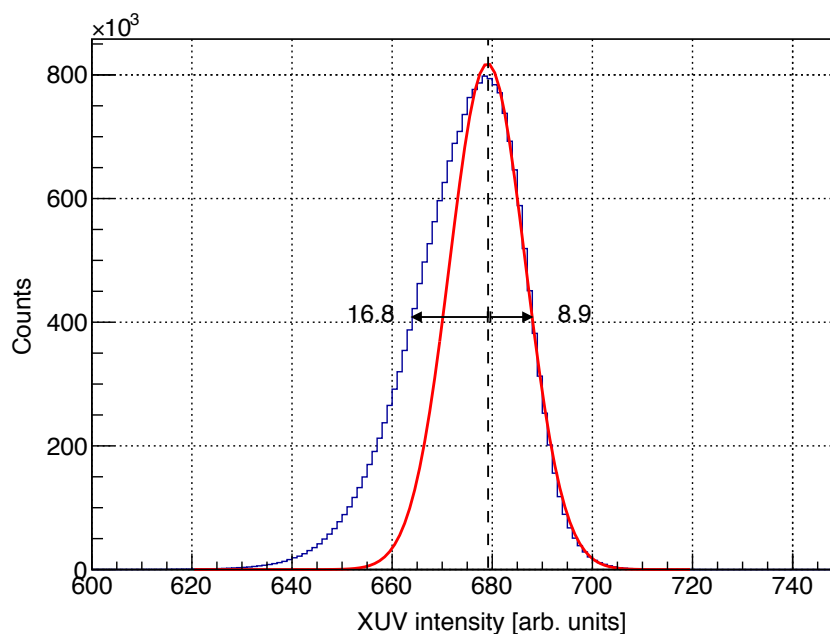


**Figure 5.11:** Intensity distribution of the high harmonics beam recorded indirectly by converting the current generated by the photons on a copper plate. The distribution is asymmetric limited on the high intensity side by the maximal laser power of the infrared beam.

It should be noted that a sampling of the pulse using an analog to digital converter (ADC) should give better results. At the time of the experiments, only a prototype of such a device was available and the integration of an analogue device that feeds a signal into a single TDC channel was more straightforward.

## 5.7 Data Analysis

The time-to-digital converter records the raw detector time signals with respect to a trigger channel. This channel was fed with the signal of a photodiode in the regenerative amplifier of the laser system. The correct time of each channel with respect to the photoionization is then obtained by subtracting the trigger time from the recorded timing signal of every channel. The time-of-flight and the anode positions are obtained from the signals as described in Section 5.3.

As the classical equations of motion of the ions and electrons in the electric field of the spectrometer are well known, the initial momenta of electrons and ions can be reconstructed from the position and time information. This assumes a correct assignment of the mass of the ions. The identification of the ion mass to charge ratio can be obtained from the time-of-flight spectrum. As the TOF depends on the ratio of mass  $M$  and charge  $q$  of the ion as  $\sqrt{M/q}$ , the ions can be assigned a specific TOF at a given electric field strength. For a homogeneous field of strength  $E$  accelerated over a length  $s$ , the time-of-flight is given by

$$t_{ion} = \sqrt{\frac{2s m}{E q}}. \quad \text{TOF in a homogeneous field} \quad (5.14)$$

In order to get more accurate results, the acceleration field in front of the ion detector has to be taken into account modifying the TOF calculation.

Figure 5.12 shows a typical TOF spectrum recorded from ionization of argon gas with the 11<sup>th</sup>, 13<sup>th</sup>, and 15<sup>th</sup> harmonics. The use of a back-focusing mirror complicates the TOF distribution as ions can be created from the un-focused incoming beam as well as from the focused beam. The small offset between the target and the incoming beam is visible by different TOF values from the different starting positions of the ionization. In the argon TOF distribution shown here, the ions created in the jet arrive after the ions that are created a few millimeters closer to the detector. When ions are imaged on the opposite detector, one would expect the target ions to arrive earlier. However, ions created further away from the detector acquire more energy from the field and might catch up or even pass ions created closer to the detector when a drift field is used.

The post processing of the recorded lmf data files was performed using the lmf2root program package written in C++ including modules developed by Markus Schöffler, Till Jahnke, and Achim Czasch. The calibration and processing of the data, as well as the equations for calculation of the electron and ion momenta were performed according to standard procedures for COLTRIMS detectors and can be found in a variety of published works ( e.g. see [178, 68]).

### 5.7.1 Operation at High Count Rates

As the absorption probability of a photon at usual gas jet densities is very low, common ion hit rates in COLTRIMS experiments at a synchrotron are on the order of 1 in 1000 shots, i.e. much smaller than 1. At synchrotron repetition rates of few MHz, the detectors have no problem handling the flux of a few thousand ions per second, and only one to few ions can be observed per shot. The conditions at the present high flux laser source are very different.

A synchrotron delivers about  $10^{13}$  photons/sec. At a MHz repetition rate this corresponds to  $\sim 10^7$  photons per shot. If a monochromator is used the flux is reduced by around two orders of magnitude. The High Harmonics beamline delivers around  $10^{10}$  photons/shot, about 1000 times more photons in every single laser shot while the total flux of this harmonics source is about one order of magnitude lower due to the low repetition rate of 50 Hz. The high photon rate and the corresponding high ionization rate creates new challenges that are discussed in the following.

As multiple particles hit the detector in a very small time interval, the detector signal can easily saturate the amplifier. This causes a depletion of charge in the amplifier that reduces the baseline for subsequent hits. The effect can pertain for hundreds of microseconds effectively blinding the detector for events arriving in this time interval. This has been observed in hits from scattered photons, as well as in the ion signal from strong ionization channels. The problem can be addressed by preventing the amplification of pulses above

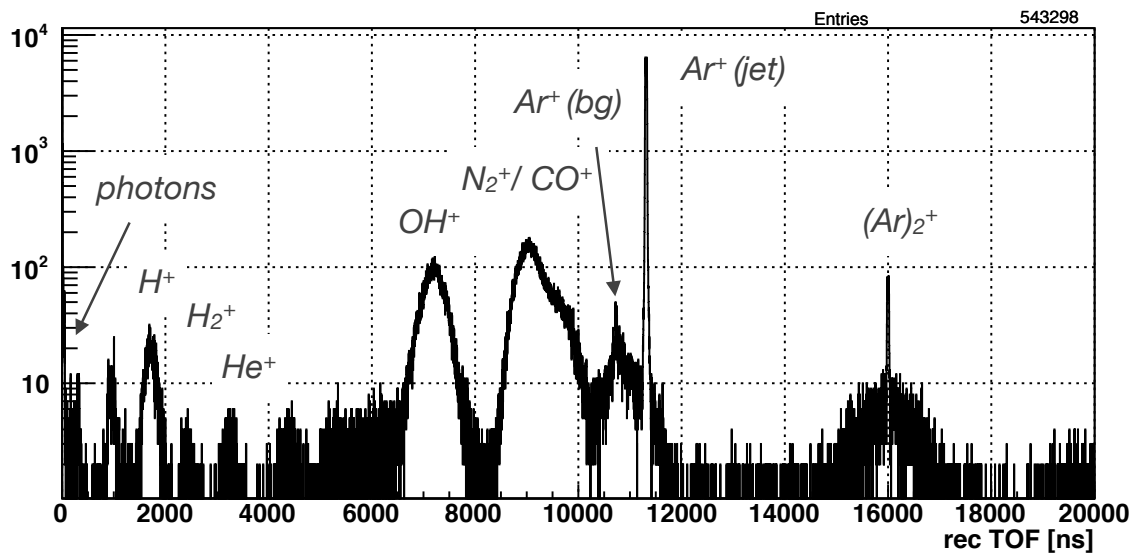


**Figure 5.12:** Ion time-of-flight spectrum recorded on the DLD detector by ionization of an argon gas jet at 6.2 bar using the filtered 11<sup>th</sup>, 13<sup>th</sup>, and 15<sup>th</sup> harmonic. The strongest and very sharp peaks corresponds to Ar<sup>+</sup> ions created in the gas jet. The smaller and broader peak at shorter TOF is made from Ar<sup>+</sup> ions that were ionized by the direct unfocused beam. It is shifted to shorter times as the incoming beam enters the spectrometer a few mm closer to the DLD detector side. The peak at 16  $\mu$ s corresponds to Argon dimers that are created at the nozzle. As the chamber was not baked out for this measurement and sealed with large viton o-rings, a strong background from dissociation of water and N<sub>2</sub> is present.

a certain raw pulse height. At the time of writing, updated fast amplifiers are being developed that do not show such charge depletion effects. In practice, the ion hit rate was usually sufficiently reduced after insertion of all filters and mirrors or problems could be avoided by adjusting the spectrometer field to move the ions affected out of the temporal depletion region.

Meanwhile, a signal rate can be problematic even below saturation if the time spread of the ions is small. Hit distributions of tens to hundreds of ions required changes to the usual procedures of online data analysis. Plotting only the first few ions recorded can result in strange or empty online spectra. At excessive hit rates, the position reconstruction of the delay-line anode fails as the detector processing program, *Cobold PC*, cannot find matching signal pairs any more. The limit for successful reconstruction is given by the amount of pulses on the anode at any given time. As a rule of thumb, this corresponds to about two pulses per maximal signal runtime,  $t_{run}$ , on the anode layers .

$$\boxed{N_{hit} = \frac{2}{t_{run}}} \quad \text{Multi-hit limit} \quad (5.15)$$

This limit can be difficult to find, because the displayed hit rate usually includes all recorded ions, while the instant hit rate might be strongly varying over the entire time-of-flight spectrum.

For extremely high hit rates, the reconstruction of the detector positions can become prohibitively expensive in terms of computation time. For a number of  $N$  recorded signals from a single anode layer, the amount of combinations that the program has to check is  $N!$ . This scaling is quite dramatic as the following example illustrates:  $N = 3$  results in 6 combinations, while  $N = 10$  generates already  $\sim 3.6 \cdot 10^6$  combinations. Therefore, a program feature was introduced, labelled *Hellfire Mode*, that handles even extremely high hit rates that do not appear feasible using normal data processing. In Hellfire mode, one predefines a region-of-interest  $t_a \pm \Delta t$  for the time-of-flight of the ions that one wishes to record. The acquisition software then discards any TDC channel entries,  $t_{ch[i]}$ , that have a timestamp outside the interval

$$t_a - \Delta t < t_{ch[i]} < t_a + \Delta t + t_{run} \quad \text{Hellfire mode condition} \quad (5.16)$$

Figure 5.13 shows spectra of an example file at high count rates. In this experiment oxygen was ionized using the unfiltered harmonic spectrum. This resulted in count rates up to 50 hits per laser shot. The actual rate was much higher as the TDC was gated to accept only events within a certain window. As the ions were sufficiently spread in time, the reconstruction was successful even at such high hit rate.

If one wishes to record ions in coincidence, the recording rate needs to stay below the coincidence limit of one reaction per shot. This does not correspond to the total ion rate but rather to the rate of “good events”, in the sense of the events of interest, which needs to be kept at one per shot. However, great care is to be taken that these events can be identified unambiguously in the post processing process, such as by energy or momentum conservation considerations. Otherwise, misidentified ions will enter the data as false coincidences.

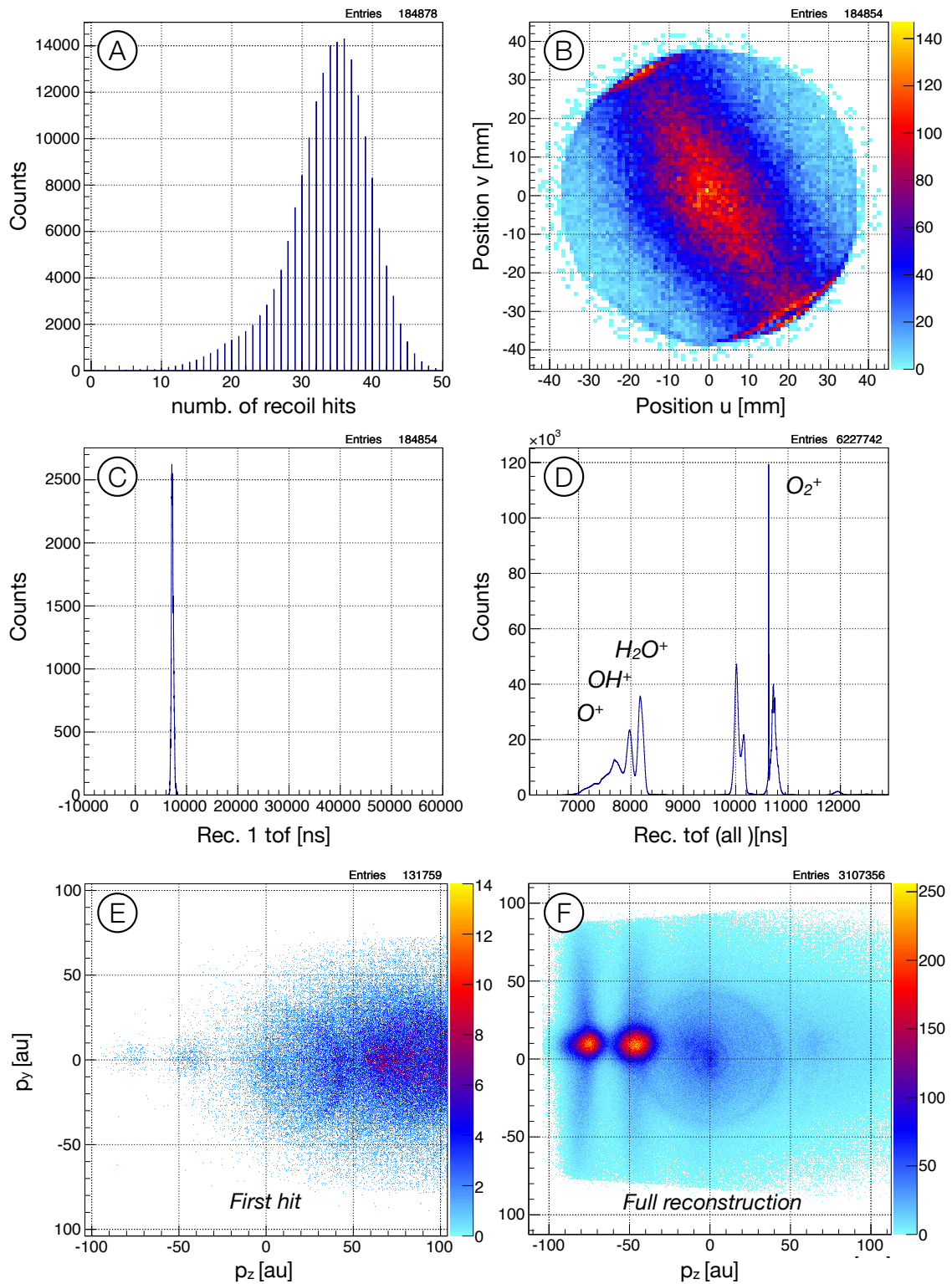


**Figure 5.13:** Ion spectra measured from ionization of oxygen using the unfiltered harmonics spectrum. Ion TOFs below  $6 \mu\text{s}$  were rejected from the TDC. (A) Number of hits that could be reconstructed from the detector signals. (B) Position picture of reconstructed hits. (C) Ion time-of-flight spectrum from the first hit. (D) TOF spectrum of all hits. (E) Ion momenta  $p_z$  vs  $p_y$  from the first hit only. (F) Momenta from full reconstruction of all signals using Hellfire Mode.



## 6 Experimental Results

In this chapter, the first measurements performed with the MISTERS end-station will be reviewed. Much of the initial months of operation were taken up by commissioning of the machine and understanding the capabilities and limitations of the XUV beamline, the XUV-spectrometer and the COLTRIMS end-station in combination with a high-flux harmonic source. Therefore, many of the experiments are taken at non-ideal conditions or some parameters are not well adjusted just yet. The low repetition rate of just 50 Hz prevented from optimizing many of those parameters usually adjusted within minutes at the beginning of a run. In most cases, a better parameter value or a mistake made in the set-up phase of an experiment was only discovered after a full overnight run. Hence, many of the presented results leave room for an improved measurement and could be seen as a starting point for further investigations.

After the first attempts with ethylene as a target, it became very clear that the complexity of the harmonics source required a more precise understanding of the processes started by the ionization using multiple harmonics. Therefore, simpler molecules such as  $\text{H}_2$  and  $\text{O}_2$  were used as initial targets. As it turns out, even hydrogen, the simplest neutral molecule, exhibits a wealth of transitions when illuminated by a few color VUV-XUV and infrared beam that challenge our understanding of the system.

The design of this apparatus was steered towards enabling pump-probe studies using VUV, XUV, and IR pulse pairs. With a pulse length on the order of  $\sim 10 - 20$  fs, the envelope of the harmonics beam is suitable to investigate dynamics of the nuclei. As will be shown in this chapter, the co-propagating infrared beam can be used as a powerful tool for observing molecular dynamics as well as for controlling ionization and dissociation. The phase-locked infrared field can be delayed with respect to the attosecond pulse train allowing to control quantum and optical interference on an attosecond time scale.

### 6.1 Data Analysis Information

#### 6.1.1 Reconstruction of the 3D Momenta

The positions of impact and the time-of-flight of the particles measured on each detector are converted to momentum vectors in 3D by inserting the measured spectrometer geometry and calibrated values for the electric and the magnetic field strength into the well-known equations of motion of particles in the spectrometer. As the mass is not measured directly, the momenta rely on the correct assignment of the time-of-flight to a certain mass/charge ratio. In the case of electrons, the assignment is simple as negative ions that could be attracted to the positively charged detector side are much slower than the light electrons.

A more detailed description of the momentum reconstruction and the calibration process, as well as the equations of motion in the spectrometer can be found in [160], as well as in a number of other thesis works from the group of Reinhard Dörner at the University of Frankfurt (download at [66]) and from the J. R. McDonald Laboratory at Kansas State University [69].

### 6.1.2 Momentum Visualization

The laboratory coordinate system used in the following spectra is shown in Figure 6.1. The laser beam enters the MISTERS spectrometer parallel to the spectrometer plates which corresponds to the x-direction (see also Figure 5.2). The gas jet is oriented in the y-direction. The electrons and ions created in the ionization experiments fly along the z-direction towards the detectors mounted perpendicularly to the time-of-flight direction, the x-y plane. The polarization axis of the harmonic radiation is oriented horizontally along the z-direction. It follows the polarization of the generating fundamental beam whose exact orientation is controlled by a wave plate in the compressor chamber and adjusted to be perpendicular to the rotation axis of the silicon mirror in order to yield minimal reflectivity of the fundamental beam (see Section 4.2). Because of the high suppression of the infrared beam with polarization along the z-direction, the residual infrared light arriving at the MISTERS end-station is oriented along the y-direction, in which the silicon surfaces reflect strongly (see Figure 4.11).

In Figure 6.2, the method of visualizing the 3D momentum distributions is explained. Instead of slicing a 3D distribution along one axis and projecting it onto the perpendicular plane, conical cuts are performed that preserve the available phase space of a given distribution. A simple slice weighs smaller momenta stronger than larger momenta. This is due to the fact that an expanded sphere (larger momenta) occupies more space in all directions, and it will expand beyond of a small section along one direction. This effect is compensated, when the data is plotted within a fixed angle  $\theta_i = p_i/|p|$ , instead of a fixed distance along one axis. The resulting projections give a clearer picture of the three dimensional momentum distributions created from the particle emission.

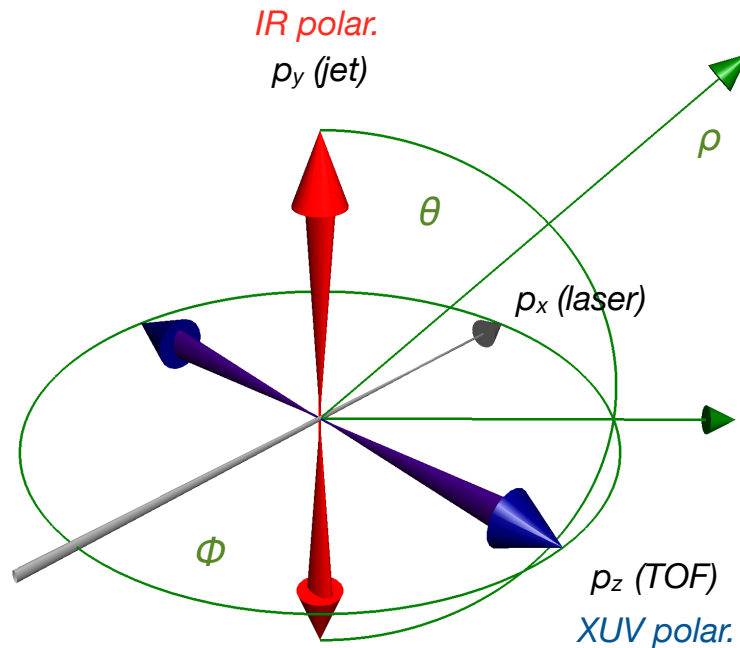


**Figure 6.1:** Schematic of the laboratory coordinate system in the MISTERS momentum imaging setup. The x-axis corresponds to the laser propagation direction, the y-axis to the jet direction, and the z-direction corresponds to the time-of-flight direction of the ions and electrons. The polarization of the high harmonics radiation is oriented along the z-direction, perpendicular to the infrared polarization (y-axis).

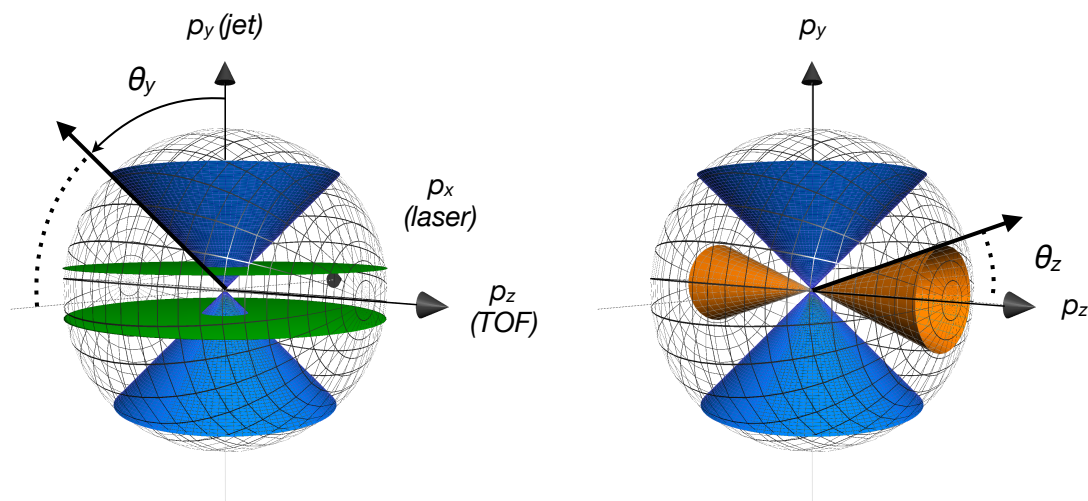


**Figure 6.2:** Visualization of the cuts in the momentum space used for reproducing the measured 3D-momenta in 2D plots. A simple slice is shown in green in the x-z-plane (left picture). In order to correct for the available phase space, 2D plots of the data (e.g. x-z) are created by applying the condition  $|\cos \theta_y| < 0.8$  on the  $\theta$  angle of the remaining axis ( $\theta_y = p_y/|p|$ ). This corresponds to the volume outside the blue cones (indicated by a dotted line). For high resolution spectra ( $\text{O}_2$  measurements), only events along the z-axis, the direction with maximal resolution (see 5.3.3), were selected. The condition  $|\cos \theta_z| > 0.8$  selects events inside a cone along the z-axis, shown in orange on the right.

### 6.1.3 VUV Pulse Sequences

In several measurements, fluoride windows were used in one arm of the pump-probe interferometer to create a VUV-only probe pulse. The interpretation of those spectra can be very difficult, due to the complex pulse structure. As explained in Section 4.1.1, the windows exhibit good transmission in the IR and the VUV spectrum but reject orders above the 5<sup>th</sup> harmonic. Meanwhile, each transmitted color, the infrared, the 3<sup>rd</sup>, and the 5<sup>th</sup> harmonic, acquires a different delay with respect to the pump pulse traveling through vacuum. Figure 6.3 illustrates this pulse scheme.

The delay stage in the Split-Mirror Interferometer can be adjusted to a position where the pulse traveling through vacuum overlaps in time with a specific harmonic in the VUV arm containing the fluoride window. The VUV arm needs to be moved upstream with respect to the overlap position in vacuum. The shortened path length compensates for the slower propagation of the pulses in the window. The remaining two colors precede or come after the XUV pulse but all three colors are still present in the pulse train and could interact with the target. This needs to be considered when discussing possible transitions.

In the data presented here, positive delays always correspond to a probe pulse arriving after the pump pulse unless otherwise specified. The overlap positions for each filter are measured from ion yield measurements (see Section 4.1.1).

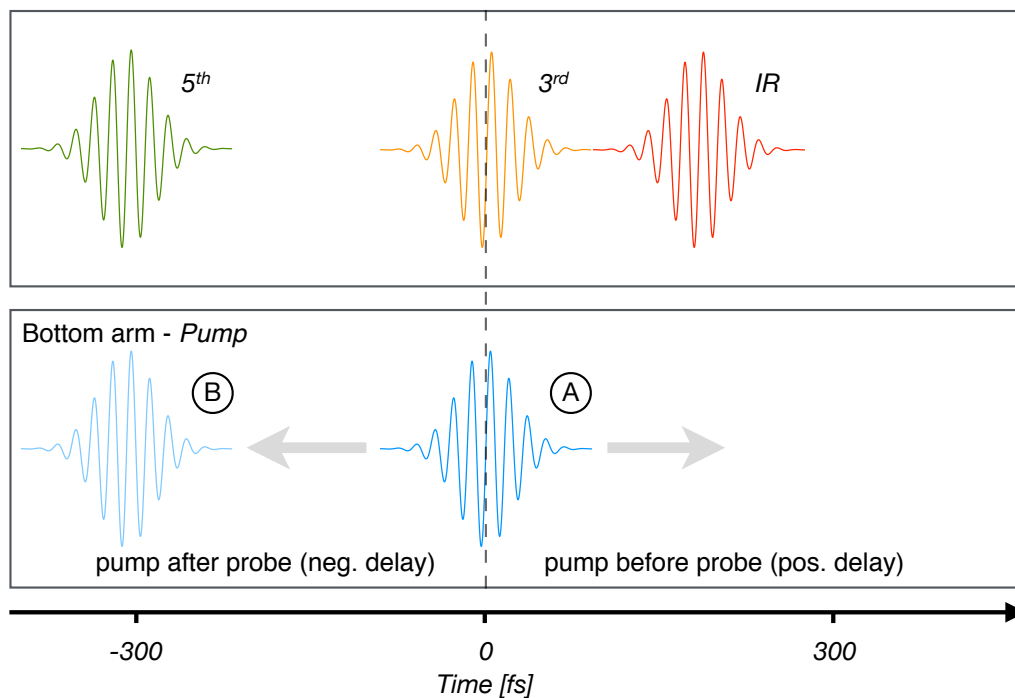


**Figure 6.3:** Schematic of the pulse sequence obtained by covering one arm of the laser beam with a fluoride window (top). As explained in Section 4.1.1, dispersion in the window separates the infrared and the transmitted harmonics, 3<sup>rd</sup> and 5<sup>th</sup>, in time creating a pulse sequence separated by hundreds of femtoseconds. In position (A), the delay stage is adjusted for overlap of the 3<sup>rd</sup> harmonic with the XUV radiation in the probe arm, equivalent to 0 fs delay. At this position, the infrared beam preceded the XUV radiation of the pump arm, and the 5<sup>th</sup> harmonic will arrive later. At delay position (B), around 300 fs, the 5<sup>th</sup> harmonic will overlap in time with the pump pulse while the IR and the 3<sup>rd</sup> harmonic of the probe arm have passed the target before the pump pulse. The outlined pump-probe scheme can be reversed with respect to the top and the bottom arm in the laboratory, when the fluoride window is located in the bottom arm.

## 6.2 Argon Single Ionization

In order to demonstrate the coincidence capabilities of the MISTERS end-station, argon was chosen as a target for its simple electronic structure. A tin filter was inserted into the harmonics beam resulting in a spectrum containing only the 11<sup>th</sup>, 13<sup>th</sup>, and the 15<sup>th</sup> harmonic, corresponding to photon energies of 16.9, 20.0, and 23.0 eV. With an ionization threshold of 15.8 eV, each harmonic singly ionizes the target. The resulting ions were collected on the DLD detector, and the electrons were guided onto the Hexanode detector using a homogeneous electric field of 4.1 V/cm and a magnetic field of 5.6 G.

In Figure 6.4, ion spectra obtained in this experiment are presented. The TOF-spectrum (a) shows sharp peaks for the Ar<sup>+</sup> ion, as well as for singly ionized (Ar)<sub>2</sub><sup>+</sup> dimers formed in the nozzle. The detector picture (b) shows a line along the x-direction corresponding to the ionization of background gas by the unfocused XUV beam. Argon ions created in the laser focus form a sharp dot slightly below the gas line. This shift is mainly caused by the

jet speed. However, due to the back-focusing geometry, there can be an additional offset if the laser focus is not centered in the  $y$ -direction.

The broad round shadow in the top of the image is caused by ions created on the surface of the electron detector that subsequently travelled across the spectrometer. This is a well-known effect that appears in certain spectrometer/ electric field configurations. The channels of the MCP plates have an angle of  $8^\circ$  with respect to the surface normal. Ions accelerated and ejected in the channel direction would hit the ion detector on the opposite side of the spectrometer with an offset of 53 mm. This estimate neglects the acceleration of the ions along the spectrometer axis which shortens the flight time and thus reduces the offset. Hence, the observed displacement of the detector shadow seems to agree with the expected shift.

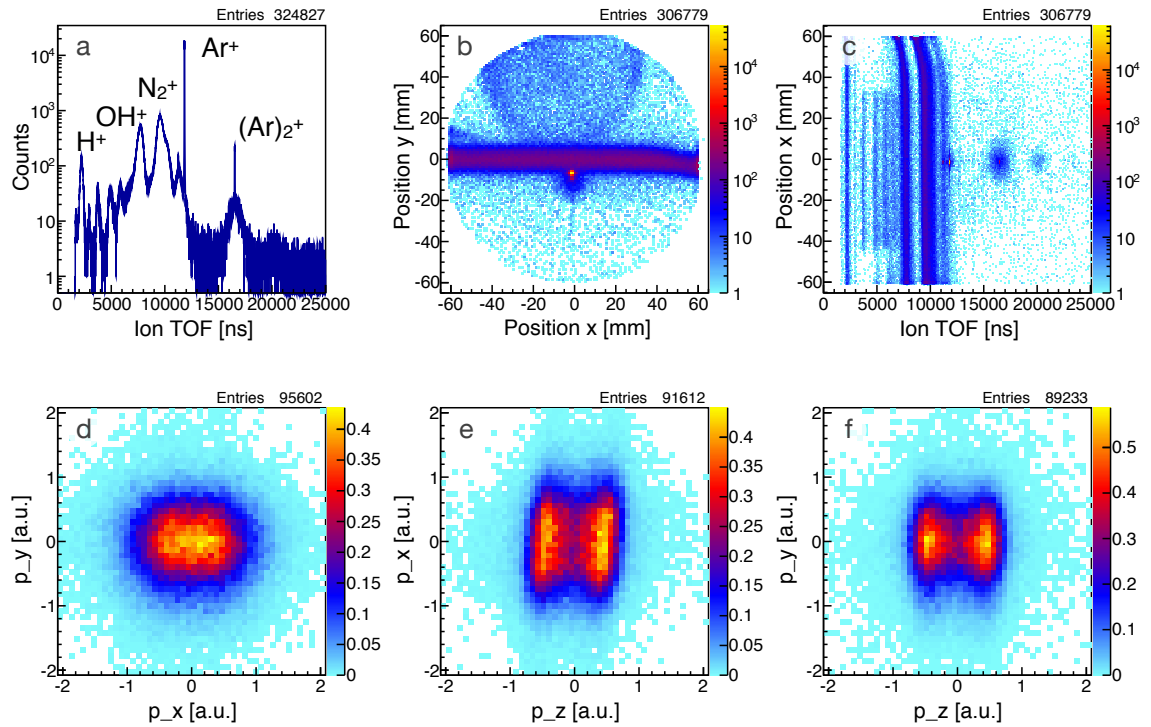


**Figure 6.4:** Ion spectra obtained in the single ionization of argon gas using three harmonics at 16.9, 20, and 23 eV photon energy. (a) Time-of-flight spectrum, (b) reconstructed ion positions on the DLD detector, (c) TOF-position spectrum in the  $x$ -direction, (d)-(f)  $\text{Ar}^+$  ion momentum slices (normalized intensity).

In spectrum (c), the position in  $x$ -direction is plotted with respect to the ion time-of-flight. The histogram reveals the source of the various fragment ions observed. The gas line visible in the detector picture is split up into the individual ion masses ( $\text{OH}^+$ ,  $\text{H}_2\text{O}^+$ ). The bend in the lines at large positive  $x$ -position is a result of field distortion caused by a metal plate mounted to the back-focusing mirror. This plate was left disconnected by accident and its position close to the spectrometer allowed the electric field lines to penetrate the spectrometer through the opening made for the laser beam. The argon ions from the monomer, dimer and even the trimer can be easily distinguished as round spots along the central axis at  $x \simeq 0$  of the spectrum.

The momentum plots in the bottom row show a distribution mainly along the  $z$ -direction which corresponds to the polarization axis of the XUV beam. The distribution is broadened in the  $x$ -direction due to the larger target uncertainty from the long Raleigh-length (see

Section 5.2). The slightly slanted distribution, away from the light direction,  $x$ , in spectrum (e) is a result of the tilt of the focusing mirror required for the back-focused XUV beam to hit the gas jet, which has an offset of  $\sim 3$  mm to the incoming laser beam.

The electron spectra are presented in Figure 6.5. The raw TOF spectrum in (a) shows a sharp peak at 542 fs caused by scattered photons hitting the detector. The electrons created in the argon ionization form a multi peak structure on top of a wide background. The raw detector position picture in (b) shows a hot-spot in the top left likely caused by secondary electrons that are created by scattered photons inside the spectrometer. Significant efforts were made to reduce this background after this experiment but the exact source of the photon-scattering was not confirmed at the time of writing and requires more tests. The electrons produced in the experiment are only faintly visible in this picture but become much clearer in (e) below, after applying a filter condition described in the following.

Ions and electrons created in the ionization of one atom need to have opposite momenta as the momentum of the photon can usually be neglected at sub keV photon energies. For coincident events, the sum of the electron and the ion momenta forms a distribution around zero in each spatial direction. Its width is defined by the momentum resolution.

$$|p_{elec} + p_{ion}| < a \quad \text{Coincidence Filter} \quad (6.1)$$

In Figure (c), the sum of the electron and the ion momenta is plotted versus its difference in the z-direction. Using the filter condition 6.1, coincident events are clearly extracted from the background in the plots (d) - (i).

The so called *Fish spectrum* in (d) shows the TOF versus the position of the electrons in the x-direction. The gyration nodes of the magnetic field are visible around 60 and 120 ns. The second node is close to the electron distribution indicating that the combination of electric and magnetic field was not adjusted optimally. This can be attributed to the slow feedback of the experimental parameters in the online spectra inherent to the low laser repetition rate of just 50 Hz. The filtered position picture in (e) displays clearly the electron distributions from argon ionization.

The lowest electronic state of the  $\text{Ar}^+$  ion is split due to spin-orbit coupling into the  $^2\text{P}_{1/2}$  state at 15.76 eV and the  $^2\text{P}_{3/2}$  state at 15.93 eV ionization energy. As the bandwidth ( $\sim 300$  meV) of the harmonics exceeds the splitting, three single peaks are observed in the electron spectrum (f), corresponding to  $E_{el} = Ip - E_{\gamma q}$  for each harmonic energy present in the beam. The electron momenta in the plots (g) - (i) display the preferential ionization along the z-direction corresponding to the polarization axis of the XUV beam.

### 6.3 Selection Rules for Optical Transitions

In any electronic transition, not only the energy and the momentum but also the total values of the angular momentum, the spin, and the parity of all particles involved in the transition need to be conserved. The ground state of the hydrogen atom is identified as  $X^1\Sigma_g^+$ . The capital letter  $X$  stands for the ground state while excited states are ordered with letters increasing with the minimal energy of the state. Capital letters stand for singlet, lower case letters for triplet states according to the number of spin orientations of the state. In the case of linear molecules, the projection of the angular momentum onto the molecular axis,  $\Lambda$ , is indicated by a capital greek letter with  $\Lambda = 0, 1, 2 \rightarrow \Sigma, \Pi, \Delta$ . The lower case letters  $g$  or  $u$ , gerade or ungerade, indicate the symmetry of a parity inversion. The signs  $^+$  or  $^-$  represent the symmetry of the molecular state under reflection through a plane containing the internuclear axis.

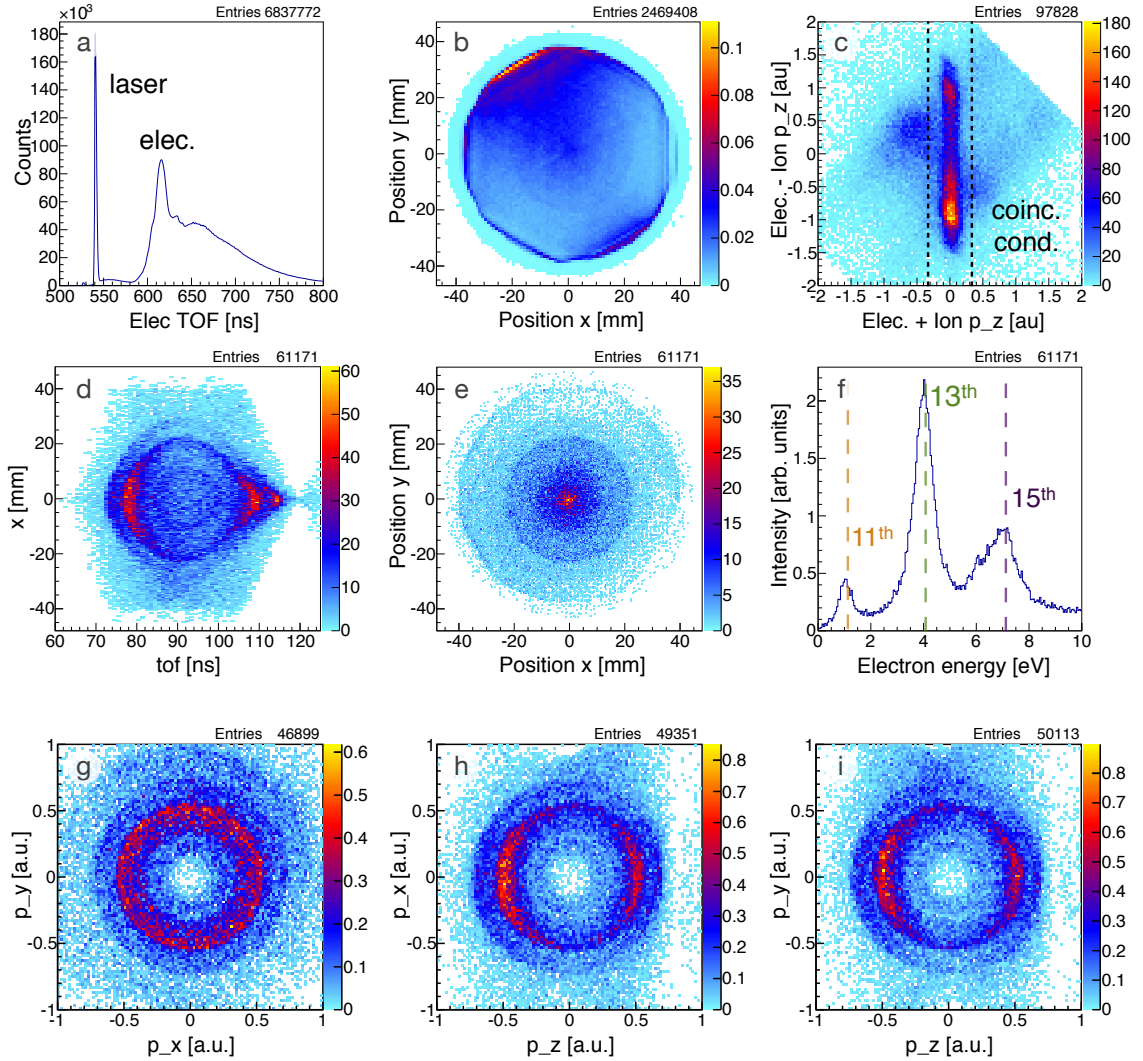


**Figure 6.5:** Electron spectra obtained in an electron-ion coincident measurement of argon single ionization using the photon energies 16.9, 20, and 23 eV corresponding to the harmonic orders 11, 13, and 15 of 808 nm. (a) Raw electron TOF spectrum, (b) raw hexanode detector picture, (c) sum vs difference of electron and ion momenta. The dashed line indicates the filter condition for selecting electron-ion coincidence events along the vertical line at  $|p_{z,elec} + p_{z,ion}| = 0$ . This filter was applied to the following spectra (d) - (i). (d) Electron TOF vs x-position (*fish spectrum*), (e) coincidence filtered electron position, (f) electron energy spectrum. The vertical dashed lines indicate the energy corresponding to ionization from a specific harmonic. (g) - (i) Electron momenta in all three spatial directions (cuts as illustrated in Figure 6.2).

A transition induced by photons of low energy ( $< 1$  keV) follows the dipole selection rules. In short, the multiplicity remains unchanged ( $\Delta s = 0$ ) but the parity of the electronic wavefunction changes ( $g \rightarrow u$  or vice-versa). The symmetry of the electronic state changes according to the angular momentum projection of the photon. A transition with  $\Delta\Lambda = 0$  is called a parallel transition, while  $\Delta\Lambda = 1$  is referred to as a perpendicular transition. If the molecule is ionized, these selection rules are lifted, as the electron can balance out the angular momentum and symmetry. A detailed description of molecular transitions and selection rules can be found in [64]. For hydrogen molecules in the ground state the optically allowed transitions have  $\Sigma_u$  or  $\Pi_u$  symmetry [45]. In transitions involving several photons the parity operation is multiplied such that no change of parity is obtained in a 2-photon transition.

## 6.4 Hydrogen Molecules

The hydrogen molecule is the simplest neutral molecule consisting of only two protons and two electrons. On the road towards studying complex molecular systems, a thorough understanding of the processes initiated by a sequence of pulses ranging from the infrared to the XUV spectrum in the simplest linear molecule is required before pump-probe schemes can be used to study molecules that have a more complicated electronic or nuclear structure. Due to the high lying electronic states and relatively fast nuclear wave-packet dynamics, the neutrally excited hydrogen molecule could not be studied using standard spectroscopy tools used in femtochemistry. For example, the 7<sup>th</sup> and the 9<sup>th</sup> harmonics of the fundamental IR laser field, and pulse durations on the order of tens of femtoseconds are necessary to induce and probe the dynamics of a neutrally excited H<sub>2</sub> molecule. Such pulses could not be generated before using frequency doubling crystals, which is the most common method for up-converting the fundamental frequency of femtosecond laser pulses in femtochemistry. Attosecond physics, on the other hand, has been focused mostly on the use of XUV pulses, either in the form of attosecond pulse trains or isolated attosecond pulses. Therefore, the dynamics of a neutrally excited H<sub>2</sub> molecule had been out of reach for both attosecond physics and femtosecond chemistry. Thus, H<sub>2</sub> is an ideal test bed for developing and testing VUV attosecond tools that would allow us to breach the gap between attosecond physics and femtosecond chemistry. Only recently it was shown that below-the-threshold harmonics (i.e. the 7<sup>th</sup> and the 9<sup>th</sup> harmonics) can be used to coherently control the dynamics of neutrally excited H<sub>2</sub> molecules on an attosecond time scale [129]. In this chapter, we show how coherent, multi-color VUV pulses can be used to measure the dynamics of a neutrally excited molecule. We used 3D ion momentum imaging to unravel complex dissociative dynamics and show that understanding such dynamics, even in the simple excited H<sub>2</sub> molecule, still represents a major theoretical and experimental challenge.

### 6.4.1 Experimental Parameters

The electronic structures of H<sub>2</sub> and D<sub>2</sub> are identical. Therefore, deuterium is often used as a target instead of hydrogen due to the different mass which allows to differentiate it easily from a hydrogen background produced in other processes. However, the vibrational levels of hydrogen and deuterium can differ by a few 100 meV which can result in different ion spectra. The lowest vibrational level  $v = 0$  of the ground state is slightly higher for hydrogen molecules (0.275 eV) than for deuterium molecules (0.197 eV) [45]. As the *potential energy curves (PEC)*, shown here, are set to zero for the  $v = 0$  level of the ground state, the equivalent curves for deuterium molecules would be shifted up by 0.079 eV.

In Section 2.4 an overview of the H<sub>2</sub> experiments was presented, in which combinations of XUV, VUV, and IR pulses were used to ionize and dissociate hydrogen molecules. In these experiments the neutral and the lowest cation states of hydrogen were populated. The experiments presented in this work were focused on the states and dynamics of the neutral hydrogen molecule. The ionization thresholds for H<sub>2</sub> and D<sub>2</sub> are 15.4 eV, such that the 11<sup>th</sup> or a higher harmonic is required to ionize the molecule.

In order to obtain an efficient population of the neutral states and to suppress the direct ionization of the molecule, the overall high harmonic flux is sacrificed for a better spectral sensitivity of the harmonics. This was achieved by using a gas filter cell as well as by adjusting the gas pressure in the HHG cell. A thin indium foil would be the ideal choice as a filter material to only select the 9<sup>th</sup> harmonic order, but the filters tried in this lab had extremely low transmission due to the immediate oxidization of the material rendering them unusable for experiments.

A calculation of the relative intensity of the harmonics with the current XUV-spectrometer is quite challenging. Various parameters, including the wavelength dependent reflectivity of the focusing mirror itself play a role. This is discussed in Section 4.3.2. The spectral manipulation of the gas filter cell and the pressure is briefly discussed here. A detailed description can be found in the Sections 4.1.3 and 3.4.3.

The use of an argon gas filter that strongly suppresses harmonic orders above the 9<sup>th</sup> harmonic. A detailed look at the high harmonics spectrum after applying the argon gas filter is shown in Figure 4.8 in the Chapter 4. While the 9<sup>th</sup> harmonic is reduced, the orders 11- 17 seem to have almost entirely disappeared suggesting a suppression of more than 90 %. Meanwhile, the 2<sup>nd</sup> order diffraction peaks of the 19<sup>th</sup> harmonic and above are visible with increasing strength. This agrees with the significant contribution of ionization to the  $X1s\sigma_g$  ground state of the H<sub>2</sub><sup>+</sup> ion pointing towards ionization from orders larger than the 9<sup>th</sup> harmonic or multicolor ionization by a combination of VUV and IR photons.

In some measurements, a high gas pressure was chosen in order to further reduce the contribution of higher orders. Increasing the pressure of the harmonic generation cell to 10 Torr reduces the yield of the harmonic orders 11 - 23 by about 62 %. Meanwhile the yield of the 9<sup>th</sup> harmonic is only reduced by about 35-40 % which results in an increased ratio of the 9<sup>th</sup> to higher orders by about 55 to 80 %.

In short, in the experiments at high cell pressure, the neutral states are predominantly excited while in experiments at lower cell pressure high harmonic orders increase the contribution of direct ionization. This is reflected by varying contributions of the multiple transitions observed in the different experiments.

The temporal width of the IR pulses is 45 fs, and the width of the 9<sup>th</sup> harmonic is significantly shorter, on the order of 15 fs.

The infrared beam intensity was controlled in all hydrogen and deuterium experiments by rotating the polarization axis for highest absorption from the silicon mirrors (see Section 4.2). The observed residual infrared light in the y-direction, where the reflectivity should be extinguished, is likely a result of some amount of ellipticity in the fundamental beam. The intensity of the infrared beam is expected to be on the order of  $I \approx 3 \times 10^{11}$  W/cm<sup>2</sup>, based on an estimated suppression factor of  $\sim 2 \times 10^{-5}$  obtained from two silicon mirror reflections.

The calibration of the momenta measured here relies on the correct assignment of the vibrational levels for the transitions observed. Further comparison with theoretical calculations is needed in order to reliably assign the observed structures to specific vibrational levels. This could result in a shift of the absolute energy on the order of 100 meV in the spectra shown here.

The hydrogen molecules emerging from the supersonic expansion are expected to be in the vibrational ground state as the target temperature is smaller than the vibrational spacing of  $D_2$  ( $\sim 300$  meV) and  $H_2$  ( $\sim 500$  meV) [45]. No events from double ionization were observed as a result of the lack of harmonics with sufficient energy to reach the double ionization threshold.

Several transitions were observed in the measurements including a previously unpublished one. Some transitions overlap in the fragment energy and cannot be distinguished without a coincident measurement of photoelectrons and ions. The ratio of the different transitions seems to be changing strongly with the intensity of the various harmonic orders and possibly with the intensity of the infrared field. Therefore each individual transitions identified is discussed by means of a specific data set where it is most prominent.

### 6.4.2 Wave Packet Dynamics in Neutral $H_2$

The vibrational motion in hydrogen and deuterium molecular ions has been measured in experiments using a combination of XUV and infrared light [75] and XUV/VUV pulse pairs [50]. Ranitovic *et al.* [129] reported an experiment where the coupling of different neutral states to ionic states was controlled in order to manipulate the pathway to dissociation. With this experimental setup, the motion of a nuclear wave-packet in neutral hydrogen molecules was observed by measuring the ionization yield of  $H_2^+$  ions.

Figure 6.6 (a) shows the relevant potential energy curves of the  $H_2^+$  ion. The  $H_2^+$  ionization potential energy changes as the neutral  $H_2$  molecule is taken from the equilibrium position. The 9<sup>th</sup> harmonic order in the pump pulse creates a broad nuclear wave-packet in the neutral  $B^1\Sigma_u^+$  that can be ionized by multi-photon absorption.

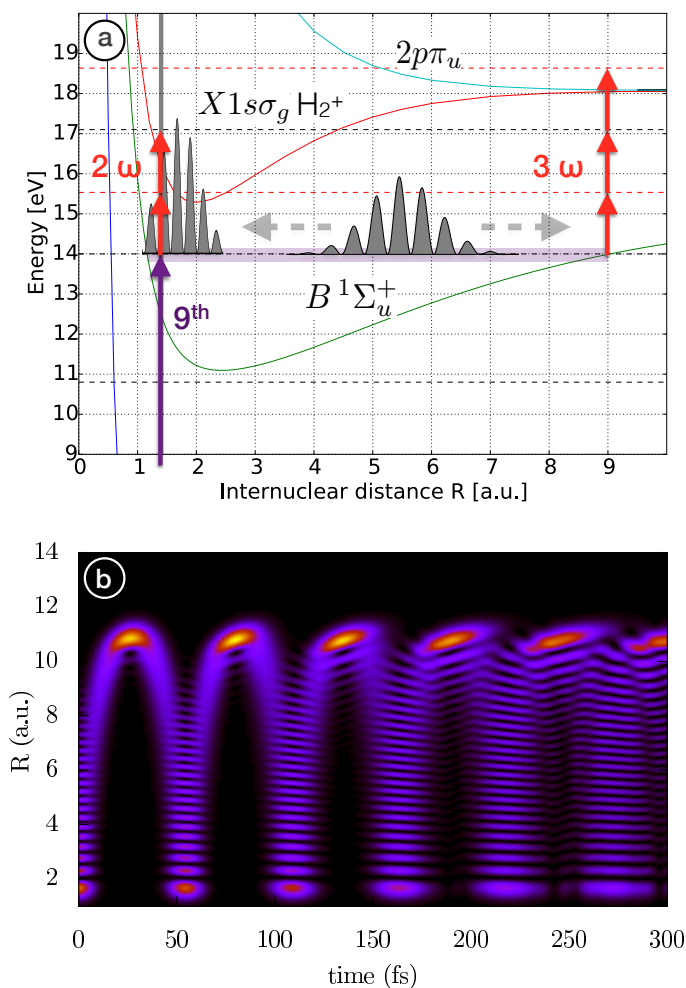
In Figure (b), the simulated motion of such a wave-packet created by the 9<sup>th</sup> harmonic order of 790 nm, corresponding to an energy of 14.1 eV, is shown. While the wavelength of the fundamental IR pulse in the experiment measures 808 nm before entering the gas cell, krypton was used at a high pressure of 10 T for high harmonic generation. At this pressure, the wavelength is blue-shifted by about 0.2 eV for the 9<sup>th</sup> harmonic raising the photon energy to about 14.1 eV. The contribution to ionization from orders above the single ionization threshold ( $> 9^{\text{th}}$  harmonic) was reduced due to the high pressure and an argon gas filter cell.

Figure 6.7 shows the measured  $H_2^+$  ion yield as a function of pump-probe delay. Below, the Fourier transform of the measurement is plotted. An oscillation of the yield at a period of 71 fs is observed with a high yield near 0 delay. Using the 9<sup>th</sup> harmonic order corresponding to 14.1 eV energy with a bandwidth of approximately 300 meV, high vibrational levels around  $v = 21$  were populated launching a nuclear wave-packet in the broad potential well of the  $B^1\Sigma_u^+$  state. The excited hydrogen molecules were ionized through one or two-photon absorption to the  $X^1s\sigma_g$  ground state of the  $H_2^+$  ion. Near the potential minimum of the  $X^1s\sigma_g$  state, one or two IR photons are sufficient to ionize the excited hydrogen molecule. As the wave-packet evolves to larger internuclear distances, the energy gap to the  $X^1s\sigma_g$  ion state increases requiring three infrared photons for ionization. This results in a maximal yield at overlap of the XUV pump pulse and the IR probe pulse and a decrease in ionization probability as the molecule stretches.

### 6.4.3 XUV-IR Transitions

To unravel the channels through which the  $H_2^+$  molecule is ionized and dissociated, we investigate the full 3D momenta of the  $H_2$  ions.

In Figure 6.8, the two main channels induced by the infrared beam causing dissociative ionization of hydrogen molecules are shown. The first channel, labeled (A), is created



**Figure 6.6:** (a) Potential energy curves of the  $\text{H}_2^+$  ion. The 9<sup>th</sup> harmonic order creates a nuclear wave-packet in the  $B^1\Sigma_u^+$  that is coupled to the  $X 1s\sigma_g$  ground state of the  $\text{H}_2^+$  ion by multi-photon ionization. (b) Simulated probability density of a nuclear wave-packet in the  $B^1\Sigma_u^+$  state excited by a VUV pulse at 14.1 eV energy as a function of internuclear distance and time. Simulation by Xiao-Min Tong [169].

from the dissociation of the  $\text{H}_2^+$  ground state, while the second channel (B) is a result of the ionization of neutrally excited  $\text{H}_2^+$  molecules. The transitions are indicated in the potential energy curves shown on the top right. The signatures of the dissociation channels (A) and (B) are shown in the momentum distributions of two different measurements on the bottom. Circles are drawn to help identify the feature in the energy spectra of each feature shown on the top left. Schematics are drawn in the center of the figure to help understand the 3D momentum distributions created by each channel in the measurement. Further ionization/dissociation channels will be discussed later on in the chapter.

### Bond Softening

In Figure 6.8 (A) (bottom left), the momentum distribution of  $\text{H}^+$  ions in the x-y plane is presented. In this experiment, the cell pressure was optimized for high flux, such that a significant amount of high orders was present. The plot shows distinct rings with high intensity in the y-direction (laser polarization) at energies around 0.2 and 0.4 eV. They are

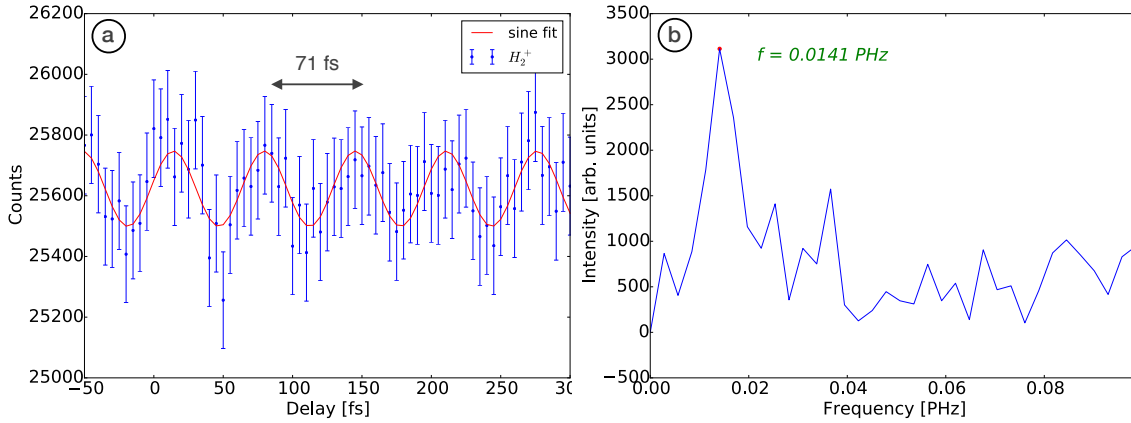
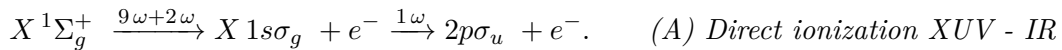


**Figure 6.7:** (a)  $H_2^+$  ion signal as a function of pump-probe delay of harmonics mainly consisting of 14.1 eV photo with contributions from higher orders. (b) Fourier transform of the delay spectrum.

formed by ion distributions that correspond to spheres of discrete energy in the momentum space with a preferential emission along the y-direction. The 3D shape is depicted in the rendering above. It should be emphasized at this point that conical cuts were used in all momentum plots as described in Section 6.1.2. Similar to slices through the center of the momentum sphere, these cuts eliminate contributions of momenta pointing along the third axis. For example, a projection on the x-y plane shows ions that were emitted in this plane with small momentum component in the z-direction.

The peaks around 0.2 and 0.4 eV have been observed previously in measurements with  $H_2$  and  $D_2$  [75, 50, 25]. They are generally attributed to the ionization of the  $H_2^+$  ground state,  $X 1s\sigma_g$ , by an XUV photon (11<sup>th</sup> harmonic order or higher) followed by a parallel transition to the dissociative  $2p\sigma_u$  state by an infrared photon [50].



Kelkensberg *et al.* [75] as well as Cao *et al.* [25] discuss the effect of the *bond softening* mechanism on the transitions (see [125] for a review). In this picture the electronic states of the molecule are dressed by the infrared field lowering the barrier of dissociation by an amount depending on the intensity. A resonant coupling of the bound  $X 1s\sigma_g$  state to the dissociative  $2p\sigma_u$  state by a single IR photon yields proton energies of 0.4 - 0.7 eV. The proton energies corresponding to resonant ionization of the various neutral states is shown in Figure A.3 in the appendix.

### Sequential Ionization

In the experiment shown in Figure 6.8 (B) (bottom right), mainly neutral states were excited by strongly suppressing harmonics above the 9<sup>th</sup> order. A contribution of the direct ionization channel, described above, at 0.2 and 0.4 eV is visible, but the proton distribution exhibits an additional feature along the y-direction that extends from zero continuously to energies around 0.15 eV. A faint isotropic ring visible at a similar energy will be discussed later in Section 6.4.5.

Dissociation process (B) is illustrated with red vertical arrows in the PEC shown on the top right. As demonstrated in Section 6.4.2, a wave-packet is created in the neutral

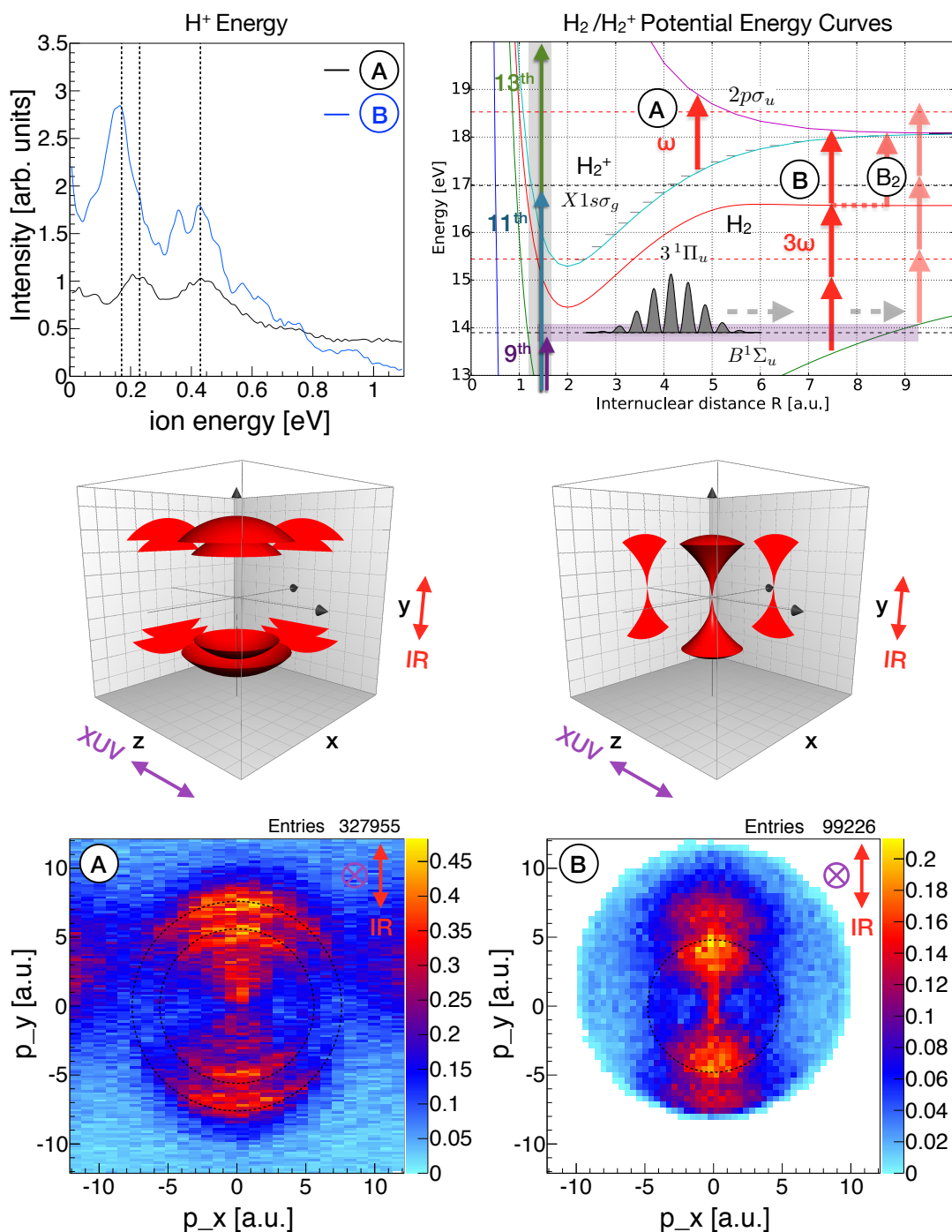
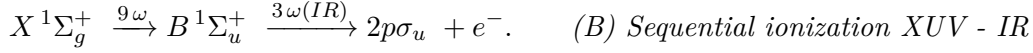
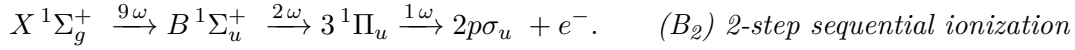


**Figure 6.8:** Dissociative ionization channels in  $\text{H}_2$  caused by XUV-IR absorption. **Top left:** Ion energy distributions for the  $\text{H}^+$  momenta shown on the bottom. **Top right:**  $\text{H}_2$  potential energy curves [113]. **Center:** 3D sketch of the momentum distributions for channel A (left) and channel B (right). **Bottom:**  $\text{H}^+$  momenta in the x-y plane. (A) Strong direct ionization ( $\text{HH} > 9^{\text{th}}$ , File 3). (B) Strong sequential ionization ( $\text{HH} < 11^{\text{th}}$ , File 2). For experiment details see Figure A.4 and Table A.2 in the appendix.

$B^1\Sigma_u^+$  state by absorption of the 9<sup>th</sup> harmonic. As the nuclear wave-packet evolves on the  $B^1\Sigma_u^+$  state, the resonant ionization to the  $2p\sigma_u$  state with three IR photons becomes energetically accessible around an internuclear distance of 7 a.u producing protons with a kinetic energy around 0.1 eV. At larger internuclear distances, the ionization leads to smaller kinetic energies with the photoelectron carrying the energy difference between the  $3\omega$  transition from the  $B^1\Sigma_u^+$  state to the electronic potential of the  $2p\sigma_u$  state.



However, an additional dissociation channel could contribute to the observed signal as it would yield a very similar ion distribution and onset energy as the process described above. Starting from the wave-packet in the  $B^1\Sigma_u^+$  state, the  $3^1\Pi_u$  state can be resonantly excited by two IR photons at an internuclear distance of  $\sim 7$  a.u.. This state fully dissociates and can be continuously ionized to the  $2p\sigma_u$  state by the absorption of a additional infrared photon.



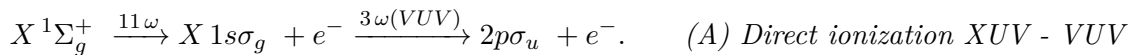
#### 6.4.4 XUV-VUV Transitions

The 3<sup>rd</sup> as well as the 5<sup>th</sup> harmonic are generated at sufficiently high flux allowing for the subsequent absorption of an XUV pulse as the pump and a VUV pulse as the probe. The features attributed to dissociative ionization in an XUV pump - VUV probe process are presented in Figure 6.9.

In measurement (A), krypton gas at 10 T cell pressure was used for the generation of high harmonics which shows a blueshift of  $\sim 200$  meV (see Section 3.4.3). In measurement (B), argon was used at the same pressure which does cause a significantly lower energy shift due to the higher saturation threshold. Additionally, half of the beam was covered with a MgF<sub>2</sub> window, reducing the overall flux of all harmonics except the 5<sup>th</sup> by a factor of 2. This resulted in a different branching ratio of the various channels and could be a result of the modified intensity distribution of the harmonic orders, as well as a difference in energy of each order. In (A) direct ionization of the  $X^1s\sigma_g$  H<sup>+</sup> ion ground state dominates, whereas the ratio of populated neutral states to ion states is higher in measurement (B).

##### (A) Direct Ionization

The ion momentum distribution in Figure (A) (bottom left), shows a strong ring corresponding to a proton emission along the z-axis (XUV polarization axis) at a fixed energy. This feature is attributed to the ionization to the  $X^1s\sigma_g$  ground state of the H<sub>2</sub><sup>+</sup> ion by harmonic pulses above the 11<sup>th</sup> order (or 9<sup>th</sup> + 2 $\omega$ ) with the subsequent projection to the  $2p\sigma_u$  state by absorption of one photon of the 3<sup>rd</sup> harmonic. A transition from the  $v = 5$  vibrational level produces a proton of approximately 1.5 eV energy. The peak is observed in both (A) and (B) with a sub structure of two peaks that corresponds to the spacing of the vibrational levels in the  $X^1s\sigma_g$  state around  $v = 5$  ( $\sim 200$  meV).



##### (B) Neutral Excitation - Dissociative Ionization

The second process is shown on the right side of the figure. (B) displays a strong dumbbell shape distribution along the z-direction. The same shape is observed along the y-direction

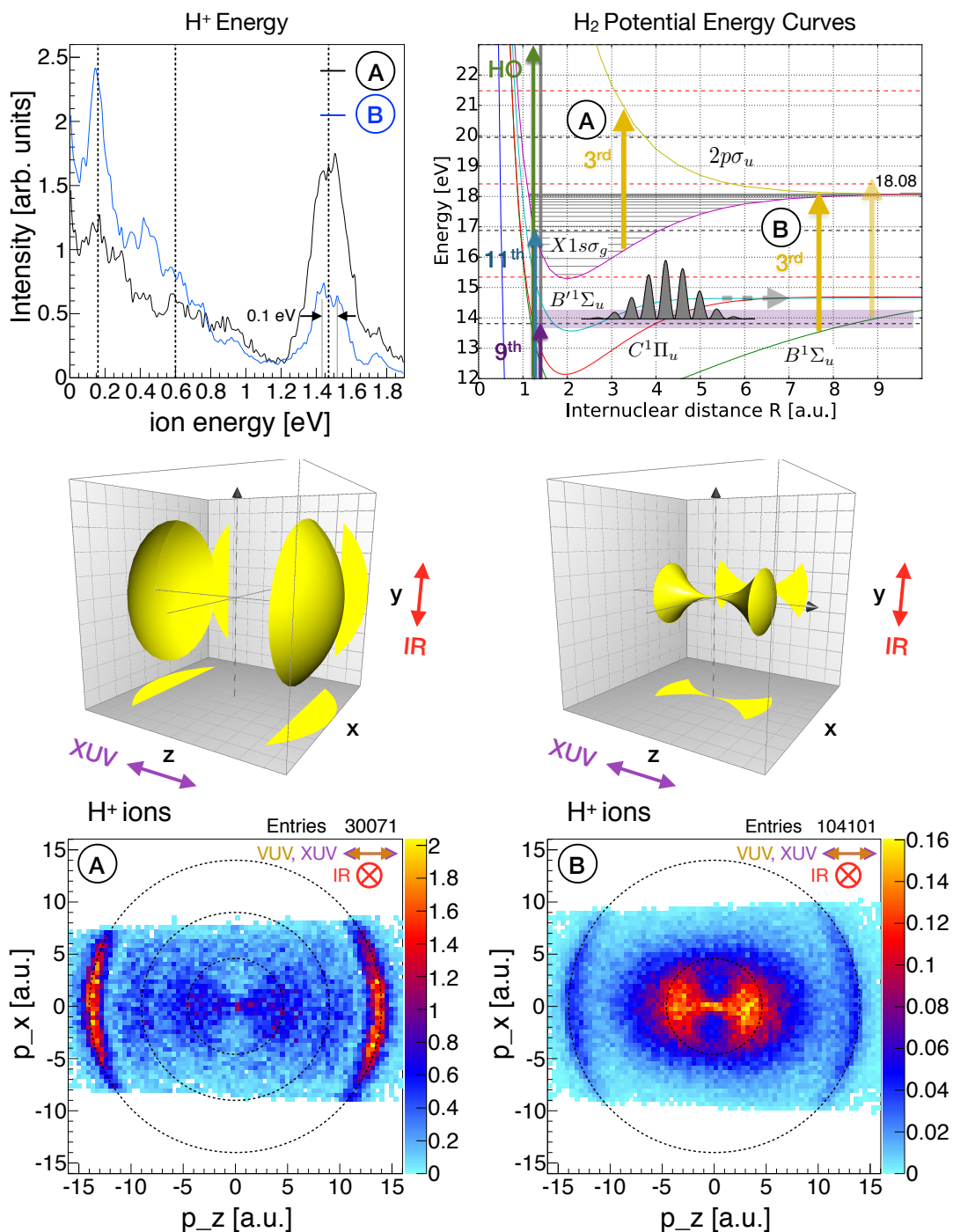


**Figure 6.9:** 2-photon XUV-VUV dissociative ionization channels in H<sub>2</sub>. **Top left:** Ion energy distributions for the H<sup>+</sup> momenta shown on the bottom. **Top right:** H<sub>2</sub> potential energy curves [113]. **Center:** 3D sketch of the momentum distributions for channel A (left) and channel B (right). **Bottom:** H<sup>+</sup> momenta in the z-y plane. **(A)** Strong direct ionization (Krypton, HH <11<sup>th</sup>, File 1). **(B)** Strong sequential ionization (Argon, HH <11<sup>th</sup>, MgF<sub>2</sub> filter in one arm, File 2). For experiment details see Figure A.4 and Table A.2 in the appendix.

shown in Figure 6.8. As discussed there, the distribution is attributed to the sequential process of excitation of the  $B^1\Sigma_u^+$  state (around  $v = 21 - 22$ ) by the 9<sup>th</sup> harmonic followed by dissociative ionization with a single photon of the 3<sup>rd</sup> harmonic, as the neutrally excited molecule stretches.



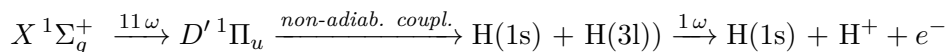
Some additional peaks in the spectrum could correspond to the ionization of the neutral states  $B^1\Sigma_u^+$ ,  $C^1\Pi_u$ , and  $B'^1\Sigma_u^+$  by the resonant absorption of a single photon of the 3<sup>rd</sup> or the 5<sup>th</sup> harmonic. The calculated proton energies for these transitions are indicated in Figure A.3 in the appendix.

### 6.4.5 Predissociation

Some features observed in the measured momenta are more difficult to assign. In Figure 6.10 (a) and (b), a faint ring is visible under the dumbbell shaped distributions along the y and the z-axis already discussed in the previous sections. As the projections to the x-y plane as well as the z-x plane show the same feature, the ring seems to correspond to an isotropic spherical distribution in momentum space as indicated in the rendering (middle row).

In an isotropic distribution, the character of the electronic transition (perpendicular or parallel) is not reflected in the ion emission. This can happen if the electronic state pre-dissociates into two neutral atoms. When the, now separated, hydrogen atoms are ionized by the absorption of a second photon, the distribution of ion fragments is isotropic.

At the energy of the 11<sup>th</sup> harmonic,  $\sim 16.9$  eV, Rydberg states of the  $n p \pi^1\Pi_u$  series can be populated in the Franck-Condon region. Above the  $H(1s) + H(3l)$  dissociation limit the  $^1\Pi_u$  states dissociate through non-adiabatic coupling ( $3p\pi^1\Pi_u$  and  $4f\pi^1\Pi_u$ ) into this limit [55]. The excitation of the neutral  $D'^1\Pi_u$  state at 16.9 eV photon energy followed by pre-dissociation to the  $H(1s) + H(3l)$  at 16.57 eV (indicated by a dotted line in the potential energy curves) would yield a proton energy of  $\sim 0.17$  eV which is close to the observed energy.



This represents one possible channel, but other pre-dissociating states and coupling pathways might be accessible as well.

### 6.4.6 3-Step Dissociative Ionization

Figure 6.11, shows a momentum distribution observed in the dissociative ionization of  $D_2$ . In this experiment,  $D_2$  was illuminated by harmonics generated in argon at 8T. This pressure was above the optimal yield for high orders. In combination with an argon gas filled attenuation cell, the contribution of harmonics above the 9<sup>th</sup> order were attenuated, yielding mostly VUV harmonics below the  $D_2$  ionization threshold.

The momenta in the z-y plane, Figure 6.11 (d) display a surprising x-shaped distribution that corresponds to energies from 0 - 0.1 eV, as indicated in the energy spectrum in (a) (Top left). In Histogram (c), the ion energy is plotted versus the emission angle in the z-y plane. The angular distribution for the energy region corresponding to the central clover-leaf feature is shown in (e) and in (f) as a polar plot. In the three dimensional

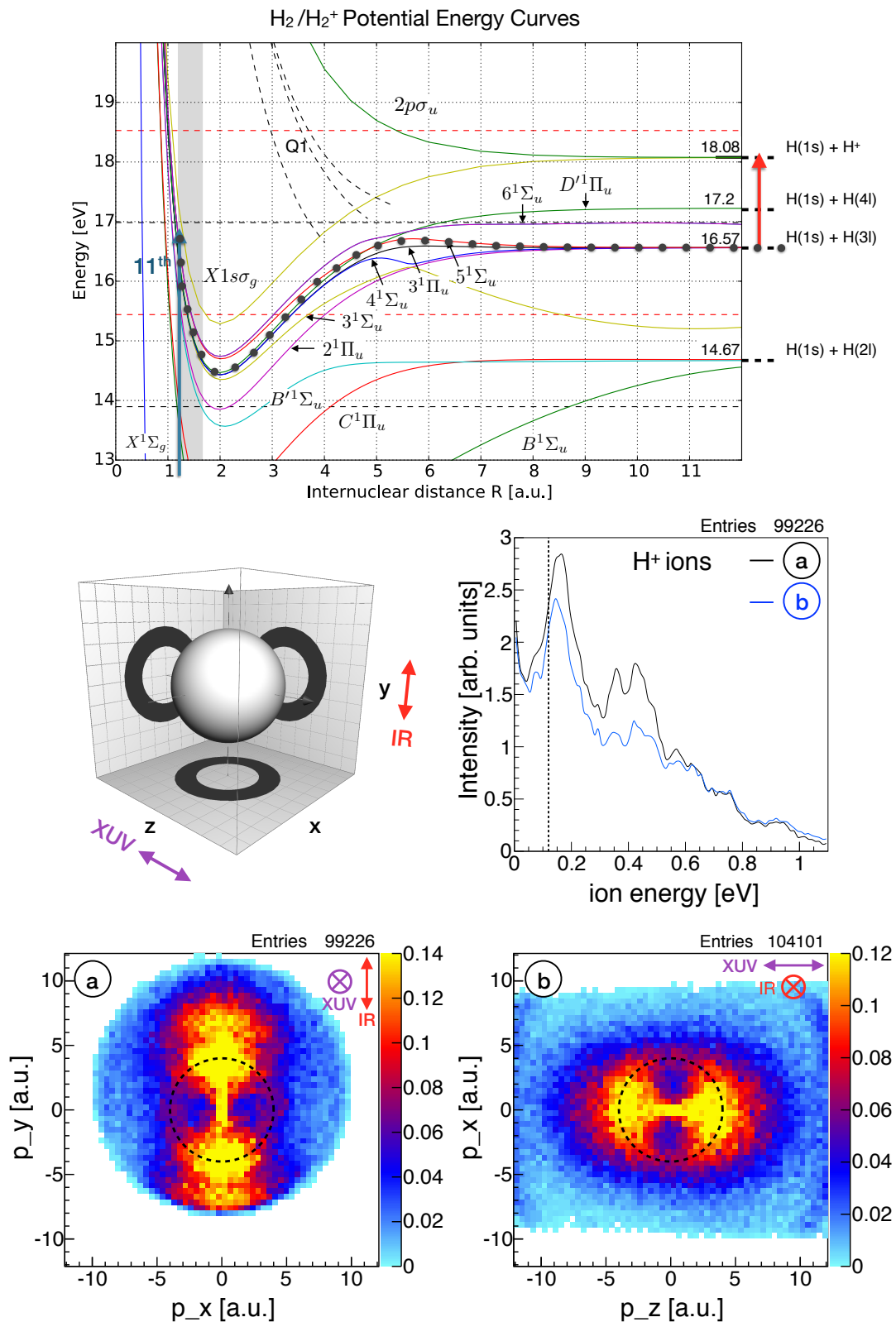


**Figure 6.10:** **Top:** Potential energy curves of optically allowed H<sub>2</sub> states in the relevant energy range and their dissociation limits [113]. **Center:** 3D sketch of the momentum distribution corresponding to predissociation. Ion energy distributions corresponding to the momenta below. **Bottom:** H<sup>+</sup> momenta in the x-y (a) and the z-x plane (b) from sequential ionization (Argon, HH <11<sup>th</sup>, MgF<sub>2</sub> filter in one arm, File 2). For experiment details see Figure A.4 and Table A.2 in the appendix.

momentum space, the structure corresponds to a clover leaf or x-shaped distribution in the z-y plane, as depicted in blue in Figure 6.12 (a).

A very similar feature was observed in an experiment by Wei Cao [24] using the 9<sup>th</sup> harmonic order as the pump pulse followed by a probe pulse of the infrared field. They used a monochromator which rejected the contributions of all other harmonics to the spectrum. He indicates the possible mixing of  $\Sigma$  and  $\Pi$  states as the origin of the x-shaped structure but did not conclude on the origin of the observed distribution.

Such an ion emission pattern is surprising as it cannot result from of a dipole-transition initiated by a linearly polarized electro-magnetic field. The angular distribution of the photo-fragments in the dissociation induced by a 1-photon dipole transition is given by [126]:

$$I(\theta_\epsilon) = 1 + \frac{\beta}{2} (3 \cos^2 \theta_\epsilon - 1), \quad \textit{Photo-fragment angular distribution} \quad (6.2)$$

where  $\theta_\epsilon$  is the angle of the fragment with respect to the polarization axis and  $\beta$  is the *spatial anisotropy parameter* which takes the values  $\beta_{\parallel} = 2$  for a *parallel transition* ( $\Delta\Omega = 0$ , e.g.  $\Sigma \rightarrow \Sigma$ ) and  $\beta_{\perp} = -1$  for a *perpendicular transition* ( $\Delta\Omega = 1$ , e.g.  $\Sigma \rightarrow \Pi$ ). The resulting angular distributions have a dumbbell shape oriented along (parallel transition) or perpendicular to the polarization direction (perpendicular transition). In the transition to a neutral state the distribution corresponds to the highest probability of excitation to the particular state.

In this experimental setup, the polarization axis of the VUV/XUV beam and the IR beam are cross polarized to each other as indicated by the small pictograms in the upper hand corners of Figures 6.11 (d) and (f). Therefore, the orientation of the molecular axis in the laboratory frame for transitions of each pulse are rotated by 90° with respect to each other such that the general form of the angular distribution can be written as  $I(\theta_{IR}) = I(\theta_{XUV} - \frac{\pi}{2})$ .

If two transitions occur sequentially, the probability distribution for the total transition is written as the product of the distributions of each transition.

$$I(\theta_{\epsilon tot}) = I(\theta_{\epsilon 1}) I(\theta_{\epsilon 2}) \quad \textit{2-photon transition distribution} \quad (6.3)$$

The probability for the excitation of a neutral state in a 2-step process by a parallel transition of the XUV and a parallel transition of two IR photons can be obtained from inserting Equation 6.2 into Equation 6.3. This yields the following distribution of the molecular axis with respect to the polarization of the XUV field.

$$I(\theta_\epsilon) = I_{\parallel}(\theta_{XUV}) I_{\parallel}(\theta_{2IR}) \quad (6.4)$$

$$= A \cos^2 \theta_\epsilon \sin^4 \theta_\epsilon \quad (6.5)$$

where A is a constant. This distribution is drawn as a gray dashed line in Figure (f). It creates an x-shape corresponding to the overlap of molecular orientations for the dumbbell shaped distributions of the individual transitions of the cross-polarized XUV and IR fields. The angular distribution observed in the experiment shows more intensity along one diagonal axis than the other. This can be reproduced by taking into account a slight rotation ( $<3^\circ$ ) of the polarization axes with respect to each other, drawn as a dashed green line.

As the observed feature has the highest intensity at very small ion energies below 0.1 eV, the ionization of the neutral excited state must occur at internuclear distances beyond 7 a.u. Therefore, the proposed mechanism is a 3-step sequential process consisting of two sequential excitation steps in parallel transition by the XUV and the IR field followed

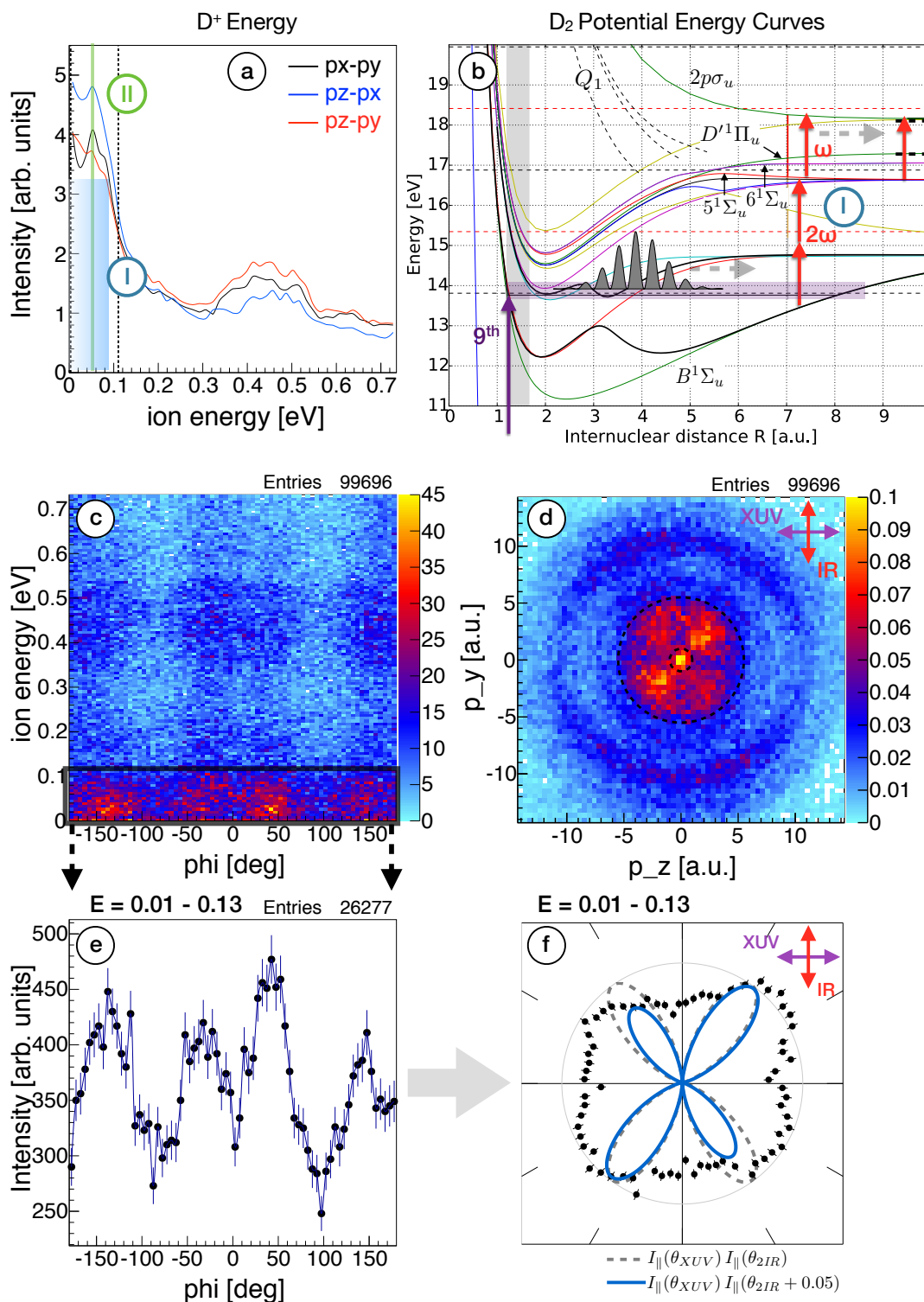
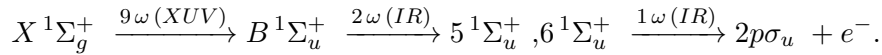


**Figure 6.11:** Dissociative ionization in  $D_2$  using HH $<11^{\text{th}}$  + IR (Ar HHG at 8T, Ar gas filter). (a)  $D^+$  Ion energy distribution for cuts in all three spatial planes. (b) Potential energy curves of  $D_2$ . (c) Ion energy vs emission angle in the z-y plane. (d)  $D^+$  momenta in the z-y plane. (e) Angular distribution as a histogram and in a polar plot (f) for ion energies 0.01 - 0.13 eV corresponding to the central x-shaped feature circled in (d). The angular distribution of two purely parallel transitions initiated by the XUV and the IR field is shown as a gray dashed line. The result of a slight rotation of the polarization axes with respect to each other is plotted as a blue solid line.

by the ionization and subsequent dissociation of the molecule in the third step by the absorption of an additional IR photon.



This dissociation process is indicated with label **(I)** in the potential energy curves in Figure 6.11. The nuclear wave-packet created in the  $B \ ^1\Sigma_u^+$  state moves to internuclear distances beyond 7 a.u. where a resonant transition to the  $5 \ ^1\Sigma_u^+$  and  $6 \ ^1\Sigma_u^+$  states can occur via the absorption of two IR photons. The large bandwidth of the wave-packet allows a coherent excitation of both states. An additional photon can ionize both states continuously as the molecule stretches further leading to an energy spectrum extending to zero kinetic energy.

### 6.4.7 Ion Emission Along the Light Propagation Axis

In Figure 6.12 (b) - (d), the momenta in all spatial directions are shown from the same measurement. The 3-step process described above produces a clover leaf structure in the z-y plane, as illustrated in blue in a 3D schematic rendering in Figure (a). This results in dumbbell shaped projections along the y-direction in the x-y plane (b) and along the z-axis in the z-x plane (c). When comparing the momentum distributions in all three spatial dimensions to the ion distribution produced by the 3-step process, the distributions in (b) and (c) show additional intensity at  $\sim 4$  a.u. momentum in the x-direction. This contribution is visualized in green in the 3D rendering. The momenta corresponding to ion emission along the x-direction peak at  $\sim 0.05$  eV energy, identified with a green line labeled **(II)** in the energy spectrum in Figure 6.11 (a).

This contribution is equally surprising, as the x-direction corresponds to the propagation direction of the photon beam where no emission is expected as it is perpendicular to the polarizations of both the XUV and the infrared beam. At the time of writing, no clear identification of this feature can be presented. Such a distribution could result from the population of a  $\Delta$  state but no state that corresponds to the measured energy was found. As an alternative, a perpendicular transition initiated by the simultaneous absorption of XUV and IR photons could require a molecular orientation that is perpendicular to both polarization vectors, a condition that is only fulfilled by ions oriented along the x-axis.

## 6.5 Oxygen Molecules

In the experiments presented in this section, the inherent sub-optical-cycle resolution ( $\sim 170$  as) of the pump-probe delay stage (see Section 4.2) is used to coherently control dissociative ionization processes in oxygen molecules ( $O_2$ ) by means of the attosecond XUV frequency comb and the femtosecond infrared field. First, we spectrally selected the 11<sup>th</sup>, 13<sup>th</sup>, and 15<sup>th</sup> harmonics to coherently populate several bound electronic states of  $O_2^+$  that pre-dissociate through non-adiabatic state coupling to multiple dissociation limits on a picosecond time scale (see Figure 6.13). Then, we use an IR pulse to coherently switch the population of different electronic states, thus, manipulating the dissociation process on an attosecond time scale. Due to the rapid dissociation processes enabled through non-adiabatic couplings, electron wave-packet interferences are strongly coupled with nuclear wave-packet dynamics, rendering theoretical calculations particularly challenging, even in a simple linear molecule. Taking advantage of the high-resolution 3D momentum imaging spectrometer coupled with attosecond XUV and femtosecond IR pulses, these experiments show that electron wave-packet interferometry involving non-Born-Oppenheimer dynamics can be performed with an energy resolution corresponding to the separation of vibrational levels of highly excited  $O_2^+$  ions.

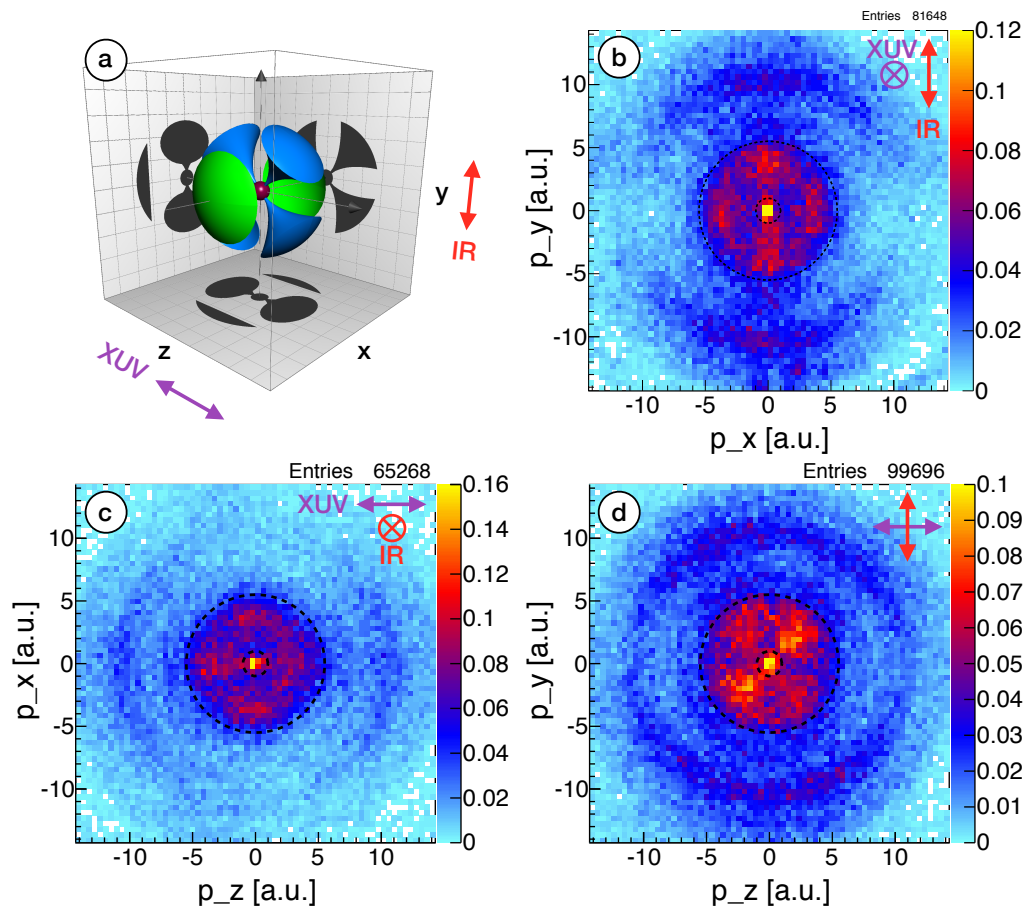


**Figure 6.12:** Momentum emission along the light propagation axis in dissociative ionization of  $D_2$  using  $HH < 11^{\text{th}} + IR$  (Ar HHG at 8T, Ar gas filter). (a) Sketch of the 3D momentum distributions created by 3-step dissociative ionization (blue) and the contribution of an additional channel (green). (b) - (d)  $D^+$  momentum distributions in all spatial directions (angular cuts  $|\cos \theta_i| < 0.8$ ).

### 6.5.1 Ultra High Resolution Spectroscopy

In the first measurement, a supersonic molecular beam was crossed with the high harmonics beam containing the 11<sup>th</sup>, 13<sup>th</sup>, and the 15<sup>th</sup> harmonic, equivalent to the photon energies 16.9, 20.0, and 23.0 eV. The remaining harmonic orders as well as the fundamental light were rejected by using a tin metal foil in both beam arms.

Similarly to hydrogen, oxygen atoms form a linear molecule but the electronic structure of a total of 16 electrons forms an extremely complex system [101, 163, 93]. The potential energy curves in the relevant XUV energy region are shown in Figure 6.13. Several bound electronic states can be populated by photons of the 13<sup>th</sup> and the 15<sup>th</sup> harmonic order. The first dissociation limit of O<sub>2</sub><sup>+</sup>, L1, lies at 18.73 eV such that no contribution to the spectrum of O<sup>+</sup> ions is expected from the 11<sup>th</sup> harmonic. The electronic states of the O<sub>2</sub><sup>+</sup> ion in the energy range of ~ 19 - 26 eV are known to pre-dissociate efficiently into a neutral oxygen atom and one oxygen ion through non-adiabatic coupling with various states present in this region. This effect has been studied using electron spectroscopy [182, 14], ion spectroscopy [95], as well as coincidence photoelectron ion spectroscopy [131, 2]. The dissociation limits below 26 eV and their electronic configurations are listed in Table 6.1.

Label	Energy [eV]	Electronic state	
		O	O <sup>+</sup>
L1	18.733	<sup>3</sup> P	<sup>4</sup> S
L2	20.700	<sup>1</sup> D	<sup>4</sup> S
L3	22.057	<sup>3</sup> P	<sup>2</sup> D
L4	22.923	<sup>1</sup> S	<sup>4</sup> S
L5	23.750	<sup>3</sup> P	<sup>2</sup> P
L6	24.024	<sup>1</sup> D	<sup>2</sup> D
L7	25.717	<sup>1</sup> D	<sup>2</sup> P

**Table 6.1:** Dissociation limits of O<sub>2</sub><sup>+</sup> in the energy range < 26 eV [182].

Figure 6.14 shows selected ion spectra recorded in this measurement. The positive ion fragments were detected on the Hexanode detector using a homogeneous extraction field of 20.3 V/cm. Projected cuts of the ion momenta in all three spatial planes are shown in plots (a) - (c). Several series of very sharp rings corresponding to O<sup>+</sup> fragments with a small energy width are observed. Ions with specific  $p_z - p_y$  combinations were filtered from the data (visible as white spots in (b) and as faint broad vertical lines in (c)) in order to reduce the contribution of water fragments. The chamber was not baked at the time and gaseous water was the main constituent of a background pressure of  $8 \times 10^{-9}$  mbar. In the raw spectra shown below, the ionization of gaseous water from the unfocused beam is visible as large spots in histogram (d) at  $y = 0$  at ion TOFs around 7400 and 7700 ns, as well as in (e), where it forms a line across the detector image. The time-of-flight spectrum in (f) shows peaks around 7400 and 7700 ns corresponding to the OH<sup>+</sup> and the H<sub>2</sub>O<sup>+</sup> ions generated from ionization of gaseous water by the unfocused beam. The O<sup>+</sup> ions produced in the dissociative ionization of molecular oxygen are spread out over a large range centered around 7100 ns. Taking advantage of the full 3D measurement of the momenta, ions originating from water dissociation were rejected from contributing to the following spectra by selecting ions with positive momenta in the z-direction only.

Figure 6.15 shows an overview of the recorded ion momenta (top), energy (center), and angular distributions (bottom). The momentum distribution of O<sup>+</sup> ions is integrated around the XUV axis with  $p_{xy} = \sqrt{p_x^2 + p_y^2}$ . For increasing the statistics, the data are

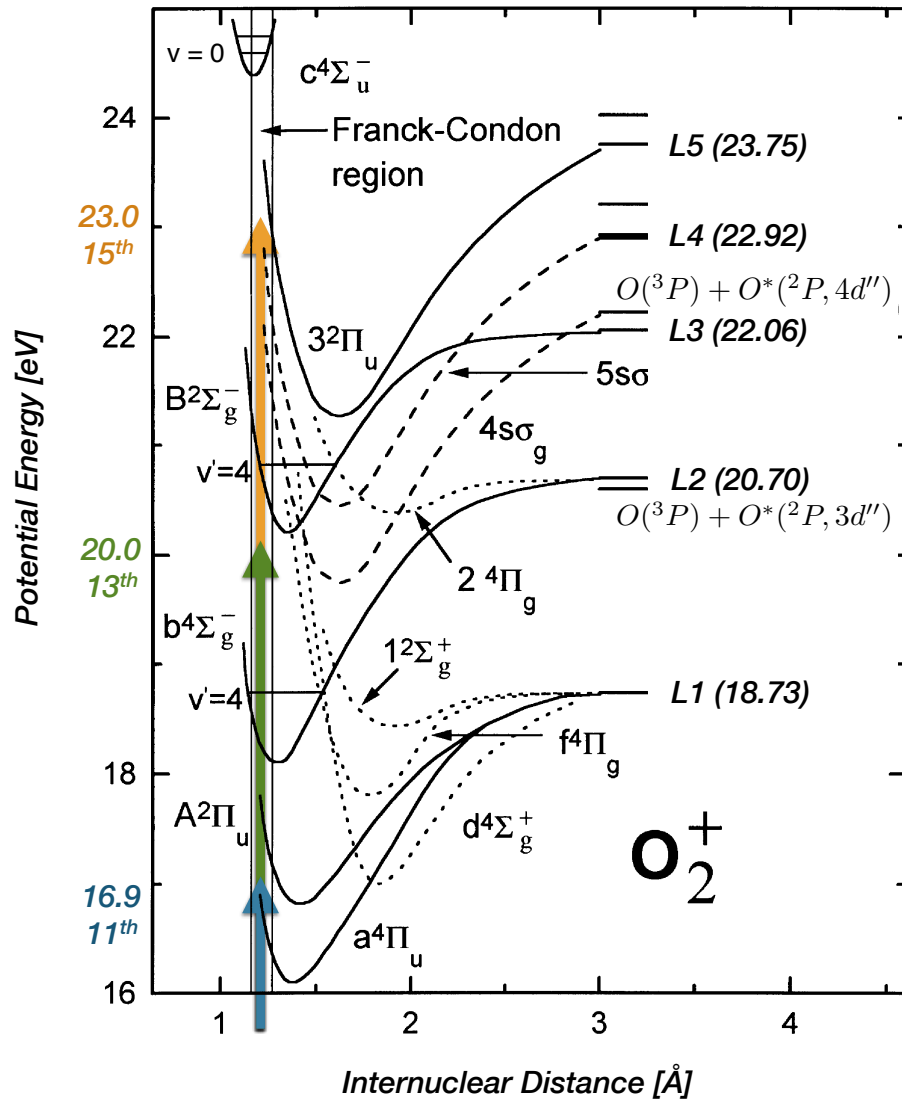
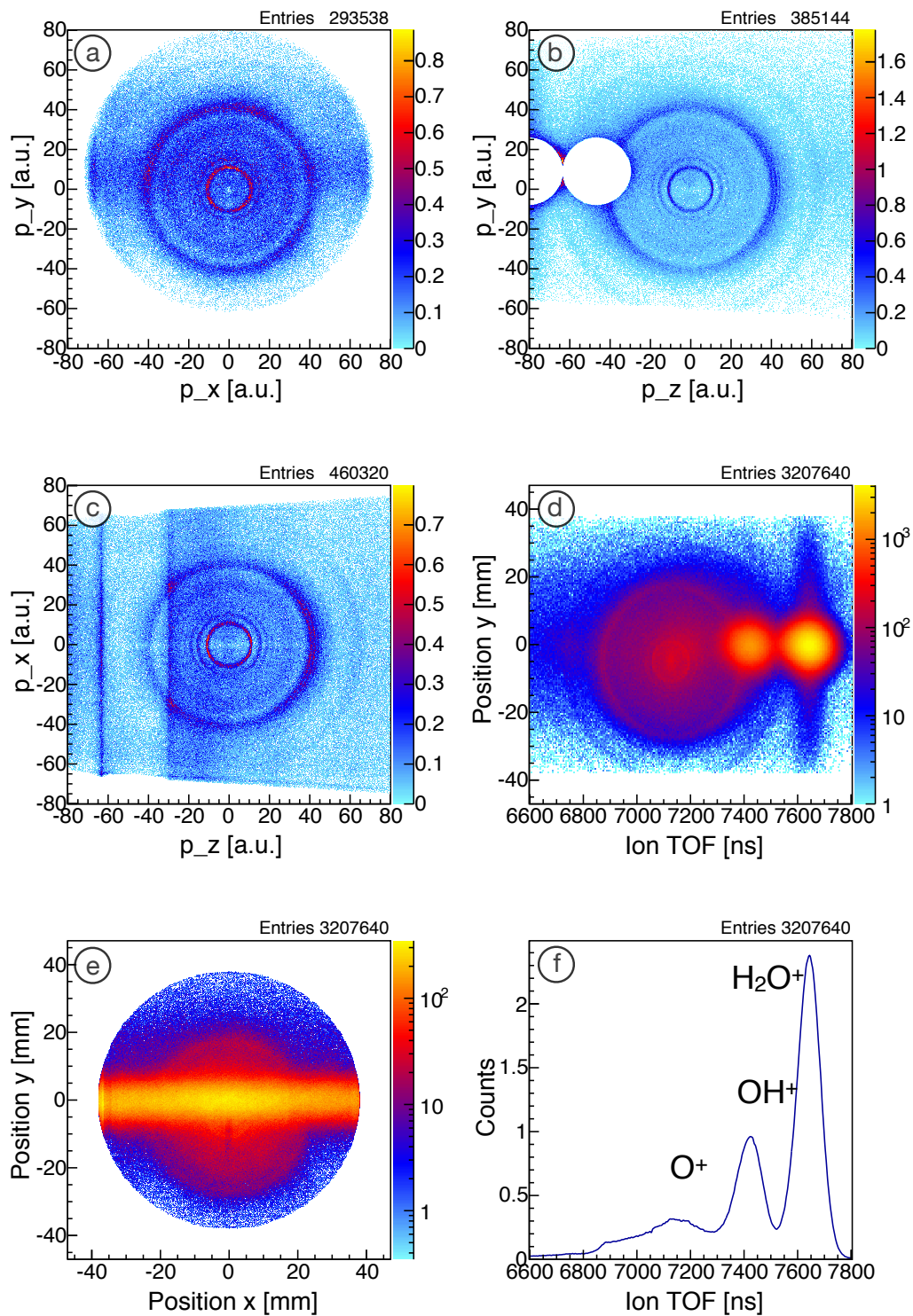


Figure 6.13: Potential energy curves of  $O_2^+$ . Curves adapted from [95].



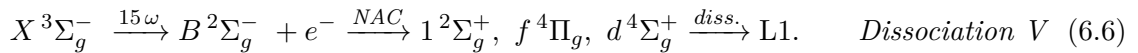
**Figure 6.14:**  $O^+$  ion spectra from single ionization of oxygen gas using three harmonics at 16.9, 20, and 23 eV photon energy. (a)-(c)  $O^+$  ion momenta ( $|\cos \theta_i| < 0.8$ , normalized intensity). Ions corresponding to  $OH^+$  and  $H_2O^+$  were rejected in the Figures (a) - (c) (see text). (d) TOF-position spectrum in the y-direction, (e) reconstructed ion positions on the Hexanode detector, (f) Time-of-flight spectrum.

mirrored at  $z=0$ . Below, the ion energy integrated over all ion emission angles is shown in black, while the spectrum for ions emitted inside a cone along the  $z$ -axis is shown in blue, as indicated by a dashed line in the momenta above. As seen in Figures 6.14 (a) - (c), the  $O^+$  kinetic energy are obtained with the highest resolution in the  $z$ -direction (43 meV energy width at 0.8 eV, for details see Section 5.3.3). Specific energy regions are indicated in the spectra and labeled with capital letters. Two series of sharp peaks, one at energies  $< 0.3$  eV (**A**), and one around 0.8 eV (**C**) dominate the spectrum. These features and various other ionization-dissociation pathways were identified and will be discussed below. For a better overview, they are labeled with the roman numerals *I* - *VII* and sorted with respect to the fragment energy. On the bottom, ion angular distributions for 4 energy regions are shown. In the Regions (**A**) and (**B**) an almost isotropic distribution is observed indicating the presence of multiple transitions with varying symmetry. In the Regions (**C**) and (**D**), the distributions have higher intensity along the polarization axis of the XUV, suggesting that mostly parallel transition contribute to this spectral range.

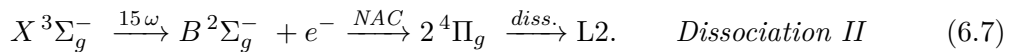
In two publications by Lafosse *et al.* [84, 85] many transitions could be clearly identified by a coincidence electron-ion 3D momentum measurement at a synchrotron light source. The vibrational structure seen in the momentum spectra has been observed in the high resolution electron spectroscopy experiments mentioned above, but to the best of my knowledge, this is the first time this structure has been observed in 3D ion spectra at such a level of detail.

### Regions (A) and (C)

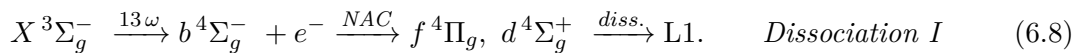
The peaks in region (**C**) correspond to the spacing of the vibrational progression of the  $B^2\Sigma_g^-$  state of the  $O_2^+$  ion with the lowest level  $v = 0$  at 20.296 eV and a spacing of 137 meV to the next vibrational state. This state dissociates into an  $O^+$  ion, which is measured here, and a neutral oxygen atom. At the energy of 23 eV, corresponding to the 15<sup>th</sup> harmonic,  $\sim 70\%$  is dissociated to the L1 limit at 18.73 eV (pathway *V*) by a non-adiabatic coupling (NAC) with the  $f^4\Pi_g$ , the  $1^2\Sigma_g^+$ , and the  $d^4\Sigma_g^+$  state [131, 84] which results in the peak series in region (**C**).



Predissociation to the L2 limit at 20.70 eV via the  $2^4\Pi_g$  state can occur starting at the  $v = 4$  vibrational level (pathway *II*) but is less likely [131, 84]. It leads to ion energies at 0.056 eV and higher as observed in region (**A**).



The  $b^4\Sigma_g^-$  state has a similar vibrational structure as the  $B^1\Sigma_u^+$  and is populated by the 13<sup>th</sup> harmonic. The vibrational states  $v = 5$  with a binding energy of 18.847 eV [106] and the levels above pre-dissociate to the L1 limit via the  $f^4\Pi_g$  and the  $d^4\Sigma_g^+$  state (pathway *I*) [84]. The resulting ion energies start at 0.059 eV and overlap with process *II* with less than 10 meV separation. Therefore, no clear assignment is possible without the coincidence measurement of the photoelectron energy.



### Region (B)

In region (**B**), from 0.3 to 0.7 eV, a broad distribution peaking around 0.4 eV is observed. Several pathways are likely contributing to the  $O^+$  ion energy spectrum.

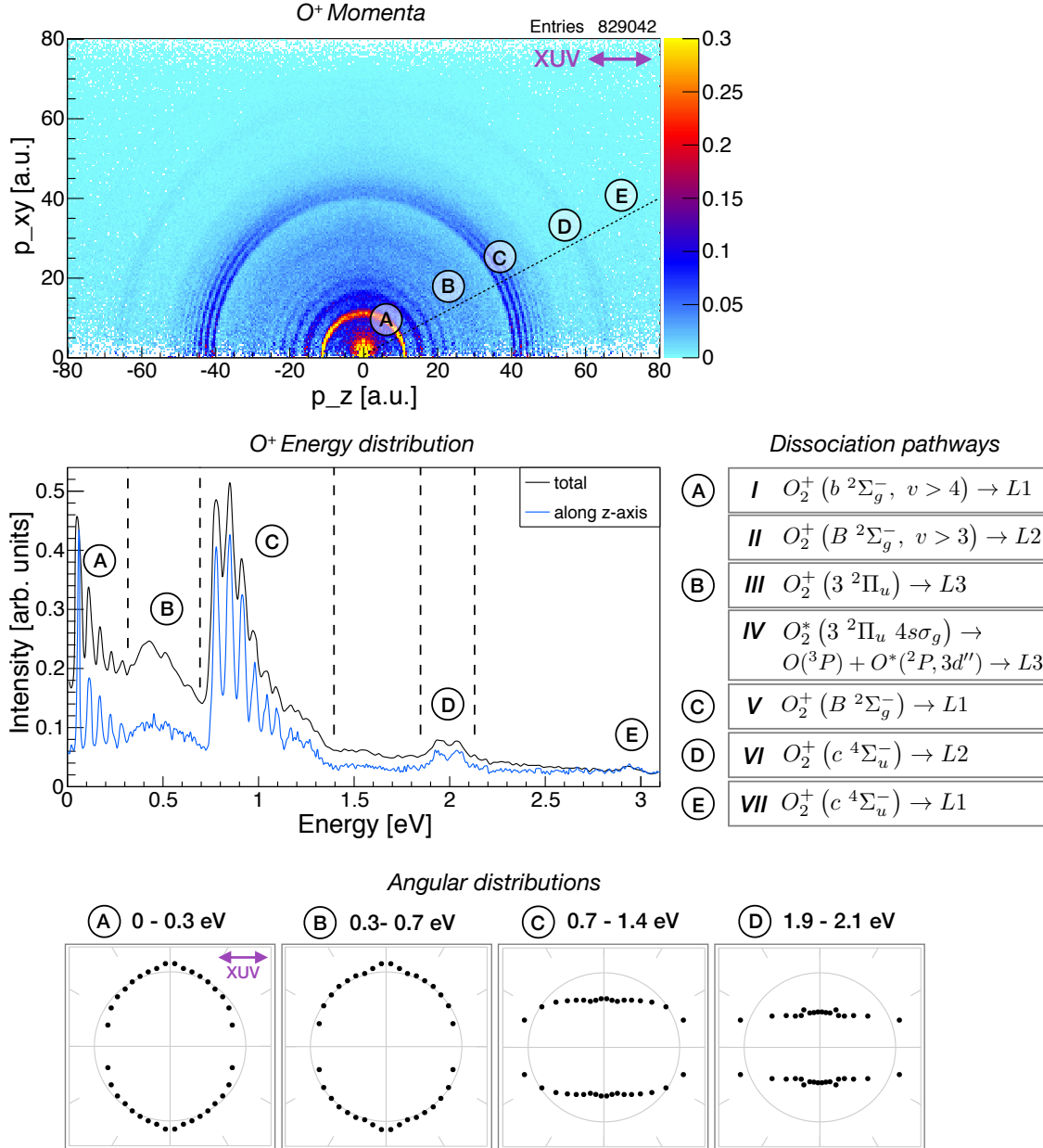
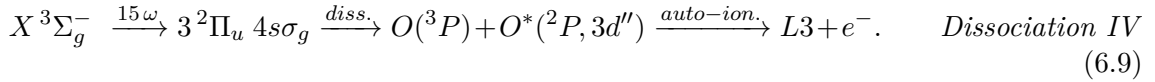


**Figure 6.15:** O<sup>+</sup> spectra measured in dissociative ionization of oxygen molecules using high harmonics with the photon energies 16.9, 20.0, and 23.0 eV (spectrally selected by using a tin filter). **(Top)** O<sup>+</sup> momentum  $p_z$  versus  $p_{xy}$ , the momentum perpendicular to the z-direction, defined as  $p_{xy} = \sqrt{p_x^2 + p_y^2}$ . Only positive z momenta are used in order to avoid contamination of the data by OH<sup>+</sup> and H<sub>2</sub>O<sup>+</sup> ions. The spectrum is mirrored horizontally at  $z = 0$ . **(Center)** O<sup>+</sup> ion energy distribution for all events (black) and for events in a cone along the z-direction (blue). The main processes responsible for the ionization and dissociation observed in the different regions of energy **(A)** - **(E)** are labeled on the right with roman numerals. The main channel consists in the ionization of the  $B \ ^2\Sigma_g^-$  state followed by dissociation through non-adiabatic coupling into the limit L1. Potential energy curves are shown in Figure 6.13. **(Bottom)** Angular distributions corresponding to the energy regions **(A)** - **(D)**.

A variety of Rydberg states have been observed in the region of 20 - 26 eV that dissociate into neutral fragments followed by autoionization [182]. At 23 eV photon energy Lafosse *et al.* [84] identified the  $3^2\Pi_u 4s\sigma_g$  Rydberg level as an important contribution to the  $O^+$  ion fragments. This state dissociates into two neutral oxygen atoms with the configuration  $O(^3P) + O^*(^2P, 3d'')$  and auto-ionizes to the atomic states of the L3 limit (pathway IV). The created ion has an energy of 0.4 eV for a photon energy of 23 eV which is broadened by the spectral bandwidth of ( $\sim 300$  meV).

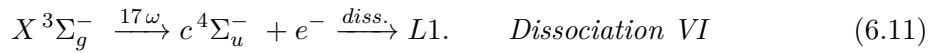


The  $3^2\Pi_u$  state of  $O_2^+$  can be populated in the Franck-Condon region with the 15<sup>th</sup> harmonic. It dissociates directly to the adiabatically connected L3 limit at 22.06 eV (pathway III) [131]. This creates a broad  $O^+$  ion spectrum centered at 0.5 eV (see also [14]).



### Regions (C) and (D)

Further features are observed in the spectrum at 2 eV as well as at 3 eV ion energy. These peaks are generated from predissociation of the  $c^4\Sigma_u^-$  state of the  $O_2^+$  ion. The state has a shallow potential well with two vibrational levels at 24.564 and 24.756 eV potential energy. Pathway VI corresponds to the predissociation into the L2 limit by tunneling [84] that produces the  $O^+$  ion fragments at 1.93 and 2.03 eV. The  $v = 0$  also pre-dissociates to the L1 limit with a fragment ion energy of 2.92 eV (pathway VII).



The harmonics 11<sup>th</sup> - 15<sup>th</sup> transmitted by the tin filter used in this experiment do not have sufficient energy to excite the  $c^4\Sigma_u^-$  state of  $O_2^+$ . Hence, the observation of dissociation from this state, although small, was surprising. However, a closer look at the theoretical transmission of tin (see Appendix Figure A.1) reveals that the transmission drops sharply between the 15<sup>th</sup> and the 17<sup>th</sup> harmonic from about 30 %, but it stays above 0.1 % with a slight increase up to 0.6 % transmission for the harmonics 19<sup>th</sup> and 23<sup>rd</sup> before the spectrum continuously decreases for higher orders. The presence of the orders 17<sup>th</sup> - 23<sup>th</sup> is confirmed in the measured XUV-spectrum in Figure 4.8 which shows weak contributions of 2<sup>nd</sup> order diffraction peaks of those orders.

### 6.5.2 IR Assisted Dissociation

A strong infrared field can be used to control the ionization and dissociation of small molecules such as oxygen and to study the dynamics induced in the laser dressed system [58, 140, 34]. In a strong field, the ionization of the molecule starts with the least bound electrons in the *highest occupied molecular orbital (HOMO)* and continues successively stripping electrons if the field strength is sufficient. Using a combination of high harmonics and a strong laser field, the influence of the field can be studied in specific electronic states. The phase-locked infrared field can be used to study molecular dynamics [168, 30] and, with sufficient interferometric stability, even electron dynamics, as shown in the next section. First, the effects of the strong field to the observed dissociative ion spectrum will be discussed in a non-time-resolved manner.

Figure 6.16 shows an overview of the ion momentum images and raw spectra obtained from irradiating a supersonic jet of oxygen molecules with the full spectrum of harmonics in combination with an infrared beam (compare to Figure 6.14 generated with selected HH only). The intensity of the infrared beam was sufficient to ionize about one oxygen molecule per shot which corresponded to less than 20 % of the total ionization rate. We estimate an intensity on the order of  $\sim 5 \times 10^{13}$  W/cm<sup>2</sup>.

The ion energy spectrum is displayed in blue in Figure 6.17 and compared with the spectrum from irradiating oxygen with a selection of high harmonics (11<sup>th</sup> - 15<sup>th</sup>) only (black), that was presented earlier (Figure 6.15). While the spectrum conserves the main features observed in the ionization using high harmonics only, we see that the presence of the IR field significantly alters the XUV-induced dissociative ionization processes in different energy regions.

In Region (D), around 2 eV and above, the peaks formed from ionization to the  $c^4\Sigma_u^-$  have become stronger while the intensity of the ion yield in the Regions (A) and (B), from 0 - 0.7 eV, has decreased with respect to the total yield. The increased population of the  $c^4\Sigma_u^-$  can be explained with the multi-photon excitation of the  $c^4\Sigma_u^-$  by simultaneous absorption of XUV/IR photons, as well as from the presence of harmonic orders above the 15<sup>th</sup> harmonic which can directly populate this state. The changes including new features that are visible at very low ion energy are discussed below.

In Figure 6.18, a detailed view of ion energies below 0.1 eV is presented. The ultra-high resolution of the setup allows to clearly distinguish features of just a few meV in the energy spectrum (a). The cuts through the momentum sphere, (b) - (d), show two isotropic sharp rings at 10 and 60 meV that are marked by dashed lines in the energy spectrum. The higher energy peak was already identified in the XUV-only measurement. It corresponds to the dissociation pathways I and II, the predissociation of vibrational level  $v = 4$  of the  $b^4\Sigma_g^-$  state to limit L1 and the  $B^2\Sigma_g^-$  state to limit L2, producing O<sup>+</sup> fragments with 57 and 56 meV energy.

The origin of the isotropic ion distribution with just 10 meV is less obvious to assign at this point. The only transition found with such low energy consists in the predissociation of the vibrational level  $v = 6$  of the  $3^2\Pi_u$  state to the dissociation limit L3. This would yield fragments with 5 meV energy. Coupling through many-electron states with  $2^2\Pi_u$  symmetry could enable the pre-dissociation of this state (see Fig. 2 in [14]). The discrepancy of 5 meV could be explained with the apparent shift of the calibration of about 2-3 meV, visible at the calculated and measured position of the identified processes I and II, as well as with the limit of the instrument resolution.

Figures 6.18 (b) and (d) show a broader process strongly oriented along the polarization direction of the infrared beam. In the energy histogram, its spectral width peaks around 25 meV, uncovered by subtracting the energy distribution of (c) from (d). This feature can be attributed to the IR enabled predissociation of high vibrational levels of the  $a^4\Pi_u^-$  state, as reported in [34, 100]. This process is equivalent to the dissociation of the  $X\ 1s\sigma_g$  ion state in molecular hydrogen by coupling one infrared photon to the dissociative potential of the  $2p\sigma_u$  state, as discussed in the previous section. The vibrational level  $v = 11$  of the  $a^4\Pi_u^-$  can be coupled to the one photon dressed  $f^4\Pi_g$  state followed by dissociation to limit L1. The dressed Floquet-state is indicated by a red dashed curve in the PEC schematic (center right). The calculated fragment ion energy is 20 meV (corrected for 808 nm from [34]). The next vibrational level yields O<sup>+</sup> ions with  $\sim 65$  meV of kinetic energy.

Another striking feature in the dissociation of oxygen in the presence of an infrared field is the sharp and discrete peak at 0 eV ion energy, visible as a central round spot in Figure 6.18 (b). The varying shape of this feature in the three momentum distributions, elongated in (c) and (d) and nearly round in (b), is a result of the different momentum resolution of

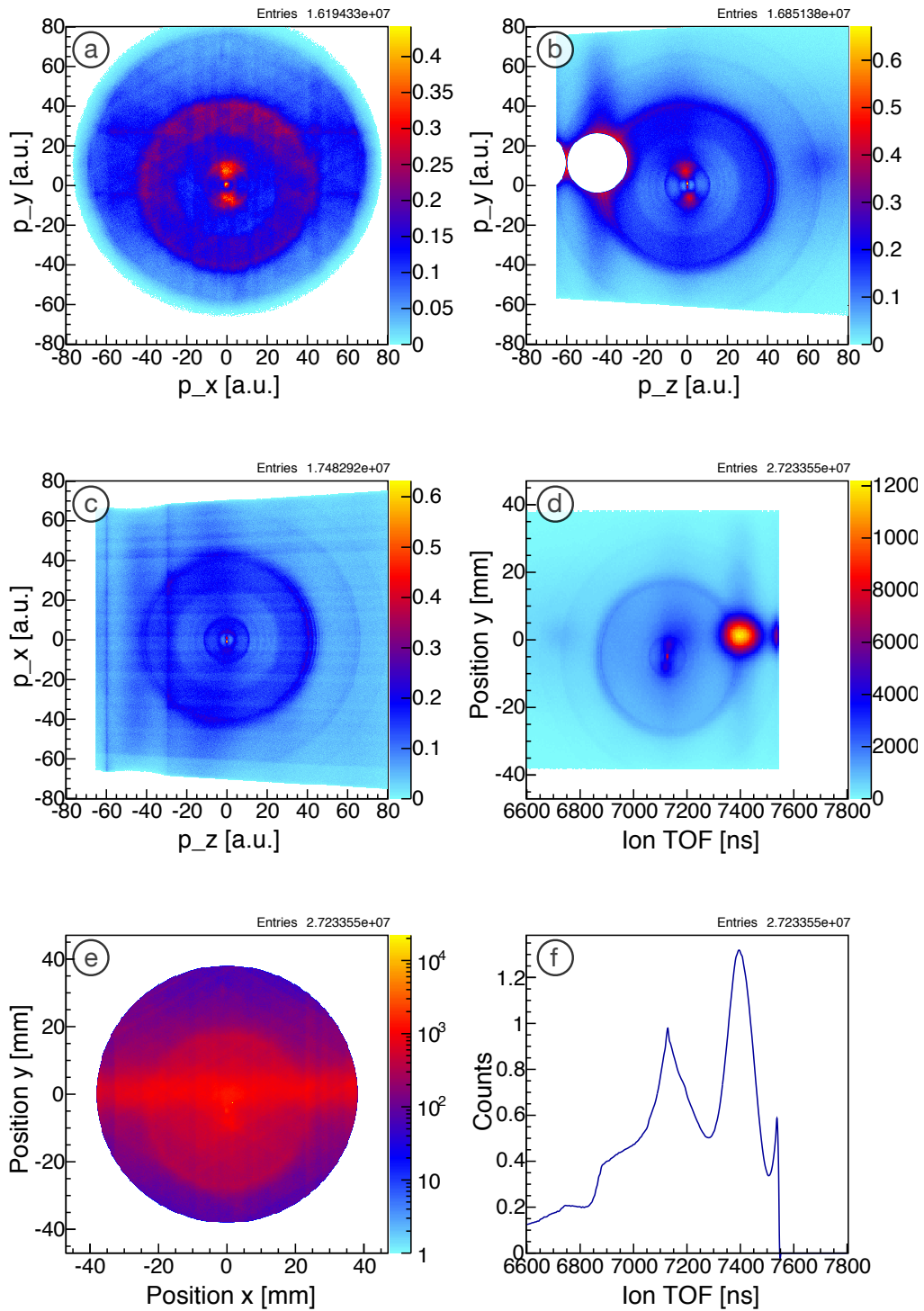


**Figure 6.16:** O<sup>+</sup> ion spectra from single ionization of oxygen gas using the harmonic orders 3 -29 in combination with the infrared field. (a)-(c) O<sup>+</sup> ion momenta ( $|\cos \theta_i| < 0.8$ , normalized intensity). Ions corresponding to OH<sup>+</sup> and H<sub>2</sub>O<sup>+</sup> were rejected in the Figures (a) - (c) (see text). (d) TOF-position spectrum in the y-direction, (e) reconstructed ion positions on the Hexanode detector, (f) Time-of-flight spectrum. Ions with TOF > 7550 ns were discarded.

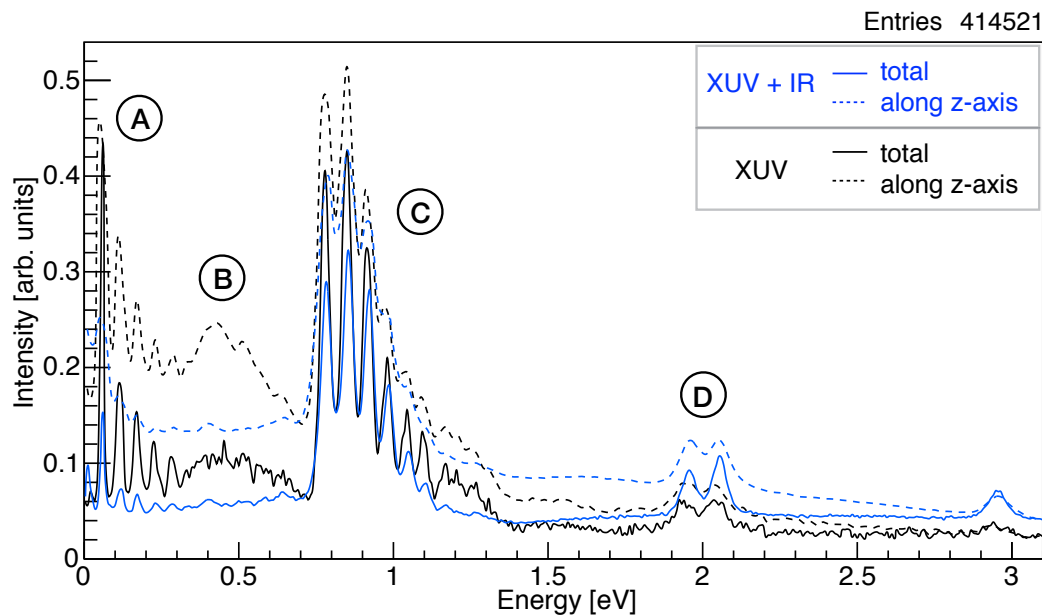


**Figure 6.17:** Comparison of the  $O^+$  ion energy distributions of ionization using the XUV and the IR field (blue) and for the XUV only (black). The dashed lines correspond to ion emission along the XUV-direction ( $z$ -axis), solid lines correspond to all spatial directions.

the apparatus in the three spatial directions, as discussed in Section 5.3.3. The dumbbell shape along the  $x$ -axes in (c) and the  $y$ -axis in (d) is an artifact caused by the binning size in combination with the cut in momentum space using the condition  $|\cos \theta_i| < 0.8$  (see Section 6.1.2). This was confirmed by looking at simple slices in momentum space that show no reduced intensity in the histogram bins at 0. The width of the distribution is expected to be caused by the instrument resolution as it seems much smaller along the  $z$ -direction which is expected to have the best resolution.

Ions with zero kinetic energy have been observed in previous investigations of dissociative ionization of  $O_2$  [140, 34, 157] but the resolution of the fragment energy was insufficient to distinguish the features observed here. One possible source of such zero kinetic energy ions is the IR enabled population of vibrational states just above the dissociation barrier that can dissociate directly. This process usually has a low probability but the integral of the observed peak is indeed only on the order of 0.3 % of the yield of the  $O^+$  fragments in the range of 0 - 1.2 eV kinetic energy.

As such low energy fragments are observed in XUV/IR experiments with other gases such as hydrogen and ethylene as well (not shown here), they could result from a sequential process where an excited neutral state is populated that dissociates up to large internuclear distances before being ionized by the absorption of one or several infrared photons.

Another option, that cannot be excluded, is the presence of doubly ionized stable  $O_2^{2+}$  ions that have the same time-of-flight as  $O^+$  ions with near zero kinetic energy. The double ionization threshold of  $O_2^{2+}$  is 36.13 eV [61]. The recoil of an electron with maximal energy  $\sim 40$  eV on an  $O_2^{2+}$  ion is still below 1 meV, such that the  $O_2^{2+}$  ion will appear at 0 kinetic energy. The 25<sup>th</sup> harmonic ( $h\nu = 38.4$  eV) or a combination of 23<sup>rd</sup> harmonic + one IR photon (36.8 eV) can populate the  $X^1\Sigma_g^+$  ground state of the  $O_2^{2+}$ . Double ionization at this energy accounts for about  $\sim 10$  % of the total ionization yield [46]. However, this number includes the autoionization of excited states above the  $O^+(^4S) + O^+(^4S)$

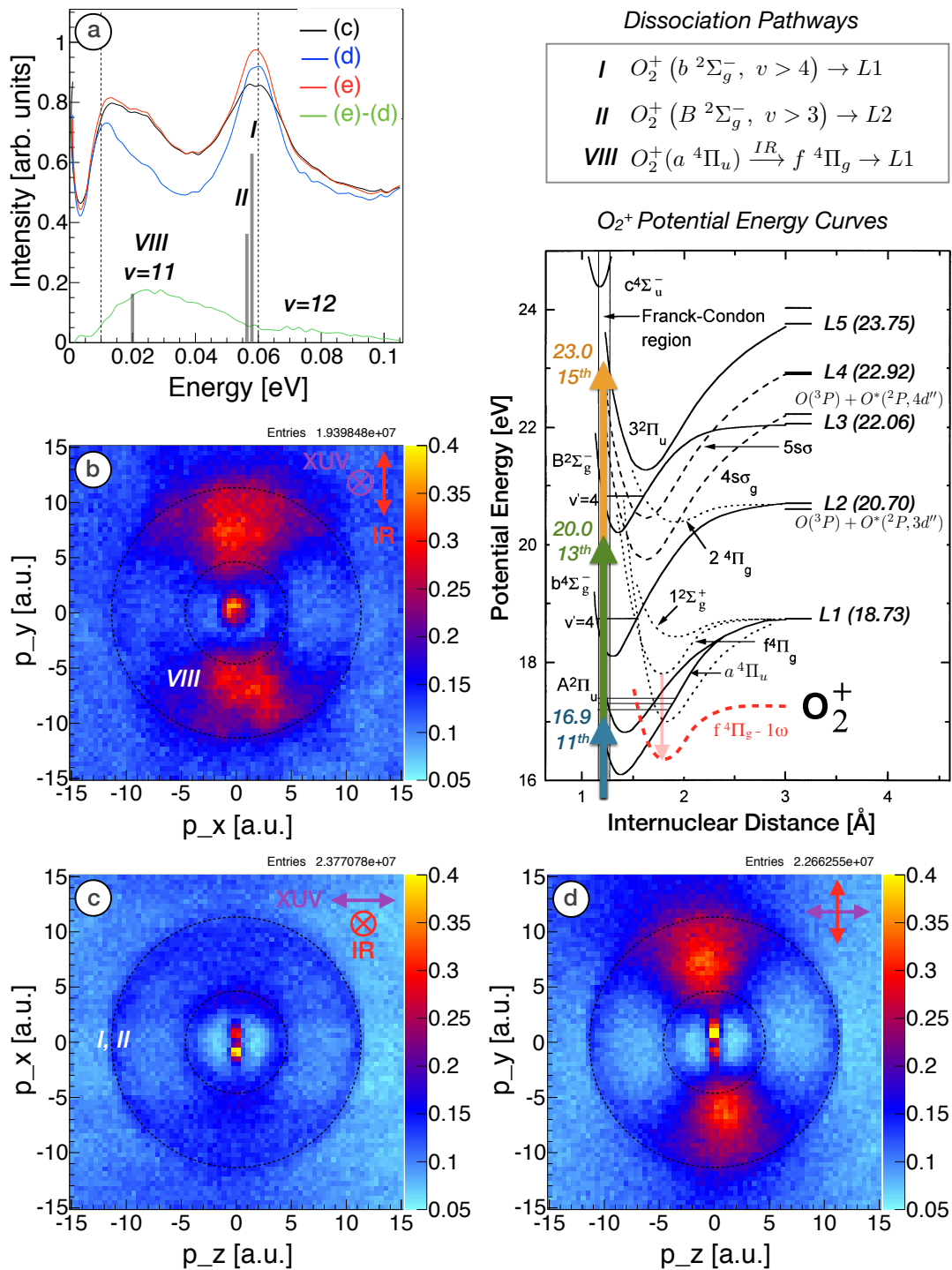


**Figure 6.18:** Low energy ions from dissociative ionization of  $O_2^+$  using the harmonics 3 - 25 in combination with an infrared field. (a) Energy spectra of  $O^+$  ions corresponding to the cuts in momentum space presented below. (b) - (c) projections of cuts in the momentum space in all three spatial directions. The suppression of events at  $p_z = 0$  is caused by the binning limitation in combination with the angular cut (see text). (Center right) Potential energy curves of  $O_2^+$ . (center top) Dissociation pathways identified in this energy region.

dissociation limit at 32.35 eV that dissociate into  $O^+$  ions with large kinetic energy, a process that is known to play an important role but was not observed here [46]. Therefore, no clear conclusion can be given on the origin of ions at  $\sim 0$  eV energy.

### 6.5.3 Coherent Attosecond Control

The ability of the Split-Mirror-Interferometer (SMI) to perform pump-probe measurements on an attosecond time-scale opens possibilities for coherently controlling dissociative ionization processes in highly excited molecules. Electron dynamics develop on an attosecond time scale and can be probed using a combination of a single attosecond pulse and a near infrared field as demonstrated by attosecond streaking [37] or the measurement of the tunneling time in strong-field ionization involving shake-up states [174]. Furthermore, attosecond pulse trains (APTs) created by HHG sources can be used in combination with the phase locked infrared field to coherently control processes by means of quantum and optical interference extending thus coherent control processes to the VUV and XUV spectral region. I used the latter approach for investigating the dissociation dynamics of oxygen molecules after single ionization with XUV pulses.

The concept of temporal coherent control of interfering quantum pathways by optical fields was introduced by Brumer and Shapiro [20] and demonstrated with femtosecond pulses in cesium by Blanchet *et al.* [17] and in molecules [57]. In these early experiments, the optical field was used to couple two (or more) coherently excited electronic states to the same final state. This leads to an interference of the different pathways resulting in a phase-modulated probability of reaching the final state.

The technique was extended to the attosecond regime in experiments where high harmonics were combined with an infrared field to coherently control the ionization in helium [72, 127], induce electron localization [156] or induce electromagnetic transparency [128]. Furthermore, the dissociation of a photo-excited molecule can be controlled coherently, such as shown in ionic states [76] and neutral states [129] of deuterium molecules. As the infrared field dresses, broadens, and shifts electronic states, the quantum interference can include new pathways that are induced by the optical field, hence, that would not be present without the influence of a moderate or strong laser field.

Figure 6.19 illustrates the pulse sequence of pump-probe experiments where an infrared probe pulse is delayed with respect to a pump pulse containing the attosecond pulse train (APT) as well as the infrared fundamental beam. The High Harmonic Generation process fixes the APT in phase to the IR pump pulse, while the probe IR is delayed relative to the XUV/IR pump.

The quantum and optical interference processes resulting in this combination of infrared and XUV fields are demonstrated in Figure 6.20. When the infrared pulses in the pump and the probe arm overlap temporally and spatially, the interference of both pulses modulates the total infrared field intensity, as shown in Figure (a). The electrical field of the pump and probe IR pulses can be written as

$$E(t) = A(t) \cos(\omega t) + B(t) \cos(\omega(t + \tau)), \quad (6.13)$$

where  $A(t)$  and  $B(t)$  are the time dependent amplitudes of the IR pump and the probe pulses,  $\omega$  is the infrared frequency, and  $\tau$  the pump-probe delay. The total field intensity as a function of the delay is [152]

$$I(\tau) = A^2 + B^2 + 2AB \cos(\omega\tau). \quad (6.14)$$

In the case of identical field strength in both arms,  $A = B$ , the intensity of the infrared field can be adjusted between zero to  $|2A|^2$  by controlling the pump-probe delay. This

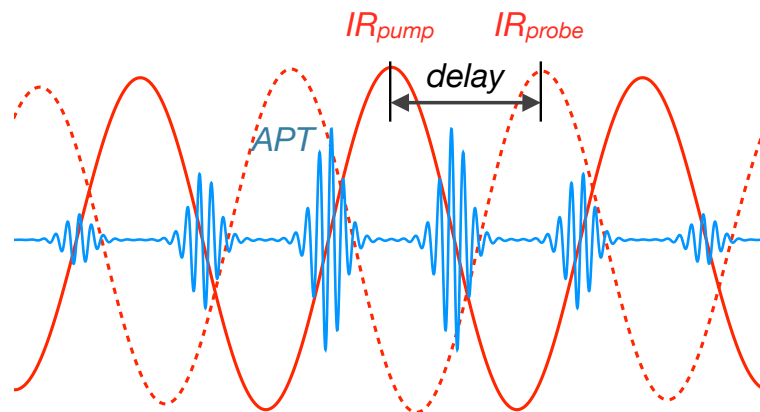


**Figure 6.19:** Temporal structure of the pulse sequence in attosecond quantum control experiments. The infrared probe pulse is delayed with respect to pump pulse consisting of the IR and the phase locked XUV attosecond pulse train (APT).

effect is called *optical interference*, and it manifests itself in a modulation of the transition probability of an IR-assisted transition with frequency  $\omega$  with respect to the pump-probe delay, indicated in (c).

*Quantum interference* arises when an electronic state is coherently populated via two (or more) different quantum pathways. This can be realized with high harmonic pulses when two electronic states are populated by neighboring odd harmonic orders, e.g.  $13\omega$  and  $15\omega$  as shown in (b). If a final state is located energetically between the two states at a distance close to the energy of the IR field two pathways lead to population of the final state: (i)  $13\omega + \omega$  and (ii)  $15\omega - \omega$ . The *quantum interference* of the two pathways leads to oscillations of the ionization probability at a frequency of  $\sim 2\omega$  equivalent to the energy spacing of the coherently excited states that can be controlled by the delay between the APT and the infrared field.

Figure (d) illustrates the signal recorded in an experiment. It contains a convolution of optical interference at the frequency of the driving field,  $\omega$ , as well as quantum interference at the frequency  $2\omega$ , corresponding to the energy difference between the coupled states. While optical interference only appears at delays where the pump and the probe pulses overlap in time, quantum interference instead persists beyond the optical overlap, as long as both states are coherently excited and both pathways to the final state are enabled by the probe. A phase lag exists between the quantum oscillation and the XUV pulse that depends sensitively on the photon energy. By extracting this quantum phase between interfering electronic wave-packets, information about the shape of the electronic potentials can be obtained [57]. In the case of a moderate to strong field, the modification of the electronic states by the infrared field can be extracted from the phase, as shown by Shivaram *et al.* [152]. They also demonstrated how the optical interference of the infrared field can be used as a reference to measure the intensity dependent quantum phase between the oscillations of the quantum paths.

Furthermore, the quantum and optical interference can be used to coherently control the population of different states and open new dissociation pathways on an attosecond time scale [129, 157]. This will be investigated in the following experiment.

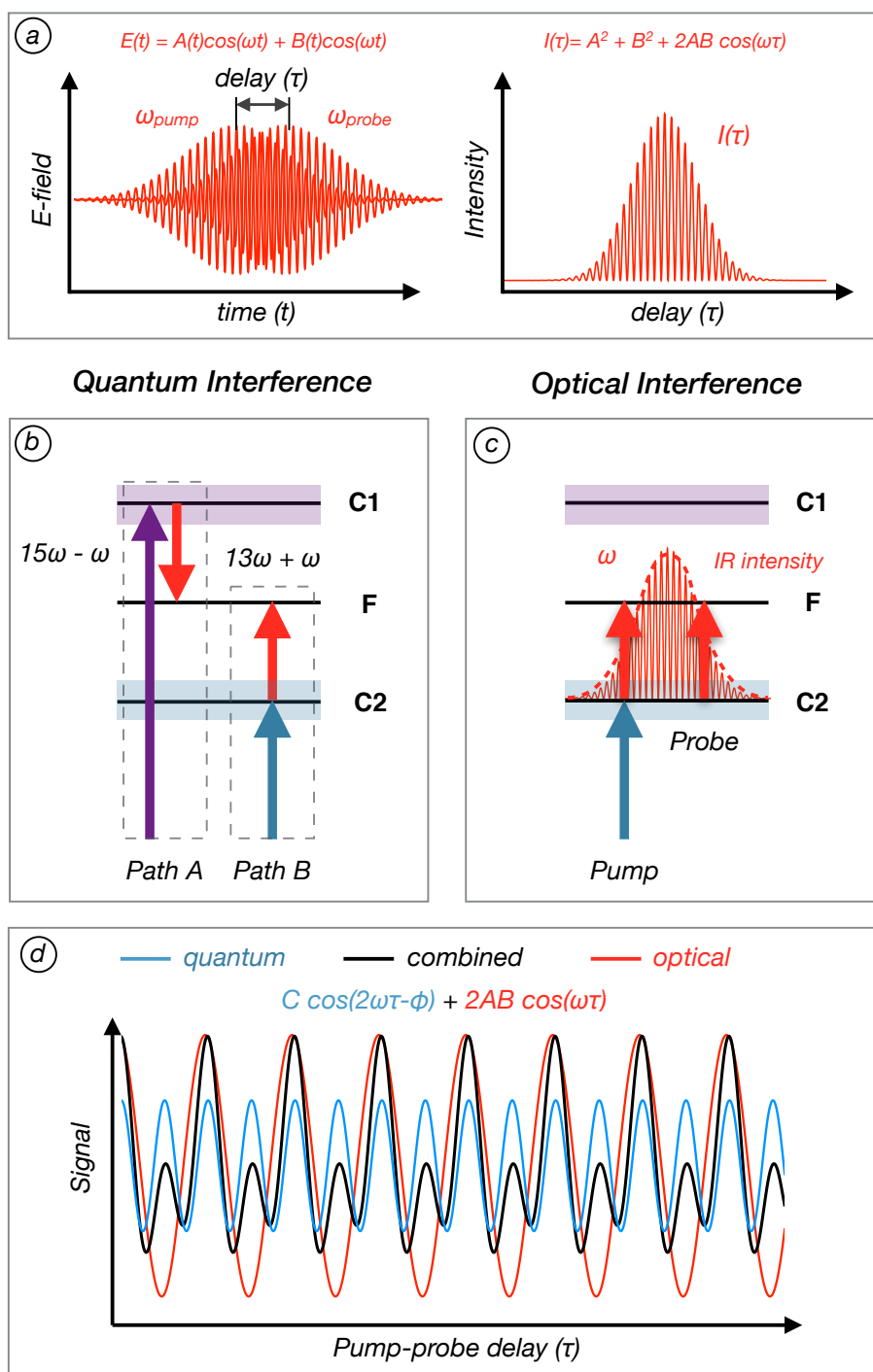


**Figure 6.20:** Schematic illustrating quantum interference formed from a coherent excitation of two electronic states C1 and C2 by neighboring odd harmonics and their coupling by an infrared field. (a) Optical interference of the infrared pump and probe pulses causes an intensity modulation of the IR field strength. (b) Quantum interference creates two pathways to final state F by coupling of neighboring states in the infrared field. The resulting yield oscillation has a frequency  $\sim 2\omega$  and a quantum phase  $\phi$ . (c) The intensity modulation caused by optical interference of the infrared pulses results in an ionization probability oscillation of the final state F at  $\omega$ . (d) Model of the signal (e.g. ion yield) resulting from the combination of both interference effects.

### Control of Dissociation in $O_2^+$

In an experiment by Siu *et al.* [157], quantum interference was used to control the yield of  $O^+$  ions in the dissociative ionization of oxygen molecules. An attosecond pulse train consisting of the harmonic orders 11 - 21 of 780 nm was intersected with an infrared probe pulse, and the ion yield and energy was recorded using velocity map imaging. The authors observed an oscillation of the ion yield of a few percent in several energy regions. In the energy range corresponding to dissociation of the  $c^4\Sigma_u^-$  state to the L1 and L2 limits (dissociation paths *VI* and *VII* in Figure 6.15), they observed a clear oscillation in phase and at twice the frequency of the optical infrared field,  $2\omega$ . Around the peak at 0.9 eV, corresponding to the dissociation of the  $B^2\Sigma_g^-$  state to limit L1 (dissociation path *V*), a heavily modulated oscillation at frequency  $\sim 2\omega$ , with a varying phase and smaller amplitude, was observed. They suggested that quantum interferences of various electronic states are involved in the observed spectrum. Due to the complex oscillation structure and the phase shift observed in the dissociation of the  $B^2\Sigma_g^-$  state, the authors note that a purely electronic process where the interference occurs in the bound ionic states is insufficient to describe the observed oscillation. Instead, it was suggested, that population transfer to different ion states and new sequential dissociation pathways might be involved in the dissociation processes. However, no clear identification of the nuclear or electronic dynamics could be given.

The electronic states of  $O_2^+$  (without modification of a strong field) are shown on the left in Figure 6.21. Various dissociation pathways were discussed in Section 6.5.1 and identified in the energy spectrum in Figure 6.15. On the right side, the complicated structure of electronic states is simplified and split up into quartet and duplet states. All bound states shown are coherently ionized by the XUV spectrum present in the experiment. The broad range of vibrational levels populated in each state is symbolized by colored horizontal peak distributions. Marked by red arrows various optically allowed one or multi-photon transitions can be initiated by the infrared field. This picture becomes even more complex when all electronic states as well as Floquet-states created by the infrared field are considered (as indicated by the examples  $f^4\Pi_g - 1\omega$  and  $1^2\Sigma_g^+ - 1\omega$ ).

Applying the previously described technique of attosecond coherent control, the MIS-TERS setup was used to manipulate the dissociation pathways of  $O_2^+$  through quantum and optical interference of coherently excited states in the  $O_2^+$  by changing the relative phase of the APT and the infrared field. The infrared field was expected to cause a population transfer of the vibrational levels of the  $B^2\Sigma_g^-$  state of  $O_2^+$  to neighboring states or a quenching of the highest vibrational states by suppressing the barrier to direct dissociation. As shown in the previous non-time-resolved measurements (see Figure 6.15), the ultra-high resolution of our apparatus allows for selecting specific electronic states or even vibrational levels by their energy, as well as by their transition geometry by taking advantage of the measured 3D momenta. Due to the limited statistics, vibrationally selected time-resolved spectra not discussed here but are shown in Figure A.8 in the appendix. I will focus on the analysis of energy ranges corresponding to specific dissociation channels.

In contrast to the experiment by Siu *et al.*, the infrared beam was added in the pump and the probe pulse producing a delay dependent infrared field intensity. The infrared probe pulse was delayed with respect to the XUV/IR pump pulse containing the full photon spectrum of IR to the 25<sup>th</sup> harmonic and the XUV and IR fields were cross polarized. The intensity of the infrared beam ( $\sim 5 \times 10^{13}$  W/cm<sup>2</sup>) was sufficient to ionize about one oxygen molecule per shot which corresponded to less than 20 % of the total ionization rate. The measurement details are noted as  $O_2$  File 3 of Table A.4 in the appendix.

Figure 6.22 shows the total yield of  $O_2^+$  (a) and  $O^+$  (b) ions with respect to the pump-probe delay for ion energies between 0 and 3.5 eV. The  $O_2^+$  yield shows an oscillation

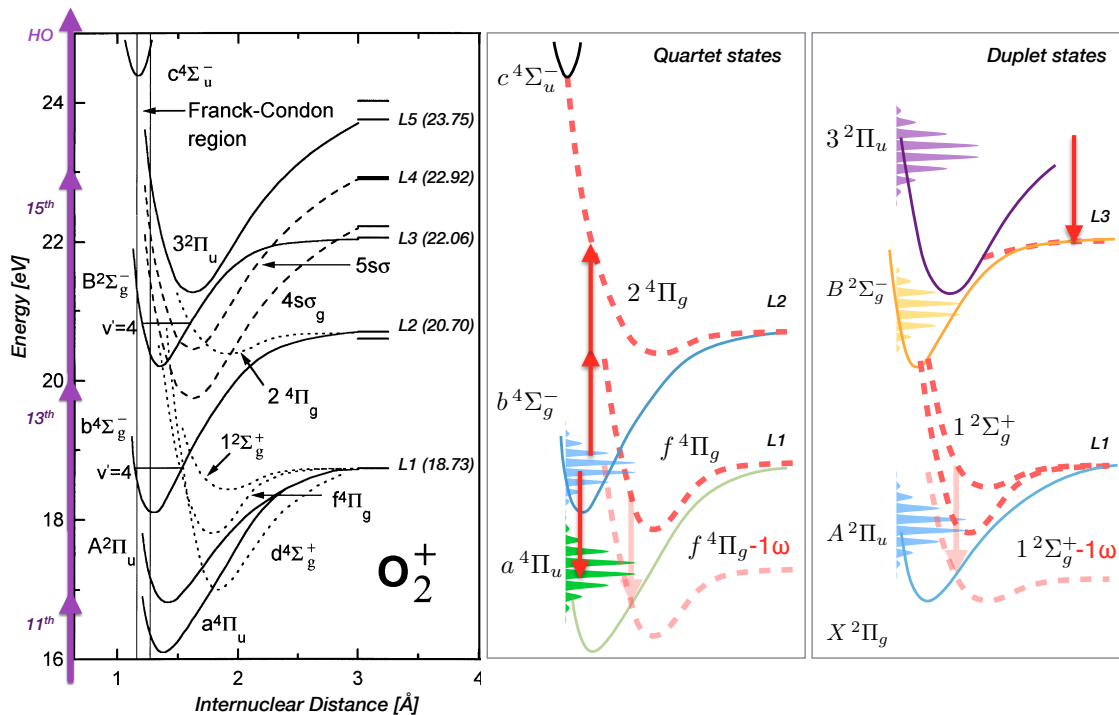


**Figure 6.21:** Potential energy curves of  $\text{O}_2^+$ . The attosecond pulse train consisting of the harmonic orders (3 - 25) and the phase locked IR beam coherently excite a variety of states that dissociate to several atomic limits. Interference of the infrared field in the pump and probe arms modulates the population of these states and possibly the dissociation pathways. Red arrows in the schematics on the right depict some optically allowed transitions ( $n\omega$  with  $n < 3$ ) in the energy range 16 -25 eV. Floquet-states generated by the IR field are labeled with  $state - 1\omega$ . Data adapted from [95].

corresponding to the period of the infrared field of 2.7 fs. This effect is a manifestation of optical interference and is attributed to the strong-field ionization by the infrared beam, as well as the ionization caused by a combination of harmonics below the threshold for  $\text{O}_2^+$  (12.07 eV [14]) and the infrared field. Adding a single infrared photon to the 9<sup>th</sup> harmonic allows ionization to the  $X^2\Pi_g$  ground state of the  $\text{O}_2^+$  ion. The  $\text{O}^+$  ion yield, shown on the right, is also modulated with respect to the pump-probe delay. The oscillation, however has a different phase as the infrared field, indicated by a dashed line. The modulation of the  $\text{O}^+$  ion yield indicates the presence of additional frequencies in the signal. In the following section we will look at ways to differentiate the multiple signals.

### Selecting Dissociation Channels through Energy and Angle Differentiation

As demonstrated in the previous section, specific dissociation pathways lead to ion energies in a particular energy region. However, if multiple dissociation channels yield fragments that overlap in energy, a particular channel cannot be isolated by selecting a specific ion energy.

As discussed previously in Section 6.4.7, the probability of an electronic transition (or ionization) initiated by an XUV photon depends on the molecular orientation with respect to the polarization axis of the electric field. For a parallel transition, no angular momentum is transferred to the electron and ionization occurs preferentially for molecules aligned to

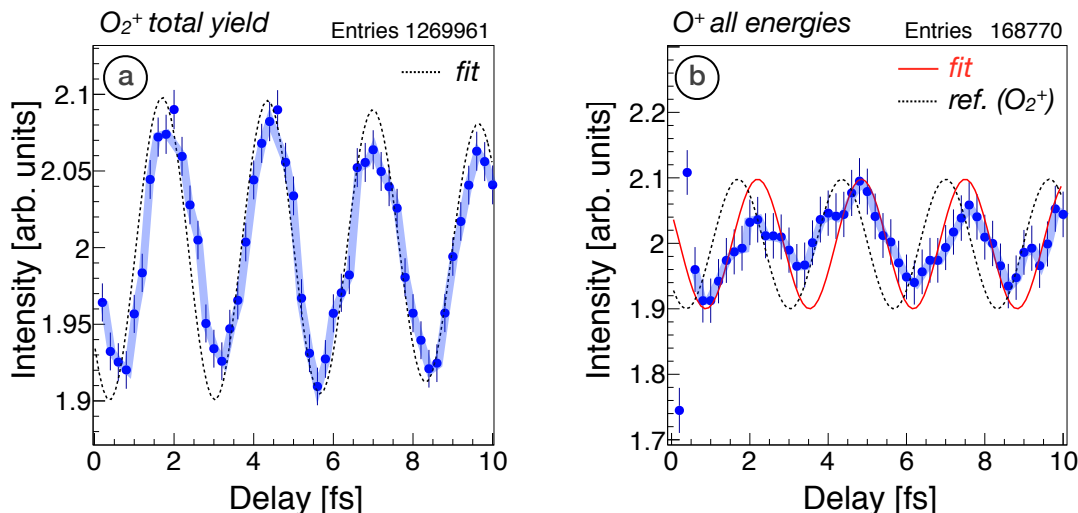


**Figure 6.22:** Time dependent data from ionization of oxygen molecules. (a) Total O<sub>2</sub><sup>+</sup> ion yield, (b) total O<sup>+</sup> ion yield for energies 0 - 3.5 eV. Pump: harmonics 3 - 29 + IR, probe: IR (Data File 3, Table A.4 in the appendix).

the polarization axis. For a perpendicular transition, the transfer of angular momentum causes a higher transition probability for a perpendicular orientation of the molecule to the polarization axis. Therefore, the infrared field dissociates and couples different electronic states with different probability, depending on the molecular orientation (see Section 6.4.7).

By selecting ions emitted at a particular angle with respect to the polarization axis, an electronic transitions corresponding to a particular angular momentum transfer can be selected. This assumes that the axial recoil approximation holds, as the ion emission direction only corresponds to the orientation of the molecular axis at the instant of ionization if the dissociation is faster than the rotation of the molecule.

Energy and angle resolved data are shown in Figure 6.23. The delay dependent yield of O<sup>+</sup> ions is plotted for two different regions of ion kinetic energy, Figure (a), 0.31 - 0.72 eV, and Figure (b), 0.72 - 1.4 eV. The two regions are marked in the ion energy spectrum shown above. The data is further split up into ions emitted along the polarization axis of the XUV beam (red) and along the IR polarization axis (blue), as illustrated in two images on the top right, demonstrating the orientation of the molecule with respect to the polarization vectors for both orientations. The molecular axes are allowed to deviate from a perfectly parallel orientation by  $\pm 37^\circ$  in each case.

Despite the high degree of differentiation, the energy and angle selected data in (a) and (b) exhibit statistically significant oscillations with a varying phase relationship. In energy region (a), ions emitted along the IR-polarization axis (blue line) seem to mostly follow the infrared field intensity at frequency  $\omega$ . Meanwhile, for ions oriented along the XUV-polarization axis (red line) a different behavior is observed. At delays of  $\sim 2 - 6$  fs the yield oscillation is out of phase with respect to the infrared intensity and then again mostly in phase with the infrared field after 6 fs. Both oscillations contain a higher frequency close to  $2\omega$ , suggesting the quantum interferences of electron wave-packets. In region (b), a similar behavior is observed with beating faster than the infrared frequency that is sometimes in phase and sometimes out of phase with the infrared field.

The observed different behavior for molecules parallel to the XUV or parallel to the IR polarization axes could correspond to the transition to different electronic states accessed by different angular momentum transfer to the molecule. As outlined above, the angular

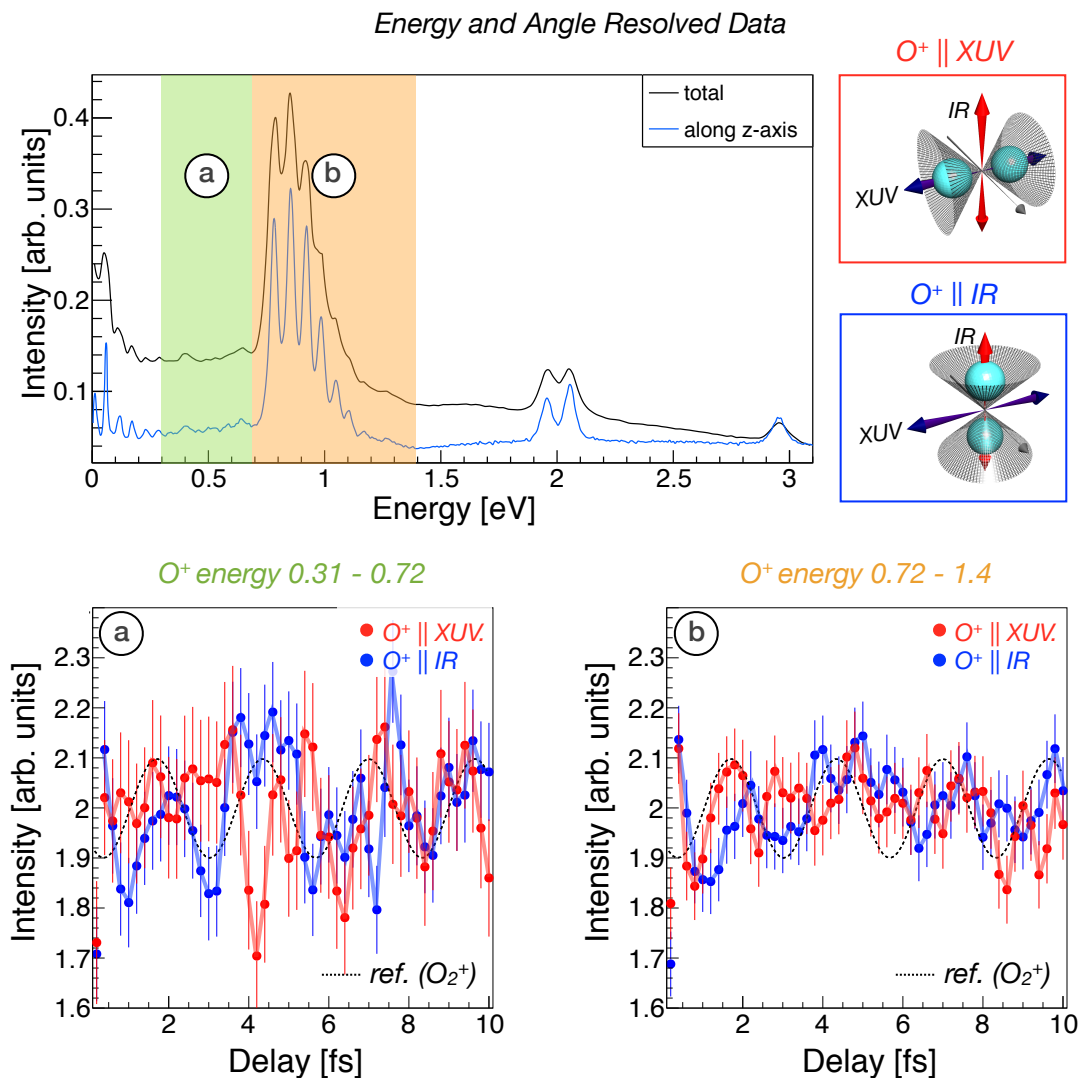


**Figure 6.23:** Time dependent data from ionization of oxygen molecules. Pump: harmonics 3 - 29 + IR, probe: IR. (a) Total  $O_2^+$  ion yield, (b) total  $O^+$  ion yield, (c)  $O^+$  ion yield with energy 0.31 - 0.72 eV for ion emission along the XUV polarization direction, perp. to IR, (blue) and parallel to the infrared polarization axis (red), as indicated in the schematic on the right. (d)  $O^+$  ion yield for energies 0.72 - 1.4 eV. In (b) - (d), yields are averaged between adjacent bins (smoothing). Colored semi-transparent lines added to guide the eye.

restrictions suggests a selection of the following transition XUV-IR 2-photon absorption schemes: (i) (red) parallel XUV transition + perpendicular IR transition, (ii) (blue) perpendicular XUV transition + parallel IR transition.

In the experiment using XUV-radiation only presented earlier, region **(a)** included  $O^+$  ions resulting from the dissociation of the  $3^2\Pi_u$  state as well as excited auto-ionizing  $O_2^*$  states to the limit L3.  $O^+$  ions found in region **(d)** are mainly the result of ionization to the  $B^2\Sigma_g^-$  state followed by dissociation via the  $f^4\Pi_g$  and  $d^4\Sigma_g^+$  state to limit L1. The  $3^2\Pi_u$  state can be coupled by one infrared photon to the lower  $B^2\Sigma_g^-$  state in a perpendicular transition and vice versa. A population transfer as well as quantum beating between the two states could therefore contribute to the observed oscillations. However, several other IR assisted transitions could produce ions in the energy range. In the duplet system, dissociation of the  $A^2\Pi_u^-$  state could be enabled by the infrared field via the  $1^2\Sigma_g^+$  state. In the quartet system, a 2-photon transition from  $b^4\Sigma_g^-$  to  $2^4\Pi_g$  leads to dissociation to limit L2.

Optically allowed transitions between  $A^2\Pi_u^-$  and  $B^2\Sigma_g^-$ , as well as between  $b^4\Sigma_g^-$  and  $c^4\Sigma_u^-$  do not seem to match the photon energy in this experiment or the number of photons required would lead to a parity violation. However, transitions involving other states as well as more photons are likely to contribute.

As presented earlier, yield oscillations at the frequency of the infrared driving field  $\omega$  are a sign of intensity dependent population transfer or added population as a result of optical interference of the infrared field in both the pump and probe arms. Oscillations at a higher frequency are expected to be a result of quantum interferences between different pathways leading to dissociation. As shown above, multiple electronic states are coherently excited by the attosecond pulse train and various transitions are enabled by the infrared field. Thus, quantum interference of those pathways is expected and likely contributes to the observed oscillations. Phase shifts with respect to the driving field could also be a result of dynamics of the nuclei including the creation of new dissociation pathways by the infrared field. Due to the long infrared pulse length of about 45 fs, nuclear dynamics in the bound states should be washed out by the averaging over many cycles. However, the nuclear wave-packet motion in these states does influence the total dissociation yield after the IR pulse has left; this results from the accumulated phase from the instant of XUV ionization to the moment of resonant coupling of different electronic states by the infrared field.

In these early attosecond coherent control experiments in highly excited molecular systems, electron and nuclear wave-packet dynamics are highly correlated. To unravel the complicated structure of the observed oscillations advanced theoretical calculations are needed to disentangle such non-Born-Oppenheimer dynamics. At this point, the statistics as well as the wide range of possible transitions does not allow to draw conclusions of the specific transitions and phase shifts. Further measurements are required to reproduce the observed features with shorter pulses. Using a multilayer mirror, a lower photon energy could be selected that limits the dissociative ionization to fewer states. A coincidence measurement of the electron energy would give better insight into the transitions involved. Nonetheless, a combined theoretical and experimental effort will be required to identify the reaction pathways. The measurement presented here showcase the possibilities to study nuclear and electron interaction with quantum control techniques in combination with a momentum imaging setup.



# 7 Conclusion and Outlook

## 7.1 Summary

Pump-probe spectroscopy using specifically tailored multi-color VUV and XUV pulses is considered a promising tool for studying femtosecond dynamics in molecules in real-time on a fundamental level. However, the presence of multiple colors in the photon spectrum of two or more pulses enables a variety of ionization and dissociation pathways that are not accessible in single photon or strong-field ionization, and therefore are not well understood. Experiments are needed that investigate the electronic states as well as the evolution of nuclear wave-packets on the potential energy curves of the molecule involved in such multi-color multi photon ionization processes.

In this work, I have investigated the complex structure of ionization and dissociation pathways on the potential energy curves in small molecules that are initiated by the absorption of a sequence of multi-color pulses in the XUV, VUV, and IR spectrum. Using femtosecond pump-probe spectroscopy, I have tracked the evolution of nuclear dynamics in neutral hydrogen molecules and identified new excitation and ionization pathways leading to the dissociative ionization of hydrogen molecules by employing 3D momentum imaging spectroscopy. These studies were extended to oxygen molecules where an XUV attosecond pulse train coherently ionized several electronic states of  $O_2^+$  followed by the dissociation of the molecule via multiple pathways. The infrared electric field of the driving laser was then used to couple the electronic and nuclear wave-packets, thus, manipulating the dissociation dynamics of the molecule on an attosecond time scale. This presents a step towards coherently controlling fundamental photo-chemical reactions in small molecules on an attosecond time scale.

In order to perform the experiments presented here, we, jointly with several coworkers<sup>1</sup>, have developed and constructed a novel experimental setup that combines an existing high-flux High Harmonic Generation light source that delivers attosecond pulse trains in the VUV and XUV spectrum with a state-of-the-art 3D momentum imaging apparatus (COLTRIMS), as well as a beamline consisting of several experimental tools enabling the selection, characterization, and propagation of the photon spectrum.

The high number of photons per pulse delivered by the HHG source enabled the observation of two-photon ionization by the absorption of XUV and VUV pulse pairs in the dissociative ionization of hydrogen molecules (see Figure 6.9). Previously unpublished dissociation pathways involving the absorption of XUV and infrared (IR) photons were identified by taking advantage of the 3D momentum imaging capabilities and the high resolution of the MISTERS end-station. Even in hydrogen, the simplest neutral molecule with just two electrons, the identification of the observed features proves to be challenging. This emphasizes the need for the investigation of benchmark systems such as diatomic and triatomic molecules for understanding the processes triggered by multi-photon absorption in the IR, VUV, and XUV spectrum. This is especially important for testing theoretical models that are essential to understand the observations in two or multi-photon absorption experiments in more complex molecules such as hydrocarbons or larger biologically relevant systems.

---

<sup>1</sup>for individual contributions see Table 6 in the acknowledgements

The combination of a supersonic molecular beam with a small focus obtained from back-focusing the beam with a short focal length mirror provided 3D momentum imaging pictures with unprecedented resolution. In oxygen molecules, the vibrational structure of multiple electronic states in the  $O_2^+$  ion could be resolved with a precision that had only been obtained previously in electron spectroscopy measurements. Taking advantage of this ultra-high ion momentum resolution, the dynamics and dissociation pathways of different vibrational states can be investigated in future experiments.

A custom Split-Mirror-Interferometer that separates the laser beam into two arms was developed to perform pump-probe measurements of the molecular dynamics in small molecules. The pulse duration of 10 to 20 femtoseconds allowed the observation of the nuclear wave-packet motion in the neutral  $B^1\Sigma_u^+$  state of hydrogen molecules in real time. In the experiment, this state was excited by a single photon of the 9<sup>th</sup> harmonic of the infrared beam and ionized by multi-photon absorption of the fundamental beam. A delay dependent oscillation of the  $H_2^+$  ion signal with a period of  $\sim 70$  fs was observed. At small internuclear distances around the Franck-Condon region, the molecule can be ionized from the neutral  $B^1\Sigma_u^+$  state to the  $X\ 1s\sigma_g$  ground state of the hydrogen ion by the interaction of two infrared photons. At larger internuclear distances, the separation between the neutral and the ionic states requires three photons for single ionization (and dissociation). As the wave packet moves in the wide potential well of the  $B^1\Sigma_u^+$  state, the ionization probability for multi-photon ionization by the infrared beam varies leading to an  $H_2^+$  ion yield that depends on the position of the wavepacket (see Figure 6.7).

A major advantage of high harmonic sources in comparison to free-electron lasers is the ability of extending the study of dynamical processes to the attosecond time domain. The interaction of the strong laser field with the medium, in this case a noble gas, creates a frequency bandwidth that can support attosecond pulses. The source used in this setup delivered attosecond pulse trains (APT) that are phase locked with the infrared driving field. The specifically developed Split-Mirror-Interferometer provided a stability on the level of  $<200$  attosecond up to picosecond time scales enabling the application of attosecond coherent control techniques to manipulate electronic and nuclear dynamics. This was demonstrated in an experiment on the dissociative ionization of oxygen.

A broad range of harmonics was used to coherently ionize several electronic states of the  $O_2^+$  molecule. The interference of the infrared field in both the pump and the probe arm gave rise to a delay dependent infrared field intensity (optical interference). By adjusting the delay between the XUV/IR pump and the IR probe pulses, I was able to modify the ionization yield of  $O_2^+$ . Two processes contribute to the time dependent ionization probability. (i) The ionization via direct multi-photon ionization of the infrared field, and (ii) the IR assisted ionization where harmonic orders below the ionization threshold (i.e. the 7<sup>th</sup> harmonic) combined with the infrared field.

The infrared beam was then used to manipulate the dissociation dynamics of excited  $O_2^+$  ions. Oscillations of the  $O^+$  yield at the frequency of the infrared field as well as at higher frequencies were observed in several dissociation channels of the  $O_2^+$  ions that are not accessible by multi-photon ionization with a strong IR-field. This is believed to be a result of an intensity dependent population shift between multiple coherently excited bound states of the  $O_2^+$  ion, as well as possibly the creation of new dissociation channels, enabled by the presence of the infrared field. Furthermore, sub-cycle oscillations of the ion yield were observed that indicate quantum interference of the different electronic states coupled by the infrared field in the probe arm.

By selecting the molecular orientation of the measured  $O^+$  ion emission direction with respect to the polarization of the laser field, I tried to select the contributions of different electronic  $O_2^+$  states to the dissociation into  $O^+$  ions. Despite the low repetition rate of the

harmonics source, this method successfully revealed signals with different phases of oscillation that could possibly correspond to different dissociation pathways. Unfortunately, the complex electronic structure of energetically overlapping dissociation pathways prevented the immediate clear identification of a particular pathway to the observed signals using the current data. The interpretation of the specific states and the corresponding quantum beating frequencies is very challenging for state-of-the-art computations and requires a combined effort of experiment and theory. Future measurements yielding higher statistics, as well as the measurement of photoelectrons and ions in coincidence, will provide further information for identifying the specific processes.

## 7.2 Outlook

The experiments with argon atoms, as well as hydrogen and oxygen molecules, presented in the previous chapter, showcase the capabilities of the novel combination of a high flux high harmonics source delivering femtosecond VUV-XUV pulses with a 3D momentum imaging setup that provides rich information for investigating molecular dynamics. Meanwhile, these experiments should be seen as a starting point for further development of this technique. Measurements that could follow-up and extend the presented results are discussed in the following section.

### Control of Dissociative Ionization of H<sub>2</sub>

The measurements performed with hydrogen and deuterium molecules have displayed a significant variation in the pathways of the channels observed indicating a strong sensitivity to the photon energy. Performing coincidence photoion - photoelectron measurements of the dissociative ionization of hydrogen molecules would provide additional information about the states involved. By varying the pressure in the HHG cell and the resulting change in the photon energy, the dominant pathways to ionization and dissociation could be changed as specific transitions are tuned in and out of resonance.

A careful characterization of the photon energies is hereby required. This can be performed by measuring both the spectrum of the fundamental beam at various gas cell pressures, as well as the harmonic spectrum in the XUV-spectrometer. The XUV-spectrometer can be calibrated by observing well known absorption lines of gases filled into the filter cell, or by comparing the measured spectrum to electron energy measurements obtained from MISTERS. The electron spectrometer energy calibration could be obtained from measuring ATI peaks from multi-photon ionization that have a well-defined energy spacing.

### Attosecond Coherent Control

Several experiments could be performed to improve the understanding of the dissociation pathways in the dissociative ionization of oxygen molecules and to try to control the coherent dynamics of specific states.

A coincidence measurement of photoions and photoelectrons in the dissociative ionization of oxygen molecules using the harmonic orders 11 - 13 will help to identify specific dissociation pathways. Selecting the 13<sup>th</sup> and the 11<sup>th</sup> harmonic only will eliminate the direct population of the  $B^2\Sigma_g^-$  and higher states, reducing the channels available for dissociation, hereby simplifying the complex dynamics. The evolution of specific channels can then be investigated by utilizing a well-defined infrared field strength, which can be achieved by inserting an IR-only filter glass in the probe arm in combination with a measurement of the infrared flux with a calibrated photo-diode/filter combination.

Furthermore, second harmonic radiation created by frequency doubling in a BBO crystal can be used to couple coherently excited states by neighboring odd harmonics. While the infrared beam can couple such states by the absorption of two photons, states lying between the harmonics will contribute to the oscillation signal. Inter-state coupling initiated by the 2<sup>nd</sup> harmonic is therefore likely to yield a simpler spectrum of yield oscillations that is easier to interpret. Furthermore, the second harmonic as a probe pulse can be considered as a perturbation to the molecule without modifying the electronic potential structure of the molecule. This is a result of the  $1/\lambda^2$  scaling of the electric field from the perturbative to the strong-field regime.

### Wave Packet Dynamics in Other Molecules

High Harmonic Generation (HHG) sources deliver photon energies in the laboratory that are otherwise only available at large scale facilities such as synchrotrons and free electron lasers. While the photon flux of HHG sources will remain much lower than the flux at free electron lasers, a practical amount of photons can already be produced for 2-photon absorption of one XUV and one VUV photon, as demonstrated in the measurements with molecular hydrogen (see Figure 6.9). At this time, the available flux is still a limiting factor in the choice of photon energy for probing a particular process (see Section 7.3 below). However, it is expected that future laser development will deliver machines that overcome this limitation. Projects in the United States (Florida State University) as well as Europe (Eli Institute, Hungary) are actively developing sources that will provide higher amounts of photons per pulse as well as repetition rates several orders of magnitude higher than in current models.

With the experience obtained from the experiments in hydrogen and oxygen, the same techniques could be applied to other molecules. The investigation of the dynamics in neutral states is a goal of such studies. Using the information from experiments performed at high repetition rates using Velocity Map Imaging (VMI) at the neighboring LBNL laboratory, on ethylene, CO<sub>2</sub>, and nitro-phenol molecules, the MISTERS end-station can complement such findings by performing electron-ion coincidence experiments or by taking advantage of the unique ultra-high resolution. Any time-resolved experiments, however, need to be targeted to a specific time-scale and process to overcome the low statistics that are obtained at the low repetition rate currently available.

## 7.3 Instrument Improvements and Development

The setup presented here faces limitations in multiple areas that will be discussed in the following section. Some of these challenges can be addressed in future experiments with improvements in the laboratory that can be implemented with more time and money. Other new developments presented here require further research or technical solutions that are not available as yet.

The low repetition rate of just 50 Hz of the present laser system was one of the most important factors limiting the capabilities of this experimental setup. Basic tasks that are routinely performed in other setups, such as the adjustment of the beam pointing, the pump-probe ratio, or the magnetic field-strength were made difficult or nearly impossible due to the lack of experimental feedback within a reasonable time period.

The strength of a COLTRIMS reaction microscope is the ability of measuring coincidences on a shot-by-shot basis which requires high repetition rates. At a repetition rate of 1 kHz, which is already delivered by a laser system in the neighboring laboratory at LBNL, the conditions will improve significantly. Not only does this allow for real-time feedback of

adjustments to the end-station and the beamline, but the increase of the repetition rate by a factor of 20 can enable experiments that are not feasible at this time. An experiment requiring two days at 1 kHz would require 40 days with the current system, much longer than the typical time for stable operation of a high power laser system.

At higher repetition rates, beyond 10 or 100 kHz, the coincidence measurement of the 3D momenta of electrons and ions provides the possibility to perform high dimensional differential measurements that have not been possible with this setup yet. In this sense, the full potential of 3D momentum imaging in the time domain has not been reached yet.

Velocity map imaging (VMI) momentum spectrometers are better suited to handle the problems of a high count rate at low repetition rates as they are not limited by the amount of ions that can be recorded per shot. They do not, however, provide the full 3D momentum information of the molecular fragments, as they measure a two dimensional distribution only. An Abel-transform algorithm with symmetry conditions is required to reconstruct the 3D momentum image. In the measurements of hydrogen and oxygen molecules presented here, it was demonstrated that all three spatial dimensions can provide useful information about the reaction. One example is the ultra-high resolution of the spectrometer that requires a specific geometric arrangement of the detectors with respect to the supersonic jet and the photon beam. In the time-of-flight direction a significantly higher resolution was obtained than in the other spatial directions (see Figure 5.8). This advantage over the VMI approach was an important feature in the studies presented here.

### Electron Acquisition

Only one coincidence measurement of electrons and ions was shown in this work. This is mainly due to the challenges connected to the acquisition of electrons created at very high photon rates in a single laser shot. At photon energies in the VUV and XUV, which is above the work function of most materials, nearly every photon impinging on a surface will create an electron. Electrons created outside of the spectrometer can be repelled by a negative bias or are steered away by the magnetic field of the Helmholtz coils. Meanwhile, electrons created by stray photons inside the spectrometer will travel to the MCP detector and create a background overlaying the electrons created in the target.

Such stray photons were a major problem with the current setup. The stray light could be reduced by confining the beam path using apertures, an iris as well as a set of collimators. However, other photons that can enter the spectrometer result from diffraction of the VUV and XUV laser beam on the back-focusing mirror surface as well as from penetrating (VUV photons only) the mirror substrate and being reflected off the rear-surface of the mirror or the mount surface. A baffle was designed to prevent photons from exiting the mirror surface at wide angles which reduced this effect. Further testing with different baffle diameters or lengths as well as with other substrate materials, such as SiC or BK7, and different substrate thicknesses is needed. Increasing the distance of the focusing mirror to the spectrometer would also help to reduce the amount of photons impinging on the spectrometer plates, but this would entail a reduction in beam intensity in the target. Such losses could be compensated by a higher harmonics flux. A very carefully collimated beam in combination with a more open spectrometer design that represents less obstacles for photons scattered off the focusing mirror surface could also be beneficial. However, the influence of large spectrometer plate spacing on the electric field geometry would require a careful investigation.

In certain experiments, a retarding field could be applied to the spectrometer reducing thereby the background of low energy electrons. In the initial experiments presented here, the ionization of background gas was of the same order of magnitude as the ionization of molecules in the target due to the large amount of residual water in the chamber. The

vacuum chamber was sealed using Viton rubber gaskets in order to allow for a quicker venting process when adjusting parts inside of the chamber. Future experiments will be performed in a fully baked chamber which will reduce the ionization of background gas by about 2 orders of magnitude. The bake-out process of the chamber was tested and optimized before attaching the chamber to the HHG beamline.

Events stemming from the ionization of warm target gas as well as from the ionization of the unfocused diverging beam could be reduced by replacing the current skimmer ( $\varnothing = 0.5$  mm) by a model with a smaller opening. The current jet geometry creates a target of approximately 1.9 mm diameter which is much larger than the laser focus. A skimmer with a diameter of 0.12 mm would result in a target sufficiently large ( $\varnothing = 0.45$  mm) to cover the entire focus while reducing both the flow of warm gas by a factor of  $\sim 4$ , as well as the ionization by the unfocused beam in the dense gas target. The ultimate pressure in the target chamber during jet operation is currently limited by the flow of gas from the 2<sup>nd</sup> jet stage to the target zone ( $\sim 1 \times 10^{-10}$  mbar).

Even with a perfect suppression of electrons created outside of the target, the measurement of electron correlation through double photoionization in a pump-probe scheme with pulses in the XUV spectrum is challenging due to the inherent large single ionization background. In order to surpass the double-ionization threshold, the energy of 1 of the 2 pulses needs to exceed the single ionization threshold. As the absorption of a single photon is more likely than the absorption of photons from both pulses, a large amount of background will be created by electrons ionized from the absorption of just one photon. Additionally, the single ionization probability is likely to surpass the double ionization probability in most cases.

One scenario of pulse choice could be the excitation of a neutral state of a molecule by the pump pulse with sufficient intensity to saturate the target such that the probe pulse is very likely to encounter an already excited molecule. With an energy below the ionization threshold, the pump pulse would not create any electrons while the ionizing probe pulse, causing a single ionization background, can be chosen at lower intensity. This scheme, although desirable, is limited to the investigation of neutral states.

A parallel effort can be made in the ability to increase the multi-hit capability of the delay-line anode by the use of a fast pulse height digitizer. Such an acquisition system is available in the laboratory but it could not be installed at the time of writing. New detector technology would improve the multi-hit capability based on ADC readout of strip lines or pixel based detectors.

### Improved Energy Selection

Another limitation in the current setup consists in the ability for selection and characterization of the photon energy. Several tools such as solid filters, gas filters, and windows were used to select a specific energy range. A special XUV-spectrometer was developed to characterize the spectrum incident on the gas target. However, the range of energies that can be selected is very limited and the transmitted bandwidth is large. If the process to be investigated is not very dominant in the selected energy range, it can be obscured by contributions from other transitions. The coincidence measurement with electrons can be an important tool to help identify the reaction pathway of particular ionic fragments.

Further experiments should take advantage of the high reflectivity and spectral selectivity of multilayer mirrors designed for the specific experiment. A B<sub>4</sub>C broadband coating was used in the experiment presented here as it offered good reflectivity in a broad range of harmonics that was suitable for performing a variety of tests during the commissioning of the setup. A custom coating for the energy required in a specific experiment in the

spectral range above  $\sim 15$  eV could increase the amount of XUV photons delivered to the target by  $\sim 20 - 50$  % at a spectral bandwidth of  $\sim 2 - 5$  eV.

The ideal tool for the selection of a specific photon energy is a monochromator. Such tools are standard at synchrotrons and have already been developed using matched grating pairs for the operation with high harmonic sources [25, 121]. Due to the additional optical components, the transmission is relatively low ( $\sim 10\%$ ) which would inhibit the ability of performing pump-probe studies with XUV-VUV pulse pairs at the flux available with this setup. If the monochromator can replace the optics required for the suppression of the infrared beam, in this case two silicon mirrors, a slightly higher flux might suffice for performing pump-probe studies. A particular challenge, however, consists in preventing damage to the monochromator grating due to the high infrared power of the fundamental beam in a high flux HHG setup. This could be addressed by a larger beam size, or a longer propagation length.

Damage to the optics, both in the multi-pass amplifier as well to the in-vacuum optics, has been a large problem in the current setup. A high power laser system requires constant maintenance and assistance from experienced researchers or technicians. In this laboratory, improvements in the multi-pass setup, the oscillator stability as well as a crystal replacement are planned but have not been performed due to the lack of time and money. Regular or in-vacuum cleaning of the silicon mirrors to maintain good reflectivity would improve the available XUV flux. Ozone or microwave based cleaning techniques are being developed and will become available soon.

There are many efforts to increase the spectral range of HHG and more specifically the flux at energies in the so-called water window. In some applications it might be feasible to obtain a sufficient flux using High Harmonic Generation in combination with the infrared field or other conversion schemes such as frequency doubling. The construction of a sufficiently bright source for 2-photon absorption at  $\sim 100$  eV or higher appears to be rather unlikely in the near future. Meanwhile the strength of high harmonics consists in delivering photon pulse in the VUV to the soft X-ray spectrum with sufficient bandwidth for attosecond pulse trains or even single attosecond pulses. New free electron laser facilities such as the European X-FEL and the extension of the LCLS in California will only provide energies as low as few hundred eV, relying on HHG sources to cover the lower spectral range. In the experiments shown here, some examples of the richness of possibilities for studying the nuclear and electronic dynamics of the neutral and ionic states in molecules were presented.

### Increasing High Harmonics Flux

As outlined above, increasing the available flux of high harmonics can be beneficial in the ability to select specific photon energies, as well for addressing photon background issues. Several ways can be pursued to improve the output flux of the current High Harmonic Generation cell.

Phase matching in the harmonics cell, thus, in many cases the total harmonics flux, can be very sensitive to the spatial mode of the generating fundamental beam. In the current setup, the crystal in the multi-pass amplifier was damaged creating an uneven beam mode. A higher quality mode is likely to improve the phase matching and therefore the harmonics flux.

The output for orders below the ionization threshold of the generation medium is not absorption limited and can be increased with a higher cell pressure. This is beneficial only in experiments where no high orders are used, such as in studies of neutral states, because the emission of high orders is suppressed due to absorption and phase matching at high cell pressures. The current cell design allowed for pressures up to 10 Torr. A modified design

with additional differential pumping sections at the entrance and exit of the cell would allow operation at much higher pressure. In the present design, thin metal shims separate the gas filled cell from the vacuum but are exchanged daily because they are widened continuously as a result of pointing instability of the laser beam. Exchanging 4 shims, needed in a differentially pumped cell, on a daily basis would be too time consuming. An active pointing stabilization of the laser beam would be required to implement such a cell.

Another interesting option for optimizing high flux for a specific wavelength is the use of multiple gas cells. The cell parameters for optimal High Harmonic Generation vary from the VUV to the XUV spectral region due to the different phase matching and absorption conditions. Therefore, using two separate cells with different lengths, pressures, and generation media would be preferable. One cell could be optimized for generating low order harmonics for the pump pulse, while the other cell could generate high harmonics used as the probe pulse with high efficiency, or vice-versa. The cells could be placed in line with the laser beam first passing through the low order cell and subsequently through a cell optimized for high orders. Alternatively, the fundamental beam could be split into two parallel arms with each passing through only one cell. Having initially separated beams has the additional advantage that no losses and no modification of the spatial mode would occur in the gap of the Split-Mirror-Interferometer, as each beam could be steered onto one parallel mirror. Currently, the deterioration of the beam profile by the mirror edges in the center of the beam increases the focus size in the target by a factor of  $\sim 2 - 3$ . Beam stability issues could arise, however, as a result of the increased separate beam path.

The addition of a BBO crystal to the beamline is not only beneficial as a tool for coherent control or ultraviolet molecular excitation, but also for increasing the high harmonic generation efficiency. A combination of the fundamental beam and the second harmonic generated in a BBO crystal has been successfully used to generate high harmonics with high efficiency [77].

## 8 Zusammenfassung

Pump-Probe-Spektroskopie mit spezifisch ausgewählten mehrfarbigen Vakuum-Ultraviolett- (VUV) und Extrem-Ultraviolett-Pulsen (XUV) gilt als vielversprechende Methode zur Untersuchung von femtosekunden Dynamik in Molekülen in Echtzeit auf fundamentaler Ebene. Nichtsdestotrotz verursacht die Präsenz von mehreren Farben im Photonenspektrum von von zwei oder mehr Pulsen eine Vielzahl von Ionisations- und Dissoziationswegen, die in Einphotonenionisation oder der Ionisation in einem starken Laserfeld nicht auftreten können und daher kaum verstanden sind. Experimente sind daher nötig, die die elektronischen Zustände sowie die Evolution von nuklearen Wellenpaketen auf den Potentialkurven des Moleküls, in mehrfarbigen Multiphoton-Ionisationsprozessen untersuchen.

Im Rahmen dieser Arbeit wurde die komplexe Struktur von Ionisations- und Dissoziationspfaden auf den Potentialkurven von kleinen Molekülen untersucht, die bei der Absorption einer Sequenz von mehrfarbigen Pulsen im XUV-, VUV- und Infrarotspektrum (IR) auftreten. Mittels Femtosekunden-Pump-Probe-Spektroskopie wurde die zeitliche Entwicklung der nuklearen Dynamik in neutralen Wasserstoffmolekülen verfolgt und neue Anregungs- und Ionisationspfade, die zur dissoziativen Ionisation von Wasserstoffmolekülen führen, konnten durch die Anwendung von 3D-Impulsspektroskopie identifiziert werden. Diese Experimente wurden auf Sauerstoffmoleküle erweitert, in denen XUV-Attosekunden-Pulszüge mehrere elektronische Zustände von  $O_2^+$  kohärent ionisierten, gefolgt von der Dissoziation des Moleküls auf verschiedenen Pfaden. Das Infrarotfeld des treibenden Lasers wurde genutzt, um die elektronischen und nuklearen Wellenpakete zu koppeln und damit die Dissoziationsdynamik des Moleküls auf einer Attosekunden-Zeitskala zu manipulieren. Dies repräsentiert einen wichtigen Schritt in Richtung der kohärenten Kontrolle von fundamentalen photochemischen Reaktionen von kleinen Molekülen auf einer Attosekunden-Zeitskala.

Um die hier präsentierten Experimente zu verwirklichen, wurde in Zusammenarbeit mit mehreren Mitarbeitern<sup>1</sup> ein neuartiger experimenteller Aufbau entwickelt und gebaut. Dieser verbindet eine bestehende besonders flussstarke Lichtquelle hoher Harmonischer (HHG), die Attosekunden-Pulszüge im VUV- und XUV-Spektrum produziert, mit einem state-of-the-art 3D-Impulsspektroskopie-Apparat sowie einem Strahlrohr mit einer Vielzahl an Werkzeugen zur Auswahl, Charakterisierung und zum Transport des Photonenspektrums.

Die große Anzahl an Photonen pro Puls der benutzten HHG-Quelle ermöglichte die Beobachtung von Zweiphotonen-Ionisation durch Absorption von XUV- und VUV- Pulspaaren in der dissoziativen Ionisation von Wasserstoffmolekülen (siehe Bild 6.9). Bislang unveröffentlichte Dissoziationspfade, verursacht durch die Absorption von XUV- und IR-Photonen, konnten durch Ausnutzen der Leistungsfähigkeit und der Auflösung des MISTERS 3D-Impulsspektroskopie Aufbaus identifiziert werden. Sogar in Wasserstoff, dem einfachsten neutralen Molekül mit lediglich zwei Elektronen, stellt sich die Identifizierung der beobachteten Prozesse als anspruchsvoll heraus. Dies unterstreicht, dass die Untersuchung von Benchmark-Systemen wie zwei- oder dreiatomigen Molekülen nötig ist, um die durch Mehrphotonen Absorption im IR-, VUV- und XUV-Spektrum ausgelösten Prozesse zu verstehen. Dies ist besonders wichtig, um theoretische Modelle zu testen, die essentiell zum Verständnis der Beobachtungen in Mehrphotonen-Absorptionsexperimenten in komplexeren Molekülen wie Kohlenwasserstoffe oder größeren biologisch relevanten Systemen sind.

---

<sup>1</sup>siehe Tabelle 6 in der Danksagung für individuelle Beiträge

Die Kombination eines molekularen Überschallgasjets und einer kleinen Fokusgröße, erreicht durch Rückfokussieren des Laserstrahls mit einem Spiegel kurzer Brennweite, lieferte 3D-Impulsspektroskopie-Bilder mit außergewöhnlicher Auflösung. In Sauerstoffmolekülen konnte die Vibrationsstruktur von mehreren elektronischen Zuständen mit einer Präzision aufgelöst werden, die bislang nur in Elektronenspektroskopie-Experimenten erreicht wurde. Die Zeitabhängigkeit der Dissoziationspfade verschiedener Vibrationszustände kann mithilfe dieser extrem hohen Ionen-Impulsauflösung in zukünftigen Experimenten untersucht werden.

Zur Messung molekularer Dynamik in kleinen Molekülen wurde ein spezielles Interferometer mit geteiltem Spiegel entwickelt, das Pump-Probe-Experimente ermöglicht. Die Pulslänge von 10-20 Femtosekunden ermöglichte die Beobachtung der Bewegung eines nuklearen Wellenpaketes im neutralen  $B^1\Sigma_u^+$  Zustand von Wasserstoffmolekülen in Echtzeit. Im Experiment wurde dieser Zustand durch die 9. Harmonische des Infrarotstrahls angeregt und durch Multiphoton-Ionisation des Infrarotstrahls ionisiert. Dabei wurde eine zeitabhängige Oszillation des  $H_2^+$  Ionensignals mit einer Periode von  $\sim 70$  fs beobachtet. Bei kleinen Kernabständen um den Franck-Condon-Bereich kann das Molekül vom  $B^1\Sigma_u^+$  Zustand zum  $X\ 1s\sigma_g$  Grundzustand des Wasserstoffions durch die Absorption von zwei Infrarotphotonen ionisiert werden. Aufgrund der Energiedifferenz der neutralen und ionischen Zustände erfordert die Ionisation (und Dissoziation) bei größeren Kernabständen die Absorption von drei Photonen. Die Bewegung des Wellenpaketes im breiten Potentialtopf des  $B^1\Sigma_u^+$  Zustandes führt zu einer positions- und damit zeitabhängigen Änderung der Ionisationswahrscheinlichkeit (siehe Bild 6.7).

Ein Hauptvorteil hoher Harmonischer Lichtquellen im Vergleich zu Freie-Elektronen-Lasern besteht in der Möglichkeit, die Untersuchung von dynamischen Prozessen auf eine Attosekunden-Zeitskala zu erweitern. Die Wechselwirkung des starken Laserfeldes mit dem Medium (Edelgas) erzeugt eine Bandbreite, die Attosekunden-Pulse ermöglicht. Die hier verwendete Quelle produziert Attosekunden-Pulszüge mit fixer Phase zum treibenden Laserfeld. Das speziell entwickelte Interferometer mit geteiltem Spiegel liefert eine Stabilität von weniger als 200 Attosekunden bis hin zu Pikosekunden-Zeitskalen, welches die Anwendung von Attosekunden-Kontrolltechniken zur Manipulation von elektronischer und Kerndynamik ermöglicht. Dies konnte in einem Experiment zur dissoziativen Ionisation von Sauerstoffmolekülen demonstriert werden. Eine breite Verteilung von hohen Harmonischen wurde genutzt, um die Dissoziationsdynamik von angeregten  $O_2^+$  Ionen zu manipulieren. Die Interferenz des Infrarotfeldes im Pump- sowie im Probe-Puls, führte zu einer verzögerungsabhängigen Infrarotfeldstärke der beiden Pulse (optische Interferenz). Durch Einstellen der Verzögerung zwischen XUV/IR-Pump und IR-Probepuls konnte die Ionisationsrate von  $O_2^+$  Ionen manipuliert werden. Zwei Prozesse tragen zur beobachteten verzögerungsabhängigen Ionisationsrate bei: (i) Die Ionisation durch direkte Multiphoton-Ionisation des Infrarotfeldes und (ii) die Ionisation durch eine Kombination von Harmonischen unter der Ionisationsschwelle (z.B. die 7. Harmonische) mit dem Infrarotfeld.

Das Infrarotfeld wurde ebenfalls verwendet, um die Dissoziation von angeregten  $O_2^+$  Ionen zu manipulieren. Sowohl Oszillationen mit der Frequenz des Infrarotfeldes, als auch höhere Frequenzen wurden in mehreren Dissoziationskanälen beobachtet, die nicht bei Multiphoton-Ionisation in einem starken Laserfeld auftreten. Es ist anzunehmen, dass diese Oszillationen durch intensitätsabhängige Verschiebungen der Besetzung zwischen verschiedenen kohärent angeregten gebundenen Zuständen der  $O_2^+$  Ionen verursacht wird sowie möglicherweise durch neue, vom starken Infrarotfeld geschaffene Dissoziationskanäle. Des Weiteren wurden Oszillationen mit etwa doppelter Frequenz des Infrarotfeldes beobachtet, die auf Quanten-Interferenz zwischen verschiedenen, durch das Infrarotfeld gekoppelten, elektronischen Zuständen hinweisen.

Durch Selektion bestimmter Molekülausrichtungen der gemessenen  $O^+$  Ionenemission im Verhältnis zur Polarisationsrichtung des Laserfeldes wurde versucht, die Beiträge verschiedener elektronischer  $O_2^+$  Zustände zur Dissoziation in  $O^+$  Ionen zu unterscheiden. Trotz der niedrigen Repetitionsrate der HHG-Quelle, konnte diese Methode erfolgreich Signale mit unterschiedlichen Phasen aufdecken, die möglicherweise verschiedenen Dissoziationspfaden entsprechen. Leider erlaubte die komplexe Struktur von energetisch überlappenden Dissoziationspfaden bislang nicht die eindeutige Zuordnung der beobachteten Signale zu einzelnen Pfaden anhand der vorliegenden Daten. Die Interpretation der spezifischen elektronischen Zustände und der entsprechenden Quantum-beat-Frequenzen ist selbst mithilfe modernster Berechnungen extrem schwierig und verlangt eine gemeinsame Anstrengung auf experimenteller sowie theoretischer Seite. Künftige Experimente mit höherer Statistik, sowie der Koinzidenzmessung von Photoelektronen und Ionen werden weitere Informationen zur Identifizierung der individuellen Prozesse liefern.

## 8.1 Ausblick

Die hier präsentierten Experimente mit Argonatomen, Wasserstoffmolekülen und Sauerstoffmolekülen demonstrieren die Möglichkeiten der neuartigen Kombination einer hohen Harmonischen Lichtquelle mit hohem Fluss von Femtosekunden-Pulsen im VUV-XUV Spektrum mit einem 3D-Impulsspektroskopie Apparates, die reichhaltige Informationen zur Untersuchung molekularer Dynamik liefert. Gleichzeitig stellen diese Experimente lediglich den ersten Schritt zur weiteren Entwicklung dieser Methode dar. Im Folgenden werden weitere Experimente diskutiert, die auf den durchgeführten Messungen aufbauen und diese erweitern.

### Kontrolle der dissoziativen Ionisation von $H_2$

Die Messungen mit Wasserstoff- und Deuteriummolekülen haben eine starke Abhängigkeit der beobachteten Dissoziationskanäle mit der Photonenenergie gezeigt. Messungen in denen Photoelektronen und Ionen in Koinzidenz gemessen werden, würden neue Informationen liefern, mit denen alle involvierten elektronischen Zustände eindeutig bestimmt werden könnten. Durch Variieren des Druckes in der hohen Harmonischen Gas-Zelle und der damit verbundenen Änderung der Photonenenergie werden verschiedene elektronische Übergänge in und aus der Resonanz gebracht, womit verschiedene Ionisations- und Dissoziationsphade besser selektiert werden könnten.

Eine sorgfältige Charakterisierung der Photonenenergie ist hierbei erforderlich. Dies kann durch die Messung des fundamentalen Infrarotstrahls bei verschiedenen Zelldrücken sowie die gleichzeitige Messung des Spektrums der Harmonischen im XUV-Spektrometer erreicht werden. Letzteres kann durch die Messung von bekannten Absorptionslinien von Gasen in der Gaszelle kalibriert werden, oder durch Vergleichen der Photonenenergie mit Messungen der Elektronenenergie im MISTERS-Impulsspektrometer. Die absolute Energieeichung des Impulsspektrometers kann anhand des festen Energieabstandes von ATI-peaks in Multiphotonen-Ionisation erhalten werden.

### Kohärente-Attosekunden-Kontrolle

Verschiedene Experimente könnten zum Verständnis der Dissoziationsmechanismen in der dissoziativen Ionisation von Sauerstoffmolekülen beitragen und darüber hinaus versuchen, die kohärente Dynamik verschiedener Zustände zu kontrollieren.

Die Koinzidenzmessung von Photoelektronen und Ionen in der dissoziativen Ionisation durch die 11. und 13. Harmonische würde dabei helfen, spezifische Dissoziationskanäle zu

identifizieren. Das Selektieren der 11. und 13. Harmonischen verhindert die direkte Anregung des  $B^1\Sigma_u^+$  und höhere Zustände, welches die Anzahl der offenen Dissoziationskanäle reduziert und damit die komplexe Dynamik des Systems vereinfacht. Die zeitliche Entwicklung spezifischer Kanäle kann dann mithilfe eines gut charakterisierten Infrarotfeldes untersucht werden, welches durch Einsetzen eines IR-transmittierenden Filterglases und der Messung des Infrarot-Flusses mit einer IR-Photodiode/Filter-Kombination erreicht werden kann.

Darüber hinaus könnte die zweite Harmonische des Infrarotfeldes durch Frequenzverdopplung in einem BBO-Kristall erzeugt werden, um elektronische Zustände zu koppeln, die durch benachbarte ungerade Harmonische angeregt werden. Das Infrarotfeld ermöglicht bereits das Koppeln dieser Zustände durch die Absorption von zwei Photonen, jedoch tragen Zustände, die zwischen den beiden harmonischen Ordnungen liegen zum beobachteten Signal bei. Das Koppeln verschiedener Zustände durch die zweite Harmonische führt daher erwartungsgemäß zu einem einfacheren Spektrum an Oszillationen, welches leichter zu interpretieren ist. Des Weiteren kann ein Probe-Puls der zweiten Harmonischen als Störung des Moleküls betrachtet werden, der dessen elektronische Struktur nicht wesentlich modifiziert. Dies folgt aus der  $1/\lambda^2$  Abhängigkeit der Beschreibung des elektrischen Feldes von Störungsrechnung zum Starkfeld-Regime.

## Wellenpaket-Dynamik in weiteren Molekülen

Die Erzeugung von hohen Harmonischen in HHG-Quellen liefert Photonenenergien im Labor, die sonst nur in Großanlagen wie Synchrotrons und Freie-Elektronen-Lasern erzeugt werden können. Obwohl der Photonenfluss von HHG-Quellen auch weiterhin deutlich geringer als von Freie-Elektronen-Lasern bleiben wird, kann bereits eine praktische Menge zur Zweiphotonen-Absorption mit einem XUV und einem VUV-Photon erzeugt werden, wie in den Messungen mit molekularem Wasserstoff demonstriert wurde (siehe Bild 6.9). Zum jetzigen Zeitpunkt ist die verfügbare Photonenzahl ein einschränkender Faktor in der Wahl der Photonenenergie zur Untersuchung eines bestimmten Prozesses (siehe folgender Abschnitt 7.3). Es ist allerdings zu erwarten, dass die Entwicklung von Lasern in der nahen Zukunft Quellen hervorbringt, die diese Limitierung überwinden. Im Rahmen von Projekten in den Vereinigten Staaten (Florida State University) sowie in Europa (Eli Institute, Hungary) werden Quellen entwickelt, deren Photonenzahl pro Schuss als auch Repetitionsraten heutige Modelle um mehrere Größenordnungen übersteigen.

Mit den Erfahrungen aus den Experimenten in Wasserstoff- und Sauerstoffmolekülen könnten die gleichen Techniken auf weitere Moleküle angewandt werden. Die Untersuchung der Dynamik von neutralen Zuständen ist ein Ziel solcher Versuche. Durch Nutzen der Ergebnisse aus Experimenten, die bei hohen Repetitionsraten mit Velocity Map Imaging (VMI) im Nachbarlabor am LBNL aufgenommen wurden, könnten komplexere Moleküle wie Kohlendioxyd, Ethylen und Nitrophenol untersucht werden. Das MISTERS 3D-Impulsspektrometer kann solche Experimente durch die Koinzidenzmessung von Elektronen und Ionen sowie die besonders hohe Auflösung ergänzen und erweitern. Zeitaufgelöste Experimente müssen jedoch auf eine bestimmte Zeitskala und eine bestimmte Reaktion optimiert werden, um das Problem niedriger Statistik bei der niedrigen Repetitionsrate des derzeitigen Lasersystems zu überwinden.

## 8.2 Verbesserung und Weiterentwicklung des Aufbaus

Die Leistungsfähigkeit des im Rahmen dieser Arbeit entwickelten experimentellen Aufbau ist in verschiedenen Bereichen begrenzt, die in diesem Abschnitt diskutiert werden. In

einigen Bereichen können die Fähigkeiten in künftigen Experimenten durch Verbesserungen im Labor mit mehr Zeit und Geld erweitert werden. Andere Bereiche erfordern weitere Forschung und technische Lösungen, die derzeit noch nicht verfügbar sind.

Die niedrige Repetitionsrate des Lasersystems von lediglich 50 Hz stellte einen der wichtigsten Faktoren dar, der die Leistungsfähigkeit des Aufbaus limitierte. Standardaufgaben, die routinemäßig in anderen Aufbauten durchgeführt werden, wie die Einstellung der Strahlposition, das Pump-Probe-Verhältnis oder die Stärke des Magnetfeldes, waren extrem schwierig oder fast unmöglich durchzuführen aufgrund der fehlenden Rückmeldung des Messapparates in einem angemessenen Zeitraum.

Die Stärke eines COLTRIMS Reaktionsmikroskopes liegt in der Fähigkeit von Koinzidenzmessungen auf Basis einzelner Schüsse, welches hohe Repetitionsraten erfordert. Eine Repetitionsrate von 1 kHz, welche das Lasersystem im Nachbarlabor am LBNL liefert, würde die experimentellen Umstände bereits deutlich verbessern. Dies würde nicht nur eine Rückmeldung der Einstellungen der Strahlrohrkomponenten und des Experimentapparates in Echtzeit erlauben, sondern eine um den Faktor 20 erhöhte Repetitionsrate würde Experimente ermöglichen, die derzeit nicht durchführbar sind. Die Durchführung eines 2 Tage dauernden Experimentes bei 1 kHz Repetitionsrate würde 40 Tage mit dem jetzigen System erfordern. Dies ist deutlich länger als der übliche Stabilitäts-Zeitraum eines Hochleistungs-Lasersystems.

Bei noch höheren Repetitionsraten größer als 10 oder 100 kHz würden die Koinzidenzmessungen der 3D-Impulse von Elektronen und Ionen darüber hinaus hoch differentielle Messungen ermöglichen, die mit dem derzeitigen Aufbau nicht möglich sind. In dieser Hinsicht ist das volle Potential von koinzidenter 3D-Impulsspektroskopie noch nicht erreicht.

Velocity Map Imaging (VMI) Impulsspektrometer sind besser auf hohe Zählraten bei niedriger Repetitionsrate ausgelegt, da sie nicht in der Zählrate pro Schuss limitiert sind. Jedoch liefern VMI-Spektrometer keine echte 3D Impulsinformation, sondern messen nur die zweidimensionale Projektion der Fragmente. Zur Rekonstruktion der 3D Impulsverteilung wird eine Abel-Transformation angewandt, die Symmetrie entlang der Polarisationsrichtung erfordert. In den Experimenten mit Wasserstoff und Sauerstoffmolekülen wurde gezeigt, dass die Impulse in allen drei Raumdimensionen nützliche Informationen über die Reaktion liefern können. Als Beispiel kann die besonders hohe Auflösung des Spektrometers genannt werden, die eine spezielle geometrische Ausrichtung des Detektors zum Überschallgasjet sowie der Photonenrichtung erfordert. In Flugzeitrichtung wurde eine deutlich höhere Auflösung erreicht, als in den anderen Raumrichtungen (siehe Bild 5.8). Dieser Vorteil im Vergleich zu VMI-Spektrometern stellte einen wichtigen Aspekt in den hier vorgestellten Experimenten dar.

## Elektronenmessung

In dieser Arbeit wurde nur ein Experiment vorgestellt, in der Elektronen und Ionen in Koinzidenz gemessen wurden. Die von der Lichtquelle produzierte hohe Anzahl an Photonen pro Schuss verursachte Elektronenraten die in vielen Fällen die maximale Aufnahme rate des Delayline-Anodendetektors überstieg. Da Photonenenergien im VUV- und XUV-Spektrum oberhalb der Austrittsarbeit der meisten Materialien liegen, erzeugt jedes auf eine Oberfläche auftreffende Photon ein Elektron. Elektronen, die außerhalb des Spektrometers entstehen, können durch ein negatives Potential des Spektrometers oder durch das magnetische Feld der Helmholtz-Spulen weggeleitet werden. Dagegen gelangen Elektronen, die durch Streuphotonen innerhalb des Spektrometers entstehen, ungestört auf den MCP-Detektor und erzeugen einen Untergrund, der das Signal von Elektronen aus der Reaktionszone überlagert.

Solche Streuphotonen stellten ein großes Problem in diesem Aufbau dar. Das Streulicht konnte durch Begrenzung des Strahlgangs mit Blenden, Kollimatoren und einer Iris begrenzt werden. Dennoch entstehen weitere Photonen, die in das Spektrometer eindringen, durch diffuse Streuung des VUV und XUV-Laserstrahls auf der Oberfläche des rückfokussierenden Spiegels, sowie durch Eindringen in das Substratmaterial des Spiegel und der darauffolgenden Reflexion von der Spiegelrückseite oder der Oberfläche des Spiegelhalters. Dieser Effekt wurde durch die Anbringung eines Dämpfers reduziert, der Photonen am Verlassen der Spiegelfläche unter weitem Winkel verhindert. Weitere Tests mit verschiedenen Längen und Durchmessern des Dämpfers sowie mit verschiedenen Spiegelmaterialien wie SiC oder BK7 und deren Substratdicke sind jedoch nötig. Ein längerer Abstand zwischen rückfokussierendem Spiegel und Spektrometer würde den Photonenuntergrund ebenfalls verringern. Gleichzeitig würde damit aber eine Reduzierung der Strahlintensität in der Reaktionszone einhergehen. Solche Verluste könnten durch einen höheren Fluss von hohen Harmonischen ausgeglichen werden. Darüber hinaus könnte ein sorgfältig kollimierter Strahl in Kombination mit einem weiter geöffneten Spektrometerdesign, das die Oberfläche für gestreute Photonen des fokussierenden Spiegels verringert, den Elektronenuntergrund verringern. Jedoch muss die mögliche Verzerrung des elektrischen Feldes, welche mit einem größeren Spektrometerplattenabstand einhergeht, sorgfältig bedacht werden.

### Verbesserte Energie-Selektion

Eine weitere Einschränkung des bestehenden Aufbaus besteht in der Auswahl und Charakterisierung der Photonenenergie. Verschiedene Werkzeuge wie Folien, Gasfilter und Fenster wurden verwendet, um spezifische Energiebereiche auszuwählen. Ein spezielles XUV-Spektrometer wurde entwickelt, um das in der Reaktionszone ankommende Photonenpektrum zu charakterisieren. Dennoch sind die Energiebereiche, die ausgewählt werden können, und deren Bandbreite ist relativ breit. Daher kann ein Prozess, der nicht besonders dominant im ausgewählten Energiebereich ist, leicht durch Beiträge anderer Übergänge überdeckt werden. Konizidenzmessungen mit Elektronen können hierbei ein wichtiges Hilfsmittel zur Identifikation bestimmter Reaktionskanäle darstellen.

Zukünftige Experimente sollten darüber hinaus spezifische Multischichtspiegel nutzen, mit denen ein hohe Reflektivität und ein geringe Bandbreite erreicht werden kann. In den hier vorgestellten Experimenten wurde ein Spiegel mit breitbandiger B<sub>4</sub>C Beschichtung verwendet, da dieser eine relativ gute Reflektivität über einen großen Bereich von harmonischen Ordnungen verfügt und damit für eine Vielzahl an Tests während der Inbetriebnahme des experimentellen Aufbaus geeignet war. Ein für eine bestimmte Photonenenergie oberhalb von  $\sim 15$  eV spezifisch entworfener Mehrschichtspiegel kann den Photonenfluss in der Reaktionszone um etwa 20 - 50 % bei einer Bandbreite von  $\sim 2 - 5$  eV steigern.

Das ideale Werkzeug zur Auswahl einer spezifischen Photonenenergie ist ein Monochromator. Monochromatoren werden standardmäßig in Synchrotrons eingesetzt und wurden bereits mithilfe von angepassten Reflexions-Gittern für HHG-Lichtquellen entwickelt [25, 121]. Aufgrund der zusätzlichen optischen Komponenten ist die Transmissionsrate eines solchen Apparates relativ gering ( $\sim 10\%$ ). Eine solche Transmissionsrate wäre mit dem Photonenfluss des bestehenden Lasersystems nicht ausreichend, um Pump-Probe-Experimente mit XUV-VUV Pulspaaren durchzuführen. Falls der Monochromator die Komponenten zur Unterdrückung des Infrarotstrahls ersetzen kann, in derzeitigen Aufbau wird dies durch zwei Silikonspiegel erreicht, könnte bereits eine geringfügig höhere Photonenzahl von hohen Harmonischen ausreichen, um Pump-Probe-Experimente zu ermöglichen. In diesem Fall könnte es sich allerdings als schwierig erweisen, eine Beschädigung der Monochromator-Gitter durch die hohe Energiedichte des Infrarotstrahls zu verhindern. Mögliche Lösungsansätze sind ein Erweitern der Strahlgröße oder eine längere Strahlpropagation.

### Erhöhung des Flusses von hohen Harmonischen

Wie bereits im vorherigen Abschnitt erwähnt, würde eine höhere Photonenzahl von hohen Harmonischen die Möglichkeiten zur Energieselektion, zur Untergrundunterdrückung, sowie die möglichen Photonenkombinationen für Pump-Probe-Experimente erweitern. Mehrere technische Lösungen könnten den Photoneffluss von hohen Harmonischen der bestehenden Gaszelle erhöhen.

Die Phasenanpassung in der Gaszelle und damit in vielen Fällen der Gesamtfluss kann extrem sensitiv von der räumlichen Strahlform des Infrarot-Grundstrahls abhängen. Im bestehenden Aufbau verursachten Beschädigungen des Kristalls im Mehrpass-Verstärker eine unregelmäßige Strahlform. Eine Strahlform höherer Qualität würde wahrscheinlich die Phasenanpassung verbessern und folglich zu einer höheren Fluss von Harmonischen führen.

Die Erzeugung von harmonischen Ordnungen unterhalb der Ionisationsschwelle des Konversionsmediums ist nicht durch Absorption limitiert und kann durch einen größeren Zelldruck erhöht werden. Dies kann jedoch nur in Experimenten genutzt werden, in denen lediglich niedrige Ordnungen verwendet werden wie etwa in der Untersuchung neutraler Zustände, da ein höherer Druck die Phasenanpassung und damit den Ertrag von höheren Ordnungen stark unterdrückt. Das gegenwärtige Zelldesign erlaubt Drücke bis zu 10 Torr (13 mbar). Eine modifizierte Zellgeometrie mit differentiell gepumpten Eintritts- und Austrittskammern würde das Betreiben der Zelle bei deutlich höheren Drücken ermöglichen.

Eine weitere vielversprechende Möglichkeit zur Erhöhung des Photonenflusses für bestimmte Wellenlängen besteht in der gleichzeitigen Nutzung mehrerer Gaszellen. Die optimalen Zellparameter für die Erzeugung von hohen Harmonischen variieren vom VUV- zum XUV-Spektrum aufgrund der unterschiedlichen Phasenanpassung und Absorptionsbedingungen. Daher wären die Verwendung von zwei Zellen mit verschiedenen Längen, Gasen und Drücken vorteilhaft. Eine Zelle könnte für die Erzeugung von niedrigen Harmonischen für den Pump-Puls optimiert werden, während in der zweiten Zelle effizient hohe Harmonische generiert werden (oder umgekehrt). Die beiden Zellen könnten hintereinander in den Strahlengang gesetzt werden, sodass der Grundstrahl in der ersten Zelle niedrige Harmonische und in der folgenden Zelle höhere Ordnungen erzeugt. Alternativ könnte der Grundstrahl in zwei parallele Arme mit jeweils einer Zelle aufgeteilt werden. Eine getrennte Strahlführung über eine größere Distanz könnte allerdings Probleme im Hinblick auf die Stabilität verursachen und damit die Zeitauflösung des Interferometers verschlechtern.



# A Appendix

## A.1 Pulse Propagation in a Dispersive Medium

Formulae taken from [119, 19, 115]. For a gaussian pulse with carrier frequency  $\omega_0$ , phase  $\phi(t)$ , amplitude  $A_t$  and temporal width  $\Delta t$ :

$$E(t) = \sqrt{A_t e^{-\ln 2 \left(\frac{2t}{\Delta t}\right)^2}} e^{-i(\omega_0 t + \phi(t))} + \text{complex conj.} \quad \text{Electric field (time domain)} \quad (\text{A.1})$$

If we perform a Fourier transform into the frequency domain and discard negative frequencies, the phase  $\phi(t)$  is converted to function of the frequency  $\phi(\omega)$ :

$$E(\omega) = \sqrt{A_\omega e^{-\ln 2 \left(\frac{2(\omega - \omega_0)}{\Delta \omega}\right)^2}} e^{-i\phi_{\text{pulse}}(\omega - \omega_0)} \quad \text{Electric field (frequency domain)} \quad (\text{A.2})$$

The angular frequency  $\omega$  is related to the observable frequency  $\nu$  by:

$$\nu = \frac{\omega}{2\pi}$$

The field after going through a dispersive medium can be written as a product of the input field and a transfer function adding a phase  $\phi_{\text{med}}(\omega - \omega_0)$  to the pulse.

$$E_{\text{out}}(\omega) = E_{\text{in}}(\omega) A(\omega) e^{-i\phi_{\text{med}}(\omega - \omega_0)} \quad \text{Electric field (dispersive medium)} \quad (\text{A.3})$$

The amplitude can be approximated by  $A(\omega) \approx 1$ . The phase  $\phi_{\text{med}}$  can be expressed in form of a Taylor series up to the third term by

$$\phi(\omega - \omega_0) = \phi_0 + \phi' \cdot (\omega - \omega_0) + \phi'' \cdot \frac{(\omega - \omega_0)^2}{2} + \dots \quad \text{Phase (dispersive medium)} \quad (\text{A.4})$$

Rewriting the expansion in terms of the wave number with  $\phi(\omega) = k(\omega)L$ :

$$k(\omega - \omega_0) = k_0 + \frac{dk}{d\omega}(\omega - \omega_0) + \frac{1}{2} \frac{d^2k}{d\omega^2}(\omega - \omega_0)^2 + \dots$$

The zero order term adds a constant to the phase. The first order contains the group velocity  $v_g$  which adds delay to the pulse.

$$k' \equiv \frac{dk}{d\omega} = \frac{1}{v_g}$$

The second order term is called group velocity dispersion  $GVD$  which changes the temporal width of the pulse.

$$k'' \equiv \frac{d^2k}{d\omega^2} = \frac{dk}{d\omega} \frac{1}{v_g}$$

The Group delay dispersion is defined by  $GDD = GVD \cdot L$ .

$$\boxed{\frac{1}{v_g} = \frac{1}{c} \left( n - \lambda \frac{\delta n}{\delta \lambda} \right)} \quad \text{Group delay} \quad (\text{A.5})$$

Material	$\lambda$ [nm]	$n$	$\frac{\delta n}{\delta \lambda}$ [ $\mu m^{-1}$ ]	$\frac{1}{v_g}$ [ $\frac{fs}{\mu m}$ ]
CaF <sub>2</sub>	808	1.4304	-0.0102	4.799
	269	1.4612	-0.2807	5.126
	162	1.5482	-2.2490	6.380
MgF <sub>2</sub>	808	1.3750	-0.0085	4.609
	269	1.3985	-0.2083	4.852
	162	1.4587	-1.4313	5.639

**Table A.1:** Refractive indices, chromatic dispersion and group delay for MgF<sub>2</sub> (ordinary axis) [91] and CaF<sub>2</sub> [33]

## A.2 Beam Losses in the Mirror Gap

Assuming a gaussian profile symmetrical to the center,  $\sigma_x = \sigma_y$  the total beam is:

$$1 = \frac{1}{2\pi\sigma^2} \int_{-\infty}^{\infty} \int_{-\infty}^{\infty} e^{-\frac{x^2-y^2}{2\sigma^2}} dx dy$$

The amount of beam lost is then calculated by:

$$\begin{aligned} L_{(a)} &= \frac{1}{2\pi\sigma^2} \int_{-\infty}^{\infty} \int_{-a}^a e^{-\frac{x^2-y^2}{2\sigma^2}} dx dy \\ &= 1 \cdot \frac{1}{\sqrt{2\pi}\sigma} \int_{-a}^a e^{-\frac{y^2}{2\sigma^2}} dy \\ &= erf\left(\frac{a}{\sqrt{2}\sigma}\right) \end{aligned}$$

Width  $a = \frac{d}{2}$  and  $\sigma = \frac{w}{2\sqrt{\ln 2}}$  follows

$$L_{(d,w)} = erf\left(\frac{d\sqrt{\ln 2}}{w}\right)$$

where  $d$  is the width of the gap and  $w$  the full width at half maximum of the gaussian beam profile.

## A.3 Reflectivity Calculation

Working with wavelengths in the VUV, it can be challenging to find materials that provide a good reflectivity in a specific spectral range. Using the *Fresnel equations*, one can calculate the reflectivity when the refractive indices are known in the specific range. The website [refractiveindex.info](http://refractiveindex.info) [130] provides a large compilation of material properties found in the literature. This simple script uses the measured data to calculate the reflectivity of a solid mirror of the chosen material in vacuum for a specific wavelength.

```

# -*- coding: utf-8 -*-
# Reflectivity calculator
"""
@author: Felix
"""
#=====#
# %%      Environment imports
#=====#
import numpy as np
import matplotlib.pyplot as plt
from PIL import Image
from scipy import ndimage
from scipy import optimize
from scipy.interpolate import interp1d
from scipy.interpolate import InterpolatedUnivariateSpline

#=====#
# %% fresnel functions
#=====#
# x is angle of normal incidence in rad
# https://en.wikipedia.org/wiki/Fresnel_equations
# s polarization
def R_s(ang_deg,n2):
    n1 = 1 #vac
    x = ang_deg*np.pi/180
    nomin = n1*np.cos(x) - n2*np.sqrt(1-(n1/n2*np.sin(x))**2)
    denom = n1*np.cos(x) + n2*np.sqrt(1-(n1/n2*np.sin(x))**2)
    return np.abs(nomin/denom)**2

# p polarization
def R_p(ang_deg,n2):
    n1 = 1 #vac
    x = ang_deg*np.pi/180
    nomin = n1*np.sqrt(1-(n1/n2*np.sin(x))**2) - n2*np.cos(x)
    denom = n1*np.sqrt(1-(n1/n2*np.sin(x))**2) + n2*np.cos(x)
    return np.abs(nomin/denom)**2

#=====#
# %%      Import ref data
#=====#
dat = np.genfromtxt('/Users/Felix/LBNLGD/Drive/Filters and Mirrors/n_complex_gold.txt', skip_header=1)
kl = np.where(dat[:,1]=='nan')[0]
dat_w = dat[:,0] # wavelength in microns
dat_n = dat[:,1] #all

id = int(np.where(np.isnan(dat[:,0]))[0])
n = dat[0:id,1] + 1j*dat[id+1:,1]
nr = n.real
k = n.imag
w = dat[0:id,0]

#=====#
# %%create interpolation for n(w)
#=====#
fig_spline =plt.figure()

w_intp = np.arange(0.025,0.12,0.001)
nr_intp = InterpolatedUnivariateSpline(w,nr,k=2)

plt.scatter(w,nr,color='r',label='nr data')
plt.plot(w_intp,nr_intp(w_intp),label='nr spline',color='red')

k_intp = InterpolatedUnivariateSpline(w,k,k=2)
plt.scatter(w,k,color='b',label='k data')
plt.plot(w_intp,k_intp(w_intp),label='k spline')
plt.legend(loc =2, fontsize=16)

def n_intp(w):
    return nr_intp(w)+1j*k_intp(w)

plt.ylabel('Refractive index n')
plt.xlabel('Wavelength [nm]')

#=====#
# %% plot R_s(x,n2) vs angle
#=====#
angles = np.arange(0.1,89.9,0.01)
w_ex = 0.12
aplots = plt.plot(angles,R_s(angles,n_intp(w_ex)))
aplotp = plt.plot(angles,R_p(angles,n_intp(w_ex)))

#=====#

```

```

# %% plot R_s(x,n2) vs wavelength using interpolated n
#
=====
fig2x = plt.figure()
ax1 = fig2x.add_subplot(111)
ax2 = ax1.twinx()

wavel = np.arange(0.025,0.12,0.01)
angle = 70
eplot = ax1.plot(wavel,R_s(angle,n_intp(wavel)),label='materialx',linewidth=2)

#limits
ax1.set_xlim(0.03,0.12)
ax2.set_xlim(ax1.get_xlim())

#harmonics ticks
harm = np.arange(7,25,2)
harm_nm = 0.808/harm
def tick_labels2(X):
    return ["%.0fth" % z for z in X]

#change x-axis labels to nm
def tick_labels1(X):
    V= X*1000
    return ["%.0f" % z for z in V]
nm_labels = tick_labels1(ax1.get_xticks())
ax1.set_xticklabels(nm_labels)
ax1.set_xlabel(r"Wavelength [nm]")
ax1.set_ylabel(r"Reflectivity")
#lines
for i in range(0,len(harm)):
    ax1.axvline(harm_nm[i], ymin=0, ymax=1,color = 'gray',linestyle = '--')

harm_ticks = harm_nm
harm_labels = tick_labels2(harm)
ax2.set_xticks(harm_ticks)
ax2.set_xticklabels(harm_labels[0:-2])
ax2.set_xlabel(r"Harmonic order for 808 nm")

ax1.set_ylim(0.2,0.6)
legend =ax1.legend()
plt.show()

```

## A.4 Additional Filter Spectra

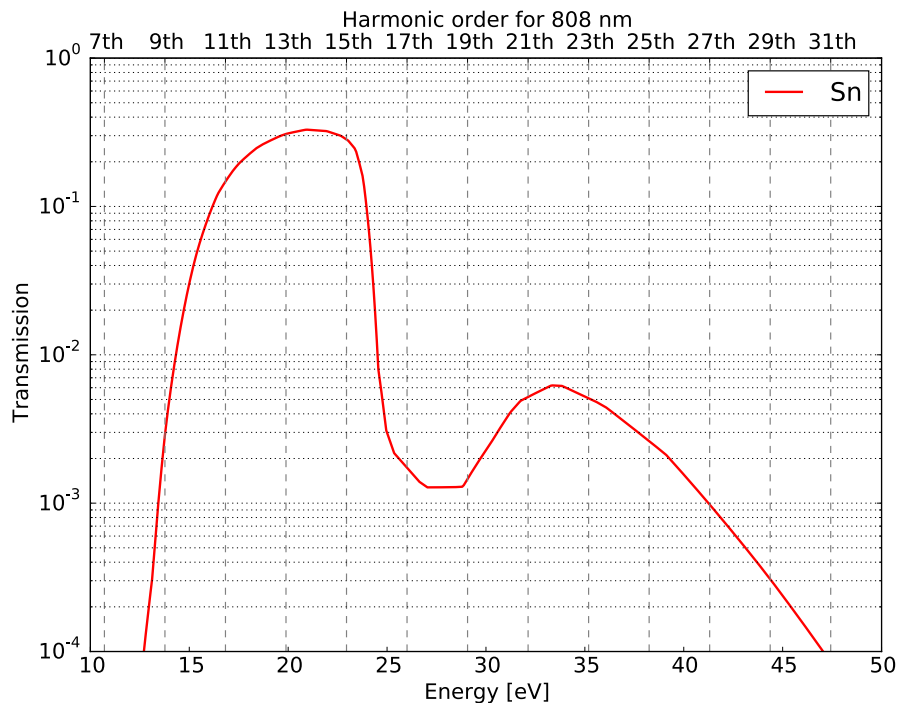


**Figure A.1:** Calculated transmission of a tin filter with a thickness of 150  $\mu\text{m}$ . Data taken from [32].

## A.5 Supersonic Jet Measurements

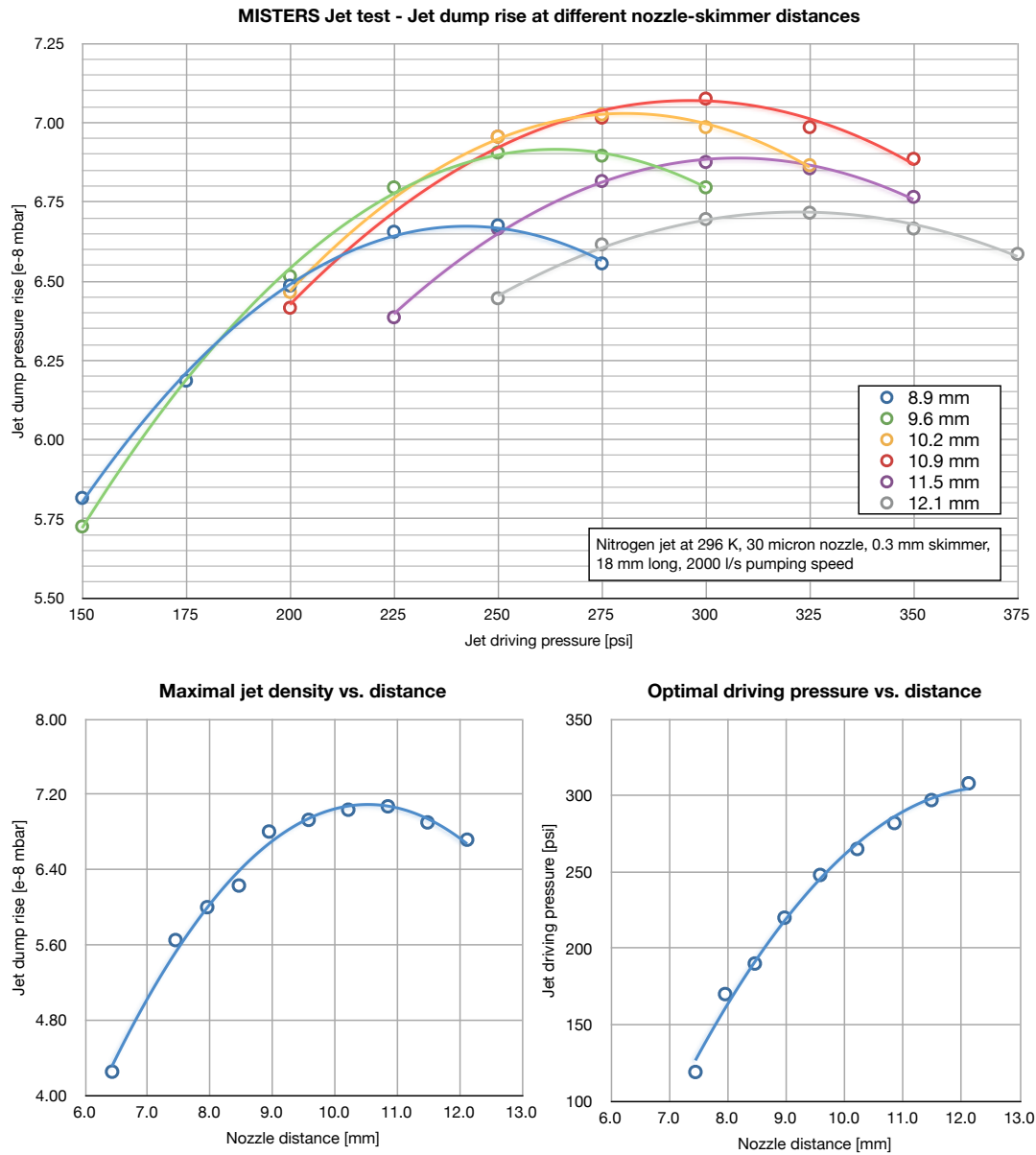


**Figure A.2:** Curves showing the dependence of the pressure rise in the jet dump with respect to the nozzle-skimmer distance as well as the driving pressure. The absolute distance has an error of  $\sim 2$  mm.

## A.6 Calculated transition energies for H<sub>2</sub>

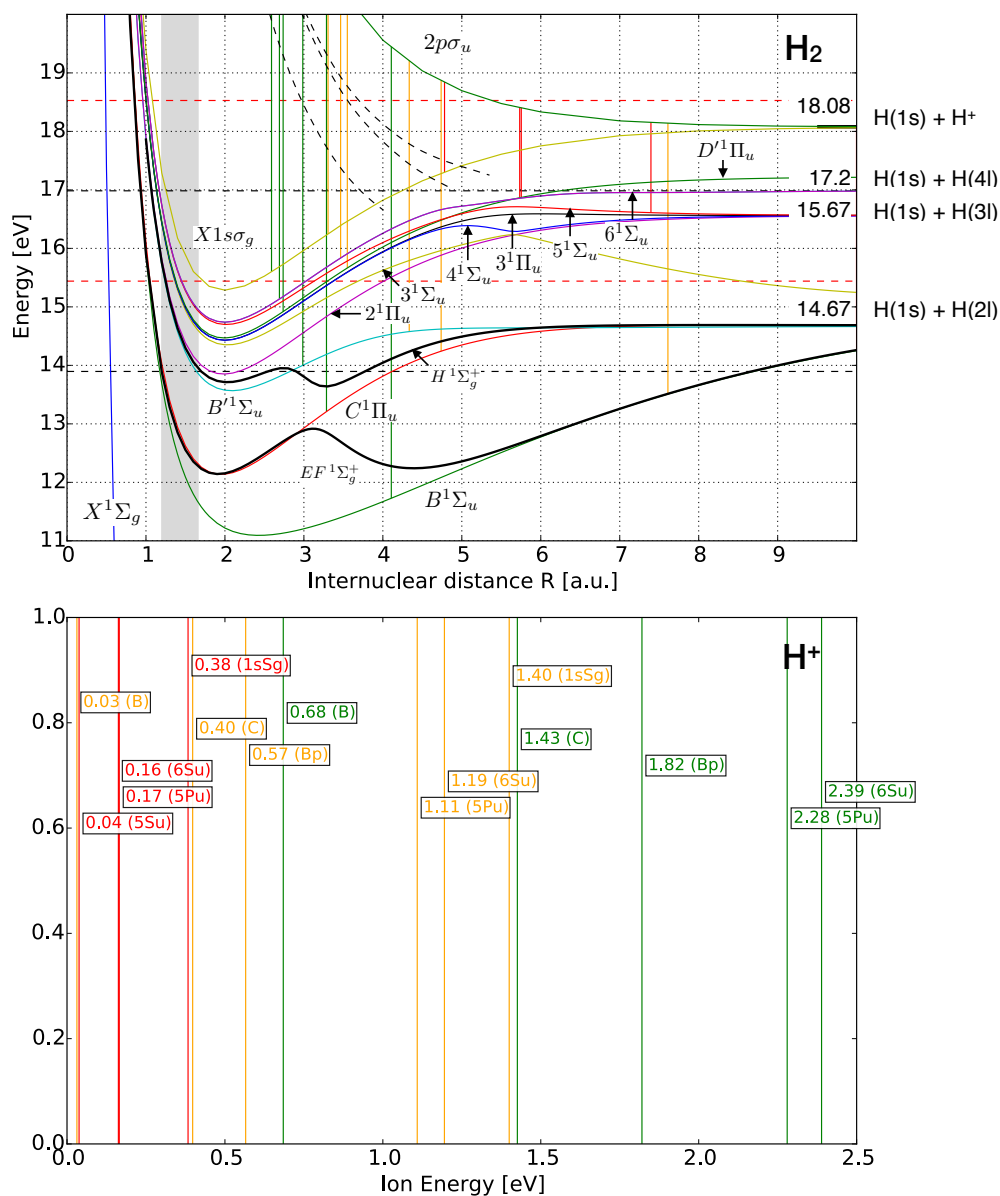


**Figure A.3:** Calculated proton energies for dissociative ionization of H<sub>2</sub> using high order harmonics of 808 nm.

## A.7 Additional MISTERS Spectra

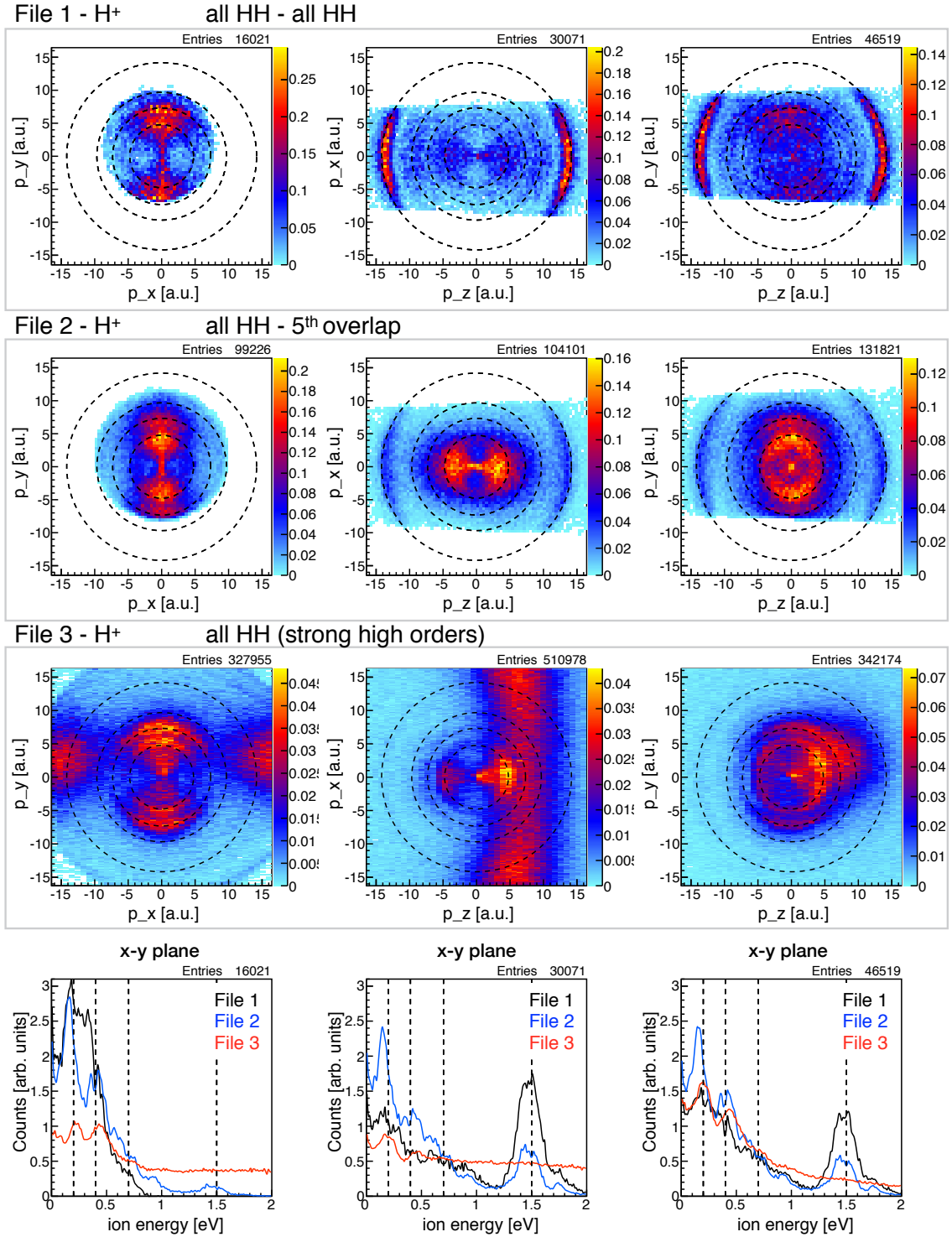


**Figure A.4:** Hydrogen ion, H<sup>+</sup>, momentum distributions and energy spectra for 3 measurements. **(File 1)** Pump: strong HH<11<sup>th</sup>; probe: same as pump (Kr HHG at 10 T, Ar gas filter). **(File 2)** Pump: strong HH<11; probe: 5<sup>th</sup> HH (Ar HHG at 10 T, Ar gas filter, MgF<sub>2</sub> in probe arm). **(File 3)** Pump: strong HH>11; probe: IR, 3<sup>rd</sup>, 5<sup>th</sup> delayed (Ar 5T, Ar gas filter, MgF<sub>2</sub> in probe arm). See Table A.2 for details.

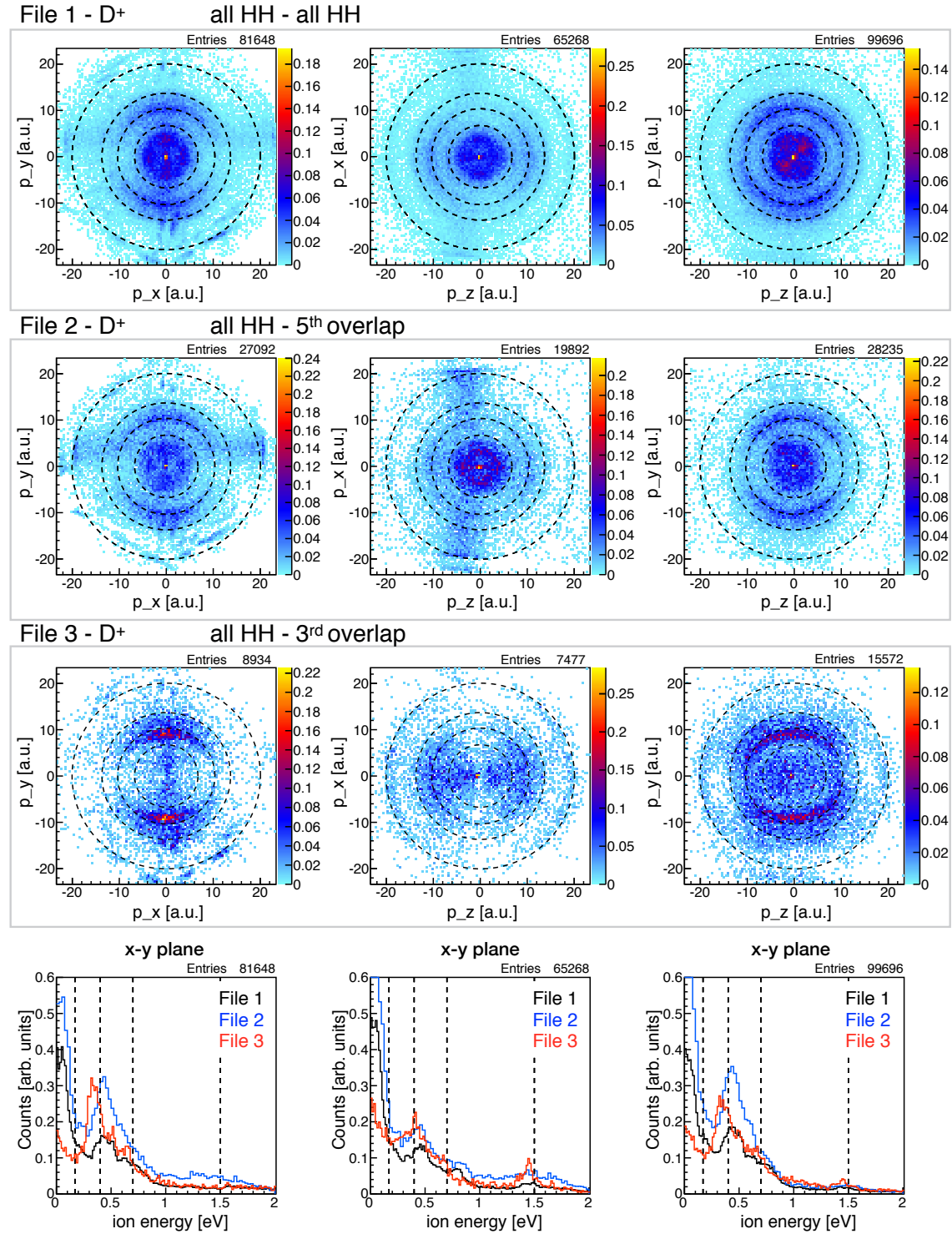


**Figure A.5:** Deuterium ion, D<sup>+</sup>, momentum distributions and energy spectra for 3 measurements. **(File 1)** Pump: strong HH<11<sup>th</sup>; probe: same as pump (Ar HHG at 8T, Ar gas filter, scan -50 to 450 fs) **(File 2)** Pump: strong HH>11; probe: 5<sup>th</sup> overlap HH (Ar HHG at 5.9T, Ar gas filter, CaF<sub>2</sub> in probe arm, scan -100 to +400 fs) **(File 3)** Pump: strong HH<11; probe: 3<sup>rd</sup> overlap HH (Ar HHG at 8T, Ar gas filter, CaF<sub>2</sub> in probe arm, no scan). See Table A.3 for details.

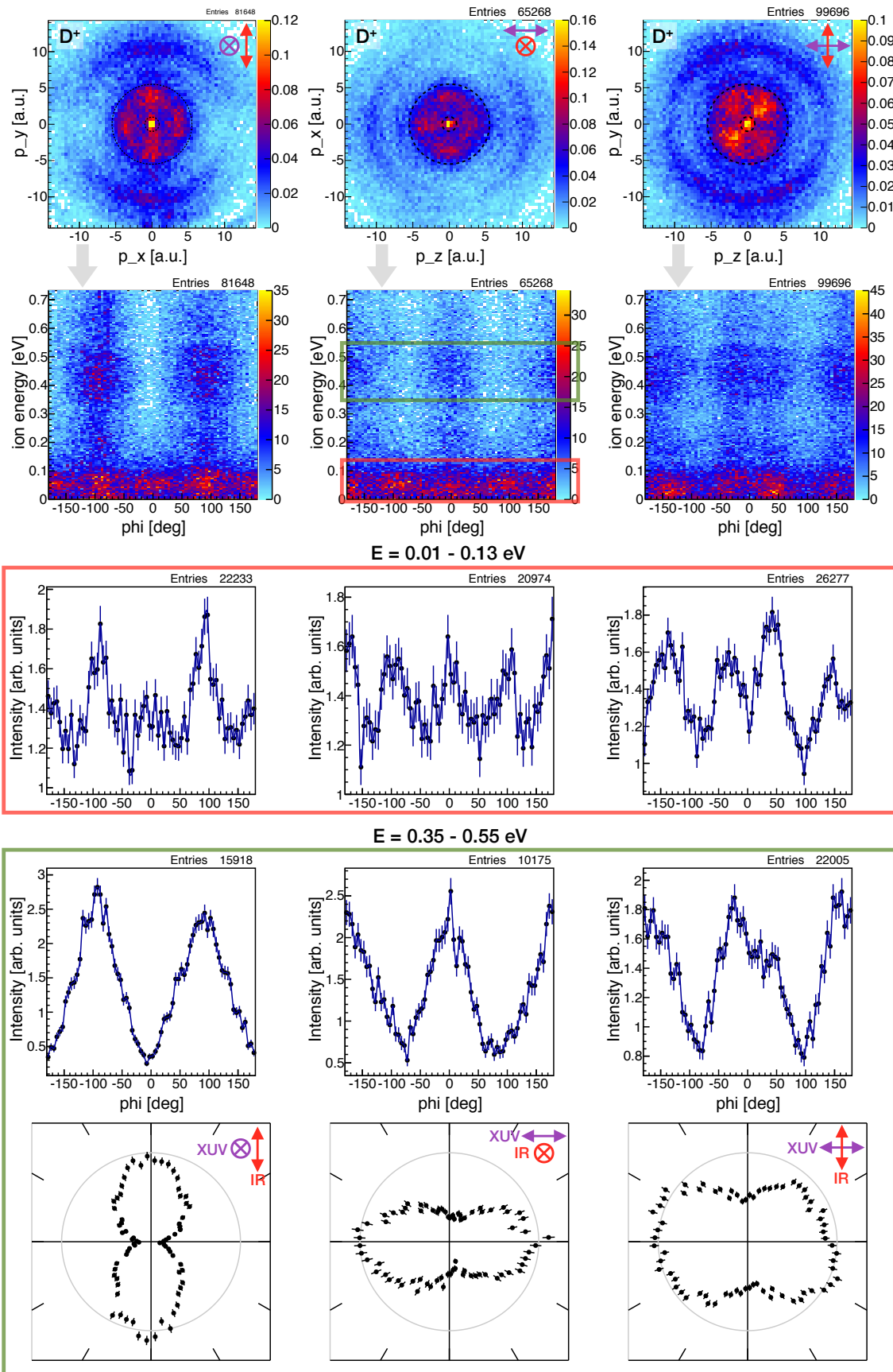


**Figure A.6:**  $D^+$  momentum and angular distributions for specific energy regions. Experiment details: Pump: strong HH<11<sup>th</sup>; probe: same as pump (Ar HHG at 8T, Ar gas filter, scan -50 to 450 fs) See File 1 in Table A.3 for details.

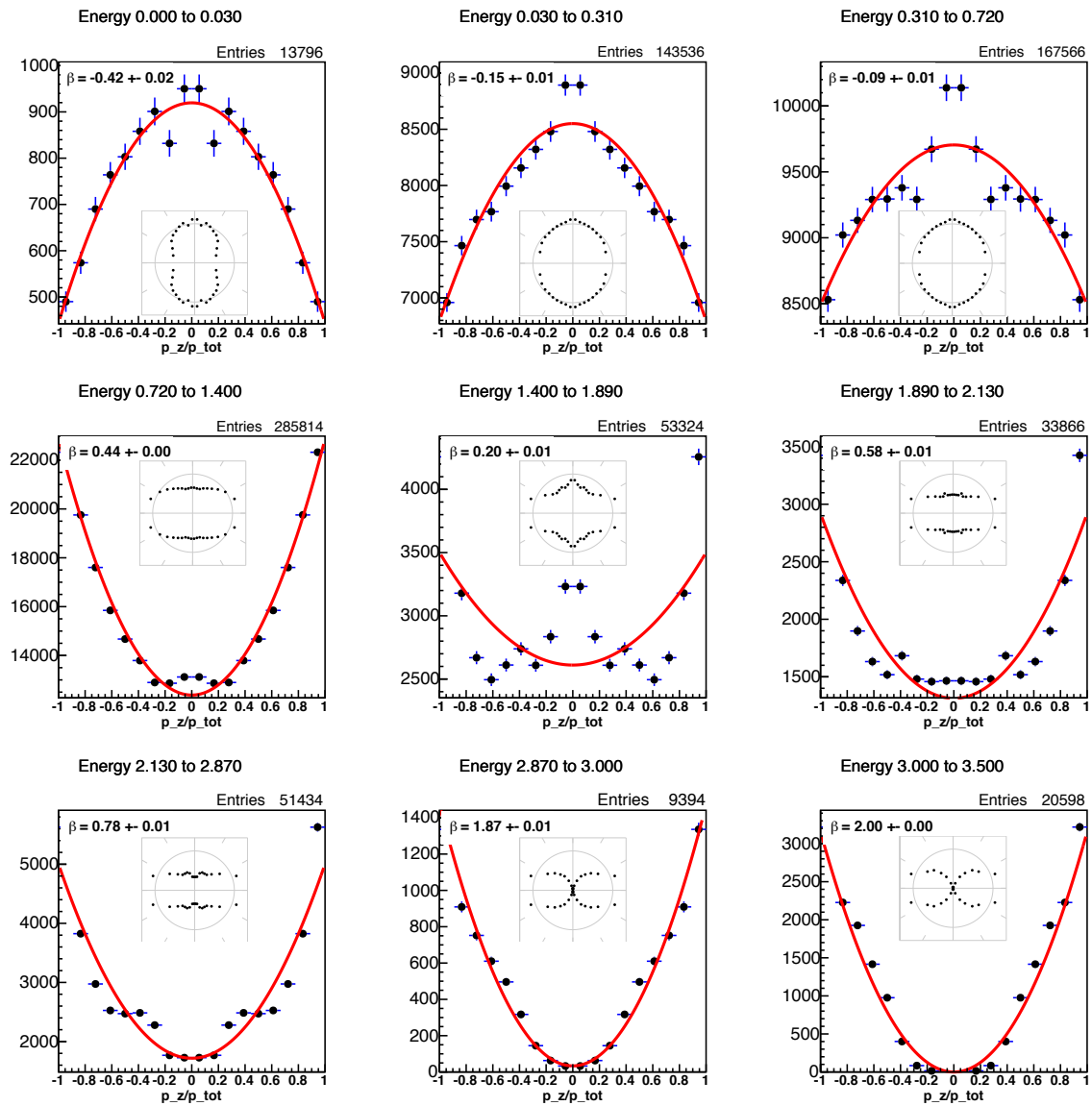


**Figure A.7:** Angular distributions of  $O_2$  ions from ionization using the tin filtered harmonics spectrum. Above 2.5 eV ion energy, the loss of detection solid angle causes a decrease in signal near 0. See File 1 in Table A.4

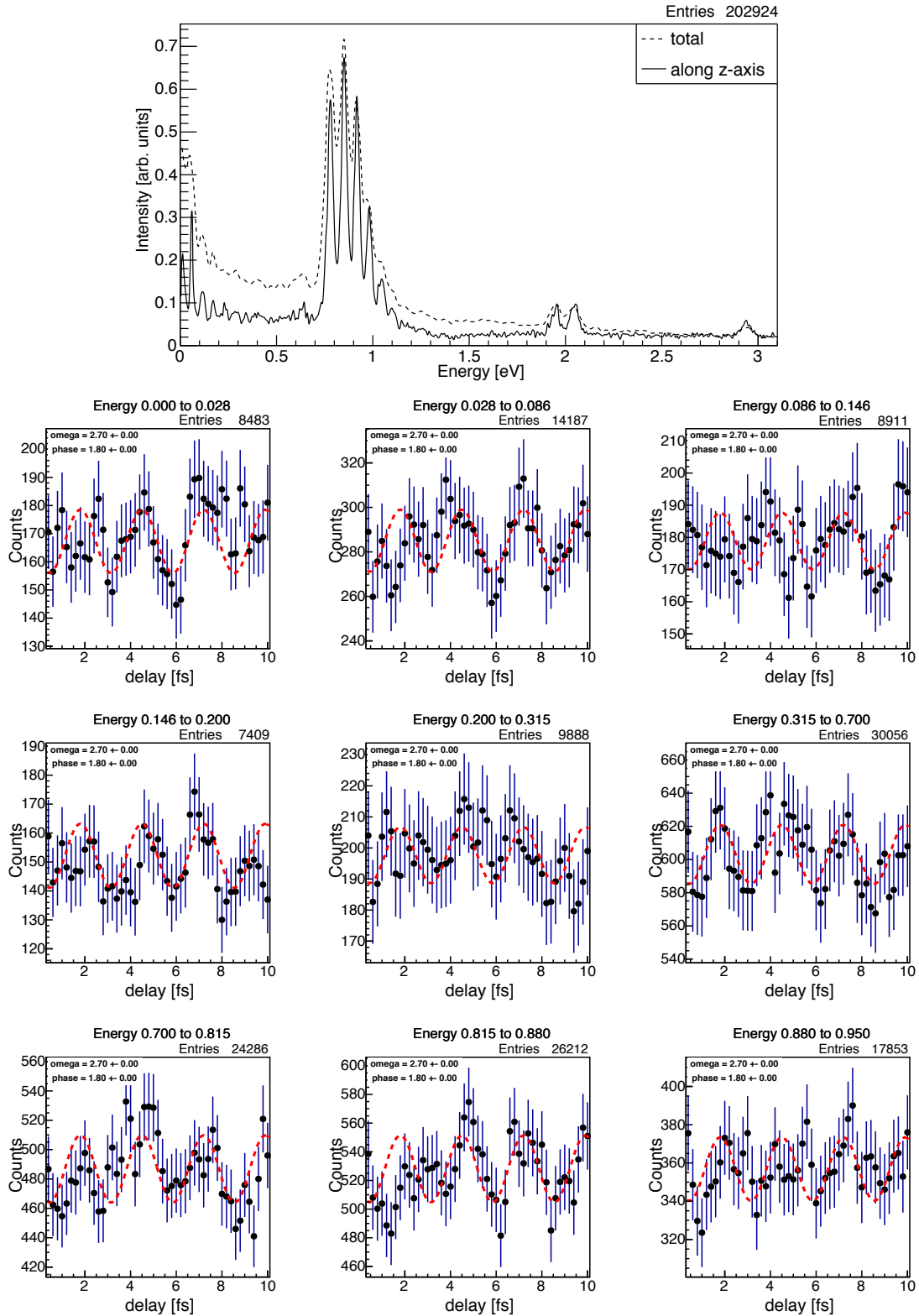


**Figure A.8:** Top: O<sup>+</sup> ion energy distribution from XUV/IR pump - IR probe (See File 3 in Table A.4). Bottom: Delay dependent O<sup>+</sup> ion yield for different regions of ion energy. A cosine at the IR frequency is shown as a red dashed line for reference. Only positive momenta were selected to exclude contributions from gaseous water.

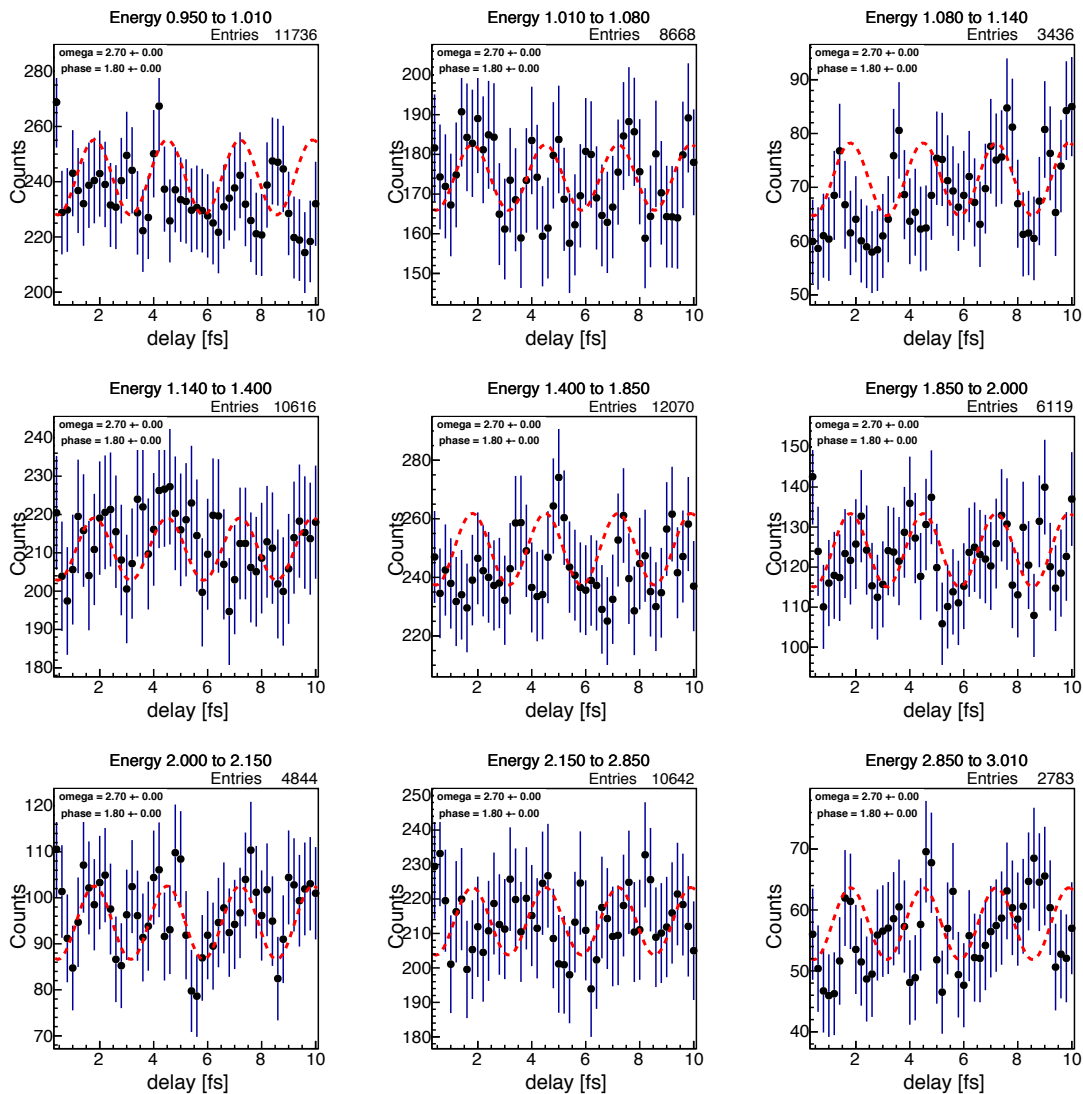


**Figure A.9:** Delay dependent  $O^+$  ion yield for different regions of ion energy, continued from Figure A.8.

## A.8 Measurement parameters

File 1	H <sub>2</sub>	05/22/2014
Laser pulse energy:		54 mJ before compression
HHG:		Kr, 10 Torr, high order yield $\sim 200$ nV/s
Filters:		Ar cell, 3 Torr
		bottom arm: -, top arm: -, $t_0 = 5290$
IR:		minimized
Scan:		-50 to +300 fs, 5 fs stepsize
Jet:		H <sub>2</sub> 60 psi
Spectrometer:		Acceleration - drift setting
		Hex grid: -100, DLD grid: -21
		Hex MCP F: -2200, Anode holder: +31
File 2	H <sub>2</sub>	05/27/2014
Laser pulse energy:		56 mJ before compression
HHG:		Ar, 10 Torr, high order yield $\sim 200$ nV/s
Filters:		Ar cell, 3 Torr
		bottom arm: -, top arm: MgF <sub>2</sub> , $t_0 = 5525$
IR:		minimized
Scan:		-70 to +20 fs, 10 fs stepsize
Jet:		H <sub>2</sub> 100 psi
Spectrometer:		Acceleration - drift setting
		Hex grid: -150, DLD grid: -21
		Hex MCP F: -2208, Anode holder: +53
File 3	H <sub>2</sub>	07/30/2014
Laser pulse energy:		58 mJ before compression
HHG:		Ar, 5 Torr, high order yield $\sim 200$ nV/s
Filters:		Ar cell, 3 Torr
		bottom arm: -, top arm: MgF <sub>2</sub> , $t_0 = 5290$
IR:		minimized
Scan:		-100 to +300 fs, 5 fs stepsize
Jet:		H <sub>2</sub> 200 psi
Spectrometer:		Acceleration - drift setting
		Hex grid: -541, DLD grid: -72
		Hex MCP F: -2456, Anode holder: -178

**Table A.2:** Instrument parameter of for the hydrogen measurements shown in this work.

File 1	D <sub>2</sub>	12/09/2014
Laser pulse energy:	59 mJ before compression	
HHG:	Ar, 8 Torr, high order yield 190 nV/s (2 <sup>nd</sup> diode*)	
Filters:	Ar cell, 3 Torr	
	bottom arm: -, top arm: -, $t_0 = 5290$	
IR:	minimized	
Scan:	-50 to +450 fs, 10 fs stepsize	
Jet:	D <sub>2</sub> 110 psi	
Spectrometer:	Homogeneous field	
	Hex grid: -601, DLD grid: -51	
	Hex MCP F: -2454, Anode holder: -172	
File 2	D <sub>2</sub>	12/05/2014
Laser pulse energy:	59 mJ before compression	
HHG:	Ar, 5.9 Torr, high order yield 190 nV/s (2 <sup>nd</sup> diode*)	
Filters:	Ar cell, 3 Torr	
	bottom arm: CaF <sub>2</sub> , top arm: -, $t_0 = 4864$	
IR:	minimized	
Scan:	-100 to +400 fs, 5 fs stepsize	
Jet:	D <sub>2</sub> 60 psi	
Spectrometer:	Homogeneous field	
	Hex grid: -500, DLD grid: -50	
	Hex MCP F: -2452, Anode holder: -172	
File 3	D <sub>2</sub>	12/10/2014
Laser pulse energy:	57 mJ before compression	
HHG:	Ar, 8 Torr, high order yield 210 nV/s (2 <sup>nd</sup> diode*)	
Filters:	Ar cell, 3 Torr	
	bottom arm: CaF <sub>2</sub> , top arm: -, $t_0 = 5044$	
IR:	minimized	
Scan:	at 3 <sup>rd</sup> overlap position only	
Jet:	D <sub>2</sub> 110 psi	
Spectrometer:	Homogeneous field	
	Hex grid: -601, DLD grid: -51	
	Hex MCP F: -2454, Anode holder: -172	

**Table A.3:** Instrument parameters for the deuterium measurements shown in this work. (\*) HH flux measurement performed using an Al-coated diode after 2 silicon mirror reflections (XUV reflectivity per reflection  $\sim 0.6$ ).

<b>File 1</b>	<b>O<sub>2</sub></b>	<b>09/26/2014</b>
Laser pulse energy:	55 mJ before compression	
HHG:	Ar, 4.2 Torr, high order yield 260 nV/s	
Filters:	tin filter covering both arms	
IR:	minimized	
Scan:	no scan	
Jet:	O <sub>2</sub> 100 psi	
Spectrometer:	Homogeneous field	
	Hex grid: -850, DLD grid: -101	
	Hex MCP F: -2452, Anode holder: -198	
<b>File 2</b>	<b>O<sub>2</sub></b>	<b>01/14/2015</b>
Laser pulse energy:	52 mJ before compression	
HHG:	Ar, 5.7 Torr, high order yield 169 nV/s (2 <sup>nd</sup> diode*)	
Filters:	bottom arm: CaF <sub>2</sub> , top arm: -, $t_0 = 5090$	
IR:	0.9 cnts/shot	
Scan:	-0.6 to +3.3 fs, 0.65 fs stepsize	
Jet:	O <sub>2</sub> 100 psi	
Spectrometer:	Homogeneous field	
	Hex grid: -850, DLD grid: -101	
	Hex MCP F: -2452, Anode holder: -172	
<b>File 3</b>	<b>O<sub>2</sub></b>	<b>11/25/2014</b>
Laser pulse energy:	57 mJ before compression	
HHG:	Ar, 1.9 Torr .	
	max high order yield $\sim 90$ nV/s at 5.2 Torr (2 <sup>nd</sup> diode*)	
Filters:	bottom arm: CaF <sub>2</sub> , top arm: -, $t_0 = 5090$	
IR:	1 cnt/shot, $\sim 20$ % ionization from IR	
Scan:	0 to 10 fs, 10 fs stepsize	
Jet:	O <sub>2</sub> 100 psi	
Spectrometer:	Homogeneous field	
	Hex grid: -850, DLD grid: -101	
	Hex MCP F: -2452, Anode holder: -172	

**Table A.4:** Instrument parameters of for the oxygen measurements shown in this work. (\*) HH flux measurement performed using an Al-coated diode after 2 silicon mirror reflections (XUV reflectivity per reflection  $\sim 0.6$ ).

---

<b>Argon</b>	<b>01/29/2015</b>
Laser pulse energy:	57 mJ before compression
HHG:	Ar, 2.1 Torr max high order yield 180 nV/s at 5.2 Torr (2 <sup>nd</sup> diode*)
Filters:	tin covering both arms, $t_0 = 5090$
IR:	minimized
Scan:	no scan
Jet:	Ar 90 psi
Spectrometer:	Homogeneous field Hex grid: -300, DLD grid: -454 Hex MCP F: -101, Anode holder: -2237 DLD MCP F: -2349, Anode holder: +26 Magnetic field $\sim 5.6$ G
Flux reduced by closing collimator slits between SMI and XUV-spectrometer. Clear aperture on phosphor screen (exit of SMI) $\sim 1.6$ mm.	

---

**Table A.5:** Instrument parameters of for the argon measurement.

# Bibliography

- [1] W. Ackermann et al. Operation of a free-electron laser from the extreme ultraviolet to the water window. *Nature Photonics*, 1(6):336–342, June 2007. doi: 10.1038/nphoton.2007.76.
- [2] T. Akahori, Y. Morioka, M. Watanabe, T. Hayaishi, K. Ito, and M. Nakamura. Dissociation processes of O<sub>2</sub> in the VUV region 500–700 Å. *Journal of Physics B: Atomic and Molecular Physics*, 18(11):2219, June 1985. doi: 10.1088/0022-3700/18/11/015.
- [3] D. Akoury, K. Kreidi, T. Jahnke, T. Weber, A. Staudte, M. Schöffler, N. Neumann, J. Titze, L. P. H. Schmidt, A. Czasch, O. Jagutzki, R. A. C. Fraga, R. E. Grisenti, R. D. Muiño, N. A. Cherepkov, S. K. Semenov, P. Ranitovic, C. L. Cocke, T. Osipov, H. Adaniya, J. C. Thompson, M. H. Prior, A. Belkacem, A. L. Landers, H. Schmidt-Böcking, and R. Dörner. The Simplest Double Slit: Interference and Entanglement in Double Photoionization of H<sub>2</sub>. *Science*, 318(5852):949–952, Sept. 2007. doi: 10.1126/Science.1144959.
- [4] E. Allaria et al. Highly coherent and stable pulses from the FERMI seeded free-electron laser in the extreme ultraviolet. *Nature Photonics*, 6(10):699–704, Oct. 2012. doi: 10.1038/nphoton.2012.233.
- [5] T. K. Allison. Private communication, June 2013.
- [6] T. K. Allison, T. W. Wright, A. M. Stooke, C. Khurmi, J. van Tilborg, Y. Liu, R. W. Falcone, and A. Belkacem. Femtosecond spectroscopy with vacuum ultraviolet pulse pairs. *Optics Letters*, 35(21):3664, Oct. 2010. doi: 10.1364/OL.35.003664.
- [7] T. K. Allison, H. Tao, W. J. Glover, T. W. Wright, A. M. Stooke, C. Khurmi, J. van Tilborg, Y. Liu, R. W. Falcone, T. J. Martínez, and A. Belkacem. Ultrafast internal conversion in ethylene. II. Mechanisms and pathways for quenching and hydrogen elimination. *The Journal of Chemical Physics*, 136(12):124317, 2012. doi: 10.1063/1.3697760.
- [8] T. K. Allison III. *Femtosecond molecular dynamics studied with vacuum ultraviolet pulse pairs*. PhD thesis, University of California, Berkeley, 2010. URL <https://escholarship.org/uc/item/6w5264r4.pdf>.
- [9] M. Ammosov, N. Delone, and V. Krainov. Tunnel ionization of complex atoms and of atomic ions in an alternating electromagnetic field. *JETP*, 64(6):2008, 1986. URL <http://www.jetp.ac.ru/cgi-bin/e/index/e/64/6/p1191?a=list>.
- [10] J. Andruszkow et al. First Observation of Self-Amplified Spontaneous Emission in a Free-Electron Laser at 109 nm Wavelength. *Physical Review Letters*, 85(18):3825–3829, Oct. 2000. doi: 10.1103/PhysRevLett.85.3825.
- [11] J. A. Armstrong, N. Bloembergen, J. Ducuing, and P. S. Pershan. Interactions between Light Waves in a Nonlinear Dielectric. *Physical Review*, 127(6):1918–1939, Sept. 1962. doi: 10.1103/PhysRev.127.1918.

- [12] S. Baker, J. S. Robinson, C. A. Haworth, H. Teng, R. A. Smith, C. C. Chirilă, M. Lein, J. W. G. Tisch, and J. P. Marangos. Probing Proton Dynamics in Molecules on an Attosecond Time Scale. *Science*, 312(5772):424–427, Apr. 2006. doi: 10.1126/Science.1123904.
- [13] P. Balcou, P. Salières, A. L’Huillier, and M. Lewenstein. Generalized phase-matching conditions for high harmonics: The role of field-gradient forces. *Physical Review A*, 55(4):3204–3210, Apr. 1997. doi: 10.1103/PhysRevA.55.3204.
- [14] P. Baltzer, B. Wannberg, L. Karlsson, M. Carlsson Göthe, and M. Larsson. High-resolution inner-valence uv photoelectron spectra of the  $o_2$  molecule and configuration-interaction calculations of  $^2\pi_u$  states between 20 and 26 eV. *Physical Review A*, 45(7):4374–4384, Apr. 1992. doi: 10.1103/PhysRevA.45.4374.
- [15] E. P. Benis, D. Charalambidis, T. N. Kitsopoulos, G. D. Tsakiris, and P. Tzallas. Two-photon double ionization of rare gases by a superposition of harmonics. *Physical Review A*, 74(5):051402, Nov. 2006. doi: 10.1103/PhysRevA.74.051402.
- [16] J. Berkowitz. *Photoabsorption, photoionization, and photoelectron spectroscopy*. Academic Press, New York, 1979. ISBN 0-12-091650-9. URL <http://www.ScienceDirect.com/Science/book/9780120916504>.
- [17] V. Blanchet, C. Nicole, M.-A. Bouchene, and B. Girard. Temporal Coherent Control in Two-Photon Transitions: From Optical Interferences to Quantum Interferences. *Physical Review Letters*, 78(14):2716–2719, Apr. 1997. doi: 10.1103/PhysRevLett.78.2716.
- [18] I. A. Bocharova, H. Mashiko, M. Magrakvelidze, D. Ray, P. Ranitovic, C. L. Cocks, and I. V. Litvinyuk. Direct Coulomb-explosion imaging of coherent nuclear dynamics induced by few-cycle laser pulses in light and heavy hydrogen. *Physical Review A*, 77(5):053407, May 2008. doi: 10.1103/PhysRevA.77.053407.
- [19] T. Brabec and F. Krausz. Intense few-cycle laser fields: Frontiers of nonlinear optics. *Reviews of Modern Physics*, 72(2):545–591, Apr. 2000. doi: 10.1103/RevModPhys.72.545.
- [20] P. Brumer and M. Shapiro. Control of unimolecular reactions using coherent light. *Chemical Physics Letters*, 126(6):541–546, May 1986. doi: 10.1016/S0009-2614(86)80171-3.
- [21] P. H. Bucksbaum, A. Zavriyev, H. G. Muller, and D. W. Schumacher. Softening of the  $h_2^+$  molecular bond in intense laser fields. *Physical Review Letters*, 64(16):1883–1886, Apr. 1990. doi: 10.1103/PhysRevLett.64.1883.
- [22] K. S. Budil, P. Salières, A. L’Huillier, T. Ditmire, and M. D. Perry. Influence of ellipticity on harmonic generation. *Physical Review A*, 48(5):R3437–R3440, Nov. 1993. doi: 10.1103/PhysRevA.48.R3437.
- [23] S. E. Canton, E. Plésiat, J. D. Bozek, B. S. Rude, P. Decleva, and F. Martín. Direct observation of Young’s double-slit interferences in vibrationally resolved photoionization of diatomic molecules. *Proceedings of the National Academy of Sciences*, 108(18):7302–7306, Mar. 2011. doi: 10.1073/pnas.1018534108.
- [24] W. Cao. *Pump-probe study of atoms and small molecules with laser driven high order harmonics*. PhD thesis, Kansas State University, Kansas, 2014. URL <https://jrm.phys.ksu.edu/Research/Theses/Cao/WeiCao2014.zip>.

- [25] W. Cao, G. Laurent, I. Ben-Itzhak, and C. L. Cocke. Identification of a Previously Unobserved Dissociative Ionization Pathway in Time-Resolved Photospectroscopy of the Deuterium Molecule. *Physical Review Letters*, 114(11):113001, Mar. 2015. doi: 10.1103/PhysRevLett.114.113001.
- [26] Z. Chang and P. Corkum. Attosecond photon sources: the first decade and beyond. *Journal of the Optical Society of America B*, 27(11):B9, Nov. 2010. doi: 10.1364/JOSAB.27.0000B9.
- [27] Z. Chang, A. Rundquist, H. Wang, M. M. Murnane, and H. C. Kapteyn. Generation of Coherent Soft X Rays at 2.7 nm Using High Harmonics. *Physical Review Letters*, 79(16):2967–2970, Oct. 1997. doi: 10.1103/PhysRevLett.79.2967.
- [28] M. Chini, K. Zhao, and Z. Chang. The generation, characterization and applications of broadband isolated attosecond pulses. *Nature Photonics*, 8(3):178–186, Mar. 2014. doi: 10.1038/nphoton.2013.362.
- [29] P. B. Corkum. Plasma perspective on strong field multiphoton ionization. *Physical Review Letters*, 71(13):1994–1997, Sept. 1993. doi: 10.1103/PhysRevLett.71.1994.
- [30] P. Cörlin, A. Fischer, M. Schönwald, A. Sperl, T. Mizuno, U. Thumm, T. Pfeifer, and R. Moshhammer. Probing calculated  $o_2^+$  potential-energy curves with an XUV-IR pump-probe experiment. *Physical Review A*, 91(4):043415, Apr. 2015. doi: 10.1103/PhysRevA.91.043415.
- [31] Cronologic. Cronologic GmbH, 2015. URL [http://www.cronologic.de/products/time\\_measurement/](http://www.cronologic.de/products/time_measurement/).
- [32] CXRO. Center for X-Ray Optics, 2015. URL <http://www.cxro.lbl.gov>.
- [33] M. Daimon and A. Masumura. High-Accuracy Measurements of the Refractive Index and its Temperature Coefficient of Calcium Fluoride in a Wide Wavelength Range from 138 to 2326 nm. *Applied Optics*, 41(25):5275, Sept. 2002. doi: 10.1364/AO.41.005275.
- [34] S. De, M. Magrakvelidze, I. A. Bocharova, D. Ray, W. Cao, I. Znakovskaya, H. Li, Z. Wang, G. Laurent, U. Thumm, M. F. Kling, I. V. Litvinyuk, I. Ben-Itzhak, and C. L. Cocke. Following dynamic nuclear wave packets in N<sub>2</sub>, O<sub>2</sub>, and CO with few-cycle infrared pulses. *Physical Review A*, 84(4):043410, Oct. 2011. doi: 10.1103/PhysRevA.84.043410.
- [35] A. D. DiChiara, E. Sistrunk, T. A. Miller, P. Agostini, and L. F. DiMauro. An investigation of harmonic generation in liquid media with a mid-infrared laser. *Optics Express*, 17(23):20959, Nov. 2009. doi: 10.1364/OE.17.020959.
- [36] T. D. Donnelly, T. Ditmire, K. Neuman, M. D. Perry, and R. W. Falcone. High-Order Harmonic Generation in Atom Clusters. *Physical Review Letters*, 76(14):2472–2475, Apr. 1996. doi: 10.1103/PhysRevLett.76.2472.
- [37] M. Drescher, M. Hentschel, R. Kienberger, M. Uiberacker, V. Yakovlev, A. Scrinzi, T. Westerwalbesloh, U. Kleineberg, U. Heinzmann, and F. Krausz. Time-resolved atomic inner-shell spectroscopy. *Nature*, 419(6909):803–807, Oct. 2002. doi: 10.1038/{Nature}01143.

- [38] P. Eckle, M. Smolarski, P. Schlup, J. Biegert, A. Staudte, M. Schöffler, H. G. Müller, R. Dörner, and U. Keller. Attosecond angular streaking. *Nature Physics*, 4(7):565–570, July 2008. doi: 10.1038/nphys982.
- [39] M. Eckstein, C.-H. Yang, M. Kubin, F. Frassetto, L. Poletto, H.-H. Ritze, M. J. J. Vrakking, and O. Kornilov. Dynamics of N<sub>2</sub> Dissociation upon Inner-Valence Ionization by Wavelength-Selected XUV Pulses. *The Journal of Physical Chemistry Letters*, 6(3):419–425, Feb. 2015. doi: 10.1021/jz5025542.
- [40] P. Emma et al. First lasing and operation of an ångström-wavelength free-electron laser. *Nature Photonics*, 4(9):641–647, Sept. 2010. doi: 10.1038/nphoton.2010.176.
- [41] A. T. J. B. Eppink and D. H. Parker. Velocity map imaging of ions and electrons using electrostatic lenses: Application in photoelectron and photofragment ion imaging of molecular oxygen. *Review of Scientific Instruments*, 68(9):3477–3484, Sept. 1997. doi: 10.1063/1.1148310.
- [42] T. Ergler, B. Feuerstein, A. Rudenko, K. Zrost, C. D. Schröter, R. Moshhammer, and J. Ullrich. Quantum-Phase Resolved Mapping of Ground-State Vibrational  $h_2$  Wave Packets via Selective Depletion in Intense Laser Pulses. *Physical Review Letters*, 97(10):103004, Sept. 2006. doi: 10.1103/PhysRevLett.97.103004.
- [43] T. Ergler, A. Rudenko, B. Feuerstein, K. Zrost, C. D. Schröter, R. Moshhammer, and J. Ullrich. Spatiotemporal Imaging of Ultrafast Molecular Motion: Collapse and Revival of the  $d_2^+$  Nuclear Wave Packet. *Physical Review Letters*, 97(19):193001, Nov. 2006. doi: 10.1103/PhysRevLett.97.193001.
- [44] U. Fano and J. W. Cooper. Spectral Distribution of Atomic Oscillator Strengths. *Reviews of Modern Physics*, 40(3):441–507, July 1968. doi: 10.1103/RevModPhys.40.441.
- [45] U. Fantz and D. Wunderlich. Franck–Condon factors, transition probabilities, and radiative lifetimes for hydrogen molecules and their isotopomers. *Atomic Data and Nuclear Data Tables*, 92(6):853–973, Nov. 2006. doi: 10.1016/j.adt.2006.05.001.
- [46] R. Feifel, J. H. D. Eland, and D. Edvardsson. Valence double ionization of O<sub>2</sub> at photon energies below and above the molecular double ionization threshold. *The Journal of Chemical Physics*, 122(14):144308, Apr. 2005. doi: 10.1063/1.1872836.
- [47] T. Ferger. *Untersuchung der Mehr-Teilchen-Dynamik in Stößen von 200 keV H- mit Helium und Aufbau eines kalten atomaren Wasserstoff targets für Ionisationsexperimente*. Dissertation, Universität Heidelberg, 2006.
- [48] M. Ferray, A. L’Huillier, X. F. Li, L. A. Lompre, G. Mainfray, and C. Manus. Multiple-harmonic conversion of 1064 nm radiation in rare gases. *Journal of Physics B: Atomic, Molecular and Optical Physics*, 21(3):L31, Feb. 1988. doi: 10.1088/0953-4075/21/3/001.
- [49] P. A. Franken, A. E. Hill, C. W. Peters, and G. Weinreich. Generation of Optical Harmonics. *Physical Review Letters*, 7(4):118–119, Aug. 1961. doi: 10.1103/PhysRevLett.7.118.
- [50] Y. Furukawa, Y. Nabekawa, T. Okino, S. Saugout, K. Yamanouchi, and K. Midorikawa. Nonlinear Fourier-transform spectroscopy of d<sub>2</sub> using high-order harmonic radiation. *Physical Review A*, 82(1):013421, July 2010. doi: 10.1103/PhysRevA.82.013421.

- [51] T. Gebert, D. Rompotis, M. Wieland, F. Karimi, A. Azima, and M. Drescher. Michelson-type all-reflective interferometric autocorrelation in the VUV regime. *New Journal of Physics*, 16(7):073047, July 2014. doi: 10.1088/1367-2630/16/7/073047.
- [52] O. Ghafur, W. Siu, P. Johnsson, M. F. Kling, M. Drescher, and M. J. J. Vrakking. A velocity map imaging detector with an integrated gas injection system. *Review of Scientific Instruments*, 80(3):033110, Mar. 2009. doi: 10.1063/1.3085799.
- [53] S. Ghimire, A. D. DiChiara, E. Sistrunk, P. Agostini, L. F. DiMauro, and D. A. Reis. Observation of high-order harmonic generation in a bulk crystal. *Nature Physics*, 7(2):138–141, Feb. 2011. doi: 10.1038/nphys1847.
- [54] A. Giusti-Suzor, X. He, O. Atabek, and F. H. Mies. Above-threshold dissociation of  $h_2^+$  in intense laser fields. *Physical Review Letters*, 64(5):515–518, Jan. 1990. doi: 10.1103/PhysRevLett.64.515.
- [55] M. Glass-Maujean, S. Klumpp, L. Werner, A. Ehresmann, and H. Schmoranzer. The study of the  $D'I\text{I}u1$  state of  $H_2$ : Transition probabilities from the ground state, predissociation yields, and natural linewidths. *The Journal of Chemical Physics*, 128(9):094312, Mar. 2008. doi: 10.1063/1.2835006.
- [56] M. Glass-Maujean, C. Jungen, H. Schmoranzer, A. Knie, I. Haar, R. Hentges, W. Kielich, K. Jänkälä, and A. Ehresmann.  $h_2$  Superexcited States: Experimental and Theoretical Characterization of their Competing Decay-Channel Fluorescence, Dissociation, and Ionization. *Physical Review Letters*, 104(18):183002, May 2010. doi: 10.1103/PhysRevLett.104.183002.
- [57] R. J. Gordon, L. Zhu, and T. Seideman. Using the Phase of Light as a Photochemical Tool. *The Journal of Physical Chemistry A*, 105(18):4387–4394, May 2001. doi: 10.1021/jp003910b.
- [58] C. Guo, M. Li, J. P. Nibarger, and G. N. Gibson. Single and double ionization of diatomic molecules in strong laser fields. *Physical Review A*, 58(6):R4271–R4274, Dec. 1998. doi: 10.1103/PhysRevA.58.R4271.
- [59] P. M. Guyon, T. Baer, L. F. A. Ferreira, I. Nenner, A. Tabche-Fouhaile, R. Botter, and T. R. Govers. Observation of dissociative states of  $O_2^+$  by threshold photoelectron-photoion coincidence. *Journal of Physics B: Atomic and Molecular Physics*, 11(5):L141, Mar. 1978. doi: 10.1088/0022-3700/11/5/005.
- [60] P. M. Guyon, A. V. Golovin, C. J. K. Quayle, M. Vervloet, and M. Richard-Viard. Electron Emission from Aligned Superexcited  $O^*$  Atoms Produced in Photodissociation of  $O_2$  in the 22.20–22.36 eV Region. *Physical Review Letters*, 76(4):600–603, Jan. 1996. doi: 10.1103/PhysRevLett.76.600.
- [61] R. I. Hall, G. Dawber, A. McConkey, M. A. MacDonald, and G. C. King. Vibrational structure of the  $o_2^{2+}$  ground state observed by threshold photoelectron coincidence spectroscopy. *Physical Review Letters*, 68(18):2751–2754, May 1992. doi: 10.1103/PhysRevLett.68.2751.
- [62] Hamamatsu Photonics K.K. Technical Information: MCP assembly, Sept. 2006. URL <http://www.hamamatsu.com>.
- [63] S. E. Harris. Generation of Vacuum-Ultraviolet and Soft X-Ray Radiation Using High-Order Nonlinear Optical Polarizabilities. *Physical Review Letters*, 31(6):341–344, Aug. 1973. doi: 10.1103/PhysRevLett.31.341.

- [64] G. Herzberg. *Molecular Spectra and Molecular Structure: Spectra of Diatomic Molecules*. New York, NY : Van Nostrand, 1957-1967. URL <https://archive.org/details/molecularspectra032774mbp>.
- [65] Y. Hikosaka, T. Aoto, R. I. Hall, K. Ito, R. Hirayama, N. Yamamoto, and E. Miyoshi. Inner-valence states of  $O_2^+$  and dissociation dynamics studied by threshold photoelectron spectroscopy and a configuration interaction calculation. *The Journal of Chemical Physics*, 119(15):7693–7700, Oct. 2003. doi: 10.1063/1.1608854.
- [66] Institute for Nuclear Physics. Atomic Physics, Institut für Kernphysik, Goethe University Frankfurt, 2015. URL <http://www.atom.uni-frankfurt.de/publications/>.
- [67] M. Y. Ivanov and P. B. Corkum. Generation of high-order harmonics from inertially confined molecular ions. *Physical Review A*, 48(1):580–590, July 1993. doi: 10.1103/PhysRevA.48.580.
- [68] T. Jahnke. "Interatomic Coulombic Decay" Experimentelle Untersuchung eines neuartigen, interatomaren Abregungsmechanismus. Dissertation, Goethe Universität Frankfurt, 2005. URL <http://www.atom.uni-frankfurt.de/publications/files/TillJahnke2005.pdf>.
- [69] James R. Macdonald Laboratory, Kansas State University. Publications, 2015. URL <https://jrm.phys.ksu.edu/publications.html>.
- [70] Y. H. Jiang, T. Pfeifer, A. Rudenko, O. Herrwerth, L. Foucar, M. Kurka, K. U. Kühnel, M. Lezius, M. F. Kling, X. Liu, K. Ueda, S. Düsterer, R. Treusch, C. D. Schröter, R. Moshhammer, and J. Ullrich. Temporal coherence effects in multiple ionization of  $n_2$  via XUV pump-probe autocorrelation. *Physical Review A*, 82(4):041403, Oct. 2010. doi: 10.1103/PhysRevA.82.041403.
- [71] Y. H. Jiang, A. Rudenko, J. F. Pérez-Torres, O. Herrwerth, L. Foucar, M. Kurka, K. U. Kühnel, M. Toppin, E. Plésiat, F. Morales, F. Martín, M. Lezius, M. F. Kling, T. Jahnke, R. Dörner, J. L. Sanz-Vicario, J. van Tilborg, A. Belkacem, M. Schulz, K. Ueda, T. J. M. Zouros, S. Düsterer, R. Treusch, C. D. Schröter, R. Moshhammer, and J. Ullrich. Investigating two-photon double ionization of  $d_2$  by XUV-pump\char21{XUV-probe experiments. *Physical Review A*, 81(5):051402, May 2010. doi: 10.1103/PhysRevA.81.051402.
- [72] P. Johnsson, J. Mauritsson, T. Remetter, A. L’Huillier, and K. J. Schafer. Attosecond Control of Ionization by Wave-Packet Interference. *Physical Review Letters*, 99(23):233001, Dec. 2007. doi: 10.1103/PhysRevLett.99.233001.
- [73] I. Kawata, H. Kono, and Y. Fujimura. Adiabatic and diabatic responses of  $H_2^+$  to an intense femtosecond laser pulse: Dynamics of the electronic and nuclear wave packet. *The Journal of Chemical Physics*, 110(23):11152–11165, June 1999. doi: doi:10.1063/1.478002.
- [74] L. Keldysh. Ionization in the Field of a Strong Electromagnetic Wave. 20(5):1307, 1965. URL <http://www.jetp.ac.ru/cgi-bin/e/index/e/20/5/p1307?a=list>.
- [75] F. Kelkensberg, C. Lefebvre, W. Siu, O. Ghafur, T. T. Nguyen-Dang, O. Atabek, A. Keller, V. Serov, P. Johnsson, M. Swoboda, T. Remetter, A. L’Huillier, S. Zherebtsov, G. Sansone, E. Benedetti, F. Ferrari, M. Nisoli, F. Lépine, M. F.

- Kling, and M. J. J. Vrakking. Molecular Dissociative Ionization and Wave-Packet Dynamics Studied Using Two-Color XUV and IR Pump-Probe Spectroscopy. *Physical Review Letters*, 103(12):123005, Sept. 2009. doi: 10.1103/PhysRevLett.103.123005.
- [76] F. Kelkensberg, W. Siu, J. F. Pérez-Torres, F. Morales, G. Gademann, A. Rouzée, P. Johnsson, M. Lucchini, F. Calegari, J. L. Sanz-Vicario, F. Martín, and M. J. J. Vrakking. Attosecond Control in Photoionization of Hydrogen Molecules. *Physical Review Letters*, 107(4):043002, July 2011. doi: 10.1103/PhysRevLett.107.043002.
- [77] I. J. Kim, C. M. Kim, H. T. Kim, G. H. Lee, Y. S. Lee, J. Y. Park, D. J. Cho, and C. H. Nam. Highly Efficient High-Harmonic Generation in an Orthogonally Polarized Two-Color Laser Field. *Physical Review Letters*, 94(24):243901, June 2005. doi: 10.1103/PhysRevLett.94.243901.
- [78] M. F. Kling, C. Siedschlag, A. J. Verhoef, J. I. Khan, M. Schultze, T. Uphues, Y. Ni, M. Uiberacker, M. Drescher, F. Krausz, and M. J. J. Vrakking. Control of Electron Localization in Molecular Dissociation. *Science*, 312(5771):246–248, Apr. 2006. doi: 10.1126/Science.1126259.
- [79] Y. Kobayashi, T. Sekikawa, Y. Nabekawa, and S. Watanabe. 27-fs extreme ultraviolet pulse generation by high-order harmonics. *Optics Letters*, 23(1):64, Jan. 1998. doi: 10.1364/OL.23.000064.
- [80] O. Kornilov, R. Wilcox, and O. Gessner. Nanograting-Based Compact Vuv Spectrometer and Beam Profiler for in-Situ Characterization of High-Order Harmonic Generation Light Sources. *Review of Scientific Instruments*, July 2010. URL <http://www.osti.gov/scitech/biblio/985835>.
- [81] V. P. Krainov. Theory of barrier-suppression ionization of atoms. *Journal of Nonlinear Optical Physics & Materials*, 04(04):775–798, Oct. 1995. doi: 10.1142/S0218863595000343.
- [82] J. L. Krause, K. J. Schafer, and K. C. Kulander. High-order harmonic generation from atoms and ions in the high intensity regime. *Physical Review Letters*, 68(24):3535–3538, June 1992. doi: 10.1103/PhysRevLett.68.3535.
- [83] M. Krikunova, M. Adolph, T. Gorkhover, D. Rupp, S. Schorb, C. Bostedt, S. Roling, B. Siemer, R. Mitzner, H. Zacharias, and T. Möller. Ionization dynamics in expanding clusters studied by XUV pump-probe spectroscopy. *Journal of Physics B: Atomic, Molecular and Optical Physics*, 45(10):105101, May 2012. doi: 10.1088/0953-4075/45/10/105101.
- [84] A. Lafosse, J. C. Brenot, A. V. Golovin, P. M. Guyon, K. Hoejrup, J. C. Houver, M. Lebech, and D. Doweck. Vector correlations in dissociative photoionization of O<sub>2</sub> in the 20–28 eV range. I. Electron-ion kinetic energy correlations. *The Journal of Chemical Physics*, 114(15):6605–6617, Apr. 2001. doi: 10.1063/1.1354182.
- [85] A. Lafosse, J. C. Brenot, P. M. Guyon, J. C. Houver, A. V. Golovin, M. Lebech, D. Doweck, P. Lin, and R. R. Lucchese. Vector correlations in dissociative photoionization of O<sub>2</sub> in the 20–28 eV range. II. Polar and azimuthal dependence of the molecular frame photoelectron angular distribution. *The Journal of Chemical Physics*, 117(18):8368–8384, Nov. 2002. doi: 10.1063/1.1512650.

- [86] A. Lafosse, M. Lebech, J. C. Brenot, P. M. Guyon, L. Spielberger, O. Jagutzki, J. C. Houver, and D. Dowek. Molecular frame photoelectron angular distributions in dissociative photoionization of H<sub>2</sub> in the region of the Q1 and Q2 doubly excited states. *Journal of Physics B: Atomic, Molecular and Optical Physics*, 36(23):4683, Dec. 2003. doi: 10.1088/0953-4075/36/23/007.
- [87] G. Lambert, A. Andreev, J. Gautier, L. Giannessi, V. Malka, A. Petralia, S. Sebban, S. Stremoukhov, F. Tissandier, B. Vodungbo, and P. Zeitoun. Spatial properties of odd and even low order harmonics generated in gas. *Scientific Reports*, 5, Jan. 2015. doi: 10.1038/srep07786.
- [88] J. I. Larruquert and R. A. M. Keski-Kuha. Multilayer Coatings with High Reflectance in the Extreme-Ultraviolet Spectral Range of 50 to 121.6 nm. *Applied Optics*, 38(7):1231, Mar. 1999. doi: 10.1364/AO.38.001231.
- [89] M. Lewenstein, P. Balcou, M. Y. Ivanov, A. L’Huillier, and P. B. Corkum. Theory of high-harmonic generation by low-frequency laser fields. *Physical Review A*, 49(3): 2117–2132, Mar. 1994. doi: 10.1103/PhysRevA.49.2117.
- [90] A. L’Huillier, K. J. Schafer, and K. C. Kulander. Higher-order harmonic generation in xenon at 1064 nm: The role of phase matching. *Physical Review Letters*, 66(17): 2200–2203, Apr. 1991. doi: 10.1103/PhysRevLett.66.2200.
- [91] H. H. Li. Refractive index of alkaline earth halides and its wavelength and temperature derivatives. *Journal of Physical and Chemical Reference Data*, 9(1): 161–290, Jan. 1980. doi: 10.1063/1.555616.
- [92] Y. Liang, S. Augst, S. L. Chin, Y. Beaudoin, and M. Chaker. High harmonic generation in atomic and diatomic molecular gases using intense picosecond laser pulses—a comparison. *Journal of Physics B: Atomic, Molecular and Optical Physics*, 27(20):5119, Oct. 1994. doi: 10.1088/0953-4075/27/20/024.
- [93] P. Lin and R. R. Lucchese. Theoretical studies of cross sections and photoelectron angular distributions in the valence photoionization of molecular oxygen. *The Journal of Chemical Physics*, 116(20):8863–8875, May 2002. doi: 10.1063/1.1467902.
- [94] J. Liu, D. Sprecher, C. Jungen, W. Ubachs, and F. Merkt. Determination of the ionization and dissociation energies of the deuterium molecule (D<sub>2</sub>). *The Journal of Chemical Physics*, 132(15):154301, Apr. 2010. doi: 10.1063/1.3374426.
- [95] Y. Lu, Z. He, J. Cutler, S. Southworth, W. Stolte, and J. Samson. Dissociative photoionization study of O<sub>2</sub>. *Journal of Electron Spectroscopy and Related Phenomena*, 94(1-2):135–147, June 1998. doi: 10.1016/S0368-2048(97)00099-6.
- [96] C. Lyngå, M. B. Gaarde, C. Delfin, M. Bellini, T. W. Hänsch, A. L’Huillier, and C.-G. Wahlström. Temporal coherence of high-order harmonics. *Physical Review A*, 60(6):4823–4830, Dec. 1999. doi: 10.1103/PhysRevA.60.4823.
- [97] A. L. Lytle. *Phase Matching and Coherence of High-Order Harmonic Generation in Hollow Waveguides*. PhD thesis, University of Colorado Boulder, 2008. URL [https://jila.colorado.edu/sites/default/files/assets/files/publications/lytle\\_thesis.pdf](https://jila.colorado.edu/sites/default/files/assets/files/publications/lytle_thesis.pdf).
- [98] J. J. Macklin, J. D. Kmetec, and C. L. Gordon. High-order harmonic generation using intense femtosecond pulses. *Physical Review Letters*, 70(6):766–769, Feb. 1993. doi: 10.1103/PhysRevLett.70.766.

- [99] M. Magrakvelidze, F. He, T. Niederhausen, I. V. Litvinyuk, and U. Thumm. Quantum-beat imaging of the nuclear dynamics in  $h_2^+$ : Dependence of bond softening and bond hardening on laser intensity, wavelength, and pulse duration. *Physical Review A*, 79(3):033410, Mar. 2009. doi: 10.1103/PhysRevA.79.033410.
- [100] M. Magrakvelidze, C. M. Aikens, and U. Thumm. Dissociation dynamics of diatomic molecules in intense laser fields: A scheme for the selection of relevant adiabatic potential curves. *Physical Review A*, 86(2):023402, Aug. 2012. doi: 10.1103/PhysRevA.86.023402.
- [101] C. M. Marian, R. Marian, S. D. Peyerimhoff, B. A. Hess, R. J. Buenker, and G. Seger. Ab initio CI calculation of O<sub>2</sub> + predissociation phenomena induced by a spin-orbit coupling mechanism. *Molecular Physics*, 46(4):779–810, July 1982. doi: 10.1080/00268978200101591.
- [102] L. S. L. S. Marks and T. Baumeister. *Standard handbook for mechanical engineers*. McGraw-Hill, 1967.
- [103] F. Martín, J. Fernández, T. Havermeier, L. Foucar, T. Weber, K. Kreidi, M. Schöffler, L. Schmidt, T. Jahnke, O. Jagutzki, A. Czasch, E. P. Benis, T. Osipov, A. L. Landers, A. Belkacem, M. H. Prior, H. Schmidt-Böcking, C. L. Cocke, and R. Dörner. Single Photon-Induced Symmetry Breaking of H<sub>2</sub> Dissociation. *Science*, 315(5812):629–633, Feb. 2007. doi: 10.1126/Science.1136598.
- [104] F. Mauger, C. Chandre, and T. Uzer. Recollisions and Correlated Double Ionization with Circularly Polarized Light. *Physical Review Letters*, 105(8):083002, Aug. 2010. doi: 10.1103/PhysRevLett.105.083002.
- [105] A. McPherson, G. Gibson, H. Jara, U. Johann, T. S. Luk, I. A. McIntyre, K. Boyer, and C. K. Rhodes. Studies of multiphoton production of vacuum-ultraviolet radiation in the rare gases. *Journal of the Optical Society of America B*, 4(4):595, Apr. 1987. doi: 10.1364/JOSAB.4.000595.
- [106] F. Merkt, P. M. Guyon, and J. Hepburn. High-resolution threshold photoelectron spectrum of molecular oxygen. *Chemical Physics*, 173(3):479–484, July 1993. doi: 10.1016/0301-0104(93)80162-3.
- [107] K. Midorikawa, Y. Nabekawa, and A. Suda. XUV multiphoton processes with intense high-order harmonics. *Progress in Quantum Electronics*, 32(2):43–88, 2008. doi: 10.1016/j.pquantelec.2008.04.001.
- [108] K. Miyazaki and H. Takada. High-order harmonic generation in the tunneling regime. *Physical Review A*, 52(4):3007–3021, Oct. 1995. doi: 10.1103/PhysRevA.52.3007.
- [109] Y. Nabekawa, H. Hasegawa, E. J. Takahashi, and K. Midorikawa. Production of Doubly Charged Helium Ions by Two-Photon Absorption of an Intense Sub-10-fs Soft X-Ray Pulse at 42 eV Photon Energy. *Physical Review Letters*, 94(4):043001, Jan. 2005. doi: 10.1103/PhysRevLett.94.043001.
- [110] Y. Nabekawa, T. Shimizu, T. Okino, K. Furusawa, H. Hasegawa, K. Yamanouchi, and K. Midorikawa. Conclusive Evidence of an Attosecond Pulse Train Observed with the Mode-Resolved Autocorrelation Technique. *Physical Review Letters*, 96(8):083901, Feb. 2006. doi: 10.1103/PhysRevLett.96.083901.

- [111] P. A. Norreys, M. Zepf, S. Moustazis, A. P. Fews, J. Zhang, P. Lee, M. Bakarezos, C. N. Danson, A. Dyson, P. Gibbon, P. Loukakos, D. Neely, F. N. Walsh, J. S. Wark, and A. E. Dangor. Efficient Extreme UV Harmonics Generated from Picosecond Laser Pulse Interactions with Solid Targets. *Physical Review Letters*, 76(11):1832–1835, Mar. 1996. doi: 10.1103/PhysRevLett.76.1832.
- [112] M. Odenweller, N. Takemoto, A. Vredenburg, K. Cole, K. Pahl, J. Titze, L. P. H. Schmidt, T. Jahnke, R. Dörner, and A. Becker. Strong Field Electron Emission from Fixed in Space  $h_2^+$  Ions. *Physical Review Letters*, 107(14):143004, Sept. 2011. doi: 10.1103/PhysRevLett.107.143004.
- [113] A. Palacios. Private Communication, 2015.
- [114] N. A. Papadogiannis, L. A. A. Nikolopoulos, D. Charalambidis, G. D. Tsakiris, P. Tzallas, and K. Witte. Two-Photon Ionization of He through a Superposition of Higher Harmonics. *Physical Review Letters*, 90(13):133902, Apr. 2003. doi: 10.1103/PhysRevLett.90.133902.
- [115] R. Paschotta. *Encyclopedia of laser physics and technology*. Wiley-VCH, Weinheim, 2008. ISBN 978-3-527-40828-3.
- [116] H. Pauly. *Atom, Molecule, and Cluster Beams I*, volume 28 of *Springer Series on Atomic, Optical, and Plasma Physics*. Springer Berlin Heidelberg, Berlin, Heidelberg, 2000. ISBN 978-3-642-08623-6 978-3-662-04213-7. URL <http://link.springer.com/10.1007/978-3-662-04213-7>.
- [117] E. Pellegrin, I. Sics, J. Reyes-Herrera, C. Perez Sempere, J. J. Lopez Alcolea, M. Langlois, J. Fernandez Rodriguez, and V. Carlino. Characterization, optimization and surface physics aspects of in situ plasma mirror cleaning. *Journal of Synchrotron Radiation*, 21(Pt 2):300–314, Mar. 2014. doi: 10.1107/S1600577513032402.
- [118] A. Peralta Conde, J. Kruse, O. Faucher, P. Tzallas, E. P. Benis, and D. Charalambidis. Realization of time-resolved two-vacuum-ultraviolet-photon ionization. *Physical Review A*, 79(6):061405, June 2009. doi: 10.1103/PhysRevA.79.061405.
- [119] T. Pfeifer, C. Spielmann, and G. Gerber. Femtosecond x-ray Science. *Reports on Progress in Physics*, 69(2):443, Feb. 2006. doi: 10.1088/0034-4885/69/2/R04.
- [120] Pfeiffer Vacuum GmbH. *Vacuum Technology Book*, volume 2. Pfeiffer Vacuum GmbH, Apr. 2013. URL [http://www.pfeiffer-vacuum.com/filepool/File/Literature/VTB/Vacuum-Technology-Book-II-Part-2.pdf?request\\_locale=en\\_US&referer=2012](http://www.pfeiffer-vacuum.com/filepool/File/Literature/VTB/Vacuum-Technology-Book-II-Part-2.pdf?request_locale=en_US&referer=2012).
- [121] L. Poletto, P. Villoresi, E. Benedetti, F. Ferrari, S. Stagira, G. Sansone, and M. Nisoli. Temporal characterization of a time-compensated monochromator for high-efficiency selection of extreme-ultraviolet pulses generated by high-order harmonics. *Journal of the Optical Society of America B*, 25(7):B44, July 2008. doi: 10.1364/JOSAB.25.000B44.
- [122] D. Polli, P. Altoè, O. Weingart, K. M. Spillane, C. Manzoni, D. Brida, G. Tomasello, G. Orlandi, P. Kukura, R. A. Mathies, M. Garavelli, and G. Cerullo. Conical intersection dynamics of the primary photoisomerization event in vision. *Nature*, 467(7314):440–443, Sept. 2010. doi: 10.1038/{Nature}09346.

- [123] T. Popmintchev, M.-C. Chen, P. Arpin, M. M. Murnane, and H. C. Kapteyn. The attosecond nonlinear optics of bright coherent X-ray generation. *Nature Photonics*, 4(12):822–832, Dec. 2010. doi: 10.1038/nphoton.2010.256.
- [124] T. Popmintchev, M.-C. Chen, D. Popmintchev, P. Arpin, S. Brown, S. Ališauskas, G. Andriukaitis, T. Balčiunas, O. D. Mücke, A. Pugzlys, A. Baltuška, B. Shim, S. E. Schrauth, A. Gaeta, C. Hernández-García, L. Plaja, A. Becker, A. Jaron-Becker, M. M. Murnane, and H. C. Kapteyn. Bright Coherent Ultrahigh Harmonics in the keV X-ray Regime from Mid-Infrared Femtosecond Lasers. *Science*, 336(6086):1287–1291, Aug. 2012. doi: 10.1126/Science.1218497.
- [125] J. H. Posthumus. The dynamics of small molecules in intense laser fields. *Reports on Progress in Physics*, 67(5):623–665, May 2004. doi: 10.1088/0034-4885/67/5/R01.
- [126] T. P. Rakitzis and R. N. Zare. Photofragment angular momentum distributions in the molecular frame: Determination and interpretation. *The Journal of Chemical Physics*, 110(7):3341–3350, Feb. 1999. doi: 10.1063/1.478200.
- [127] P. Ranitovic, X. M. Tong, B. Gramkow, S. De, B. DePaola, K. P. Singh, W. Cao, M. Magrakvelidze, D. Ray, I. Bocharova, H. Mashiko, A. Sandhu, E. Gagnon, M. M. Murnane, H. C. Kapteyn, I. Litvinyuk, and C. L. Cocke. IR-assisted ionization of helium by attosecond extreme ultraviolet radiation. *New Journal of Physics*, 12(1):013008, 2010. doi: 10.1088/1367-2630/12/1/013008.
- [128] P. Ranitovic, X. M. Tong, C. W. Hogle, X. Zhou, Y. Liu, N. Toshima, M. M. Murnane, and H. C. Kapteyn. Controlling the XUV Transparency of Helium Using Two-Pathway Quantum Interference. *Physical Review Letters*, 106(19):193008, May 2011. doi: 10.1103/PhysRevLett.106.193008.
- [129] P. Ranitovic, C. W. Hogle, P. Rivière, A. Palacios, X.-M. Tong, N. Toshima, A. González-Castrillo, L. Martin, F. Martín, M. M. Murnane, and H. Kapteyn. Attosecond vacuum UV coherent control of molecular dynamics. *Proceedings of the National Academy of Sciences*, 111(3):912–917, Jan. 2014. doi: 10.1073/pnas.1321999111.
- [130] RefractiveIndex. RefractiveIndex.info, 2015. URL <http://refractiveindex.info/?shelf=main&book=He&page=Mansfield>.
- [131] M. Richard-Viard, O. Dutuit, M. Lavollée, T. Govers, P. M. Guyon, and J. Durup. O+2 ions dissociation studied by threshold photoelectron–photoion coincidence method. *The Journal of Chemical Physics*, 82(9):4054–4063, May 1985. doi: 10.1063/1.448846.
- [132] RoentDek. RoentDek Handels GmbH, 2015. URL <http://www.roentdek.com>.
- [133] H. Rottke, J. Ludwig, and W. Sandner. Two-photon dissociative photoionization and photodissociation of single rotational states. *Journal of Physics B: Atomic, Molecular and Optical Physics*, 30(18):4049, Sept. 1997. doi: 10.1088/0953-4075/30/18/008.
- [134] F. Salmassi. Private communication, 2014.
- [135] I. Sánchez and F. Martín. Resonant dissociative photoionization of  $h_2$  and  $d_2$ . *Physical Review A*, 57(2):1006–1017, Feb. 1998. doi: 10.1103/PhysRevA.57.1006.

- [136] I. Sánchez and F. Martín. Dissociative photoionization of  $h_2$  and  $d_2$  by (30–37)-eV photons via  $^1\Pi_u$  states. *Physical Review A*, 60(3):2200–2206, Sept. 1999. doi: 10.1103/PhysRevA.60.2200.
- [137] A. S. Sandhu, E. Gagnon, R. Santra, V. Sharma, W. Li, P. Ho, P. Ranitovic, C. L. Cocke, M. M. Murnane, and H. C. Kapteyn. Observing the Creation of Electronic Feshbach Resonances in Soft X-ray-Induced  $O_2$  Dissociation. *Science*, 322(5904):1081–1085, Nov. 2008. doi: 10.1126/Science.1164498.
- [138] G. Sansone, F. Kelkensberg, J. F. Pérez-Torres, F. Morales, M. F. Kling, W. Siu, O. Ghafur, P. Johnsson, M. Swoboda, E. Benedetti, F. Ferrari, F. Lépine, J. L. Sanz-Vicario, S. Zherebtsov, I. Znakovskaya, A. L’Huillier, M. Y. Ivanov, M. Nisoli, F. Martín, and M. J. J. Vrakking. Electron localization following attosecond molecular photoionization. *Nature*, 465(7299):763–766, June 2010. doi: 10.1038/Nature09084.
- [139] H. Satzger, D. Townsend, M. Z. Zgierski, S. Patchkovskii, S. Ullrich, and A. Stolow. Primary processes underlying the photostability of isolated DNA bases: Adenine. *Proceedings of the National Academy of Sciences*, 103(27):10196–10201, May 2006. doi: 10.1073/pnas.0602663103.
- [140] A. M. Sayler, P. Q. Wang, K. D. Carnes, B. D. Esry, and I. Ben-Itzhak. Determining laser-induced dissociation pathways of multielectron diatomic molecules: Application to the dissociation of  $o_2^+$  by high-intensity ultrashort pulses. *Physical Review A*, 75(6):063420, June 2007. doi: 10.1103/PhysRevA.75.063420.
- [141] K. Schnorr, A. Senftleben, M. Kurka, A. Rudenko, L. Foucar, G. Schmid, A. Broska, T. Pfeifer, K. Meyer, D. Anielski, R. Boll, D. Rolles, M. Kübel, M. F. Kling, Y. H. Jiang, S. Mondal, T. Tachibana, K. Ueda, T. Marchenko, M. Simon, G. Brenner, R. Treusch, S. Scheit, V. Averbukh, J. Ullrich, C. D. Schröter, and R. Moshhammer. Time-Resolved Measurement of Interatomic Coulombic Decay in  $ne_2$ . *Physical Review Letters*, 111(9):093402, Aug. 2013. doi: 10.1103/PhysRevLett.111.093402.
- [142] K. Schnorr, A. Senftleben, M. Kurka, A. Rudenko, G. Schmid, T. Pfeifer, K. Meyer, M. Kübel, M. Kling, Y. Jiang, R. Treusch, S. Düsterer, B. Siemer, M. Wöstmann, H. Zacharias, R. Mitzner, T. Zouros, J. Ullrich, C. Schröter, and R. Moshhammer. Electron Rearrangement Dynamics in Dissociating  $i_2^{n+}$  Molecules Accessed by Extreme Ultraviolet Pump-Probe Experiments. *Physical Review Letters*, 113(7):073001, Aug. 2014. doi: 10.1103/PhysRevLett.113.073001.
- [143] M. S. Schöffler, J. Titze, N. Petridis, T. Jahnke, K. Cole, L. P. H. Schmidt, A. Czasch, D. Akoury, O. Jagutzki, J. B. Williams, N. A. Cherepkov, S. K. Semenov, C. W. McCurdy, T. N. Rescigno, C. L. Cocke, T. Osipov, S. Lee, M. H. Prior, A. Belkacem, A. L. Landers, H. Schmidt-Böcking, T. Weber, and R. Dörner. Ultrafast Probing of Core Hole Localization in  $N_2$ . *Science*, 320(5878):920–923, May 2008. doi: 10.1126/Science.1154989.
- [144] G. D. Scholes, G. R. Fleming, A. Olaya-Castro, and R. van Grondelle. Lessons from Nature about solar light harvesting. *Nature Chemistry*, 3(10):763–774, Oct. 2011. doi: 10.1038/nchem.1145.
- [145] O. Schubert, M. Hohenleutner, F. Langer, B. Urbanek, C. Lange, U. Huttner, D. Golde, T. Meier, M. Kira, S. W. Koch, and R. Huber. Sub-cycle control of

- terahertz high-harmonic generation by dynamical Bloch oscillations. *Nature Photonics*, 8(2):119–123, Feb. 2014. doi: 10.1038/nphoton.2013.349.
- [146] S. Schulz, I. Grguraš, C. Behrens, H. Bromberger, J. T. Costello, M. K. Czwalińska, M. Felber, M. C. Hoffmann, M. Ilchen, H. Y. Liu, T. Mazza, M. Meyer, S. Pfeiffer, P. Prędki, S. Schefer, C. Schmidt, U. Wegner, H. Schlarb, and A. L. Cavalieri. Femtosecond all-optical synchronization of an X-ray free-electron laser. *Nature Communications*, 6:5938, Jan. 2015. doi: 10.1038/ncomms6938.
- [147] A. Scrinzi, M. Geissler, and T. Brabec. Ionization Above the Coulomb Barrier. *Physical Review Letters*, 83(4):706–709, July 1999. doi: 10.1103/PhysRevLett.83.706.
- [148] T. Sekikawa, T. Ohno, T. Yamazaki, Y. Nabekawa, and S. Watanabe. Pulse Compression of a High-Order Harmonic by Compensating the Atomic Dipole Phase. *Physical Review Letters*, 83(13):2564–2567, Sept. 1999. doi: 10.1103/PhysRevLett.83.2564.
- [149] T. Sekikawa, T. Katsura, S. Miura, and S. Watanabe. Measurement of the Intensity-Dependent Atomic Dipole Phase of a High Harmonic by Frequency-Resolved Optical Gating. *Physical Review Letters*, 88(19):193902, Apr. 2002. doi: 10.1103/PhysRevLett.88.193902.
- [150] B. Shan, S. Ghimire, and Z. Chang. Effect of orbital symmetry on high-order harmonic generation from molecules. *Physical Review A*, 69(2):021404, Feb. 2004. doi: 10.1103/PhysRevA.69.021404.
- [151] H. J. Shin, D. G. Lee, Y. H. Cha, K. H. Hong, and C. H. Nam. Generation of Nonadiabatic Blueshift of High Harmonics in an Intense Femtosecond Laser Field. *Physical Review Letters*, 83(13):2544–2547, Sept. 1999. doi: 10.1103/PhysRevLett.83.2544.
- [152] N. Shivaram, H. Timmers, X.-M. Tong, and A. Sandhu. Attosecond-Resolved Evolution of a Laser-Dressed Helium Atom: Interfering Excitation Paths and Quantum Phases. *Physical Review Letters*, 108(19):193002, May 2012. doi: 10.1103/PhysRevLett.108.193002.
- [153] A. E. Siegman. *Lasers*. Univ. Science Books, Mill Valley, Calif, 1986. ISBN 978-0-935702-11-8 0-935702-11-3 978-0-935702-11-8 0-19-855713-2.
- [154] A. E. Siegman. Defining, measuring, and optimizing laser beam quality. volume 1868, pages 2–12, 1993. doi: 10.1117/12.150601.
- [155] R. E. F. Silva, F. Catoire, P. Rivière, H. Bachau, and F. Martín. Correlated Electron and Nuclear Dynamics in Strong Field Photoionization of  $h_2^+$ . *Physical Review Letters*, 110(11):113001, Mar. 2013. doi: 10.1103/PhysRevLett.110.113001.
- [156] K. P. Singh, F. He, P. Ranitovic, W. Cao, S. De, D. Ray, S. Chen, U. Thumm, A. Becker, M. M. Murnane, H. C. Kapteyn, I. V. Litvinyuk, and C. L. Coker. Control of Electron Localization in Deuterium Molecular Ions using an Attosecond Pulse Train and a Many-Cycle Infrared Pulse. *Physical Review Letters*, 104(2):023001, Jan. 2010. doi: 10.1103/PhysRevLett.104.023001.
- [157] W. Siu, F. Kelkensberg, G. Gademann, A. Rouzée, P. Johnsson, D. Doweck, M. Lucchini, F. Calegari, U. De Giovannini, A. Rubio, R. R. Lucchese, H. Kono, F. Lépine, and M. J. J. Vrakking. Attosecond control of dissociative ionization of O<sub>2</sub>

- molecules. *Physical Review A*, 84(6):063412, Dec. 2011. doi: 10.1103/PhysRevA.84.063412.
- [158] C. Spielmann, N. H. Burnett, S. Sartania, R. Koppitsch, M. Schnürer, C. Kan, M. Lenzner, P. Wobrauschek, and F. Krausz. Generation of Coherent X-rays in the Water Window Using 5-Femtosecond Laser Pulses. *Science*, 278(5338):661–664, Oct. 1997. doi: 10.1126/{Science}.278.5338.661.
- [159] H. Stapelfeldt and T. Seideman. Colloquium: Aligning molecules with strong laser pulses. *Reviews of Modern Physics*, 75(2):543–557, Apr. 2003. doi: 10.1103/RevModPhys.75.543.
- [160] A. Staudte. *Subfemtosecond Electron Dynamics of H<sub>2</sub> in Strong Fields or The Quest for the Molecular Clock*. Dissertation, Goethe Universität Frankfurt, Frankfurt am Main, 2005. URL <http://www.atom.uni-frankfurt.de/publications/files/AndreStaudte2005.pdf>.
- [161] A. Staudte, D. Pavičić, S. Chelkowski, D. Zeidler, M. Meckel, H. Niikura, M. Schöffler, S. Schössler, B. Ulrich, P. P. Rajeev, T. Weber, T. Jahnke, D. M. Villeneuve, A. D. Bandrauk, C. L. Cocke, P. B. Corkum, and R. Dörner. Attosecond Strobing of Two-Surface Population Dynamics in Dissociating *d*<sub>2</sub>. *Physical Review Letters*, 98(7):073003, Feb. 2007. doi: 10.1103/PhysRevLett.98.073003.
- [162] A. Staudte, S. Patchkovskii, D. Pavičić, H. Akagi, O. Smirnova, D. Zeidler, M. Meckel, D. M. Villeneuve, R. Dörner, M. Y. Ivanov, and P. B. Corkum. Angular Tunneling Ionization Probability of Fixed-in-Space *h*<sub>2</sub> Molecules in Intense Laser Pulses. *Physical Review Letters*, 102(3):033004, Jan. 2009. doi: 10.1103/PhysRevLett.102.033004.
- [163] R. E. Stratmann and R. R. Lucchese. A graphical unitary group approach to study multiplet specific multichannel electron correlation effects in the photoionization of O<sub>2</sub>. *The Journal of Chemical Physics*, 102(21):8493–8505, June 1995. doi: 10.1063/1.468841.
- [164] D. Strickland and G. Mourou. Compression of amplified chirped optical pulses. *Optics Communications*, 55(6):447–449, Oct. 1985. doi: 10.1016/0030-4018(85)90151-8.
- [165] F. P. Sturm. *Photo and Auger Electron Angular Distributions of Fixed-in-Space CO<sub>2</sub>*. Diplomarbeit, Goethe Universität Frankfurt, 2009. URL [http://www.atom.uni-frankfurt.de/publications/files/Felix\\_Sturm\\_2009.pdf](http://www.atom.uni-frankfurt.de/publications/files/Felix_Sturm_2009.pdf).
- [166] E. Takahashi, Y. Nabekawa, T. Otsuka, M. Obara, and K. Midorikawa. Generation of highly coherent submicrojoule soft x rays by high-order harmonics. *Physical Review A*, 66(2):021802, Aug. 2002. doi: 10.1103/PhysRevA.66.021802.
- [167] I. Thomann, A. Bahabad, X. Liu, R. Trebino, M. M. Murnane, and H. C. Kapteyn. Characterizing isolated attosecond pulses from hollow-core waveguides using multi-cycle driving pulses. *Optics Express*, 17(6):4611, Mar. 2009. doi: 10.1364/OE.17.004611.
- [168] H. Timmers, N. Shivaram, and A. Sandhu. Ultrafast Dynamics of Neutral Superexcited Oxygen: A Direct Measurement of the Competition between Autoionization and Predissociation. *Physical Review Letters*, 109(17):173001, Oct. 2012. doi: 10.1103/PhysRevLett.109.173001.

- [169] X.-M. Tong. Private communication, 2015.
- [170] V. Tosa, E. Takahashi, Y. Nabekawa, and K. Midorikawa. Generation of high-order harmonics in a self-guided beam. *Physical Review A*, 67(6):063817, June 2003. doi: 10.1103/PhysRevA.67.063817.
- [171] F. Trinter, J. B. Williams, M. Weller, M. Waitz, M. Pitzer, J. Voigtsberger, C. Schober, G. Kastirke, C. Müller, C. Goihl, P. Burzynski, F. Wiegandt, T. Bauer, R. Wallauer, H. Sann, A. Kalinin, L. P. H. Schmidt, M. Schöffler, N. Sisourat, and T. Jahnke. Evolution of Interatomic Coulombic Decay in the Time Domain. *Physical Review Letters*, 111(9):093401, Aug. 2013. doi: 10.1103/PhysRevLett.111.093401.
- [172] P. Tzallas, D. Charalambidis, N. A. Papadogiannis, K. Witte, and G. D. Tsakiris. Direct observation of attosecond light bunching. *Nature*, 426(6964):267–271, Nov. 2003. doi: 10.1038/{Nature}02091.
- [173] P. Tzallas, E. Skantzakis, L. a. A. Nikolopoulos, G. D. Tsakiris, and D. Charalambidis. Extreme-ultraviolet pump-probe studies of one-femtosecond-scale electron dynamics. *Nature Physics*, 7(10):781–784, Oct. 2011. doi: 10.1038/nphys2033.
- [174] M. Uiberacker, T. Uphues, M. Schultze, A. J. Verhoef, V. Yakovlev, M. F. Kling, J. Rauschenberger, N. M. Kabachnik, H. Schröder, M. Lezius, K. L. Kompa, H.-G. Muller, M. J. J. Vrakking, S. Hendel, U. Kleineberg, U. Heinzmann, M. Drescher, and F. Krausz. Attosecond real-time observation of electron tunnelling in atoms. *Nature*, 446(7136):627–632, Apr. 2007. doi: 10.1038/{Nature}05648.
- [175] W. Vanroose, F. Martín, T. N. Rescigno, and C. W. McCurdy. Complete Photo-Induced Breakup of the H<sub>2</sub> Molecule as a Probe of Molecular Electron Correlation. *Science*, 310(5755):1787–1789, Dec. 2005. doi: 10.1126/{Science}.1120263.
- [176] C.-G. Wahlström, J. Larsson, A. Persson, T. Starczewski, S. Svanberg, P. Salières, P. Balcou, and A. L’Huillier. High-order harmonic generation in rare gases with an intense short-pulse laser. *Physical Review A*, 48(6):4709–4720, Dec. 1993. doi: 10.1103/PhysRevA.48.4709.
- [177] S. J. Weber, B. Manschwetus, M. Billon, M. Böttcher, M. Bougeard, P. Breger, M. Géléoc, V. Gruson, A. Huetz, N. Lin, Y. J. Picard, T. Ruchon, P. Salières, and B. Carré. Flexible attosecond beamline for high harmonic spectroscopy and XUV/near-IR pump probe experiments requiring long acquisition times. *Review of Scientific Instruments*, 86(3):033108, Mar. 2015. doi: 10.1063/1.4914464.
- [178] T. Weber. *Untersuchung der verschränkten Bewegung freier Elektronenpaare emittiert aus Ein- und Zweizentren Coulomb-Potentialen in Photoabsorptionsprozessen*. Dissertation, Goethe Universität Frankfurt, 2003.
- [179] T. Weber, A. O. Czasch, O. Jagutzki, A. K. Müller, V. Mergel, A. Kheifets, E. Rotenberg, G. Meigs, M. H. Prior, S. Daveau, A. Landers, C. L. Cocke, T. Osipov, R. Díez Muiño, H. Schmidt-Böcking, and R. Dörner. Complete photo-fragmentation of the deuterium molecule. *Nature*, 431(7007):437–440, Sept. 2004. doi: 10.1038/{Nature}02839.

- [180] W. C. Wiley and I. H. McLaren. Time-of-Flight Mass Spectrometer with Improved Resolution. *Review of Scientific Instruments*, 26(12):1150–1157, Dec. 1955. doi: 10.1063/1.1715212.
- [181] T. Wilhein, S. Rehbein, D. Hambach, M. Berglund, L. Rymell, and H. M. Hertz. A slit grating spectrograph for quantitative soft x-ray spectroscopy. *Review of Scientific Instruments*, 70(3):1694–1699, Mar. 1999. doi: 10.1063/1.1149653.
- [182] A. A. Wills, A. A. Cafolla, and J. Comer. The production of autoionizing states of atomic oxygen by the photodissociation of O<sub>2</sub>. *Journal of Physics B: Atomic, Molecular and Optical Physics*, 24(18):3989–4000, Sept. 1991. doi: 10.1088/0953-4075/24/18/013.
- [183] T. W. Wright. Private communication, Nov. 2015.
- [184] J. Wu, M. Kunitski, M. Pitzer, F. Trinter, L. P. H. Schmidt, T. Jahnke, M. Magrakvelidze, C. B. Madsen, L. B. Madsen, U. Thumm, and R. Dörner. Electron-Nuclear Energy Sharing in Above-Threshold Multiphoton Dissociative Ionization of h<sub>2</sub>. *Physical Review Letters*, 111(2):023002, July 2013. doi: 10.1103/PhysRevLett.111.023002.
- [185] J. Wu, M. Magrakvelidze, L. Schmidt, M. Kunitski, T. Pfeifer, M. Schöffler, M. Pitzer, M. Richter, S. Voss, H. Sann, H. Kim, J. Lower, T. Jahnke, A. Czasch, U. Thumm, and R. Dörner. Understanding the role of phase in chemical bond breaking with coincidence angular streaking. *Nature Communications*, 4, July 2013. doi: 10.1038/ncomms3177.
- [186] D. Xenakis, O. Faucher, D. Charalambidis, and C. Fotakis. Observation of two-XUV-photon ionization using harmonic generation from a short, intense laser pulse. *Journal of Physics B: Atomic, Molecular and Optical Physics*, 29(12):L457, June 1996. doi: 10.1088/0953-4075/29/12/003.
- [187] L. H. Yu, L. DiMauro, A. Doyuran, W. S. Graves, E. D. Johnson, R. Heese, S. Krinsky, H. Loos, J. B. Murphy, G. Rakowsky, J. Rose, T. Shaftan, B. Sheehy, J. Skaritka, X. J. Wang, and Z. Wu. First Ultraviolet High-Gain Harmonic-Generation Free-Electron Laser. *Physical Review Letters*, 91(7):074801, Aug. 2003. doi: 10.1103/PhysRevLett.91.074801.
- [188] A. H. Zewail. Femtochemistry: Atomic-Scale Dynamics of the Chemical Bond†. *The Journal of Physical Chemistry A*, 104(24):5660–5694, June 2000. doi: 10.1021/jp001460h.
- [189] K. Zhao, Q. Zhang, M. Chini, Y. Wu, X. Wang, and Z. Chang. Tailoring a 67 attosecond pulse through advantageous phase-mismatch. *Optics Letters*, 37(18):3891, Sept. 2012. doi: 10.1364/OL.37.003891.
- [190] Z. X. Zhao and T. Brabec. Tunnel ionization of open-shell atoms. *Journal of Physics B: Atomic, Molecular and Optical Physics*, 39(22):L345, Nov. 2006. doi: 10.1088/0953-4075/39/22/L01.
- [191] X. Zhu, X. Liu, Y. Li, M. Qin, Q. Zhang, P. Lan, and P. Lu. Molecular high-order-harmonic generation due to the recollision mechanism by a circularly polarized laser pulse. *Physical Review A*, 91(4):043418, Apr. 2015. doi: 10.1103/PhysRevA.91.043418.

- [192] M. Zohrabi, J. McKenna, B. Gaire, N. G. Johnson, K. D. Carnes, S. De, I. A. Bocharova, M. Magrakvelidze, D. Ray, I. V. Litvinyuk, C. L. Cocke, and I. Ben-Itzhak. Vibrationally resolved structure in O<sub>2</sub><sup>+</sup> dissociation induced by intense ultrashort laser pulses. *Physical Review A*, 83(5):053405, May 2011. doi: 10.1103/PhysRevA.83.053405.



# Acknowledgements

*“Anytime you see a turtle up on top of a fence post, you know he had some help.”*

— Alex Haley

Finally, I would like to thank those many people that have helped and supported me on this roller-coaster ride that finally concludes with this dissertation. During the past six years, many people have helped me bring MISTERS to life and to finally write this thesis. It has not always been easy, but I feel incredibly fortunate to have had the help of so many skilled and thoughtful people. When I came to Berkeley, I was full of excitement and curiosity about this project. I certainly did not anticipate the full scope and the difficulty of this task, but, looking back - I would probably do it again. Leaving the wonderful environment with many people in Reinhard Dörner's group in Frankfurt, life at LBNL can seem at times lonely. Working at a national lab with very few students but world class researchers from many fields has certainly a different feel than the lively university environment. Working more independently, however, I have learned so much from all those incredible mentors in the various groups and fields at LBNL. In the following, I will try to list all those contributions. Meanwhile, I might forget some, for which I would like to apologize in advance.

I would like to start the list of acknowledgements with my advisor at LBNL. Thorsten Weber is the father of the MISTERS end-station. He planned, funded and directed the project and constructed most parts of the end-station. Among many good and bad times, including the trouble with the UHV chamber manufacturer that held us back for months, or delays related to the laser, I will not forget when we lifted the entire chamber with a big crane and tightened the massive bolts of the wire seal on the largest flange with combined force and a one meter long steel extension of the wrench. I am indebted to him for the help, support, and trust he has given me throughout the entire time, including this one little push that came at the right time to get me 'walking on my own' and 'steering the wagon'. Especially, I would like to thank Thorsten for always taking care of his people when it comes to health and safety issues and in the administrative jungle at LBNL.

It was a great fortune that Predrag Ranitovic joined the group, when the beamline and the MISTERS end-station were finally operational and had started to see it's first light. With his experience with High Harmonic Generation experiments in combination with COLTRIMS and his large source of ideas and inspiration, he was an indispensable push for the project. I am very thankful that he has taken me on as his student teaching me attosecond science and being positive.

I would not have been able to obtain my PhD with a project performed at a laboratory in California without the generous offer and help of my doctoral advisor Reinhard Dörner. He made my stay at LBNL possible and recommended me for a scholarship at the Studienstiftung des deutschen Volkes. He was the reason why I started with atomic physics, and his knowledge, inspiration, and excitement for atomic and molecular physics to find answers to those stunning questions of the quantum world is a motivation to continue working in this field.

As the division director and group leader, Ali Belkacem has provided and nourished the ground on which MISTERS has grown and advised on the project along the way. I am thankful for his support and the opportunity to work in his group.

The first person, who needs to be named for the practical contributions to the projects succes is Travis Wright, my fellow graduate student. Not only has he build the laser system and HHG source providing the photons for MISTERS, he has been the comrade in the trenches of daily lab operation and the medic for any laser issues. Irina Bocharova has worked relentlessly for more than 2 years as a post-doc on the MISTERS project before we could finally move it to the laser laboratory. She has been an invaluable asset and driving force on planing the Split-Mirror-Interferometer and the XUV-Spectrometer and was a wonderful office-, lab mate and friend. Dipanwita Ray joined the MISTERS project when we moved the end-station to the laser system. We have spent many long and hard work days together in the lab, and her little chocolate treats prevented us from going crazy when the mode-locking of the oscillator dropped, again...

As I have mentioned in the beginning, the incredible amount of inspiring and smart people at LBNL is a great resource that makes this place special. Among those great mentors are David A.L. Kilcoyne and Dan Slaughter. They have always been there for me when I needed advice or help with whatever it was. Since my first days at LBNL during my diploma thesis, David has become a great friend. I admire his expertise and incredible handy-ness while keeping it classy with a tie on the beamline. With Dan, I have spent days and nights at the FEL in Stanford, in the lab at LBNL, as well as under water in the ocean near Monterey.

Niranjan Shivaram has worked on the MISTERS project for a few months with all his great scientific drive and knowledge before developing a VMI end-station in the neighboring lab. Thank you the help and for patiently answering my questions. I am also thankful to James Cryan, our former laser wizard, and Elio Champenois, the wizard padawan, for their help with the laser and answers to optics, computational, and scientific questions. Tom Allison built the first HHG setup in our group at LBNL and advised on the construction of the new laboratory. His notes and advice were an invaluable resource. With Bishwanath Gaire I have worked on numerous COLTRIMS beamtimes before I focused exclusively on making MISTERS work. His knowledge of molecular physics and his patience are endless. From the COLTRIMS team I would also like to thank Averell Gatton who has helped me on numerous occasions, as well as Jonas Rist and Joshua Brown Williams during their stays at LBNL.

Our collaboration with the Center for X-Ray Optics (CXRO) has contributed in numerous ways to the MISTERS project. Specifically I would like to mention, Seno Rekawa and Nathan Smith for the development and construction of the Split-Mirror-Interferometer (SMI) and Paul Denham for designing electronics and the sensors used in the SMI and the back-focussing mirror. Special thanks to Rene Delano from the CXRO machine shop for teaching me how to make technical drawings and to design mechanical parts in better ways. Rene is the true master machinist at LBNL, and he deserves great respect for his precision and ability to understand what the scientist meant to draw (but forgot). Thanks also to Kurt Kruger for teaching me machining with the lathe and the mill.

While spending most of the time in Berkeley, it was great to still have all the support of the people in Frankfurt. Markus Schöffler worked with me at LBNL when I came back to Berkeley and stayed an advisor and friend throughout the years. Achim Czasch provided not only the COBOLD version with the framework to run the MISTERS data acquisition with a translation stage but was always incredibly helpful and available when things didn't work. Many thanks to him, Ottmar and the rest of the RoentDek team. With his incredible knowledge of electronics, Lothar Schmidt built a pulse-height-to-time converter,

and answered many questions sent from Berkeley. With his great humor and thoughtfulness Till Jahnke made sure that no 'kids' were forgotten, not even the lost son in California.

I would like to thank Alicia Palacios, Xiao-Min Tong, and Bob Lucchese for providing potential energy curves and calculations shown in this thesis. Also, I would like to acknowledge fruitful discussions with Dan Haxton, Bill McCurdy, and Tom Rescigno. Thanks to Thorsten, Predrag, Dan, David, and Reinhard for their proofreading and suggestions for improving this manuscript. Thanks to Café Strada, the Berkeley Law School, and the BSC for providing me good coffee and great space to write this thesis. I would like to acknowledge generous funding from the University of Frankfurt, LBNL (University of California), and the Studienstiftung des deutschen Volkes.

Of course my time at Berkeley was not spent entirely in the lab. Whenever I had the chance, I tried to go outside and enjoy nature, America's true treasure. Special thanks to the sun which shines almost every day in Berkeley, something priceless if you work in a lab without windows. Many friendships developed over the years which gave me the balance I needed to work with passion and energy on this project for 6 years. Naming all those would be too long of a list to add here. Berkeley is a truly special place because of all the smart and inspiring people. The Hillegass Parker Coop was my home for almost 6 years, and I met many wonderful students and formed many lasting friendships.

At last I want to thank my parents, my sister and my family, as they are truly responsible for where life has lead me and Irene for continuing this journey together.

**Table 6:** Acknowledgement of the major contributions to the project presented in this work. This list does not include all the people who contributed to different parts of the project through advice or help as mentioned in the text above. The overall concept and senior project leader was T. Weber.

Component	Design & Construction	Figure
<b>MISTERS End-Station</b>		
UHV chamber	T. Weber, M. Weckenbrock, F. Sturm, I. Bocharova	5.1,5.10
Jet source	T. Weber, I. Bocharova, F. Sturm	5.3
Focusing optics	F. Sturm, T. Weber	5.4
Spectrometer	F. Sturm, T. Weber, I. Bocharova	5.2,5.5
<b>XUV Source</b>		
Laser system	T. Wright, Ch. Khurmi, T. Allison	3.6
HHG source	T. Wright, Ch. Khurmi, T. Allison	3.7
<b>XUV Beamline</b>		
Solid filters	F. Sturm, T. Wright, T. Allison	4.6
Gas filter cell	F. Sturm, T. Wright, D. Ray	4.7
Split-Mirror-Interferometer	I. Bocharova, F. Sturm, CXRO	4.10
XUV spectrometer	I. Bocharova, F. Sturm	4.15
Different. pump. stage	F. Sturm, T. Weber	4.21
Vacuum alignment irises and beam surveillance	F. Sturm, T. Wright	4.22,4.23,4.24
<b>Operation &amp; Experiments</b>		
Data acquisition	F. Sturm, T. Wright, D. Ray, P. Ranitovic, T. Weber	
Data analysis	F. Sturm	

# Index

- (A) Direct ionization XUV - IR, [108](#)
- (A) Direct ionization XUV - VUV, [110](#)
- (B) Sequential ionization XUV - IR, [110](#)
- (B) Sequential ionization XUV - VUV, [112](#)
- (B<sub>2</sub>) 2-step sequential ionization, [110](#)
- 2-photon transition distribution, [114](#)
- 3-step model, [19](#), [21](#)
  
- above-threshold ionization (ATI), [26](#)
- Absorption length, [28](#)
- absorption length, [28](#)
- absorption limited HHG, [29](#)
- ADK theory, [20](#)
- attosecond pulse train, [23](#)
- Axial Recoil Approximation, [72](#)
  
- barrier suppression ionization, [20](#)
- Beam lost in mirror gap, [54](#)
- beta barium borate (BBO), [5](#)
- Blueshift of the n<sup>th</sup> harmonic, [37](#)
- blueshifting, [61](#)
- bond softening, [108](#)
- bond-softening, [15](#)
- Born-Oppenheimer approximation, [3](#)
  
- capacitive distance sensor, [80](#)
- chirped pulse amplification (CPA), [31](#)
- COBOLD PC, [85](#)
- Cobold PC, [94](#)
- Coherence length, [29](#)
- coherence length, [29](#)
- coherent attosecond control, [7](#)
- Coincidence Filter, [102](#)
- Cold Target Recoil Ion Momentum Spectroscopy (COLTRIMS), [71](#)
- COLTRIMS, [6](#), [80](#)
- conductivity, [65](#)
- Conductivity of a long tube, [65](#)
- Conductivity of an orifice, [65](#)
- constant fraction discriminator (CFD), [85](#)
- cutoff law, [23](#)
  
- Diffraction on a grating, [57](#)
- Dispersion mismatch, [27](#)
- Dissociation I, [123](#)
- Dissociation II, [123](#)
- Dissociation III, [123](#)
- Dissociation IV, [123](#)
- Dissociation V, [123](#)
- Dissociation VI, [123](#)
- Dissociation VII, [123](#)
  
- electric dipole approximation, [78](#)
- electric dipole operator, [78](#)
- Electric dipole transition, [78](#)
- Electric field (dispersive medium), [153](#)
- Electric field (frequency domain), [153](#)
- Electric field (time domain), [153](#)
- electronic states, [3](#)
- electrostatic defocusing lens, [84](#)
- Electrostatic focusing lens, [84](#)
- Empirical speed ratio for molecules, [77](#)
- Energy per degree of freedom, [76](#)
  
- Femtochemistry, [4](#), [9](#)
- Fish spectrum, [102](#)
- fish spectrum, [103](#)
- fluorescence, [3](#)
- Fourier transform, [106](#)
- Free-electron lasers (FELs), [12](#)
- frequency comb, [25](#)
- Frequency of the n<sup>th</sup> harmonic, [23](#)
- Fresnel equations, [155](#)
  
- Gaussian beam waist at focus, [28](#)
- Geometrical phase shift, [28](#)
- Group delay, [42](#), [153](#)
- Guy phase shift, [28](#)
  
- Hellfire Mode, [94](#)
- Hellfire mode condition, [94](#)
- Hexanode, [82](#)
- HHG blue shift, [37](#)
- High Harmonic Generation (HHG), [12](#), [19](#), [21](#)

- highest occupied molecular orbital (HOMO), 9, 124
- homogeneous acceleration region, 84
- Keldysh Parameter, 21
- Lecher line, 82
- Linear Variable Differential Transformer (LVDT), 80
- list-mode files (lmf), 85
- load resistor, 86
- Maximal Harmonic Energy, 23
- MISTERS, 7
- molecular flow, 65
- Momentum Imaging Spectroscopy for Time Resolved Studies (MISTERS), 72
- Multi-hit limit, 94
- multi-photon ionization, 20
- optical harmonics, 20
- optical interference, 129
- Parallel momentum half-width, 77
- parallel transition, 114
- perpendicular transition, 114
- Perturbative terms, 20
- Phase (dispersive medium), 153
- Phase matching, 26
- Phase matching terms, 27
- Phase velocity shift, 26
- Photo-fragment angular distribution, 114
- Photon energy, 22
- Plasma frequency, 27
- Plasma phase shift, 27
- Polarisation in linear optics, 19
- polarization density, 19
- Polarization in a medium, 19
- Polarization in the perturbative regime, 19
- Ponderomotive Energy, 21
- potential energy curves (PEC), 104
- Pulse delay in a dispersive medium, 42
- pump-probe spectroscopy, 4, 10
- Quantum interference, 129
- quantum interference, 129
- Raleigh length, 28
- Reaction Microscope, 71
- reaction microscope, 6
- Refractive index change, 37
- resonant two-photon absorption, 78
- Resonant two-photon absorption probability, 78
- Second order perturbation, 20
- seeding, 12
- self focusing, 31
- self phase modulation, 31
- self-amplified spontaneous emission (SASE), 12
- self-phase modulation (SPM), 37
- Sellmeier equation, 27
- sequential two-photon absorption, 78
- SMI delay calculation, 54
- spatial anisotropy parameter, 114
- Speed ratio, 76
- speed ratio, 76
- strong-field regime, 19
- susceptibility, 19
- Target density, 75
- Target diameter, 75
- Temperature of the expanded jet, 76
- time-to-digital converters (TDCs), 85
- TOF in a homogeneous field, 92
- toroidal mirror, 78
- Transverse momentum uncertainty, 77
- tunneling ionization, 20
- turbo molecular pump (TMP), 75
- undulators, 10
- variable gap undulators, 12
- Velocity Map Imaging (VMI), 15, 71
- voltage dividers, 86
- water window, 23
- Wavelength-position conversion, 59
- Wavevector in a dispersive medium, 27
- zone-of-silence, 75

# Curriculum Vitae

Felix Paul Sturm

## Persönliche Daten

Anschrift	Am Dachsberg 114 60435 Frankfurt am Main
Email	mail@xsturm.de
Geburtsdatum	16.06.1983, Frankfurt am Main
Nationalität	Deutsch



## Bildungsweg

06/2002	Abitur, Musterschule Frankfurt, Note: 1,1
2003 - 2009	Studium der Physik an der Goethe-Universität Frankfurt
05/2005	Vordiplom in Physik, Note: <i>gut</i>
08/2005 - 06/2006	Studium der Physik an der Ecole Normale Supérieure, Paris
06/2009	Diplom in Physik, Note: <i>sehr gut (mit Auszeichnung)</i> ; Titel: "Photo- and Auger Electron Angular Distributions of Fixed-in-Space CO <sub>2</sub> "
8/2009 - 12/2015	Promotion in Physik an der Goethe-Universität Frankfurt

## Zivildienst

11/2002 - 08/2003	Clementine Kinderhospital, Frankfurt
-------------------	--------------------------------------

## Stipendien und Preise

2002	Apollinaire-Preis für besondere Leistung im Schulfach Französisch
2005	Stipendium Europäisches Exzellenzprogramm des Deutschen Akademischen Auslandsdienstes (DAAD)
2010	Auszeichnung der Diplomarbeit mit dem Phillip-Siedler-Preis des Frankfurter Physikalischen Vereins
2010	Promotionsstipendium der Studienstiftung des deutschen Volkes

## Forschungsaufenthalte

2007 (1 Woche)	BESSY II, Berlin
2007 - 2008 (1Jahr)	Lawrence Berkeley National Laboratory, Berkeley (CA), USA
2008 (1 Woche)	BESSY II, Berlin
2009 (1 Woche)	BESSY II, Berlin
(2 Wochen)	Technische Universität Wien, Österreich
2009 - 2015 (6 Jahre)	Lawrence Berkeley National Laboratory, Berkeley (CA), USA
2010 (2 Wochen)	BESSY II, Berlin
(1 Woche)	FLASH, Hamburg
2011 (2 Wochen)	LCLS, Stanford, USA
2012 (1 Woche)	LCLS, Stanford, USA
(1 Woche)	BESSY II, Berlin
2014 (1 Woche)	BESSY II, Berlin

## Konferenzen

2009	RAS	Riezlern
	DPG	Hamburg
2010	UXSS	SLAC, Stanford (CA), USA
	DAMOP	Houston (TX), USA
	ICUP	Snowmass (CO), USA
2011	DAMOP	Atlanta (GO), USA
	ISWAMP	Dublin, Ireland
2012	DAMOP	Anaheim (CA), USA
2013	DAMOP	Quebec City, Canada
2014	DAMOP	Madison (WI), USA
2015	ISWAMP	Hamburg
	ICPEAC	Toledo, Spain

## Akademische Lehrer

Frankfurt, Paris:

Prof. Dr. W. Aßmus, Prof. Dr. J. Baumeister, Prof. Dr. J.M. Berroir,  
Prof. Dr. J. Bliedtner, Prof. Dr. R. Dörner, Prof. Dr. M. Huth, PD. Dr. T. Jahnke, Prof.  
Dr. J. Jacoby, Prof. Dr. P. Kopietz, Prof. Dr. H. Roskos, Dr. M. Schöffler, Prof. Dr. Dr.  
h.c. H. Stöcker

LBNL:

Dr. A. Belkacem, Dr. O. Gessner, Dr. P. Ranitovic, Dr. T. Weber,

## Publikationen

- [1] B. Gaire, I. Bocharova, F. P. Sturm, N. Gehrken, J. Rist, H. Sann, M. Kunitski, J. Williams, M. S. Schöffler, T. Jahnke, B. Berry, M. Zohrabi, M. Keiling, A. Moradmand, A. L. Landers, A. Belkacem, R. Dörner, I. Ben-Itzhak, and T. Weber. Hydrogen and fluorine migration in photo-double-ionization of 1,1-difluoroethylene (1,1-C<sub>2</sub>H<sub>2</sub>F<sub>2</sub>) near and above threshold. *Physical Review A*, 89(4):043423, Apr. 2014. doi: 10.1103/PhysRevA.89.043423.
- [2] B. Gaire, S. Y. Lee, D. J. Haxton, P. M. Pelz, I. Bocharova, F. P. Sturm, N. Gehrken, M. Honig, M. Pitzer, D. Metz, H.-K. Kim, M. Schöffler, R. Dörner, H. Gassert, S. Zeller, J. Voigtsberger, W. Cao, M. Zohrabi, J. Williams, A. Gatton, D. Reedy, C. Nook, T. Müller, A. L. Landers, C. L. Cocke, I. Ben-Itzhak, T. Jahnke, A. Belkacem, and T. Weber. Photo-double-ionization of ethylene and acetylene near threshold. *Physical Review A*, 89(1):013403, Jan. 2014. doi: 10.1103/PhysRevA.89.013403.
- [3] B. Gaire, D. J. Haxton, F. P. Sturm, J. Williams, A. Gatton, I. Bocharova, N. Gehrken, M. Schöffler, H. Gassert, S. Zeller, J. Voigtsberger, T. Jahnke, M. Zohrabi, D. Reedy, C. Nook, A. L. Landers, A. Belkacem, C. L. Cocke, I. Ben-Itzhak, R. Dörner, and T. Weber. Auger decay and subsequent fragmentation pathways of ethylene following K-shell ionization. *Physical Review A*, 92(1):013408, July 2015. doi: 10.1103/PhysRevA.92.013408.
- [4] L. F. Gomez, K. R. Ferguson, J. P. Cryan, C. Bacellar, R. M. P. Tanyag, C. Jones, S. Schorb, D. Anielski, A. Belkacem, C. Bernando, R. Boll, J. Bozek, S. Carron, G. Chen, T. Delmas, L. Englert, S. W. Epp, B. Erk, L. Foucar, R. Hartmann, A. Hexemer, M. Huth, J. Kwok, S. R. Leone, J. H. S. Ma, F. R. N. C. Maia,

- E. Malmerberg, S. Marchesini, D. M. Neumark, B. Poon, J. Prell, D. Rolles, B. Rudek, A. Rudenko, M. Seifrid, K. R. Siefertmann, F. P. Sturm, M. Swiggers, J. Ullrich, F. Weise, P. Zwart, C. Bostedt, O. Gessner, and A. F. Vilesov. Shapes and vorticities of superfluid helium nanodroplets. 345(6199):906–909, Aug. 2014. doi: 10.1126/science.1252395.
- [5] K. Kreidi, P. Demekhin, T. Jahnke, T. Weber, T. Havermeier, X.-J. Liu, Y. Morisita, S. Schössler, L. Schmidt, M. Schöffler, M. Odenweller, N. Neumann, L. Foucar, J. Titze, B. Ulrich, F. Sturm, C. Stuck, R. Wallauer, S. Voss, I. Lauter, H. Kim, M. Rudloff, H. Fukuzawa, G. Prümper, N. Saito, K. Ueda, A. Czasch, O. Jagutzki, H. Schmidt-Böcking, S. Scheit, L. Cederbaum, and R. Dörner. Photo- and Auger-Electron Recoil Induced Dynamics of Interatomic Coulombic Decay. *Physical Review Letters*, 103(3), July 2009. doi: 10.1103/PhysRevLett.103.033001.
- [6] K. Kreidi, T. Jahnke, T. H. Weber, T. Havermeier, R. E. Grisenti, X. Liu, Y. Morisita, S. Schössler, L. P. H. Schmidt, M. Schöffler, M. Odenweller, N. Neumann, L. Foucar, J. Titze, B. Ulrich, F. Sturm, C. Stuck, R. Wallauer, S. Voss, I. Lauter, H. K. Kim, M. Rudloff, H. Fukuzawa, G. Prümper, N. Saito, K. Ueda, A. Czasch, O. Jagutzki, H. Schmidt-Böcking, S. K. Semenov, N. A. Cherepkov, and R. Dörner. Localization of inner shell photoelectron emission and interatomic Coulombic decay in neon dimers. *Journal of Physics: Conference Series*, 212:012007, Feb. 2010. doi: 10.1088/1742-6596/212/1/012007.
- [7] A. Menssen, C. Trevisan, M. Schoffler, T. Jahnke, I. Bocharova, F. Sturm, N. Gehrken, B. Gaire, H. Gassert, S. Zeller, J. Voigtsberger, A. Kuhlins, A. Gatton, J. Sartor, D. Reedy, C. Nook, B. Berry, M. Zohrabi, A. Kalinin, A. Belkacem, R. Dörner, T. Weber, A. Landers, T. Rescigno, C. McCurdy, and J. Williams. Molecular frame photoelectron angular distributions for core ionization of ethane, carbon tetrafluoride and 1,1-difluoroethylene. *Journal of Physics B: Atomic, Molecular and Optical Physics*, 2015 submitted.
- [8] T. Osipov, T. Weber, T. N. Rescigno, S. Y. Lee, A. E. Orel, M. Schöffler, F. P. Sturm, S. Schössler, U. Lenz, T. Havermeier, M. Kühnel, T. Jahnke, J. B. Williams, D. Ray, A. Landers, R. Dörner, and A. Belkacem. Formation of inner-shell autoionizing  $\text{CO}^{\{+\}}$  states below the  $\text{CO}^{\{2+\}}$  threshold. *Physical Review A*, 81(1), Jan. 2010. doi: 10.1103/PhysRevA.81.011402.
- [9] M. Pitzer, M. Kunitski, A. S. Johnson, T. Jahnke, H. Sann, F. Sturm, L. P. H. Schmidt, H. Schmidt-Böcking, R. Dörner, J. Stohner, J. Kiedrowski, M. Reggelin, S. Marquardt, A. Schießer, R. Berger, and M. S. Schöffler. Direct Determination of Absolute Molecular Stereochemistry in Gas Phase by Coulomb Explosion Imaging. 341(6150):1096–1100, June 2013. doi: 10.1126/science.1240362.
- [10] S. Semenov, K. Kreidi, T. Jahnke, T. Weber, T. Havermeier, R. Grisenti, X. Liu, Y. Morisita, L. Schmidt, M. Schöffler, M. Odenweller, N. Neumann, L. Foucar, J. Titze, B. Ulrich, F. Sturm, H. Kim, K. Ueda, A. Czasch, O. Jagutzki, N. Cherepkov, and R. Dörner. Interatomic Coulombic decay of fixed-in-space neon dimers. *Physical Review A*, 85(4), Apr. 2012. doi: 10.1103/PhysRevA.85.043421.
- [11] A. Shavorskiy, A. Cordones, J. Vura-Weis, K. Siefertmann, D. Slaughter, F. Sturm, F. Weise, H. Bluhm, M. Strader, H. Cho, M.-F. Lin, C. Bacellar, C. Khurmi, M. Hertlein, J. Guo, T. Tyliczszak, D. Prendergast, G. Coslovich, J. Robinson, R. A. Kaindl, R. W. Schoenlein, A. Belkacem, T. Weber, D. M. Neumark, S. R. Leone, D. Nordlund, H. Ogasawara, A. R. Nilsson, O. Krupin, J. J. Turner, W. F. Schlotter,

- M. R. Holmes, P. A. Heimann, M. Messerschmidt, M. P. Minitti, M. Beye, S. Gul, J. Z. Zhang, N. Huse, and O. Gessner. Time-resolved x-ray photoelectron spectroscopy techniques for real-time studies of interfacial charge transfer dynamics. *AIP Conference Proceedings*, 1525(1):475, Apr. 2013. doi: doi:10.1063/1.4802374.
- [12] K. R. Siefertmann, C. D. Pemmaraju, S. Neppl, A. Shavorskiy, A. A. Cordones, J. Vura-Weis, D. S. Slaughter, F. P. Sturm, F. Weise, H. Bluhm, M. L. Strader, H. Cho, M.-F. Lin, C. Bacellar, C. Khurmi, J. Guo, G. Coslovich, J. S. Robinson, R. A. Kaindl, R. W. Schoenlein, A. Belkacem, D. M. Neumark, S. R. Leone, D. Nordlund, H. Ogasawara, O. Krupin, J. J. Turner, W. F. Schlotter, M. R. Holmes, M. Messerschmidt, M. P. Minitti, S. Gul, J. Z. Zhang, N. Huse, D. Prendergast, and O. Gessner. Atomic-Scale Perspective of Ultrafast Charge Transfer at a Dye–Semiconductor Interface. *The Journal of Physical Chemistry Letters*, pages 2753–2759, July 2014. doi: 10.1021/jz501264x.
- [13] N. Sisourat, H. Sann, N. Kryzhevoi, P. Kolorenč, T. Havermeier, F. Sturm, T. Jahnke, H.-K. Kim, R. Dörner, and L. Cederbaum. Interatomic Electronic Decay Driven by Nuclear Motion. *Physical Review Letters*, 105(17), Oct. 2010. doi: 10.1103/PhysRevLett.105.173401.
- [14] F. Sturm, M. Schöffler, S. Lee, T. Osipov, N. Neumann, H.-K. Kim, S. Kirschner, B. Rudek, J. Williams, J. Daughetee, C. Cocke, K. Ueda, A. Landers, T. Weber, M. Prior, A. Belkacem, and R. Dörner. Photoelectron and Auger-electron angular distributions of fixed-in-space CO<sub>2</sub>. *Physical Review A*, 80(3), Sept. 2009. doi: 10.1103/PhysRevA.80.032506.
- [15] F. P. Sturm, T. W. Wright, D. Ray, I. A. Bocharova, P. Ranitovic, A. Belkacem, and T. Weber. Time Resolved 3D Momentum Imaging of Molecular Dynamics with VUV-XUV Pulse Pairs. *Review of Scientific Instruments*, 2015 in preparation.
- [16] F. P. Sturm, T. W. Wright, D. Ray, I. A. Bocharova, P. Ranitovic, A. Belkacem, and T. Weber. Dynamically Induced Dissociative Ionization of Hydrogen Molecules in Multicolor Multi-Photon VUV/IR fields. *Physical Review A*, 2016 in preparation.
- [17] F. Trinter, M. S. Schöffler, H.-K. Kim, F. P. Sturm, K. Cole, N. Neumann, A. Vredenburg, J. Williams, I. Bocharova, R. Guillemin, M. Simon, A. Belkacem, A. L. Landers, T. Weber, H. Schmidt-Böcking, R. Dörner, and T. Jahnke. Resonant Auger decay driving intermolecular Coulombic decay in molecular dimers. Dec. 2013. doi: 10.1038/nature12927.
- [18] J. Williams, C. Trevisan, M. Schöffler, T. Jahnke, I. Bocharova, H. Kim, B. Ulrich, R. Wallauer, F. Sturm, T. Rescigno, A. Belkacem, R. Dörner, T. Weber, C. McCurdy, and A. Landers. Imaging Polyatomic Molecules in Three Dimensions Using Molecular Frame Photoelectron Angular Distributions. *Physical Review Letters*, 108(23), June 2012. doi: 10.1103/PhysRevLett.108.233002.
- [19] J. B. Williams, C. S. Trevisan, M. S. Schöffler, T. Jahnke, I. Bocharova, H. Kim, B. Ulrich, R. Wallauer, F. Sturm, T. N. Rescigno, A. Belkacem, R. Dörner, T. Weber, C. W. McCurdy, and A. L. Landers. Probing the dynamics of dissociation of methane following core ionization using three-dimensional molecular-frame photoelectron angular distributions. *Journal of Physics B: Atomic, Molecular and Optical Physics*, 45(19):194003, Oct. 2012. doi: 10.1088/0953-4075/45/19/194003.